GIACOMO BACCO

ADVANCED DESIGN AND OPTIMIZATION OF ANISOTROPIC SYNCHRONOUS MACHINES

University of Padova
Department of Industrial Engineering

PhD Course in Industrial Engineering
Electrical Energy Engineering

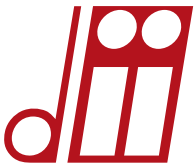

xxxii phd cycle

Advanced Design and Optimization of Anisotropic Synchronous Machines

Candidate
Giacomo Bacco

Supervisor
Prof. Nicola Bianchi

PhD School Coordinator
Prof. Paolo Colombo

Curriculum Coordinator
Prof. Roberto Turri

30 September 2019

Giacomo Bacco: *Advanced Design and Optimization of Anisotropic Synchronous Machines,* © September 2019

I have not failed. I've just found 10 000 ways that won't work.

— Thomas Alva Edison

ABSTRACT

This work covers many research aspects of anisotropic synchronous motors, which are synchronous reluctance (SyR), permanent magnet assisted synchronous reluctance (PMaSyR) and interior permanent magnet (IPM) machines. In fact, all these kinds of machines exhibit quite a strong reluctance torque component, hence the name anisotropic.

From the early 2000s, the design of electric machines started to deeply rely on finite element analysis (FEA) coupled to automatic optimization algorithms. This workflow enabled the machine designer to make fewer initial sizing hypotheses and to explore a wider design space. The drawbacks of this approach are that the time required is long and that the computational resources needed are quite large. However, the computing performances have always been improving over the years, especially when multi-processor architectures became widespread. Therefore nowadays it is common to employ tens or even hundreds of cores on cluster PCs to perform FEA during optimization runs.

The thesis is structured as follows. The first part gives the background knowledge needed to develop the topics covered in the following. This comprehends an introduction to the machines studied, some general knowledge about magnetic materials, some basic concepts about the differential evolution (DE) algorithm, and the drawing of fluid rotor flux-barriers.

The second part deals with the analytical modeling of SyR and PMaSyR machines. The complete model is nonlinear and may become convoluted to develop especially in an industrial environment. Therefore, using simplifying assumptions, a handful of simple equations can be derived. This simple model is also extended and applied to asymmetric rotor structures, which try to compensate torque harmonics.

The third part focuses on applied multi-objective optimizations coupled to FEA for many different case studies. In particular, a SyR motor (SyRM) for pumping applications is optimized, prototyped and tested. Then, a feasibility study on a very low speed PMaSyR motor is carried out through multi-objective optimization. After that, high speed SyRMs are studied and optimized to understand the power limits of this kind of machine. Finally, the DE multi-objective optimization algorithm is also applied to improve the sensorless-control capabilities of anisotropic machines by design.

SOMMARIO

Questo lavoro analizza molti aspetti di ricerca dei motori sincroni anisotropi, che includono le macchine sincrone a riluttanza pura (SyR), a riluttanza assistita da magneti (PMaSyR) e le macchine a magneti permanenti interni (IPM). Infatti, tutte queste macchine esibiscono una forte componente di riluttanza, da cui il nome anisotrope.

Dai primi anni 2000, la progettazione di macchine elettriche ha cominciato a basarsi in modo consistente sull'analisi agli elementi finiti (FEA) accoppiata ad algoritmi di ottimizzazione automatici. Questo flusso di lavoro permette al progettista di fare un minor numero di ipotesi preliminari e di esplorare uno spazio di progetto più ampio. Gli svantaggi di questo approccio sono che il tempo richiesto è lungo e che le risorse computazionali richieste possono essere elevate. Tuttavia, le prestazioni dei computer migliorano di anno in anno, e in particolar modo con la diffusione delle architetture a multi-processore. Pertanto oggigiorno è comune impiegare decine o persino centinaia di *core* su *cluster* di PC per effettuare analisi agli elementi finiti durante un'ottimizzazione.

La tesi è strutturata nel seguente modo. La prima parte copre le conoscenze di base necessarie a sviluppare gli argomenti trattati nel seguito. C'è quindi un'introduzione alle macchine studiate, delle conoscenze generali sui materiali magnetici e ferromagnetici, alcuni concetti di base sull'algoritmo di ottimizzazione *differential evolution* (DE) utilizzato, e il disegno delle barriere fluide dei rotori di macchine a riluttanza.

Nella seconda parte si sono sviluppati modelli analitici di macchine SyR e PMaSyR. Il modello completo è non lineare e può diventare abbastanza complesso da sviluppare, specialmente in un contesto industriale. Pertanto, usando alcune ipotesi semplificative, si possono derivare alcune semplici equazioni di progetto. Questo modello semplice è anche esteso e applicato a strutture di rotore asimmetriche, che tentano di compensare alcune armoniche di coppia.

La terza parte si concentra sull'applicazioni di ottimizzazioni multi-obiettivo accoppiate a FEA per alcuni casi di studio. In particolare, si è ottimizzato, prototipato e testato un motore SyRper pompe centrifughe. Poi, è stato condotto uno studio di fattibilità per un motore PMaSyR attraverso ottimizzazioni multi-obiettivo. Dopodiché si sono studiati motori SyRper alte velocità e si sono dedotti i limiti di potenza di questa macchina. Infine l'ottimizzazione DE multi-obiettivo è stata anche applicata per migliorare le capacità di controllo *sensorless* delle macchine anisotrope già in fase di progetto.

CONTENTS

Part I

BACKGROUND KNOWLEDGE

1 INTRODUCTION

The use of synchronous electric machines is becoming more and more widespread thanks to their numerous advantages: high efficiency over a wide range of operation, high power factor, constant torque up to the base speed, high torque density, quick dynamics, simple control laws, and so on.

Among them, the anisotropic synchronous machines are even better in almost every regard: higher torque density for Interior Permanent Magnet (IPM) motors, wide region of high efficiency operation, wide Constant Power Speed Range (CPSR), intrinsic sensorless-control capability, rectangular magnets in lower amount, cheaper ferrite magnets if the reluctance torque component is sufficiently strong.

When compared to Induction Motors (IMs), synchronous machines appear more expensive if rare-earth (RE) magnets are employed, they require the inverter, they may present some additional issues when a fault occurs, they are susceptible to demagnetization if not properly designed, and so on. However, synchronous motors do not only represent alternatives to IM but, thanks to their performance, they are also valid alternatives for many mechanical, pneumatic or hydraulic actuators that are very common in a plethora of applications: among these, two notable examples are aircrafts and ground vehicles.

The interest in Synchronous Reluctance (SyR) and Permanent Magnet assisted Synchronous Reluctance (PMaSyR) machines is growing up in recent years. They have been proposed as valid alternatives to permanent magnet and induction machines in both constant-speed and variable-speed applications (Moghaddam et al., 2012b; Barcaro et al., 2014a; Fratta et al., 1992; Barcaro, 2011; Taghavi et al., 2017; Vagati et al., 1998; Miller et al., 1991; Lipo, 1991; Lipo et al., 1994; Kamper, 2013). These machines exhibit several advantages (Jahns et al., 1996; Wang et al., 2000). Among the others, they are:

- low cost,
- high torque density,
- overall good efficiency (Boglietti et al., 2005),
- wide flux-weakening capability (Chalmers et al., 1998),
- good fault-tolerance,
- sensorless rotor position detection capability,
- robust structure.

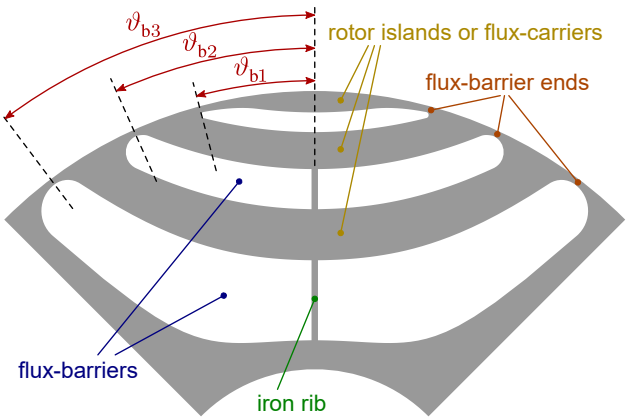

Figure 1.1
Cross section of one rotor pole of the SyR machine.

Although the intrinsic advantages of these machines, a thoughtful design is key to reach the goals of good performance and high efficiency (Staton et al., 1993; Matsuo et al., 1994; Zhao et al., 2015). In fact, these machines have quite a complex rotor structure. The sketch of one rotor pole of a Synchronous Reluctance Machine (SyRM) is shown in Figure 1.1. The flux lines are deflected by the rotor geometry which guides them along preferential paths. To obtain proper performance, the rotor anisotropy (i.e. the ratio between the d-axis and q-axis inductance) has to be necessarily high (Staton et al., 1993; Lipo et al., 1994; Moghaddam et al., 2014; Moghaddam et al., 2010). In particular, one of the most important design step is the choice of the number of flux-barriers and their end-angles (Vagati et al., 1992; Bianchi et al., 2009b; Pellegrino et al., 2013). The torque ripple, which characterizes the torque waveform (Moghaddam et al., 2012b), is due to the interaction between the stator space harmonics and the rotor anisotropy. A wrong rotor design may cause a decrease of the average torque but also very high torque ripple. The peak-to-peak ripple can even reach 100% the average value if the rotor flux-barriers are incorrectly designed. In the past, such an issue has been highlighted in various works. Different approaches have been adopted so as to minimize the torque ripple.

Differently from other machine topologies, rotor skewing is not enough to minimize the torque ripple (Fratta et al., 1993; Jahns et al., 1996; Bianchi et al., 2008b; Bacco et al., 2017). In fact, the skewing modifies the d- and q-axis with respect to the stator, so that it modifies the torque contribution, along the rotor axisl length. The SyR machines are mainly analyzed using Finite Element Analysis (FEA) (Kamper et al., 1996; Miller et al., 2000; Vagati et al., 2000; Alotto et al., 2011). The results are precise and useful for achieving a specific geometry to be prototyped, but they only refer to particular solutions. In other words, it is difficult to find general design rules, since the analysis is focused on a single objective. For instance, information of the harmonic impact, caused by the stator magnetomotive force (MMF) or the rotor geometry, is lost. In addition, it is more difficult to quantify the impact of the stator slot number, or the number of rotor flux-barriers, or the winding displacement, and so forth.

A strategy that is often applied has been proposed in (Fratta et al., 1993; Vagati et al., 1998). Starting from an analytical model, the electromagnetic torque is computed after deriving the magnetic quantities. The model is based on the assumption that the rotor flux-barrier ends are evenly spaced. In other words, there is the same angle between adjacent flux-barrier ends. From this analysis, a guideline to select the number of rotor segments (and so flux-barriers) per pole pair is obtained according to the stator slots Q and the number of pole pairs p, i.e. $n_r = Q/p \pm 4$. The FEA results and the tests are in good agreement with the analytical predictions. However, these works strictly depend on the assumption above and do not consider the iron saturation.

In (Moghaddam et al., 2012a) it is shown that a better torque ripple is obtained when the angle of the first (the smaller) flux-barrier-end is increased with respect to the others. In other words, the flux-barrier ends are all evenly spaced but the first one, whose angle has to be optimized. This result has been obtained by means of a parametric analysis based on finite element simulations. Then, the results depend on the particular number of slots, air gap thickness, electric loading, et cetera.

A different approach has been adopted in (Barcaro et al., 2009; Bianchi et al., 2008b; Bianchi et al., 2006). An analytical model has been developed so as to consider all the MMF space harmonics produced by the stator winding and their interaction with the rotor anisotropy. The advantage of the analytical model is that the impact of each harmonic is considered separately, to evaluate which is the most critical. The model allows plotting the average torque and the torque harmonics as functions of the rotor barrier-end positions, obtaining some maps, which are used as guidelines for a proper design. In particular, the best angles which minimize the torque ripple are clearly individuated. In (Barcaro et al., 2010) the model has been extended to consider the iron losses in the stator teeth.

An interesting application of such maps is the combination of the flux-barrier angles in the same rotor, to obtain a sort of compensation of the torque harmonics. According to the results drawn in these torque maps (Bianchi et al., 2006), rotor using laminations with different flux-barriers are proposed (solution referred to as "Romeo and Juliet"), or laminations with different flux-barrier shapes in north and south poles (solution referred to as "Machaon").

A completely different approach is proposed in (Kano et al., 2004; Lopez-Torres et al., 2018), which is based on a lumped-parameter magnetic network. The model considers the saturation of the magnetic parts of the machine by means of nonlinear reluctances in the circuit. The authors show satisfactory results and claim that they are achieved in a reasonably short time. Anyway, even if this approach is different from FEA, it bears the same drawback of the lack of generality, since the network is built on the basis of a given geometry and, therefore, the results refer to that specific machine.

In this work, a nonlinear analytical model for SyR and PMaSyR is derived in Chapter 5, which is later simplified in Chapter 6 to highlight the real source of the torque ripple.

In a lot of applications, the recent trend is to couple the electric machine directly to the mechanical shaft, to avoid the use of a gearbox. This is due to a number of reasons:

- increased overall efficiency
- increased system reliability
- reduced weight
- reduced overall footprint of the system
- reduced maintenance cost
- reduced noise

This trend affects low-speed as well as high-speed applications. In fact, most of the presented advantages are shared by both categories. But the most prominent advantage is certainly the higher reliability of the overall system. This is a very important requirement when the machine is installed in harsh environments (Grauers, 1996; Lampola, 1998; Popescu et al., 2013; Zhou et al., 2017).

Low speed machines find applications in energy production, electrical propulsion, industrial automation, pumps and so on. They typically employs strong RE magnets with high pole numbers. A feasibility study on a high-torque low-speed PMaSyR motor is shown in Chapter 7.

On the other hand, high-speed electric machines are more and more used in many applications, such as turbochargers, racing engines and fuel pumps (Gerada et al., 2014; Zhu et al., 1997; Castagnini et al., 2002). The additional advantage that they have is the higher power density. Among the others, Permanent Magnet (PM) machines are an attractive solution for high-speed applications. They have reduced size, high power density and high efficiency. On the other hand, due to the high-speed of rotation and high rated frequency, high-speed PM machine design requires to take into account different problems. Surface-mounted Permanent Magnet (SPM) machines are usually adopted in such systems for their high torque density thanks to rare-earth PMs. Rare-earth PMs creates the flux density at the air-gap, which induces the electro-motive force in the stator winding. No magnetizing current is necessary, reducing the total current amplitude and the Joule losses. A retaining sleeve is necessary to keep PMs on the rotor against the centrifugal force, though. Sleeve material must be non-conductive in order to avoid additional rotor losses. For this purpose, a carbon fiber sleeve is usually adopted for its low conductivity and high tensile strength (Binder et al., 2006; Zhang et al., 2015). However, the carbon fiber exhibits a low thermal conductivity, reducing the heat transfer from the rotor to the air-gap (Howey et al., 2012). This involves a difficult rotor cooling so rotor losses have to be minimized. In fact, the main

issue for magnets at high-speed, in addition to the mechanical stress, is the internally generated heat caused by flux pulsation due to stator slotting (Alberti et al., 2008; Boules, 1981), air-gap space harmonics (Bianchi et al., 2009c; Boules, 1981), and asynchronous fields due to time harmonics in the current waveforms (Lu et al., 2002; Mecrow et al., 1993; Van der Veen et al., 1997).

The cost of rare-earth PMs, the risk of their demagnetization and the necessary sleeve adoption require to consider other alternatives such as the SyR machine. The SyR motor has not been deeply studied for high speed applications (Ikäheimo, J. and Kolehmainen, J. and Känsäkangas, T. and Kivelä V. and Moghaddam, Reza Rajabi, 2014), where permanent magnet machines are mainly considered (Boules, 1981; Zhu et al., 1997; Castagnini et al., 2002; Bianchi et al., 2004). The design of SyR machines for high-speed applications has to be carried out considering both magnetic and mechanical aspects. In particular, the iron ribs must be accurately designed with the aim of achieving the minimum flux leakage in the ribs and ensuring the structural integrity. All these aspects are shown explained in Chapter 9, where the design of this kind of machines is carried out starting from analytical models and continuing with advanced optimization techniques that consider mechanical issues during the run.

As mentioned, SyR machines have an intrinsic saliency which allows for sensorless position estimation at low speeds using high-frequency (HF) voltage injection (Corley et al., 1998; Jeong et al., 2005; Yang et al., 2017). However, iron cross-saturation reduces the effectiveness of this position estimation algorithm creating an estimation error (Guglielmi et al., 2006; Bianchi et al., 2013; Barcaro et al., 2016). The typical solution for this problem is to add a compensation angle or equivalently tilt the high-frequency voltage vector to correct the estimated position (Zhu et al., 2007; Kuehl et al., 2012). In case of heavily saturated machines, this kind of strategy is not enough, though. In fact, the algorithm could even not converge. This aspect has been analyzed in (Kwon et al., 2017; Manzolini et al., 2018), where different kind of compensations were proposed to extend the self-sensing feasibility torque range. Even though these compensation techniques proved to be effective, they require additional effort for their implementation and also some information about the machine magnetic behavior. In Chapter 10 this issue has been tackle at an early design phase, embedding proper self-sensing capabilities into the design optimization of the motor.

1.1 SYNCHRONOUS MACHINES VOLTAGE EQUATIONS

The general equations of passive-rotor synchronous machines are basically the voltage-balance due to the resistive voltage drop and the induced back electromotive force in the winding.

$$\begin{cases} u_a = Ri_a + \dfrac{\mathrm{d}\lambda_a}{\mathrm{d}t} \\ u_b = Ri_b + \dfrac{\mathrm{d}\lambda_b}{\mathrm{d}t} \\ u_c = Ri_c + \dfrac{\mathrm{d}\lambda_c}{\mathrm{d}t} \end{cases} \begin{array}{l} \xRightarrow{\mathcal{C}} \\ \\ \xRightarrow{\mathcal{P}} \end{array} \begin{array}{l} \underline{u}^s = R\underline{i}^s + \dfrac{\mathrm{d}\underline{\lambda}^s}{\mathrm{d}t} \\ \\ \underline{u}^r = R\underline{i}^r + \dfrac{\mathrm{d}\underline{\lambda}^r}{\mathrm{d}t} + \mathrm{j}\omega^r\underline{\lambda}^r \end{array}$$

The phase voltage equations can be transformed in the equivalent two-phase $\alpha\beta$ stationary reference frame using the Clarke's transformation ($\mathcal{C}$), or in the equivalent two-phase dq rotating synchronous reference frame using the Park's transformation ($\mathcal{P}$). This last voltage equation is the most useful for modeling and analyzing synchronous machines, and it can also be written in matrix form

$$\boldsymbol{u} = R\boldsymbol{i} + \frac{\mathrm{d}\boldsymbol{\lambda}}{\mathrm{d}t} + \omega\boldsymbol{J}\boldsymbol{\lambda}$$

$$\begin{Bmatrix} u_d \\ u_q \end{Bmatrix} = R\begin{Bmatrix} i_d \\ i_q \end{Bmatrix} + \frac{\mathrm{d}}{\mathrm{d}t}\begin{Bmatrix} \lambda_d \\ \lambda_q \end{Bmatrix} + \omega\begin{bmatrix} 0 & -1 \\ 1 & 0 \end{bmatrix}\begin{Bmatrix} \lambda_d \\ \lambda_q \end{Bmatrix}$$

From this matrix equation, the input active power can be determined, pre-multiplying by $\boldsymbol{i}^{\mathrm{T}}$

$$\underbrace{\boldsymbol{i}^{\mathrm{T}}\boldsymbol{u}}_{\text{Input power}} = \underbrace{\boldsymbol{i}^{\mathrm{T}}R\boldsymbol{i}}_{\text{Joule losses}} + \underbrace{\boldsymbol{i}^{\mathrm{T}}\frac{\mathrm{d}\boldsymbol{\lambda}}{\mathrm{d}t}}_{\substack{\text{Magn. energy variation} \\ \text{p. unit of time}}} + \underbrace{\omega\,\boldsymbol{i}^{\mathrm{T}}\boldsymbol{J}\boldsymbol{\lambda}}_{\text{Output power}} \tag{1.1}$$

This expression is valid as long as any dissipative phenomena in the ferromagnetic material is neglected. In the previous transformation, the power-invariant version was used, but it is more usual to adopt the amplitude-invariant (power-variant) space vector transformations. In that case, (1.1) becomes

$$\frac{3}{2}\boldsymbol{i}^{\mathrm{T}}\boldsymbol{u} = \frac{3}{2}\boldsymbol{i}^{\mathrm{T}}R\boldsymbol{i} + \frac{3}{2}\boldsymbol{i}^{\mathrm{T}}\frac{\mathrm{d}\boldsymbol{\lambda}}{\mathrm{d}t} + \frac{3}{2}\omega\boldsymbol{i}^{\mathrm{T}}\boldsymbol{J}\boldsymbol{\lambda} \tag{1.2}$$

And the electromagnetic torque expression can be determined from the last term of (1.2) as

$$T_{\mathrm{em}} = \frac{3}{2}p\,\boldsymbol{i}^{\mathrm{T}}\boldsymbol{J}\boldsymbol{\lambda} = \frac{3}{2}p\left(\lambda_d i_q - \lambda_q i_d\right) \tag{1.3}$$

where p is the number of pole pairs. The second term of (1.1) is the stored magnetic energy variation per unit of time. This can be verified remembering the magnetic energy expression

$$W_{\mathrm{m}} = \int_0^{\lambda} i(\lambda')\,\mathrm{d}\lambda \tag{1.4}$$

and taking the derivative with respect to time

$$\frac{\mathrm{d}W_\mathrm{m}}{\mathrm{d}t} = \frac{\mathrm{d}W_\mathrm{m}}{\mathrm{d}\lambda}\frac{\mathrm{d}\lambda}{\mathrm{d}t} = i\frac{\mathrm{d}\lambda}{\mathrm{d}t}$$

Actually, (1.2) expresses only the active power balance happening inside the machine during the electromechanical energy conversion. However, starting from the space vector expression in complex form

$$\underline{u} = R\underline{i} + \frac{\mathrm{d}\underline{\lambda}}{\mathrm{d}t} + \mathrm{j}\omega\underline{\lambda}$$

and multiplying it by $\underline{i}^*$, it is possible to obtain both the active and reactive power balance

$$\underline{u}\underline{i}^* = R\underline{i}\underline{i}^* + \frac{\mathrm{d}\underline{\lambda}}{\mathrm{d}t}\underline{i}^* + \mathrm{j}\omega\underline{\lambda}\underline{i}^* \tag{1.5}$$

and splitting the real and imaginary part

$$\begin{cases} u_d i_d + u_q i_q = R\left(i_d^2 + i_q^2\right) + \dfrac{\mathrm{d}\lambda_d}{\mathrm{d}t} i_d + \dfrac{\mathrm{d}\lambda_q}{\mathrm{d}t} i_q + \omega\left(\lambda_d i_q - \lambda_q i_d\right) \\ u_q i_d - u_d i_q = \dfrac{\mathrm{d}\lambda_d}{\mathrm{d}t} i_q - \dfrac{\mathrm{d}\lambda_q}{\mathrm{d}t} i_d + \omega\left(\lambda_d i_d + \lambda_q i_q\right) \end{cases} \tag{1.6}$$

Let us analyze each term individually. $u_d i_d + u_q i_q$ represents the input active power at the electrical terminals of the electric machine. $R\left(i_d^2 + i_q^2\right)$ are the stator winding Joule losses. $\frac{\mathrm{d}\lambda_d}{\mathrm{d}t} i_d + \frac{\mathrm{d}\lambda_q}{\mathrm{d}t} i_q$ represents the change in the stored magnetic energy in a unit of time. $\omega\left(\lambda_d i_q - \lambda_q i_d\right)$ is the output electromechanical power.

Now, looking at the reactive power balance, there is $u_q i_d - u_d i_q$, which is the input reactive power. $\omega\left(\lambda_d i_d + \lambda_q i_q\right)$ is the reactive power used to keep the machine rotating magnetization. The last term is $\frac{\mathrm{d}\lambda_d}{\mathrm{d}t} i_q - \frac{\mathrm{d}\lambda_q}{\mathrm{d}t} i_d$, and it requires some additional steps for the full comprehension.

$$\begin{aligned} \frac{\mathrm{d}\lambda_d}{\mathrm{d}t} i_q - \frac{\mathrm{d}\lambda_q}{\mathrm{d}t} i_d &= \frac{\mathrm{d}(\lambda_d i_q)}{\mathrm{d}t} - \frac{\mathrm{d}(\lambda_q i_d)}{\mathrm{d}t} - \lambda_d \frac{\mathrm{d}i_q}{\mathrm{d}t} + \lambda_q \frac{\mathrm{d}i_d}{\mathrm{d}t} \\ &= \underbrace{\frac{\mathrm{d}(\lambda_d i_q - \lambda_q i_d)}{\mathrm{d}t}}_{\frac{\mathrm{d}T_\mathrm{m}}{\mathrm{d}t}} - \lambda_d \frac{\mathrm{d}i_q}{\mathrm{d}t} + \lambda_q \frac{\mathrm{d}i_d}{\mathrm{d}t} \end{aligned}$$

So the first term of the last row is the derivative of the electromagnetic torque, and it is somehow related to the torque ripple of the machine. It is also very reasonable for the ripple to be associated with the reactive power, since it has zero average torque and it causes only oscillations.

2

MAGNETIC MATERIALS

All materials can be classified in terms of their magnetic behavior falling into one of five categories, depending on their magnetic susceptibility.

The two most common types of magnetism are diamagnetism and paramagnetism, which account for most of the periodic table of elements at room temperature (see Figure 2.1). These elements are usually referred to as nonmagnetic, whereas those which are referred to as magnetic are actually classified as ferromagnetic. The only other type of magnetism observed in pure elements at room temperature is antiferromagnetism. Finally, magnetic materials can also be classified as ferrimagnetic although this is not observed in any pure element but can only be found in compounds, such as the mixed oxides, known as ferrites, from which ferrimagnetism derives its name (Rawlings, 2009).

When a field, $\boldsymbol{H}$ is applied to a material, it responds by producing a magnetic field, called magnetization and referred to as $\boldsymbol{M}$. This magnetization is a measure of the magnetic moment per unit volume of material. The applied field is the one that would be present if the field were applied to a vacuum. However, due to magnetization, the total flux of magnetic field lines is taken into account by the magnetic induction, $\boldsymbol{B}$, also called magnetic flux density. It counts exactly the magnetic flux crossing a unit area of the material. The flux is produced by both the external applied field and the internal reaction field. Therefore these quantities are related through

$$\boldsymbol{B} = \mu_0(\boldsymbol{H} + \boldsymbol{M}) \tag{2.1}$$

Then the magnetic susceptibility, χ_m, can be defined, measuring this reaction and identifying the type of magnetic material:

$$\chi_m = \frac{\boldsymbol{M}}{\boldsymbol{H}}$$

The other parameter which relates the magnetic induction and the magnetic field is the permeability of the material

$$\mu = \frac{\boldsymbol{B}}{\boldsymbol{H}}$$

All these relationships are summarized in the following equations:

$$\boldsymbol{B} = \mu\boldsymbol{H} = \mu_0\mu_r\boldsymbol{H} = \mu_0\boldsymbol{H} + \boldsymbol{J} = \mu_0(\boldsymbol{H} + \boldsymbol{M}) = \mu_0(1 + \chi_m)\boldsymbol{H} \tag{2.2}$$

where

$$\mu_r = \frac{\mu}{\mu_0} = \chi_m + 1$$

and $\boldsymbol{J}$ is the magnetic polarization, also referred to as the intensity of magnetization.

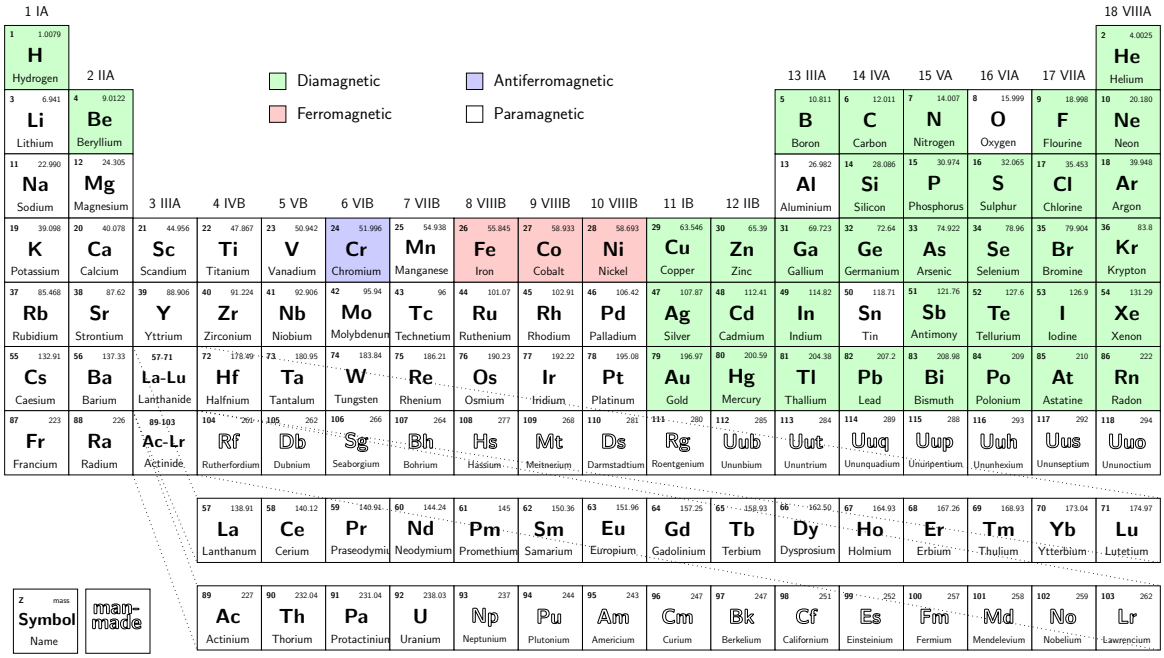

Figure 2.1
Periodic table. Elements are classified according to their magnetic behavior.

2.1 FERROMAGNETIC MATERIALS

Ferromagnetic materials are magnetic even without the external applied field. They exhibit spontaneous magnetization as a result of the ordered internal magnetic moments.

Ferromagnetism is only possible when atoms are arranged in a lattice and the atomic magnetic moments can interact to align parallel to each other. In 1907 Weiss postulated the presence of magnetic domains within the material, which are regions where the atomic magnetic moments are aligned. The movement of these domains determines how the material responds to a magnetic field. Consequently the susceptibility is a function of applied magnetic field and usually ferromagnetic

Table 2.1
Susceptibility reference value at room temperature for each type of magnetic material (Rawlings, 2009).

Type of magnetism	**Susceptibility**	**Example**	
Diamagnetism	Small and negative	Cu	$-0.77 \cdot 10^{-6}$
Paramagnetism	Small and positive	Mn	$66.10 \cdot 10^{-6}$
Ferromagnetism	Large and positive, function of the applied field	Fe	Up to $\sim 100\,000$
Antiferromagnetism	Small and positive	Cr	
Ferrimagnetism	Large and positive, function of the applied field	Ba Ferrite	Up to ~ 3

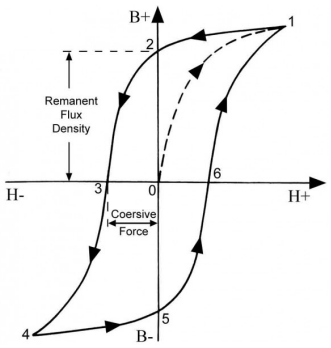

Figure 2.2
Example of a ferromagnetic material *B-H* curve.

materials are compared in terms of saturation magnetization rather than susceptibility.

In Figure 2.1 it can be seen that the only ferromagnetic materials at room temperature are Iron, Cobalt and Nickel.

The relation between the magnetizing force $\boldsymbol{H}$ and the flux density or magnetic induction $\boldsymbol{B}$ which it produces in a ferromagnetic material is of considerable importance. It is most conveniently expressed by means of characteristic curves.

For purposes of explanation, a ferromagnetic material is considered to be placed in a region where the magnetic field intensity can be varied. The magnetization force is varied through changing the current in the coil. The material is originally demagnetized. If the flux density is measured as a function of the magnetizing force, and the relation is plotted, the *first magnetization* curve is obtained (the path 0-1 in Figure 2.2).

This curve is sometimes referred to as the *rising* magnetization curve. If H is now decreased, a different relation between B and H is found, as is shown by the curve 1-2, which lies above the rising curve. A flux density, given by the 1-2 on the plot, remains when H is made zero. This flux density is called the *remanence* or *remanent magnetism*. To reduce the flux density to zero, a magnetizing force 2-3 must be applied in the direction opposite to that of the force formerly applied. For certain conditions of magnetization, as discussed below, this magnetizing force is called the *coercive force*.

As H becomes more negative until it reaches the minimum value, the relation between B and H follows the curve 3-4. Then if H is increased from the minimum value through 0, to the maximum value, the curve follows a path such as 4-5-6-1.

The points does not coincide exactly after the first turns but, after many cycles, the path becomes a closed loop.

So the values of B on the falling curve are greater than those on the rising curve. Thus the material has the property of tending to oppose a change in the value of the flux density. This property is known as *hysteresis*, which is a term meaning a *lagging behind*. The obtained closed loop is known as a *hysteresis loop*.

When the properties of different magnetic materials are compared, some of the properties are denoted by special terms. Those of major interest are:

REMANENCE is the flux density, or magnetic induction, which remains in a magnetic material after the removal of an applied magnetizing force

COERCIVE FORCE H_c for a magnetic material is the magnitude of the magnetizing force at which the flux density is zero when the material is being symmetrically magnetized

In many magnetic problems, the history of the material is unknown. Many magnetic calculations are therefore performed using a magnetization curve, called the *normal magnetization curve*, which is obtained by drawing a single-valued curve through the tips of a series of increasingly larger symmetrical hysteresis loops.

DIAMAGNETIC MATERIALS Diamagnetism is present in every material but empty space. The materials opposes the external magnetic field. Generally other magnetic properties hide it due to their greater effect.

PARAMAGNETIC MATERIALS Paramagnetic materials are nonmagnetic without an applied field, while they are magnetic once the field is applied. The susceptibility is positive but small.

2.2 PERMANENT MAGNETS

The sustained success of permanent-magnet use in industry was leaded by the improved magnetic characteristics in terms of energy, remanence and coercivity, which permitted marked reductions in motor framesize for the same output compraed with motors using ferrite (ceramic) magnets. However, ceramic magnets are considerably cheaper. Both ceramic and NdFeB (Neodymium, Iron and Boron) magnets are sensitive to temperature and special care must be taken in design for working temperature above 100°C. For very high temperature applications Alnico or rare-earth cobalt magnets must be used (Samarium-Cobalt is usable up to 200°C or even more).

For lowest cost, ferrite or ceramic magnets are the universal choice. This class of magnet materials has been steadily improved and is now available with remanence of 0.38 T or more and almost straight demagnetization characteristic throughout the second quadrant. The temperature characteristics of ferrite magnets can be tailored to the application requirements so that maximum performance is obtained at the normal operating temperature, which may be as high as 100°C.

2.2.1 *B-H loop and magnetization characteristic*

The starting-point for understanding magnet characteristics is the *B-H* loop or 'hysteresis loop', report in Figure 2.3(a). The *x*-axis measures the magnetizing force or field intensity H in the material. The *y*-axis is the magnetic flux-density in the material. An unmagnetized sample has $B = 0$ and $H = 0$ and therefore starts out at the origin. If it is subjected to a magnetic field, as for example in a magnetizing fixture

Table 2.2
Magnetic, mechanical and thermal properties of magnetic materials (Miller, 1989).

Property	Unit	Alnico 5-7	Ceramic	Sm_2Co_{17}	NdFeB
B_r	T	1.35	0.405	1.06	1.12
$\mu_0 H_c$	T	0.074	0.37	0.94	1.06
$(BH)_{max}$	MGOe	7.5	3.84	26.0	30.0
μ_{rec}		1.9	1.1	1.03	1.1
Specific gravity		7.31	4.8	8.2	7.4
Resistivity	$\mu\Omega$ cm	47	$>1 \cdot 10^4$	86	150
Thermal expansion	$10^{-6}/°C$	11.3	13	9	3.4
B_r temp. coeff.	%/°C	−0.02	−0.2	−0.025	−0.1
Saturation H	kOe	3.5	14.0	>40	>30

(an electromagnet with specially shaped pole pieces to focus flux into the magnet), then B and H in the magnet will follow the curve OA as the external ampere-turns are increased. If the external ampere-turns are switched off, the magnet relaxes along AB. Its operating point (H, B) will depend on the shape of the magnet and the permeance of the surrounding 'magnetic circuit'. If the magnet is surrounded by a highly permeable magnetic circuit, that is, if it is 'keepered', then its poles are effectively shorted together so that $H = 0$ and the flux-density is then the value at point B, the remanence B_r. The remanence is the maximum flux-density that can be retained by the magnet at a specified temperature after being magnetized to saturation. External ampere-turns applied in the opposite direction cause the magnet's operating point to follow the curve from B through the second quadrant to C.

A *hard* PM material is one in which the hysteresis loop is straight throughout the second quadrant, where the magnet normally operates in service. In this case the recoil line is coincident with the second-quadrant section of the hysteresis loop. This is characteristic of ceramic, rare-earth/cobalt, and NdFeB magnets, and the recoil permeability is usually between 1.0 and 1.1. *Soft* PM materials are those with a 'knee' in the second quadrant, such as Alnico. While Alnico magnets have very high remanence and excellent mechanical and thermal properties, they are limited in the demagnetizing field they can withstand. It should be noted that compared with lamination steels even the soft PM materials are very hard: in other words, the hysteresis loop of a typical nonoriented electrical steel is very narrow compared with that of even the Alnico magnets.

The most important part of the B-H loop is the second quadrant. This is called the demagnetization curve. In the absence of externally applied ampere-turns the magnet's operating point is at the intersection of the demagnetization curve and the *load line*, whose slope is the product of μ_0 and the permeance coefficient of the external circuit.

Recalling equation (2.2), the first term is the flux-density that would exist if the magnet were removed and the magnetizing force remained at the value H. Therefore the second term can be regarded as the contribution of the magnet to the flux-density within its own volume. Clearly if the demagnetization curve is straight, and if its relative slope and therefore the recoil permeability are both unity, then J is constant.

Figure 2.3
Permanent magnet characteristic *B-H* curves (Miller, 1989).

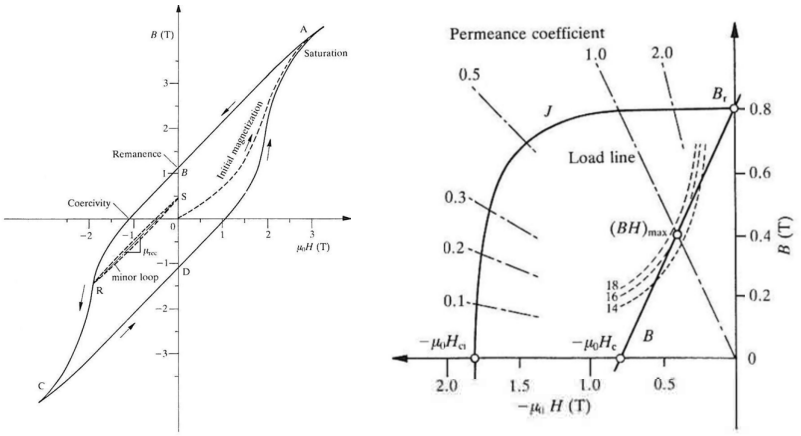

(a) Example of a magnet *B-H* curve.

(b) Example of a magnet second quadrant characteristic with load lines.

In most hard magnets the recoil permeability is slightly greater than 1 and there is a slight decrease of J as the negative magnetizing force increases, but this is reversible down to the 'knee' of the *B-H* loop (which may be in either the second or the third quadrant, depending on the material and its grade.

Evidently the magnet can recover or recoil back to its original flux-density as long as the magnetization is constant. The coercive force required to permanently demagnetize the magnet is called the intrinsic coercivity and this is shown as H_{cJ}.

Another parameter often calculated is the magnet energy product, which is simply the product of B and H in the magnet. This is not the actual stored magnet energy, which depends on the history or trajectory by which the magnet arrived at its operating point and usually cannot be calculated except under very artificial conditions. The energy product is a measure of the stored energy but, more importantly, it gauges how hard the magnet is working to provide flux against the demagnetizing influence of the external circuit.

2.2.2 *Temperature effects*

2.2.2.1 *High-temperature effects*

Exposure to sufficiently high temperatures for long enough periods produces metallurgical changes which may impair the ability of the material to be magnetized and may even render it nonmagnetic. There is also a temperature, called the Curie temperature, at which all magnetization is reduced to zero. After a magnet has been raised above the Curie temperature it can be remagnetized to its prior condition provided that no metallurgical changes have taken place. The temperature at which significant metallurgical changes begin is lower than the Curie temperature in the case of the rare-earth/cobalt magnets, NdFeB, and Alnico; but in ceramic ferrite magnets it is the other way round. Therefore ceramic magnets can be safely demagnetized by heating them just

above the Curie point for a short time. This is useful if it is required to demagnetize them for handling or finishing purposes. Table 2.3 shows these temperatures for some of the important magnets used in motors.

Table 2.3
Metallurgical change and Curie temperature.

	Metallurgical change [°C]	Curie temperature [°C]
Alnico 5	550	890
Ceramics	1080	450
$SmCo_5$	300	700
Sm_2Co_{17}	350	800
NdFeB	200	310

2.2.2.2 *Reversible losses*

The *B-H* loop changes shape with temperature. Over a limited range the changes are reversible and approximately linear, so that temperature coefficients for the remanence and coercivity can be used. Table 2.4 gives some typical data.

Table 2.4
Reversible temperature coefficients [%/°C].

	B_r	H_c	H_{cJ}
Alnico 5-7	−0.02		
Ceramics	−0.19	0.20	
$SmCo_5$	−0.04		−0.25
Sm_2Co_{17}	−0.02		−0.20
NdFeB	−0.11		−0.60

Ceramic magnets have a positive coefficient of H_c, whereas the high-energy magnets lose coercivity as temperature increases. In ceramic magnets the knee in the demagnetization curve moves down towards the third quadrant, and the permeance coefficient at the knee decreases. Thus ceramic magnets become better able to resist demagnetization as the temperature increases up to about 120°C. The greatest risk of demagnetization is at low temperatures when the remanent flux density is high and the coercivity is low; in a motor, this results in the highest short-circuit current when the magnet is least able to resist the demagnetizing ampere-turns.

All the magnets lose remanence as temperature increases. For a working temperature of 50°C above an ambient of 20°C, for instance, a ceramic magnet will have lost about 10 per cent. This is spontaneously recovered as the temperature falls back to ambient.

2.2.3 *Simple magnetic circuits*

Consider the example of Figure 2.4(a): let the iron be ideal, and let the magnet and the gap have the same section area:

$$S_m = S_g = S$$

Figure 2.4
Examples of simple magnetic circuits and magnet characteristic.

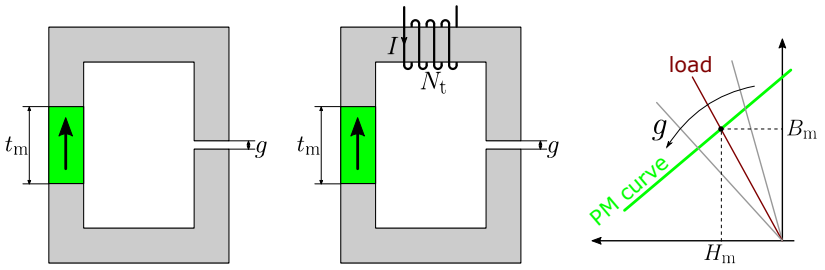

(a) Simple magnetic circuit with the inset of a PM.

(b) Simple magnetic circuit with a PM and a coil.

(c) Magnet characteristic at load.

Then we can write

$$\begin{cases} H_m\, t_m + H_g\, g = 0 & \text{Ampère's Law} \\ B_m\, S_m = B_g\, S_g & \text{Gauss's Law} \\ B_g = \mu_0\, H_g & \\ B_m = B_{rem} + \mu_{rec}\mu_0 H_m & \text{magnet 2nd quadrant characteristic} \end{cases}$$

Substituting the second and the third equations into the first one

$$H_m\, t_m + \frac{B_g}{\mu_0}\, g = 0 \qquad \Longrightarrow \qquad B_m = -\mu_0 \frac{t_m}{g}\, H_m$$

This equation expresses the load line of the magnetic circuit. Moving on to the last equation of the system

$$B_m = B_{rem} - \mu_{rec}\mu_0\, \frac{g}{\mu_0 t_m}\, B_m$$

$$B_m = \frac{B_{rem}}{1 + \mu_{rec}\, \frac{g}{t_m}} \tag{2.3}$$

So, through this equation, one can see the effect of changing the air-gap length or the magnet thickness.

If we add a coil around the ferromagnetic core, like shown in Figure 2.4(b), Ampère's Law becomes

$$H_m\, t_m + H_g\, g = N_t I \qquad \Longrightarrow \qquad B_m = -\mu_0 \frac{t_m}{g}\, H_m + \mu_0 \frac{N_t I}{g}$$

This causes a shift of the load line rightwards or leftwards, depending on the sign of the current. A high-valued positive current could saturate the iron while a negative one could demagnetize the magnet. It is important to stay sufficiently far away from the knee of the demagnetization curve.

2.2.4 *Finite Element simulations of PM*

As explained in Subsection 2.2.1 and shown in Figure 2.3(a), a hard magnet characteristic is almost a straight line in the second quadrant. This feature simplifies their simulation in Finite Element (FE) programs.

Typically, the magnet supplier makes available

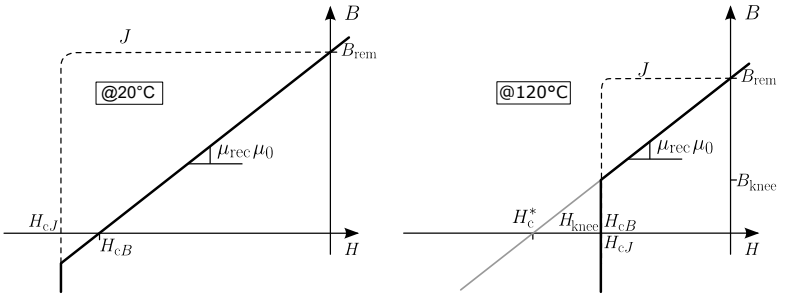

(a) Demagnetization characteristic at standard room temperature.

(b) Demagnetization characteristic at 120°C.

Figure 2.5
Illustration of the effect of temperature on the demagnetization characteristic of hard magnetic material.

- remanence at 20°C
- recoil permeability
- coercive field at 20°C

Furthermore, for simulations at a higher temperature, we also require:

- temperature coefficient for B_{rem}
- temperature coefficient for H_{cJ}

The recoil permeability could be obtained through

$$\mu_{\mathrm{rec}} = \frac{B_{\mathrm{rem}}}{\mu_0 |H_{cB}|}$$

Thanks to the temperature coefficients, it is possible to get the residual flux density $B_{\mathrm{rem}}^{@T}$ and the coercive force $H_{cJ}^{@T}$ at the required temperature T. Then the value of the coercivity to use for the FE program is

$$H_c^* = \frac{-B_{\mathrm{rem}}^{@T}}{\mu_{\mathrm{rec}}\mu_0}$$

At this point, we have to verify where the knee of the curve is. If it is below the x-axis (which means $|H_c^*| < |H_{cJ}|$), the coercivity H_c^* can be safely used. Otherwise, the magnet flux density should be checked in order not to irreversibly damage the magnet. In fact, it has to be true

$$B_{\mathrm{m}} > B_{\mathrm{knee}}$$

where

$$B_{\mathrm{knee}} = B_{\mathrm{rem}} + \mu_{\mathrm{rec}}\mu_0 H_{\mathrm{knee}}$$

2.3 LOSSES IN MAGNETIC MATERIALS

The iron losses in the magnetic parts of rotating electrical machines are also referred to as core losses or magnetic losses. They are generated by the changing magnetic field in the stator and in the rotor cores. They

are usually divided in two components: hysteresis and eddy currents losses.

It should be kept in mind that the engineering approach of iron loss separation into different loss types (hysteresis losses and eddy current losses for example) and related models represents an empirical approach which tries to separate the different physical influences due to frequency and flux density variations in electromagnetic systems into different components. However, it does not explain the real physical phenomena of the iron losses directly. From a physical point of view, both the hysteresis losses and the eddy current losses in the conducting ferromagnetic materials are based on Joule heating. They are caused by the same physical phenomena: every change in magnetization (which also occurs at DC magnetization) is a movement of magnetic domain walls and creates (microscopic and macroscopic) eddy currents which, in turn, create Joule heating. The fact that hysteresis losses also arise at almost zero frequency is due to the fact that even if the macroscopic magnetization change is very slow, the local magnetization inside the domains is changing rapidly and discrete in time, which generates eddy current losses. Nevertheless, the loss separation shows in most cases good correlation with measurements and has therefore its justification in the engineering science.

2.3.1 *Hysteresis losses*

The hysteresis cycle explained in Section 2.1 causes an effective dissipation of energy, called *hysteresis loss*, within the material when cyclic variations of magnetizing force are considered. The area enclosed by the hysteresis loop is equal to the energy loss density (expressed in $[\mathrm{J/m^3}]$). The power loss density can be determined by

$$p_{\mathrm{hy}} = f \oint H(B)\,\mathrm{d}B \quad [\mathrm{W/m^3}]$$

where f is the frequency of the magnetic field H. From now on, the subscript *hy* denotes the quantity related to hysteresis effect.

2.3.2 *Eddy current losses*

Eddy currents are created by the induced voltages in the conducting magnetic materials due to the changing magnetic flux, leading to dynamic iron losses. These eddy currents counteract the variations (time and direction) of the magnetic fields. They lead to a broadening of the hysteresis curve and thus increase the magnetic coercivity H_{c}, as it can be seen in Figure 2.6.

2.3.3 *Measuring the iron losses*

There are several international standards (e.g. IEC 60404-1, ASTM A677 , etc.) describing magnetic materials for electrical machines. In these standards, the materials are usually classified by their lamination

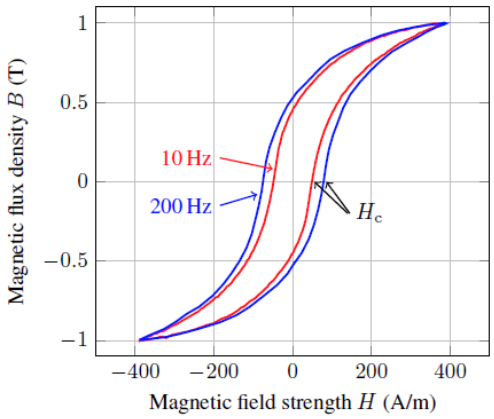

Figure 2.6
B-H hysteresis curve of a ferromagnetic material at 10 Hz (red) and 200 Hz (blue) (Krings, 2014).

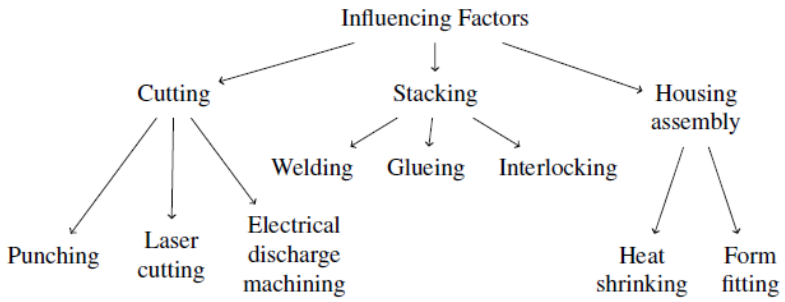

Figure 2.7
Influencing factors of the manufacturing process of electrical machine cores on the iron losses (Krings, 2014).

thickness and iron losses. The typical material M800-50A e.g. is a non-oriented 0.5 mm thick lamination sheet with maximum iron losses of 8 W/kg at 1.5 T and 50 Hz sinusoidal flux density excitation. However, these values are only the maximum guaranteed values of the iron losses. Therefore, manufacturers provide often also typical average values in their catalogues, which are closer to the real and expected values, and thus more suitable to use in iron loss calculations.

However, the manufacturing process of the magnetic machine parts is usually the main reason for discrepancies between the data sheet values and measurement results of the final assembled machine.

The challenging point about determining the value of iron losses is that it is not possible to measure them directly. Indirect thermal measurements (inverse thermal models and calorimetric measurements), magnetic field measurements (search coil windings, hall sensors, etc.) or loss separation calculations (subtracting all known other losses from the total losses) are the applied possibilities to determine indirectly iron losses in ferromagnetic materials for electrical machines.

2.3.3.1 *Mathematical formulation*

The most used mathematical formulation of iron losses is an extension of the classical Steinmetz equation, made by Jordan. One term depends linearly on the variation of the frequency, the other one depends on the

Table 2.5
Influence factors on SiFe steel sheets properties (Krings, 2014).

Factor	p_{hy}	p_{ec}	p_{ex}	J_s	H_c
Grain size (+)	−		+		−
Impurities (+)	+			−	+
Thickness (t+)	−	+			−
Internal stress (+)	+				+
Cutting/Punching process	+			−	
Pressing process		+			
Welding process	+				
Alloy content (%Si+)		−		−	

frequency squared. This means that the losses are separated into (static) hysteresis losses and (dynamic) eddy current losses:

$$p_{Fe} = p_{hy} + p_{ec} = c_{hy} f \hat{B}^2 + c_{ec} f^2 \hat{B}^2 \tag{2.4}$$

In Equation 2.4, c_{hy} and c_{ec} are the hysteresis and eddy currents coefficient, respectively. In Jordan's approach, it is assumed that the hysteresis losses are proportional to the hysteresis loop area of the material at low frequencies ($f \to 0\,\text{Hz}$).

One of the approaches to improve Equation 2.4 is to introduce an additional loss term p_{ex} to take into account the excess losses as a function of the flux density and frequency. It separates the iron loss formula p_{Fe} into three terms, the static hysteresis losses p_{hy}, dynamic eddy current losses p_{ec}, and the excess losses p_{ex}:

$$p_{Fe} = p_{hy} + p_{ec} + p_{ex} = g_{hy} f \hat{B}^2 + g_{ec} f^2 \hat{B}^2 + g_{ex} f^{1.5} \hat{B}^{1.5} \tag{2.5}$$

It has to be noted that the presented loss separation approaches do not hold if the skin effect is not negligible, which means at high frequency.

2.3.3.2 *Determination of the coefficients*

The Steinmetz formulation described by (2.4) needs only two coefficients to approximate the iron losses. And since both terms depends on B^2, we need to change the frequency to obtain the coefficients. So c_{hy} and c_{ec} could be obtained in many ways, the two most common being interpolation through two points and least squares method. Here, the former is described. The data points may be obtained from the material datasheet, or through experimental measurements on a sample of the ferromagnetic material.

Let us pick two pairs of flux density and frequency $(B_i, f_i)_{i=\{1,2\}}$, and their respective power loss density p_i. The following system can be written:

$$\begin{cases} p_1 = c_{hy} B_1^2 f_1 + c_{ec} B_1^2 f_1^2 \\ p_2 = c_{hy} B_2^2 f_2 + c_{ec} B_2^2 f_2^2 \end{cases} \tag{2.6}$$

Since all the terms but c_{hy}, c_{ec} are known, this system can be solved directly.

$$
\begin{aligned}
c_{hy} &= \frac{p_1}{B_1^2 f_1} - c_{ec} f_1 \qquad [\mathrm{W/(kg\,T^2\,Hz)}] \\
p_2 &= p_1 \frac{B_2^2}{B_1^2}\frac{f_2}{f_1} - c_{ec} B_2^2 f_1 f_2 + c_{ec} B_2^2 f_2^2 \\
c_{ec} &= \frac{p_2 - p_1 \frac{B_2^2}{B_1^2}\frac{f_2}{f_1}}{B_2^2 f_2 (f_2 - f_1)} = \frac{p_2 B_1^2 f_1 - p_1 B_2^2 f_2}{B_1^2 f_1 B_2^2 f_2 (f_2 - f_1)} \qquad [\mathrm{W/(kg\,T^2\,Hz^2)}]
\end{aligned}
$$

Alternatively, one cold use Bertotti's formulation, shown in (2.5). In this equation, g_{ec} is computed directly from the material properties, according to[1]

$$
g_{ec} = \frac{\pi^2 t^2}{6\rho\gamma} \qquad [\mathrm{W/(kg\,T^2\,Hz^2)}] \tag{2.7}
$$

where t is the thickness of the lamination material, ρ is the material electrical resistivity and γ is the material density. After that, only the two coefficients g_{hy} and g_{ex} are unknown, so a system of two equations is needed, similarly to before. That is:

$$
\begin{aligned}
p_1 &= g_{hy} B_1^2 f_1 + g_{ec} B_1^2 f_1^2 + g_{ex} B_1^{1.5} f_1^{1.5} \\
p_2 &= g_{hy} B_2^2 f_2 + g_{ec} B_2^2 f_2^2 + g_{ex} B_2^{1.5} f_2^{1.5}
\end{aligned} \tag{2.8}
$$

And so

$$
\begin{aligned}
g_{ex} &= \frac{p_1 - g_{hy} B_1^2 f_1 - g_{ec} B_1^2 f_1^2}{B_1^{1.5} f_1^{1.5}} \qquad [\mathrm{W/(kg\,T^{1.5}\,Hz^{1.5})}] \\
p_2 &= g_{hy} B_2^2 f_2 + g_{ec} B_2^2 f_2^2 + \frac{p_1 - g_{hy} B_1^2 f_1 - g_{ec} B_1^2 f_1^2}{B_1^{1.5} f_1^{1.5}} B_2^{1.5} f_2^{1.5} \\
\frac{p_2}{B_2^2 f_2} &= g_{hy} + g_{ec} f_2 + p_1 \frac{B_2^{-0.5} f_2^{0.5}}{B_1^{1.5} f_1^{1.5}} - g_{hy} \frac{B_1^2 f_1 B_2^{-0.5} f_2^{0.5}}{B_1^{1.5} f_1^{1.5}} - g_{ec} \frac{B_1^2 f_1^2 B_2^{-0.5} f_2^{0.5}}{B_1^{1.5} f_1^{1.5}}
\end{aligned}
$$

With some more algebraic steps

$$
\begin{aligned}
g_{hy}\left(1 - \frac{B_1^2 f_1 B_2^{-0.5} f_2^{0.5}}{B_1^{1.5} f_1^{1.5}}\right) &= \frac{p_2}{B_2^2 f_2} - p_1 \frac{B_2^{-0.5} f_2^{0.5}}{B_1^{1.5} f_1^{1.5}} - g_{ec} f_2 + g_{ec} \frac{B_1^2 f_1^2 B_2^{-0.5} f_2^{0.5}}{B_1^{1.5} f_1^{1.5}} \\
g_{hy} &= \frac{\frac{p_2}{B_2^2 f_2} - p_1 \frac{B_2^{-0.5} f_2^{0.5}}{B_1^{1.5} f_1^{1.5}} + g_{ec}\left(\frac{B_1^2 f_1^2 B_2^{-0.5} f_2^{0.5}}{B_1^{1.5} f_1^{1.5}} - f_2\right)}{1 - \frac{B_1^2 f_1 B_2^{-0.5} f_2^{0.5}}{B_1^{1.5} f_1^{1.5}}} \qquad [\mathrm{W/(kg\,T^2\,Hz)}]
\end{aligned}
$$

1 For the derivation of this coefficient, see Appendix D.

3 MULTI-OBJECTIVE OPTIMIZATION

This chapter presents a very brief introduction to multi-objective optimization algorithms, in particular focusing on the Differential Evolution (DE) algorithm.

3.1 PROBLEM STATEMENT

The design of electric machines is an inverse problem, it is a synthesis. These are among the most difficult problems to solve, because there is no direct way to go through it. But all these kinds of problems can be formulated in terms of minimizing an objective function:

$$\min_{x \in X} f(x)$$

Actually, we search for the value of x, within a certain interval X, which gives the global minimum of the function f. So what we are really looking forward to solve is

$$\arg\min_{x \in X} f(x) \tag{3.1}$$

Even though the problem is rather simple to state, there is actually no meaning in minimum of a vector function, so when we have more than one objective. And the variable x, is often a vector variable, so a set of parameters (which may be diameters, lengths, number of poles, et cetera). Then, the subspace (subdomain) X can be defined by simple bounds, but also by some functional relationships among some quantities. This is not such an uncommon thing, because often there are some feasibility checks on dependent variables, such as the slot opening width, or the yoke height, and so on. For all these reasons, the most simple way to solve this problem is to employ an automatic algorithm, namely an optimizer. In fact, global optimization has become widespread in solving problems in many fields of science, engineering, economics, and more. Many practical problems have objective functions which are non-differentiable, non-continuous, non-linear, noisy, with many local minima, et cetera. While this kind of problem are very difficult to solve analytically, if not impossible, they can be quite easily implemented into an optimization routine.

A very successful type of optimization algorithms is the evolutionary algorithm class. This class tries to find the minimum of a function borrowing ideas from natural evolution (reproduction, mutation, recombination and selection). Evolutionary algorithms belong to a broader class of optimizers, called stochastic, where there is a substantial amount of randomness in the search process. This family is set against the deterministic algorithms. Among the stochastic optimization algorithms, we may have (Cavazzuti, 2013):

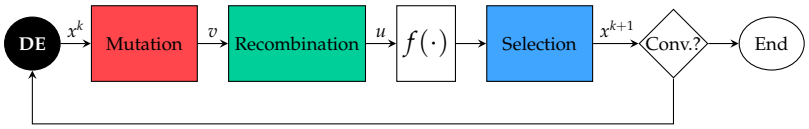

Figure 3.1
Flowchart of the optimization scheme employed by the DE.

- Simulated Annealing (SA): aims at emulating the annealing heat treatment process of steel.
- Particle Swarm Optimization (PSO): aims at emulating the social behavior of birds flocking.
- Game Theory–based Optimization (GT): aims at emulating the evolution of a game in which different players try to fulfill their own objectives. They are based on the game theory from Nash.
- Evolutionary Algorithms (EAs): aim at emulating the evolution of species by natural selection according to Darwin's theory. It is the most important category of stochastic optimization together with genetic algorithms.
- Genetic Algorithms (GAs): alike EAs, aim at emulating the evolution of species. For this reason at times they are considered a subcategory of EAs. However, EAs and GAs, in practice, have different approaches to the emulation of evolution and can also be considered two different categories of stochastic optimization algorithms.

The source of inspiration of many randomized search methods comes from the observation of nature. Concepts from biology, physics, geology, or some other field of investigation, are borrowed and implemented in a simplified model of some natural phenomena. Most of these methods are population-based algorithms, in which a set of initial samples evolves (or moves) up to convergence. Stochastic optimization methods are the most innovative and advanced approaches to optimization. Compared to deterministic optimization methods, they have both advantages and drawbacks (Cavazzuti, 2013):

- simpler mathematical background
- randomness included in the algorithm
- slower convergence towards the optimum
- wider search in the design space, so less chance to get stuck at a local minimum
- adaptable to any kind of function

One of the most effective optimization algorithm for engineering problems is the DE. The flowchart of the optimization scheme is reported in Figure 3.1. Its algorithm works through three basic principles:

1. mutation: expands the search space
2. recombination: reuses previously successful individuals
3. selection: mimics survival-of-the-fittest

3.1.1 *Mutation*

There may be many ways to perform mutation on an individual, and here are some examples:

- DE/rand/1 $v_i = x_{r_1} + F(x_{r_2} - x_{r_3})$
- DE/best/1 $v_i = x_{\text{best}} + F(x_{r_2} - x_{r_3})$
- DE/rand2best/1 $v_i = x_{r_1} + F_1(x_{r_2} - x_{r_3}) + F_2(x_{\text{best}} - x_{r_1})$
- DE/curr2best/1 $v_i = x_i + F_1(x_{r_2} - x_{r_3}) + F_2(x_{\text{best}} - x_i)$
- DE/rand/2 $v_i = x_{r_1} + F(x_{r_2} - x_{r_3} + x_{r_4} - x_{r_5})$
- DE/best/2 $v_i = x_{\text{best}} + F(x_{r_2} - x_{r_3} + x_{r_4} - x_{r_5})$
- ...

What is common among these techniques is that we add one (or more) difference vector(s) to a base individual in order to move the individual and explore more the design space. x_i is the i^{th} *individual* of the current population. After a mutation happens, we have a new individual referred to as v, called *donor*. The factors F_x are called mutation factors, and they can be constants chosen at the beginning of the optimization, or they can change their value during the optimization run, either deterministically (according to a certain law) or stochastically (included among the optimization parameters).

3.1.2 *Recombination*

The recombination step mixes successful individuals from the previous generation with current donors, to try to keep the best features.

$$u_{i,j} = \begin{cases} v_{i,j} & \text{if } \text{rand}_{i,j} \leq \text{CR} \ \vee \ j = i_{\text{rand}} \\ x_{i,j} & \text{otherwise} \end{cases} \tag{3.2}$$

The individual u_i is called *trial*, CR is the crossover ratio, and with j we are referring to the j^{th} parameter of the considered individual.

3.1.3 *Selection*

The selection block is what makes the DE really effective, since it mimics a "greedy" natural selection where only the fittest can "survive". In fact, the objective function is evaluated on the trials and, if the objective value results better than the previous generation individual, the trial survives and becomes the new generation individual. Mathematically, it translated to:

$$x_i^{k+1} = \begin{cases} u_i^k & \text{if } f(u_i^k) < f(x_i^k) \\ x_i^k & \text{otherwise} \end{cases} \tag{3.3}$$

3.2 MISSING PIECES

There are a lot of other missing details which have not been described in this chapter and are essential to perform a proper optimization, though. Nonetheless, they are out of scope of the thesis, so in the following there will be only a brief reference to these aspects.

- how to choose the population size?
- how to choose the total number of generations?
- how to choose the mutation factor and the crossover ratio?
- which is the best mutation strategy?
- how to deal with stagnation?
- how to handle constraints?
- how to deal with multi-objective optimization?

Some possible enhancements:

- asynchronous strategy: use good solutions immediately without waiting for the next generation to be created
- elitism: compare trial not only with target, but also with the worst individual, therefore keeping the most promising
- coevolution: use several populations, each working on a different subset of the design space

Some of these items are explained and developed in (Storn et al., 1997; Cavazzuti, 2013; Narzisi, 2008), where a more thorough bibliographic section is also present.

Some applications and recent advancements about optimization in electric machine can be found in (Bramerdorfer et al., 2018; Mohammadi, 2015).

4

FLUID: FREE FLUID FLUX-BARRIERS ROTOR FOR SYNCHRONOUS RELUCTANCE MOTOR DRAWING

The work done in this chapter can be cited if it has been used in a project or in a program (Bacco, 2018).[1]

The goal of this chapter is to provide a ready-to-use fully parametric drawing of the Synchronous Reluctance rotor with fluid flux-barriers.

REQUIREMENTS

Matlab or Octave or Python (NumPy + SciPy) to compute the points. The points calculation is general, so it could be implemented in any language, but Matlab/Octave were chosen here.

The calculation can bo ported to any Computer-Aided Design (CAD) engine or FEA software.

4.1 FILES NEEDED

For Matlab/Octave, the files needed for the computation are
`calc_fluid_barrier.m`, `GetFSolveOptions.m`, `isOctave.m`
while for Python it is
`fluid_functions.py`.

4.2 HOW TO USE

Open the file `fluid` and run it.

Change the machine data in the data section. All the variables have a comment next to them.

There are some "hidden" options which should be explained.

1. personal flux-barrier angles can be provided, or the program will compute them. This means that flux-barrier thicknesses and flux-carrier widths must always be provided. Optionally, the electrical flux-barrier angles can also be provided.

```
1  rotor.barrier_angles_el = [14,26,38]*2;
```

2. if the program computes them, they will result the average of the final points C′ and D′ at the rotor periphery. Alternatively, some weights can be defined which determine how close E should be to C′ or D′.

```
   rotor.barrier_end_wf = [20,50,80]/100;
```

1 Giacomo Bacco (2018). *fluid: Free Fluid Flux-Barriers Rotor for Synchronous Reluctance Motor Drawing*. DOI: 10.5281/zenodo.1214465. URL: https://github.com/gbacco5/fluid (visited on 05/11/2019)

3. by default, the flux-barrier-end is round, so the code solves an additional system to determine the correct locations of the fillet points. Such system can be skipped declaring

```
rotor.barrier_end = 'rect';
```

   and so selecting "rectangular" flux-barrier-end.

4. the inner radial iron ribs are optional, but you are free to provide different widths can be provided for every flux-barrier.

```
rotor.wrib = [1,2,4]*mm;
```

5. if you also input magnet widths, the rib is automatically enlarged to accommodate the magnet, similarly to an IPM (Interior Permanent Magnet) machine.

```
rotor.wm = [10,20,40]*mm;
```

   In this case, the output structure `barrier` also contains the location of the magnet base center point.

4.3 EXAMPLES

Here are some finished examples based on the output. The drawings are for demonstration purposes only.

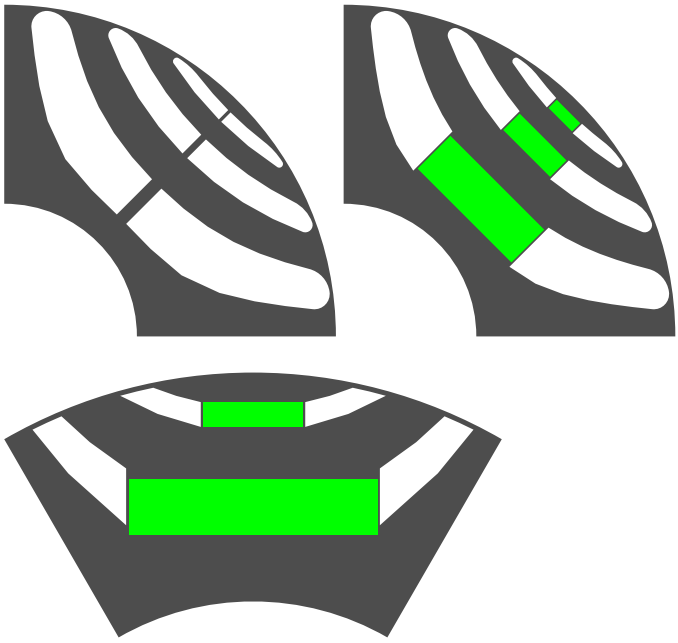

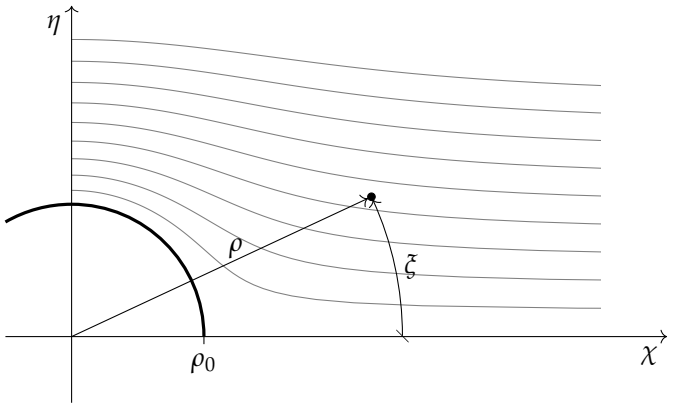

Figure 4.1
Sketch of fluid flow past a cylinder.

4.4 THEORY

4.4.1 *Flow past a cylinder*

Let ρ_0 be the radius of the cylinder, (ρ, ξ) the polar coordinate system in use (Figure 4.1). One possible solution of this problem have these potential and streamline functions:

$$\phi(\rho, \xi) = \left(\rho + \frac{\rho_0^2}{\rho}\right) \cos \xi \tag{4.1}$$

$$\psi(\rho, \xi) = \left(\rho - \frac{\rho_0^2}{\rho}\right) \sin \xi \tag{4.2}$$

Although these equations are deeply coupled, the radius ρ and the phase ξ can be obtained as a function of the other quantities. For our purposes, we use ψ.

$$\rho(\psi, \xi) = \frac{\psi + \sqrt{\psi^2 + 4\rho_0^2 \sin^2 \xi}}{2 \sin \xi}$$

$$\xi(\psi, \rho) = \arcsin\left(\frac{\rho\, \psi}{\rho^2 - \rho_0^2}\right)$$

The velocity field can also be derived through

$$v_\rho(\rho, \xi) = \frac{\partial \phi}{\partial \rho} = \left(1 - \frac{\rho_0^2}{\rho^2}\right) \cos \xi$$

$$v_\xi(\rho, \xi) = \frac{1}{\rho} \frac{\partial \phi}{\partial \xi} = -\left(1 + \frac{\rho_0^2}{\rho^2}\right) \sin \xi$$

4.4.2 *Conformal mapping*

From the reference plane, which is equivalent to a two-pole machine, we use a complex map to obtain the quantities in the actual plane. Let p be the number of pole pairs. Then:

$$\begin{aligned} \zeta &\xrightarrow{\mathcal{M}} z = \sqrt[p]{\zeta} \\ \rho\, \mathrm{e}^{\mathrm{j}\xi} &\xrightarrow{\mathcal{M}} r\, \mathrm{e}^{\mathrm{j}\vartheta} = \sqrt[p]{\rho}\, \mathrm{e}^{\mathrm{j}\xi/p} \\ \chi + \mathrm{j}\eta &\xrightarrow{\mathcal{M}} x + \mathrm{j}y \end{aligned}$$

It is easy to find the inverse map:

$$\mathcal{M}\colon \sqrt[p]{\cdot} \qquad \mathcal{M}^{-1}\colon (.)^p$$

In the transformed plane, the velocities have a different expression:

$$\begin{aligned} v_r(r,\vartheta) &= \frac{\partial\phi}{\partial r} = \frac{\partial\phi}{\partial\rho}\frac{\partial\rho}{\partial r} = p\left(r^{p-1} - \frac{R_0^{2p}}{r^{p+1}}\right)\cos p\vartheta \\ v_\vartheta(r,\vartheta) &= \frac{1}{r}\frac{\partial\phi}{\partial\theta} = \frac{1}{r}\frac{\partial\phi}{\partial\rho}\frac{\partial\rho}{\partial\theta} = -p\left(r^{p-1} + \frac{R_0^{2p}}{r^{p+1}}\right)\sin p\vartheta \end{aligned} \tag{4.3}$$

This vector field is tangent to the streamlines in every point in the transformed plane. In order to work with this field in (x, y) coordinates, we need a rotational map:

$$\begin{aligned} v_x(r,\vartheta) &= v_r\cos\vartheta - v_\vartheta\sin\vartheta \\ v_y(r,\vartheta) &= v_r\sin\vartheta + v_\vartheta\cos\vartheta \end{aligned} \tag{4.4}$$

4.4.3 *Computation of flux-barrier base points*

Refer to Figure 4.2 for the points naming scheme. Keep in mind that A' is not simply the projection of A onto the q-axis, but it represents the original starting point for the barrier sideline, so it lies on the flux-barrier streamline. The same is true for points B', B, C', C, and D', D.

Let the flux-barrier and flux-carrier thicknesses and widths be given. Then the base points for the flux-barriers can be computed easily. Let D_r be the rotor outer diameter, $w_{\mathrm{rib,t}}$ the tangential iron rib width, w_{ck} the k^{th} flux-carrier width, and t_{bk} the k^{th} flux-barrier thickness.[2] Then

$$\begin{aligned} R_\mathrm{rib} &= \frac{D_\mathrm{r}}{2} - w_{\mathrm{rib,t}} \\ R_{\mathsf{A}'_1} &= R_\mathrm{rib} - w_{\mathrm{c1}} \\ R_{\mathsf{B}'_1} &= R_{\mathsf{A}'_1} - t_{\mathrm{b1}} \\ &\vdots \end{aligned}$$

2 The main dimensions of the flux-carrier and flux-barrier differ in the names (width versus thickness). This is because we refer to width when the flux flows perpendicularly to the dimension, and to thickness when it flows in parallel.

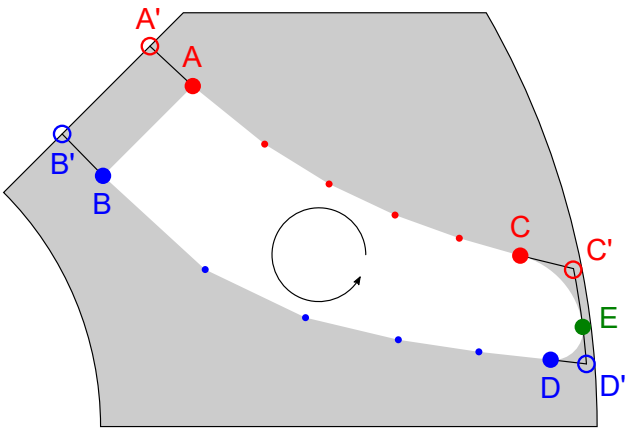

Figure 4.2
Flux-barrier base points description.

where R represents the radius from the origin. So, in general:

$$R_{A'_k} = R_{B'_{k-1}} - w_{ck}$$
$$R_{B'_k} = R_{A'_{k-1}} - t_{bk}$$

with the exception $R_{B'_0} = R_{rib}$.

Now we know both the radii and the angle—always $\pi/(2p)$—of the flux-barrier internal points. So we can compute their respective streamline value.

4.4.3.1 *Magnet insertion*

$$w_{rib,k} \leftarrow w_{rib,k} + w_{pm,k}$$

where $w_{pm,k}$ is the k^{th} magnet width.

4.4.3.2 *Central base points*

We refer to points A and B. If the rib width is zero $A \equiv A'$ and $B \equiv B'$.

The line describing the q-axis is

$$y = mx + q$$
$$m = \tan\frac{\pi}{2p}$$
$$q = \frac{w_{rib}}{2\cos\frac{\pi}{2p}}$$

and the following system can be set up to find point A

$$\begin{cases} y_A - mx_A - q = 0 \\ x_A - r_A(\psi_{A'}, \vartheta_A)\cos\vartheta_A = 0 \\ y_A - r_A(\psi_{A'}, \vartheta_A)\sin\vartheta_A = 0 \end{cases}$$

where ϑ_A is used as the third degree of freedom and r_A is then a function of it. The solution of such system can be determined solving the single equation

$$r_A(\psi_{A'}, \vartheta_A)(\sin\vartheta_A - m\cos\vartheta_A) - q = 0$$

in the unknown ϑ_A. The function $r(\psi, \vartheta)$ is simply

$$r(\psi, \vartheta) = \sqrt[p]{\rho(\psi, \vartheta/p))}$$

The same equation can be written for point B with the proper substitutions and repeated for all the flux-barriers.

4.4.4 *Outer base points*

We refer to points C, D, and E of Figure 4.2. If the flux-barrier angle, ϑ_b, is given, then

$$x_E = R_{rib} \cos(\tfrac{\pi}{2p} - \vartheta_b)$$
$$y_E = R_{rib} \sin(\tfrac{\pi}{2p} - \vartheta_b)$$

Points C and D results from the connection of the flux-barrier sidelines and point E. This connection should be as smooth as possible in order to avoid dangerous mechanical stress concentrations. We are going to use circular arcs to make this connection. So we impose the tangency between the flux-barrier sideline and the arc, between the arc and the radius through point E. The tangent to the sideline can be obtained through the velocity field described with (4.3) and (4.4).

Then we want point C to lay on the flux-barrier sideline. These conditions represent a nonlinear system of 4 equations, in 6 unknowns. So we need two more equations, which are that points C and E belong to the fillet circle with radius R.[3]

$$\begin{cases} x_C - r_C(\psi_C, \vartheta_C)\cos\vartheta_C = 0 \\ y_C - r_C(\psi_C, \vartheta_C)\sin\vartheta_C = 0 \\ (x_C - x_{O_C})^2 + (y_C - y_{O_C})^2 - R_{EC}^2 = 0 \\ (x_E - x_{O_C})^2 + (y_E - y_{O_C})^2 - R_{EC}^2 = 0 \\ (x_{O_C} - x_E)y_E - (y_{O_C} - y_E)x_E = 0 \\ (x_{O_C} - x_C)v_x(r_C, \vartheta_C) + (y_{O_C} - y_C)v_y(r_C, \vartheta_C) = 0 \end{cases}$$

The very same system can be written and solved for point D.

4.4.4.1 *Choice of initial position*

For the good convergence of the nonlinear system, we have to choose a proper initial position for the points of interest, namely C and O_C for the top part of the flux-barrier.

Since point C should be close to E and C′, a good initial guess could be

$$x_{C^{(0)}} = \frac{x_E + x_{C'}}{2}, \qquad y_{C^{(0)}} = \frac{y_E + y_{C'}}{2}$$

A slightly better guess shifts the points a bit to the left, in this way:

$$x_{C^{(0)}} = \frac{x_E + x_{C'} + 0.1x_A}{2.1}, \qquad y_{C^{(0)}} = \frac{y_E + y_{C'}}{2}$$

3 Actually a system of 5 equations and 5 unknowns may be written but the simpler solution was preferred.

On the other hand, point $\mathsf{O_C}$ lies on one edge of the triangle of vertices $\mathsf{E}, \mathsf{C}, \mathsf{O}$, where O represents the origin and where we are going to use $\mathsf{C}^{(0)}$ instead of C because it is still unknown. Then:

$$x^{(0)}_{\mathsf{O_C}} = \frac{x_{\mathsf{E}} + x_{\mathsf{C}^{(0)}} + 0}{3}\,, \qquad y^{(0)}_{\mathsf{O_C}} = \frac{y_{\mathsf{E}} + y_{\mathsf{C}^{(0)}} + 0}{3}$$

Similar considerations can be made for point D, with slight changes:

$$x_{\mathsf{D}^{(0)}} = \frac{x_{\mathsf{E}} + x_{\mathsf{D}'}}{2}\,, \qquad y_{\mathsf{D}^{(0)}} = \frac{y_{\mathsf{E}} + y_{\mathsf{D}'}}{2}$$

$$x^{(0)}_{\mathsf{O_D}} = \frac{x_{\mathsf{E}} + x_{\mathsf{D}^{(0)}} + x_{\mathsf{C}}}{3}\,, \qquad y^{(0)}_{\mathsf{O_D}} = \frac{y_{\mathsf{E}} + y_{\mathsf{D}^{(0)}} + x_{\mathsf{C}}}{3}$$

Notice that here we use point C which has already been found.

4.4.5 *Flux-barrier sideline points*

Let us consider the top flux-barrier sideline, so the one going from point A to point C. We want to create such sideline using a predetermined number of steps, N_{step}. From now on, let us call this N_k for the k^{th} flux-barrier.

One of the best way to distribute the points along the streamline is to use the potential function, ϕ, defined in (4.1). We start computing the potential for points A and C:

$$\phi_{\mathsf{A}} = \phi(\rho_{\mathsf{A}}, \xi_{\mathsf{A}})$$
$$\phi_{\mathsf{C}} = \phi(\rho_{\mathsf{C}}, \xi_{\mathsf{C}})$$

Then, we want to find $N-1$ points along the streamline between points A and C with a uniform distribution of the potential function. We define

$$\Delta\phi_{\mathsf{AC}} = \frac{\phi_{\mathsf{C}} - \phi_{\mathsf{A}}}{N}$$

So we can compute the potentials we are looking for

$$\phi_i = \phi_{\mathsf{A}} + i\Delta\phi_{\mathsf{AC}}\,, \quad i = 1, \dots, N-1$$

and finally the location of the point with this potential value and the streamline function value required to lie on the flux-barrier sideline. This translates to the following system of equations:

$$\begin{cases} \psi_{\mathsf{AC}} - \psi(\rho, \xi) = 0 \\ \phi_i - \phi(\rho, \xi) = 0 \end{cases}$$

The system is well-defined because there are two unknowns and two independent equations. This system must be solved for every flux-barrier sideline point, for the two sides, and for every flux-barrier.[4]

4 In Matlab/Octave, the "for every flux-barrier sideline point" loop has been vectorized, while the two sides has been manually split.

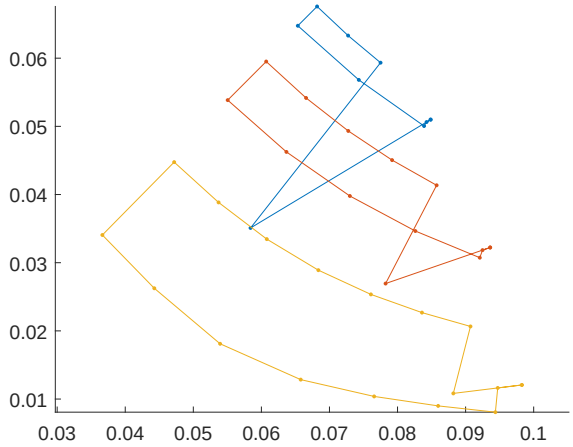

Figure 4.3
Example of the Matlab/Octave output plot.

4.4.6 *Output*

The output of the computation function in Matlab/Octave is one vector of structures (`barrier(:)`) which contains at least two fields (`X` and `Y`). The X vector is made in this way:

$$X = \begin{bmatrix} x_{\mathsf{E}} & x_{\mathsf{O_C}} & x_{\mathsf{C}} & x_{\mathsf{AC}_{N_{\text{step}}-1}} & \cdots & x_{\mathsf{AC}_1} & x_{\mathsf{A}} & \searrow \\ x_{\mathsf{B}} & x_{\mathsf{BD}_1} & \cdots & x_{\mathsf{BD}_{N_{\text{step}}-1}} & x_{\mathsf{D}} & x_{\mathsf{O_D}} & x_{\mathsf{E}} & \end{bmatrix}^{\mathrm{T}}$$

and similarly the Y vector. So the points are ordered starting from the point `E` and then moving counter-clockwise until `E` is reached again.

4.4.7 *Example of Matlab/Octave plot*

Figure 4.3 reports an example of a Matlab/Octave output plot. The V-shaped lines represent the radii of the fillet arcs.

Part II

ANALYTICAL MODELS

5

A NONLINEAR ANALYTICAL MODEL FOR THE RAPID PREDICTION OF THE TORQUE OF SYNCHRONOUS RELUCTANCE MACHINES

This chapter presents a nonlinear analytical model of the synchronous reluctance machine, used to derive both average and torque harmonics as a function of the rotor geometry.

At first, the model with linear *B-H* characteristic is described. Then the model is extended to include the saturation of some parts of the machine. Conversely to previous models, the saturation is taken into account following all the main flux lines paths inside the machine. Then a proper saturation coefficient is assigned to each of this path and applied at the air-gap. The analytical model proves to be fast and fairly accurate in any calculation. Therefore it is quick and easy to obtain the behavior of the average torque and torque ripple as a function of the rotor flux-barrier geometry. The result is presented using maps, which are essential for finding a proper combination of barrier angles that gives maximum average torque and minimum torque ripple. The torque maps are compared with those obtained from both linear analytical and finite element models. The maps computed analytically show good agreement with those derived by means of finite element analysis, and they are obtained in a much smaller computational time.

5.1 DEVELOPMENT OF THE ANALYTICAL MODEL

Suppose to distribute a single-turn, non-chorded infinitesimal coil inside the slots of a given stator lamination stack (Figure 5.1). The conductor distribution function is equal to

$$n_{\mathrm{d}}(\vartheta^{\mathrm{e}}) = \hat{n}\left[\delta\left(\vartheta^{\mathrm{e}} - \tfrac{\pi}{2}\right) - \delta\left(\vartheta^{\mathrm{e}} - \tfrac{\pi}{2} - \pi\right)\right], \quad \vartheta^{\mathrm{e}} \in [0, 2\pi]$$

where $\delta(.)$ is the Dirac delta impulse and ϑ^{e} is the electrical angular coordinate whose origin is along the magnetic axis of this coil.

It has to result one conductor from the integration of n_{d} in one semi-period[1]

$$\int_0^{\pi} n_{\mathrm{d}}(\vartheta^{\mathrm{e}}) \tfrac{D_{\mathrm{s}}}{2}\, \mathrm{d}\vartheta^{\mathrm{e}} = \int_0^{\pi} \hat{n}\, \delta\left(\vartheta^{\mathrm{e}} - \tfrac{\pi}{2}\right) \tfrac{D_{\mathrm{s}}}{2}\, \mathrm{d}\vartheta^{\mathrm{e}} = 1 \quad \Longrightarrow \quad \hat{n} = \tfrac{2}{D_{\mathrm{s}}}$$

so

$$n_{\mathrm{d}}(\vartheta^{\mathrm{e}}) = \frac{2}{D_{\mathrm{s}}}\left[\delta\left(\vartheta^{\mathrm{e}} - \tfrac{\pi}{2}\right) - \delta\left(\vartheta^{\mathrm{e}} - \tfrac{\pi}{2} - \pi\right)\right] \tag{5.1}$$

1 Remember that the integral of the Dirac delta function is 1 and the property

$$\int_{\mathbb{R}} \delta(a\tau)\, \mathrm{d}\tau = \frac{1}{|a|}$$

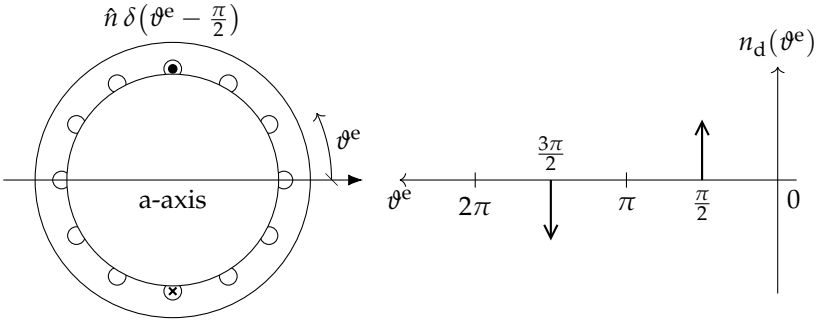

Figure 5.1
Sketch of a stator lamination with one infinitesimal coil and relative conductor distribution function plot.

where the value 2 represents the total number of conductors in one electrical period. Note that this result is valid for any number of poles and conductors. In fact defining

$$n_{\mathrm{d}}(\vartheta)=\frac{N_{\mathrm{s}}}{D_{\mathrm{s}}}\left[\delta\left(p\vartheta-\tfrac{\pi}{2}\right)-\delta\left(p\vartheta-\tfrac{\pi}{2}-\pi\right)\right],\quad \vartheta\in\left[0,\tfrac{2\pi}{p}\right] \tag{5.2}$$

and integrating over a mechanical semi-period, it results

$$\int_0^{\pi/p}\frac{N_{\mathrm{s}}}{D_{\mathrm{s}}}\,\delta\left(p\vartheta-\tfrac{\pi}{2}\right)\frac{D_{\mathrm{s}}}{2}\,\mathrm{d}\vartheta=\frac{N_{\mathrm{s}}D_{\mathrm{s}}}{2pD_{\mathrm{s}}}=\frac{N_{\mathrm{s}}}{2p}$$

which is exactly the number of series conductors per phase in one pole. Note that Equations (5.1),(5.2) represent just the first pole pair, so they have to be repeated through the operator

$$\mathrm{rep}_T\{g(t)\}=\sum_{k=-\infty}^{+\infty}g(t-kT)$$

Then

$$n_{\mathrm{d}}(\vartheta^{\mathrm{e}})=\frac{2}{D_{\mathrm{s}}}\,\mathrm{rep}_{2\pi}\left[\delta\left(\vartheta^{\mathrm{e}}-\tfrac{\pi}{2}\right)-\delta\left(\vartheta^{\mathrm{e}}-\tfrac{\pi}{2}-\pi\right)\right] \tag{5.3}$$

The conductor distribution function (5.3) is now periodic, odd and owns half-wave symmetry, so its Fourier series coefficients are

$$\begin{aligned}b_k&=\frac{1}{\pi}\int_0^{2\pi}n_{\mathrm{d}}(\vartheta^{\mathrm{e}})\sin k\vartheta^{\mathrm{e}}\,\mathrm{d}\vartheta^{\mathrm{e}}\\&=\frac{2}{\pi}\int_0^{\pi}\frac{2}{D_{\mathrm{s}}}\delta\left(\vartheta^{\mathrm{e}}-\tfrac{\pi}{2}\right)\sin k\vartheta^{\mathrm{e}}\,\mathrm{d}\vartheta^{\mathrm{e}}\\&=\frac{4}{\pi D_{\mathrm{s}}}\sin k\tfrac{\pi}{2}\end{aligned}$$

and the series is

$$n_{\mathrm{d}}(\vartheta^{\mathrm{e}})=\frac{4}{\pi D_{\mathrm{s}}}\sum_{\substack{k=1\\ k\ \mathrm{odd}}}^{+\infty}\sin k\tfrac{\pi}{2}\sin k\vartheta^{\mathrm{e}}$$

Similarly, it can be written the conductor distribution function for the other phases, specifically b and c for a three-phase machine.

$$n_{\mathrm{da}}(\vartheta^{\mathrm{e}}) = \frac{4}{\pi D_{\mathrm{s}}} \sum_k \sin k\tfrac{\pi}{2} \sin k\vartheta^{\mathrm{e}}$$
$$n_{\mathrm{db}}(\vartheta^{\mathrm{e}}) = \frac{4}{\pi D_{\mathrm{s}}} \sum_k \sin k\tfrac{\pi}{2} \sin k\big(\vartheta^{\mathrm{e}} - \tfrac{2\pi}{3}\big)$$
$$n_{\mathrm{dc}}(\vartheta^{\mathrm{e}}) = \frac{4}{\pi D_{\mathrm{s}}} \sum_k \sin k\tfrac{\pi}{2} \sin k\big(\vartheta^{\mathrm{e}} - \tfrac{4\pi}{3}\big)$$

Usually these windings are fed by a system of symmetric sinusoidal currents

$$i_{\mathrm{a}}(t) = \hat{I} \cos\big(\omega t + \alpha_i^{\mathrm{e}}\big)$$
$$i_{\mathrm{b}}(t) = \hat{I} \cos\big(\omega t + \alpha_i^{\mathrm{e}} - \tfrac{2\pi}{3}\big)$$
$$i_{\mathrm{c}}(t) = \hat{I} \cos\big(\omega t + \alpha_i^{\mathrm{e}} - \tfrac{4\pi}{3}\big)$$

such that the electric loading of the machine is

$$\mathcal{K}_{\mathrm{s}}(\vartheta^{\mathrm{e}}, t) = n_{\mathrm{da}}(\vartheta^{\mathrm{e}}) i_{\mathrm{a}}(t) + n_{\mathrm{db}}(\vartheta^{\mathrm{e}}) i_{\mathrm{b}}(t) + n_{\mathrm{dc}}(\vartheta^{\mathrm{e}}) i_{\mathrm{c}}(t)$$

The sinusoidal functions products result in

$$\begin{aligned}
&\sin k\vartheta^{\mathrm{e}} \cos\big(\omega t + \alpha_i^{\mathrm{e}}\big) \\
&+ \sin k\big(\vartheta^{\mathrm{e}} - \tfrac{2\pi}{3}\big) \cos\big(\omega t + \alpha_i^{\mathrm{e}} - \tfrac{2\pi}{3}\big) \\
&+ \sin k\big(\vartheta^{\mathrm{e}} - \tfrac{4\pi}{3}\big) \cos\big(\omega t + \alpha_i^{\mathrm{e}} - \tfrac{4\pi}{3}\big) = \\
&= \sin k\vartheta^{\mathrm{e}} \cos\big(\omega t + \alpha_i^{\mathrm{e}}\big) \\
&\quad + \Big(\sin k\vartheta^{\mathrm{e}} \cos k\tfrac{2\pi}{3} - \cos k\vartheta^{\mathrm{e}} \sin k\tfrac{2\pi}{3}\Big) \\
&\qquad \cdot \Big(\cos(\omega t + \alpha_i^{\mathrm{e}}) \cos\tfrac{2\pi}{3} + \sin(\omega t + \alpha_i^{\mathrm{e}}) \sin\tfrac{2\pi}{3}\Big) \\
&\quad + \Big(\sin k\vartheta^{\mathrm{e}} \cos k\tfrac{4\pi}{3} - \cos k\vartheta^{\mathrm{e}} \sin k\tfrac{4\pi}{3}\Big) \\
&\qquad \cdot \Big(\cos(\omega t + \alpha_i^{\mathrm{e}}) \cos\tfrac{4\pi}{3} + \sin(\omega t + \alpha_i^{\mathrm{e}}) \sin\tfrac{4\pi}{3}\Big) \\
&= \sin \nu\vartheta^{\mathrm{e}} \cos\big(\omega t + \alpha_i^{\mathrm{e}}\big) \\
&\quad + \tfrac{1}{2} \sin \nu\vartheta^{\mathrm{e}} \cos\big(\omega t + \alpha_i^{\mathrm{e}}\big) - \tfrac{3}{2} \cos \nu\vartheta^{\mathrm{e}} \sin\big(\omega t + \alpha_i^{\mathrm{e}}\big)
\end{aligned}$$

where $\nu = 6k + 1,\ k \in \mathbb{Z}$ (see Appendix A for further insights). The final result is

$$\mathcal{K}_{\mathrm{s}}(\vartheta_{\mathrm{s}}^{\mathrm{e}}, t) = \frac{6}{\pi D_{\mathrm{s}}} \hat{I} \sum_{\substack{\nu = 6k+1 \\ k \in \mathbb{Z}}}^{\infty} \sin \nu\tfrac{\pi}{2} \sin\big(\nu\vartheta_{\mathrm{s}}^{\mathrm{e}} - \omega t - \alpha_i^{\mathrm{e}}\big)$$

where $\vartheta_{\mathrm{s}}^{\mathrm{e}}$ is the electrical angular coordinate fixed with the stator and with the origin on the magnetic axis of the first phase (a). Now it is possible to substitute the previous single-turn winding (with 2 conductors)

with the single-coil equivalent winding of a distributed and chorded one. This equivalent winding has N_s series conductors per phase and its winding factor is k_w^ν. Then it is possible to define

$$\hat{K}_\mathrm{s} = \frac{3N_\mathrm{s}\hat{I}}{\pi D_\mathrm{s}}$$

and

$$K_\nu = k_\mathrm{w}^\nu \, \hat{K}_\mathrm{s} \, \sin \nu \tfrac{\pi}{2} = \frac{3\hat{I}\, k_\mathrm{w}^\nu N_\mathrm{s}}{\pi D_\mathrm{s}} \, \sin \nu \tfrac{\pi}{2}$$

so the electric loading of a symmetric three-phase winding is (Bianchi et al., 2009b; Bianchi et al., 2007; Barcaro, 2011):

$$\mathcal{K}_\mathrm{s}(\vartheta_\mathrm{s}, t) = \sum_{\substack{\nu=6k+1 \\ k\in\mathbb{Z}}}^{\infty} K_\nu \sin\left(\nu p \vartheta_\mathrm{s} - \omega t - \alpha_i^\mathrm{e}\right) \tag{5.4}$$

This is the starting point of the following analysis thanks to the fact that (5.4) contains all the harmonics generated by the discretized winding.

5.2 ANALYTICAL MODEL

The analytical model considers SyR machines with transversally laminated rotor. Furthermore, only integral-slot winding are considered. The electric loading of a symmetric three-phase distributed winding is:

$$\mathcal{K}_\mathrm{s}(\vartheta_\mathrm{s}, \vartheta_\mathrm{m}) = \sum_{\substack{\nu=6k+1 \\ k\in\mathbb{Z}}}^{\infty} \hat{K}_\nu \sin\left(\nu p \vartheta_\mathrm{s} - p\vartheta_\mathrm{m} - \alpha_i^\mathrm{e}\right) \tag{5.5}$$

where ν is the space harmonic order whose value belong to the set $\{1, -5, 7, -11, 13, \ldots\}$, $\hat{K}_\nu$ is the amplitude of the electric loading ν-th harmonic, p is the number of pole pairs, ϑ_s is the angular coordinate fixed to the stator, ϑ_m is the rotor angular position, and α_i^e is the current electric angle. It is worth noticing that (5.5) reproduces every space harmonic generated by the discretized winding.

The electric loading gives rise to the stator magnetic scalar potential, which is simply its integral, given by

$$\mathcal{U}_\mathrm{s}(\vartheta_\mathrm{s}, \vartheta_\mathrm{m}) = \int \mathcal{K}_\mathrm{s}(\vartheta_\mathrm{s}, \vartheta_\mathrm{m}) \frac{D_\mathrm{s}}{2} \, \mathrm{d}\vartheta_\mathrm{s} \tag{5.6}$$

where D_s is the stator diameter at the air-gap. For a three-phase machine it is

$$\mathcal{U}_\mathrm{s}(\vartheta_\mathrm{s}, \vartheta_\mathrm{m}) = -\frac{D_\mathrm{s}}{2} \sum_{\substack{\nu=6k+1 \\ k\in\mathbb{Z}}} \frac{\hat{K}_\nu}{p\nu} \cos(\nu p \vartheta_\mathrm{s} - p\vartheta_\mathrm{m} - \alpha_i^\mathrm{e}) \tag{5.7}$$

Similarly, the rotor magnetic scalar potential, which reacts to the stator potential, can also be expressed by means of its Fourier series expansion

$$\mathcal{U}_\mathrm{r}(\vartheta_\mathrm{r}, t) = \sum_{\xi=1}^{+\infty} \hat{U}_\xi \sin(\xi p \vartheta_\mathrm{r}) \tag{5.8}$$

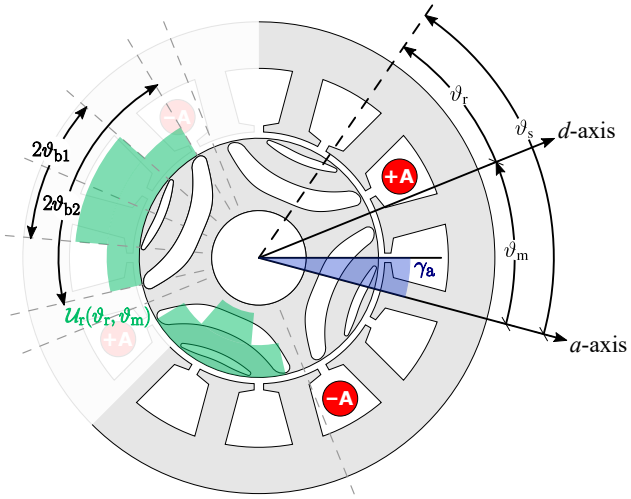

Figure 5.2
Sketch of a SyR motor with two flux-barriers per pole together with the reference axes and the barrier angle quotes. The colored area on top of the flux-barriers represents the rotor magnetic scalar potential distribution for half the machine.

It is different from zero when the flux flows in the q-axis direction, crossing the flux-barriers. The rotor magnetic scalar potentials and the rotor barrier angles are grouped in vectors:

$$\boldsymbol{u}_r = \{U_{r1}, U_{r2}, \dots, U_{rn}\}^T, \tag{5.9}$$

$$\boldsymbol{\vartheta}_b = \{\vartheta_{b1}, \vartheta_{b2}, \dots, \vartheta_{bn}\}^T \tag{5.10}$$

A quasi-diagonal matrix $\boldsymbol{G}$ can be built, given by

$$\boldsymbol{G} = \begin{bmatrix} +1 & -1 & & & \\ & +1 & -1 & & \\ & & \ddots & \ddots & \\ & & & +1 & -1 \\ & & & & +1 \end{bmatrix} \tag{5.11}$$

with $+1$ in the main diagonal and -1 in the second right-hand diagonal, such that

$$\hat{U}_\xi = \frac{4}{\pi\xi} \sin\left(\xi \tfrac{\pi}{2}\right) \left[\sin(\xi p \boldsymbol{\vartheta}_b^T) \boldsymbol{G} \boldsymbol{u}_r\right] \tag{5.12}$$

where $\sin(\xi \boldsymbol{\vartheta}_b^T)$ is a row vector of sines, $\boldsymbol{G}\boldsymbol{u}_r$ is the product of the matrix (5.11) and the vector $\boldsymbol{u}_r$, defined in (5.9). The magnetic potentials of the islands can be calculated as the solution of the magnetic circuit shown in Figure 5.3.

5.3 ROTOR MAGNETIC POTENTIALS COMPUTATION

Figure 5.3 represents the magnetic circuit of a SyR motor with N_b flux barriers. There are N_b nodes, each one at its own magnetic potential U_{rj}. The MMF generators are defined between two distinct barrier angles, and so are their reluctances. The remaining reluctances are the barriers' one.

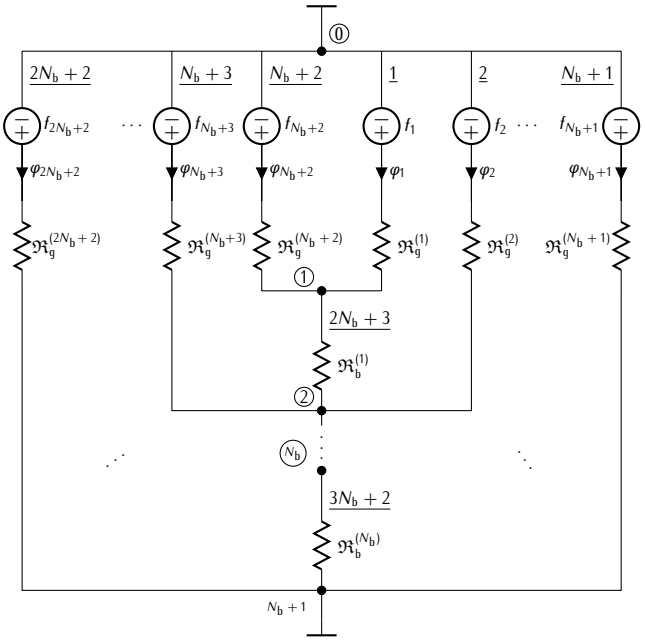

Figure 5.3
Magnetic circuit of one pole of the rotor of a SyR machine. Circled labels represent nodes while underlined labels represent edges of the circuit.

The first $N_\mathrm{b}+1$ edges connects node 0 to the nodes of the islands, so the partial incidence matrix is

$$A' = \begin{array}{c} \begin{array}{ccccc} \underline{1} & \underline{2} & \cdots & \underline{N_b} & \underline{N_b{+}1} \end{array} \\ \begin{bmatrix} +1 & +1 & \cdots & +1 & +1 \\ -1 & & & & \\ & -1 & & & \\ & & \ddots & & \\ & & & -1 & \\ & & & & -1 \end{bmatrix} \end{array} \begin{array}{l} 0 \\ 1 \\ 2 \\ \vdots \\ N_b \\ N_b{+}1 \end{array}$$

In these edges there are non-ideal (real) MMF generator, so an ideal generator in series with a reluctance. In the following $N_\mathrm{b}+1$ nodes there are the very same elements and structure, so the matrix A' is repeated.

The last part of the incidence matrix connects the following nodes between flux barrier reluctances, so it is the path followed by the flux that crosses all the barriers.

$$A'' = \begin{array}{c} \begin{array}{ccccc} \underline{2N_b{+}3} & \underline{2N_b{+}4} & \cdots & \underline{3N_b{+}1} & \underline{3N_b{+}2} \end{array} \\ \begin{bmatrix} +1 & & & & \\ -1 & +1 & & & \\ & \vdots & \ddots & \vdots & \\ & & & -1 & +1 \\ & & & & -1 \end{bmatrix} \end{array} \begin{array}{l} 1 \\ 2 \\ \vdots \\ N_b \\ N_b{+}1 \end{array}$$

$$\boldsymbol{A}_{\mathrm{c}} = \left[\begin{array}{c:c:c} \boldsymbol{A}'_{(N_b+2,N_b+1)} & \boldsymbol{A}'_{(N_b+2,N_b+1)} & \begin{array}{c}\mathbf{0}_{(1,N_b)}\\ \\ \boldsymbol{A}''_{(N_b+1,N_b)}\end{array} \end{array}\right]$$

This is the scheme of the incidence matrix. To obtain the reduced one, we drop the *first* and *last* rows, the ones at "ground" potential. The remaining nodes are located inside the rotor island. Note that some columns are filled with zeros now, and they are the extreme edges corresponding to the main channel. This means that they are not dependent on the quantities of the grid and their fluxes can be solved immediately. Thanks to the order of construction, active components are present only in the first $2N_{\mathrm{b}}+2$ edges; the rest of the circuit is made of passive components. So the circuit can be solved with the *tableau method*, which is (Chua et al., 1987)

$$\underbrace{\begin{bmatrix} \boldsymbol{A} & \mathbf{0} & \mathbf{0} \\ \mathbf{0} & -\boldsymbol{I} & \boldsymbol{A}^{\mathrm{T}} \\ \boldsymbol{R} & \boldsymbol{G} & \mathbf{0} \end{bmatrix}}_{\boldsymbol{M}} \cdot \underbrace{\begin{pmatrix} \boldsymbol{\varphi} \\ \boldsymbol{\psi} \\ \boldsymbol{u} \end{pmatrix}}_{x} = \underbrace{\begin{pmatrix} \mathbf{0} \\ \mathbf{0} \\ \boldsymbol{s} \end{pmatrix}}_{g} \tag{5.13}$$

5.3.1 *Reluctance of the flux barriers*

The reluctance of the H-th flux barrier is given by

$$\mathfrak{R}_{\mathrm{b}H} = \frac{t_{\mathrm{b}H}}{\mu_0 L_{\mathrm{stk}}\, l_{\mathrm{b}H}}$$

5.3.2 *Reluctance of partial air-gap*

There are $2N_{\mathrm{b}}+2$ reluctances in front of each generator, representing part of the air-gap reluctance

$$\mathfrak{R}_{\mathrm{g}H} = \frac{2g}{\mu_0 L_{\mathrm{stk}} D_{\mathrm{s}} \left[\vartheta_{\mathrm{b}H} - \vartheta_{\mathrm{b}(H-1)}\right]}$$

5.3.3 *mmf generator expression*

The first MMF generator comprehends the angles between $\left(\frac{\pi}{2} - \vartheta^{\mathrm{e}}_{\mathrm{b}1}\right)$ and $\frac{\pi}{2}$.

$$\begin{aligned} f_1 &= \frac{1}{\vartheta^{\mathrm{e}}_{\mathrm{b}1}} \int_{\frac{\pi}{2}-\vartheta^{\mathrm{e}}_{\mathrm{b}1}}^{\frac{\pi}{2}} \mathcal{U}_{\mathrm{s}}(\vartheta^{\mathrm{e}}_{\mathrm{r}})\, \mathrm{d}\vartheta^{\mathrm{e}}_{\mathrm{r}} \\ &= -\sum_{\nu,k} \frac{K_\nu D_{\mathrm{s}}}{2p\vartheta^{\mathrm{e}}_{\mathrm{b}1}\, \nu^2} \left[\sin\lambda_\nu \left(1-\cos\nu\vartheta^{\mathrm{e}}_{\mathrm{b}1}\right) + \cos\lambda_\nu \sin\nu\vartheta^{\mathrm{e}}_{\mathrm{b}1}\right] \end{aligned}$$

In general, given θ_H and θ_{H-1}:[2]

$$\begin{aligned} f_H &= \frac{1}{\theta_H - \theta_{H-1}} \int_{\frac{\pi}{2}-\theta_H}^{\frac{\pi}{2}-\theta_{H-1}} \mathcal{U}_\mathrm{s}(\vartheta_\mathrm{r}^\mathrm{e})\ \mathrm{d}\vartheta_\mathrm{r}^\mathrm{e} \\ &= \frac{-1}{\theta_H - \theta_{H-1}} \sum_{\nu,k} \frac{K_\nu D_\mathrm{s}}{2p\nu^2} \Big[\sin\lambda_\nu \big(\cos\nu\theta_{H-1} - \cos\nu\theta_H\big) \\ &\qquad - \cos\lambda_\nu \big(\sin\nu\theta_{H-1} - \sin\nu\theta_H\big)\Big] \end{aligned}$$

Vice versa, for the other half pole, it results

$$\begin{aligned} f_H &= \frac{1}{\theta_H - \theta_{H-1}} \int_{\frac{\pi}{2}+\theta_{H-1}}^{\frac{\pi}{2}+\theta_H} \mathcal{U}_\mathrm{s}(\vartheta_\mathrm{r}^\mathrm{e})\ \mathrm{d}\vartheta_\mathrm{r}^\mathrm{e} \\ &= \frac{-1}{\theta_H - \theta_{H-1}} \sum_{\nu,k} \frac{K_\nu D_\mathrm{s}}{2p\nu^2} \Big[\sin\lambda_\nu \big(\cos\nu\theta_H - \cos\nu\theta_{H-1}\big) \\ &\qquad + \cos\lambda_\nu \big(\sin\nu\theta_H - \sin\nu\theta_{H-1}\big)\Big] \end{aligned}$$

5.3.4 *Air-gap flux density*

The stator magnetic scalar potential, given in (5.7), can be expressed in the rotor reference frame. Since

$$\vartheta_\mathrm{s} = \vartheta_\mathrm{r} + \vartheta_\mathrm{m}$$

it results in

$$\mathcal{U}_\mathrm{s}(\vartheta_\mathrm{r}, \vartheta_\mathrm{m}) = -\sum_{\substack{\nu=6k+1 \\ k\in\mathbb{Z}}} \frac{\hat{K}_\nu D_\mathrm{s}}{2p\nu} \cos\big[\nu p\vartheta_\mathrm{r} + (\nu-1)p\vartheta_\mathrm{m} - \alpha_i^\mathrm{e}\big]$$

It is split using sine and cosine as:

$$\begin{aligned} \mathcal{U}_\mathrm{s}(\vartheta_\mathrm{r}, \vartheta_\mathrm{m}) = -\sum_{\substack{\nu=6k+1 \\ k\in\mathbb{Z}}} \frac{\hat{K}_\nu D_\mathrm{s}}{2p\nu} \Big[&\cos(\nu p\vartheta_\mathrm{r}) \cos\big((\nu-1)p\vartheta_\mathrm{m} - \alpha_i^\mathrm{e}\big) + \\ &- \sin(\nu p\vartheta_\mathrm{r}) \sin\big((\nu-1)p\vartheta_\mathrm{m} - \alpha_i^\mathrm{e}\big)\Big] \end{aligned} \tag{5.14}$$

$\mathcal{U}_\mathrm{r}(\vartheta_\mathrm{r}, \vartheta_\mathrm{m})$ also contains harmonics multiple of three and they can be grouped apart. Then, it is easy to verify that $\mathcal{U}_\mathrm{r}$ is an even function with respect to the harmonic order ξ, so positive or negative indexes can be used indifferently.

$$\mathcal{U}_\mathrm{r}(\vartheta_\mathrm{r}, \vartheta_\mathrm{m}) = \sum_{\substack{\nu=6k+1 \\ k\in\mathbb{Z}}} \hat{U}_\nu \sin(\nu p\vartheta_\mathrm{r}) + \sum_{\substack{\mu=6h+3 \\ h\in\mathbb{Z}^+}} \hat{U}_\mu \sin(\mu p\vartheta_\mathrm{r}) \tag{5.15}$$

The air-gap flux density can be expressed as the difference of the two magnetic scalar potentials (Bianchi et al., 2009b; Bianchi, 2006):

$$\mathcal{B}_\mathrm{g}(\vartheta_\mathrm{r}, \vartheta_\mathrm{m}) = \mu_0 \frac{-\mathcal{U}_\mathrm{s}(\vartheta_\mathrm{r}, \vartheta_\mathrm{m}) + \mathcal{U}_\mathrm{r}(\vartheta_\mathrm{r}, \vartheta_\mathrm{m})}{g} \tag{5.16}$$

2 For convenience of notation, let $\theta_H = \vartheta_{\mathrm{b}H}^\mathrm{e}$.

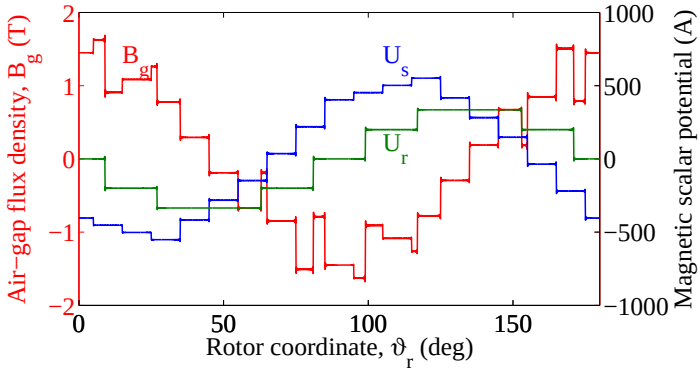

Figure 5.4
Air-gap flux density and magnetic scalar potentials of a 2-barrier SyR machine without saturation at $t = 0$.

Introducing (5.14) and (5.15) in (5.16), the air-gap flux density results in

$$\mathcal{B}_\mathrm{g} = \sum_{\substack{\nu=6k+1\\k\in\mathbb{Z}}} \frac{\mu_0 D_\mathrm{s}\,\hat{K}_\nu}{2gp\,\nu}\Big[\overbrace{\cos\big((\nu-1)\omega t-\alpha_i^\mathrm{e}\big)\cos(\nu p\vartheta_\mathrm{r})}^{\text{stator even part}} \underbrace{-\sin\big((\nu-1)\omega t-\alpha_i^\mathrm{e}\big)\sin(\nu p\vartheta_\mathrm{r})}_{\text{stator odd part}}\Big] + \\ + \underbrace{\sum_{\substack{\nu=6k+1\\k\in\mathbb{Z}}} \frac{\mu_0}{g\nu}\,\nu\hat{U}_\nu\sin(\nu p\vartheta_\mathrm{r})}_{\text{rotor without triplen harmonics}} + \underbrace{\sum_{\substack{\mu=6h+3\\h\in\mathbb{Z}^+}} \frac{\mu_0}{g\mu}\,\mu\hat{U}_\mu\sin(\mu p\vartheta_\mathrm{r})}_{\text{rotor triplen harmonics}}$$

and reordering

$$\mathcal{B}_\mathrm{g}(\vartheta_\mathrm{r},\vartheta_\mathrm{m}) = \sum_\nu\Big[\frac{\alpha_\nu}{\nu}\cos(\nu p\vartheta_\mathrm{r}) + \frac{\beta_\nu}{\nu}\sin(\nu p\vartheta_\mathrm{r})\Big] + \\ + \sum_\mu \frac{\gamma_\mu}{\mu}\sin(\mu p\vartheta_\mathrm{r}) \tag{5.17}$$

where α_ν, β_ν derives from the coefficients which multiply the cosine and sine functions under the summations in ν, while $\gamma_\mu = \mu_0\mu\hat{U}_\mu/g$.

An example of the magnetic potentials and the flux density is reported in Figure 5.4.

5.3.5 *Torque derivation*

The torque is obtained integrating the Lorentz's force density $\mathcal{K}_\mathrm{s}\mathcal{B}_\mathrm{g}$, both function of ϑ_r and ϑ_m, along the air-gap surface and multiplying the result by the lever-arm $D_\mathrm{s}/2$ (Bianchi et al., 2009b):

$$T_\mathrm{m}(\vartheta_\mathrm{m}) = -\frac{D_\mathrm{s}}{2}\int_0^{2\pi}\mathcal{B}_\mathrm{g}(\vartheta_\mathrm{r},\vartheta_\mathrm{m})\mathcal{K}_\mathrm{s}(\vartheta_\mathrm{r},\vartheta_\mathrm{m})\frac{D_\mathrm{s}L_\mathrm{stk}}{2}\,\mathrm{d}\vartheta_\mathrm{r}$$

Remembering (5.16), it can be derived

$$T_\mathrm{m} = \frac{\mu_0 D_\mathrm{s}^2 L_\mathrm{stk}}{4g}\Big[\underbrace{\int_0^{2\pi}\mathcal{U}_\mathrm{s}\mathcal{K}_\mathrm{s}\,\mathrm{d}\vartheta_\mathrm{r}}_{A} - \underbrace{\int_0^{2\pi}\mathcal{U}_\mathrm{r}\mathcal{K}_\mathrm{s}\,\mathrm{d}\vartheta_\mathrm{r}}_{B}\Big]$$

The first integral, labeled as A, is zero since $\mathcal{U}_\mathrm{s}$ and $\mathcal{K}_\mathrm{s}$ are orthogonal functions. Therefore the torque is only due to the interaction of electric loading $\mathcal{K}_\mathrm{s}$ and the magnetic scalar potential of the rotor $\mathcal{U}_\mathrm{r}$.

The final expression of the torque is

$$T_\mathrm{m}(\vartheta_\mathrm{m}) = -\frac{\mu_0 D_\mathrm{s}^2 L_\mathrm{stk}}{g} \sum_{\nu,k} \frac{\hat{K}_\nu}{\nu} \sin \nu \tfrac{\pi}{2} \cdot \\ \cdot \cos\big((\nu-1)p\vartheta_\mathrm{m} - \alpha_i^\mathrm{e}\big) \big[\sin(\nu \boldsymbol{\vartheta}^\mathrm{T}) \boldsymbol{G} \boldsymbol{u}_\mathrm{r}\big]$$

5.3.6 *Tooth flux density*

To compute the stator tooth flux density, the air-gap flux density $\mathcal{B}_\mathrm{g}(\vartheta_\mathrm{r}, \vartheta_\mathrm{m})$ in (5.17) has to be referred to the stator reference frame. It is

$$\mathcal{B}_\mathrm{g}(\vartheta_\mathrm{s}, \vartheta_\mathrm{m}) = \sum_\nu \left[\frac{\alpha_\nu}{\nu} \cos(\nu p \vartheta_\mathrm{s} - \nu p \vartheta_\mathrm{m}) + \frac{\beta_\nu}{\nu} \sin(\nu p \vartheta_\mathrm{s} - \nu p \vartheta_\mathrm{m})\right] \\ + \sum_\mu \frac{\gamma_\mu}{\mu} \sin(\mu p \vartheta_\mathrm{s} - \mu p \vartheta_\mathrm{m}) \tag{5.18}$$

The stator tooth flux density can be obtained through the scaled average of the air-gap flux density (Bianchi et al., 2008a; Han et al., 2007; Pellegrino et al., 2010):

$$B_\mathrm{t}(\vartheta_\mathrm{m}) = \frac{p_\mathrm{s}}{\alpha_\mathrm{s} w_\mathrm{t} k_\mathrm{pack}} \int_{\vartheta_d}^{\vartheta_d + \alpha_\mathrm{s}} \mathcal{B}_\mathrm{g}(\vartheta_\mathrm{s}, \vartheta_\mathrm{m}) \, \mathrm{d}\vartheta_\mathrm{s} \tag{5.19}$$

where p_s is the slot pitch, α_s the slot angle, w_t the tooth width, and k_pack is the ratio between the total effective iron and the stack length.

It can be demonstrated that the tooth flux density assumes q different behaviors, q being the number of slots per pole and per phase, defined as $q = Q/(m\,2p)$. Thus the integration extremes can be expressed as

$$\vartheta_d = (d-1)\alpha_\mathrm{s} - \gamma_\mathrm{a} \,, \qquad d = 1, \ldots, q \tag{5.20}$$

where γ_a identifies the angular position of the magnetic axis of phase a with respect to the first slot (see Figure 5.2).

5.3.7 *Stator yoke flux density*

The flux in the stator yoke—also referred to as back-iron—is obtained integrating the air-gap flux density over a pole pitch, then the flux density is

$$B_\mathrm{y}(\vartheta_\mathrm{m}) = \frac{1}{2 h_\mathrm{y} k_\mathrm{pack}} \int_{-\gamma_\mathrm{a}}^{\frac{\pi}{p} - \gamma_\mathrm{a}} \mathcal{B}_\mathrm{g}(\vartheta_\mathrm{s}, \vartheta_\mathrm{m}) \frac{D_\mathrm{s}}{2} \, \mathrm{d}\vartheta_\mathrm{s} \\ \underset{\substack{\uparrow \\ q \text{ integer}}}{=} \frac{w_\mathrm{t}}{2 h_\mathrm{y}} \sum_{i=1}^{Q/2p} B_{\mathrm{t},i}(\vartheta_\mathrm{m}) \tag{5.21}$$

where $h_\mathrm{y} = (D_\mathrm{se} - D_\mathrm{s})/2$ is the stator yoke height.

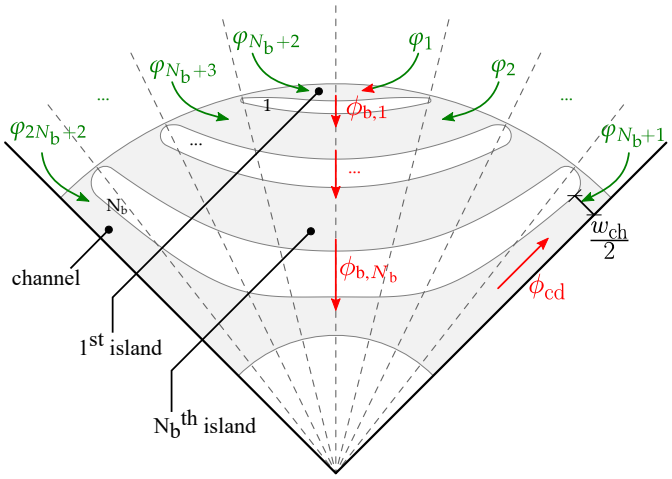

Figure 5.5
Sketch of the main parts of the rotor structure and rotor fluxes direction.

5.3.8 *Rotor fluxes*

In the linear case, the fluxes entering the rotor are directly obtained from the solution of the magnetic circuit in Figure 5.3. Both the island and the barrier fluxes are computed. The iron path closer to the shaft is referred to as channel. The remaining iron paths for the d-axis flux are referred to as islands. They assume a different potential, due to the q-axis flux, and they are numbered accordingly to the number of the barrier beneath them. The barrier fluxes are obtained solving the magnetic network depicted in Figure 5.3. The d-axis channel flux comes from $\phi_{cd} = \varphi_{N_b+1} - \varphi_{2N_b+2}$ which simply sums the two fluxes to obtain the whole direct flux of the channel. Then

$$B_{cd} = \frac{\phi_{cd}}{w_{ch}\, k_{pack} L_{stk}} \tag{5.22}$$

where $w_{ch} \approx (1 - k_{air}) D_r \sin\left(\frac{\pi}{2p} - \vartheta_{bN_b}\right)$ is an approximation of the minimum width of the channel.

For the q-axis flux of the main channel, just half of the last barrier flux can be considered, with $\phi_{cq} = \phi_{b,N_b}/2$. Thus

$$B_{cq} = \frac{\phi_{cq}}{l_{ch}\, k_{pack} L_{stk}} \tag{5.23}$$

where $l_{ch} = (D_r - D_{sh})/2$. Then, it is

$$|\boldsymbol{B}_c| = \sqrt{B_{cd}^2 + B_{cq}^2} \tag{5.24}$$

The d-axis fluxes of the islands result directly from the magnetic circuit fluxes, as

$$B_{id,j} = \frac{\varphi_j}{k_{pack} L_{stk} w_{isl,j}} \tag{5.25}$$

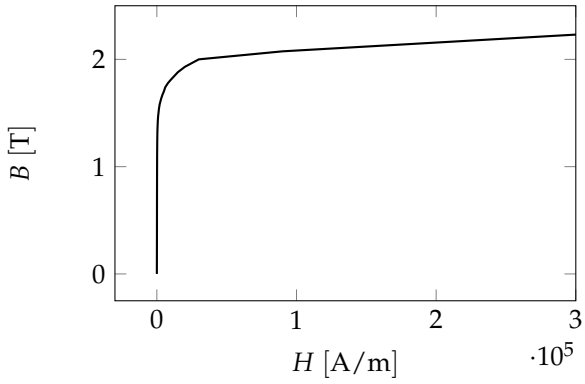

Figure 5.6
Magnetization curve of the ferromagnetic material used.

Regarding the q-axis fluxes of the islands, the average of the fluxes above and beneath each island is computed. An average cross-section area of each island is considered, so that

$$\vartheta_{\mathrm{isl},j} = \frac{\vartheta_{\mathrm{b},j} + \vartheta_{\mathrm{b},j-1}}{2} \tag{5.26}$$

$$l_{\mathrm{isl},j} = \vartheta_{\mathrm{isl},j} D_{\mathrm{s}} \tag{5.27}$$

$$\begin{pmatrix} \phi_{\mathrm{iq},1} \\ \phi_{\mathrm{iq},2} \\ \phi_{\mathrm{iq},3} \\ \vdots \\ \phi_{\mathrm{iq},N_b} \end{pmatrix} = \frac{1}{2} \begin{bmatrix} 2 & & & & \\ 1 & 1 & & & \\ & 1 & 1 & & \\ & & \ddots & \ddots & \\ & & & 1 & 1 \end{bmatrix} \begin{pmatrix} \phi_{\mathrm{b}1} \\ \phi_{\mathrm{b}2} \\ \phi_{\mathrm{b}3} \\ \vdots \\ \phi_{\mathrm{b}N_b} \end{pmatrix} \tag{5.28}$$

$$B_{\mathrm{iq},j} = \frac{\phi_{\mathrm{iq},j}}{k_{\mathrm{pack}} L_{\mathrm{stk}} l_{\mathrm{isl},j}} \tag{5.29}$$

$$|\boldsymbol{B}_{\mathrm{i},j}| = \sqrt{B_{\mathrm{id},j}^2 + B_{\mathrm{iq},j}^2} \tag{5.30}$$

5.4 ANALYTICAL MODEL WITH SATURATION

The previous analytical model works properly in case of linear behavior of ferromagnetic material, that is, in the first part of the iron B-H curve (the curve is reported in Figure 5.6). However, this condition is barely met. In SyR motors the rotor iron paths are saturated to achieve a quite high torque density and power factor. Thus, in practice, the saturation of the machine has to be taken into account.

Hereafter, the saturation is taken into account through a discretization of the flux line paths into sections. In particular, a section can be a stator tooth, a stator yoke sector, or a rotor half iron path. The path of a flux line results a succession of these sections. Therefore a magnetic voltage drop and a saturation factor are associated with each flux line and referred to the air-gap. At first the rotor iron paths are considered, and then the stator teeth and yoke.

5.4.1 *Rotor channel and islands magnetic voltage drop*

The magnetic voltage drop of the rotor channel is estimated from (5.24). Since the flux density is computed in the smallest cross-section, it is the maximum value of the channel. The average is estimated as $B_{\mathrm{c}}^{\star} = 0.85\,|\boldsymbol{B}_{\mathrm{c}}|$ and, from the iron B-H curve, the magnetic field H_{c} is obtained (in the following, it is indicated as $B \rightarrow H$). Then the magnetic voltage drop results $\psi_{\mathrm{c}} = H_{\mathrm{c}}\, l_{\mathrm{ch}}$. Similarly, the islands have a complex geometry and a different flux density in every point. The middle section of the island is considered, where the width is precisely known. It should be noted that the two half-island paths have different voltage drops due to part of the entering elementary flux that crosses the barrier and does not reclose on the other side. To recover this difference, a magnetic voltage drop is computed for every half island using the elementary flux.The procedure is sketched as follows:

$$|\boldsymbol{B}_{\mathrm{i},j}| \;\longrightarrow\; H_{\mathrm{i},j} \quad \text{then} \quad \psi_{\mathrm{i},j} = H_{\mathrm{i},j}\,\frac{l_{\mathrm{isl},j}}{2} \tag{5.31}$$

The same procedure is carried out for the second (south) half pole.

The vector of rotor magnetic voltage drops, corresponding to the sequence of channel and islands starting from the origin of ϑ_{r}, is:

$$\boldsymbol{\psi}_{\mathrm{rp}} = \{\psi_{\mathrm{c}},\, \underbrace{\psi_{\mathrm{i},N_{\mathrm{b}}}, \ldots, \psi_{\mathrm{i},1}}_{\boldsymbol{\psi}_{\mathrm{i}}^{\mathrm{N}}}\, \underbrace{\psi_{\mathrm{i},N_{\mathrm{b}}+2}, \ldots, \psi_{\mathrm{i},2N_{\mathrm{b}}+2}}_{\boldsymbol{\psi}_{\mathrm{i}}^{\mathrm{S}}},\, \psi_{\mathrm{c}}\}^{\mathrm{T}}$$

where $\boldsymbol{\psi}_{\mathrm{i}}^{\mathrm{N}}$ and $\boldsymbol{\psi}_{\mathrm{i}}^{\mathrm{S}}$ are the vectors of the first half pole (identified by the superscript N meaning North) and the second half pole (identified by the superscript S meaning South) voltage drops, respectively.

Numerically, this vector is distributed into a number of points accordingly to the angle spanned. In the end, the distribution of the rotor magnetic voltage drops is equivalent to the distribution of the scalar magnetic potentials along the air-gap.

$$\boldsymbol{\psi}_{\mathrm{r}} = \underbrace{\{\underbrace{\psi_{\mathrm{c}}, \ldots, \psi_{\mathrm{c}}}_{N_{N_{\mathrm{b}}+1}}, \underbrace{\psi_{\mathrm{i},N_{\mathrm{b}}}, \ldots, \psi_{\mathrm{i},N_{\mathrm{b}}}}_{N_{N_{\mathrm{b}}}}, \ldots, \underbrace{\psi_{\mathrm{i},1}, \ldots, \psi_{\mathrm{i},1}}_{N_1}, \ldots\}^{\mathrm{T}}}_{Res/2p}$$

where Res is the number of points used for discretizing the space $[0, 2\pi]$ along the air-gap, and the subscript of N refers to the corresponding island.

5.4.2 *Stator teeth and yoke magnetic voltage drops*

The instantaneous tooth flux density in the saturation case is obtained through the numerical integration of (5.19). Once the flux density for every tooth of interest (typically Q/p teeth for an integer-slot winding) is computed, the magnetic voltage drops are derived, as follows:

$$|B_{\mathrm{t},j}| \;\longrightarrow\; H_{\mathrm{t},j} \quad \text{then} \quad \psi_{\mathrm{t},j} = H_{\mathrm{t},j}\, h_{\mathrm{s}} \tag{5.32}$$

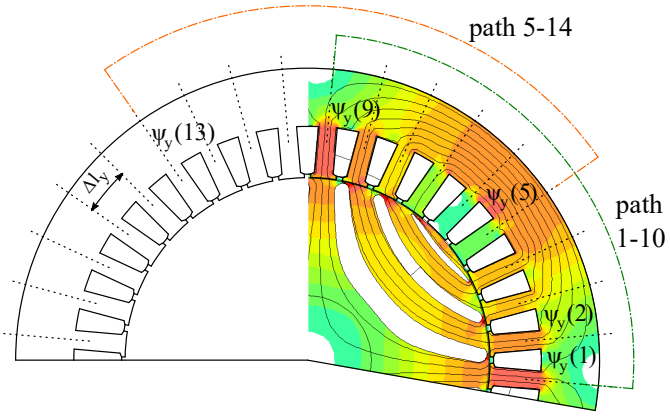

Figure 5.7
Real flux lines and main integration paths ($Q = 36, 2p = 4$).

where h_s is the tooth height.

The back-iron corresponding to a pole pair is split into Q/p parts, each one covering a slot angle, as illustrated in Figure 5.7 (dotted lines). The flux density can be derived for each part, as

$$\tilde{\phi}_y(k) = w_t L_{stk} \sum_{j=1}^{k} B_{t,j} \qquad k = 1, \ldots, Q/p \tag{5.33}$$

$$\phi_y(k) = \tilde{\phi}_y(k) - \frac{1}{Q/p} \sum_{j=1}^{Q/p} \tilde{\phi}_y(j) \tag{5.34}$$

$$B_y(k) = \frac{|\phi_y(k)|}{h_y L_{stk}} \longrightarrow H_y(k)\,, \quad \psi_y(k) = H_y(k)\,\Delta l \tag{5.35}$$

where $\Delta l = \pi(D_{se} - h_y)/Q$ is the average length of one back-iron part. Once the stator yoke voltage drops are computed in any section, the flux path for all flux lines of interest have to be correctly identified. Two of these lines are shown in Figure 5.7. Summing the voltage drops along these lines is equivalent to consider that each flux line flows for a full pole and it encounters $Q/2p$ voltage drops along its path. The voltage drops are summed with the sign of the corresponding flux in the same part. Finally, every flux line has gathered the same overall magnetic voltage drop of the actual flux line of that particular tooth. Therefore, it is

$$\psi_{yt}(n) = \left| \frac{1}{2} \sum_{k=n}^{n+\frac{Q}{2p}-1} \psi_y(k)\ \mathrm{sign}\,\phi_y(k) \right|, \quad n = 1, \ldots, Q/2p \tag{5.36}$$

where the double subscript 'yt' indicates that the yoke drop is referred to the tooth. The $\frac{1}{2}$ occurs since half the path is counted. For example, let us consider the path 1-10 shown in Figure 5.7, which covers $\psi_y(1)$ to $\psi_y(9)$: it starts from tooth number 1 (below the first slot) and it ends in tooth 10. The total magnetic voltage drop associated to this line is

$$2\psi_{yt}(1) = \psi_y(1) + \psi_y(2) + \ldots + \psi_y(9) \tag{5.37}$$

On the other hand, along the path 5-14 it is

$$\begin{aligned} 2\psi_{\mathrm{yt}}(5) &= \psi_{\mathrm{y}}(5) + \ldots + \psi_{\mathrm{y}}(9) - \psi_{\mathrm{y}}(10) - \ldots - \psi_{\mathrm{y}}(13) \\ &\cong \psi_{\mathrm{y}}(5) \end{aligned} \tag{5.38}$$

The last equivalence is the main assumption of this computation. In fact it implies that $\psi_{\mathrm{y}}(6)$ is equal to $\psi_{\mathrm{y}}(13)$ and so on, and the remaining term is just $\psi_{\mathrm{y}}(5)$. Even if the machine is not symmetrically magnetized, this is a fairly good approximation thanks to the lower value of the q-axis flux with respect to the d-axis flux. Even with high values of α_i^{e} it can be shown that this approximation is good enough.

Similarly to the rotor, the stator magnetic voltage drops can be collected and distributed along the discretization of the angular coordinate at the air-gap.

5.4.3 *Total magnetic voltage drop and saturation factor*

In order to combine the rotor and stator magnetic voltage drop distributions, the rotor position and the first tooth displacement have to be taken into account through the shift of one of the two distributions, according to the adopted reference frame. The air-gap magnetic voltage drop can be easily computed from the flux density obtained in the previous iteration.

$$\boldsymbol{\Psi}_{\mathrm{g}} = \boldsymbol{H}_{\mathrm{g}}\, g = \frac{\boldsymbol{B}_{\mathrm{g}}}{\mu_0}\, g \tag{5.39}$$

All the magnetic voltage drops are summed to obtain the total voltage drop, which is again referred to the air-gap.

$$\boldsymbol{\Psi}_{\mathrm{tot}} = \boldsymbol{\Psi}_{\mathrm{g}} + \boldsymbol{\Psi}_{\mathrm{s}}^{\mathrm{r}} + \boldsymbol{\Psi}_{\mathrm{r}} \tag{5.40}$$

where $\boldsymbol{\Psi}_{\mathrm{s}}^{\mathrm{r}}$ is the vector of stator voltage drops in the rotor reference frame. Then

$$\boldsymbol{k}_{\mathrm{sat}} = \frac{\boldsymbol{\Psi}_{\mathrm{tot}}}{\boldsymbol{\Psi}_{\mathrm{g}}} \tag{5.41}$$

This saturation factor is different from the usually adopted factor. In fact (5.41) is a distribution of saturation factors along the air-gap that better represents the saturation of the machine.

The adopted iteration scheme is fixed-point like, with a random relaxation to improve the stability of the convergence:

$$\boldsymbol{k}_{\mathrm{sat}}^{(m+1)} \leftarrow \boldsymbol{k}_{\mathrm{sat}}^{(m)} + 0.5\,\mathrm{rand}\left(\boldsymbol{k}_{\mathrm{sat}}^{(m+1)} - \boldsymbol{k}_{\mathrm{sat}}^{(m)}\right) \tag{5.42}$$

For the next iteration the updated air-gap flux density is simply

$$\boldsymbol{B}_{\mathrm{g}}^{(m+1)} = \mu_0 \frac{-\boldsymbol{U}_{\mathrm{s}} + \boldsymbol{U}_{\mathrm{r}}}{\boldsymbol{k}_{\mathrm{sat}}^{(m+1)} g} \tag{5.43}$$

and the iteration cycle restarts. The error of the method was evaluated through

$$\epsilon_{\mathrm{sat}} = \left\| \boldsymbol{k}_{\mathrm{sat}}^{(m+1)} - \boldsymbol{k}_{\mathrm{sat}}^{(m)} \right\| \tag{5.44}$$

Table 5.1
Parameters of the reference motor.

$Q = 36$	number of slots
$2p = 4$	number of poles
$y_q = 9$	coil pitch
$D_e = 200\,\text{mm}$	stator outer diameter
$D_s = 125\,\text{mm}$	stator inner diameter
$L_{stk} = 40\,\text{mm}$	lamination stack length
$g = 0.35\,\text{mm}$	air-gap thickness
$S_{slot} = 100\,\text{mm}^2$	slot section area
$J = 3\,\text{A}/\text{mm}^2$	conductor current density
$k_{fill} = 0.45$	slot fill factor
$k_{pack} = 0.95$	lamination pack factor
$k_{air} = 0.35$	ratio of rotor magnetic insulation

5.5 TORQUE MAPS

The nonlinear model is used to compute the impact of the rotor geometry on both the average torque and torque ripple. In particular, the impact of the flux-barrier-end angles is analyzed, since they heavily affect the torque ripple (Bianchi et al., 2009b). The average torque and some torque ripple harmonics are computed as a function of the flux-barrier angles, $(\vartheta_{b1}, \vartheta_{b2})$, and their amplitude is shown graphically by using maps. Figure 5.8 reports such torque maps, computed for a reference motor with two flux barriers whose data is reported in Table 5.1.

For the sake of an easy comparison, Figure 5.8 reports three *columns*, which refer to the results obtained by means of:

i. the analytical linear model (Bianchi et al., 2009b),

ii. the nonlinear model, described above,

iii. the FE method applied on the same motor geometries (Silvester et al., 1996; Bianchi, 2005; Salon, 2012).

The results on SyR motor achieved through FE analysis have been compared with experimental test several times by the authors, obtaining satisfactory agreements (Bianchi et al., 2009b; Bianchi et al., 2014; Bianchi et al., 2016; Ferrari et al., 2015) but also in other works (Vagati et al., 1998; Moghaddam, 2011; Gamba, 2017). For this reason, in the following comparison, the results computed analytically are considered to be valid if they agree with the FE results.

The *first row* reports the comparison among average torque maps. The map computed with the linear model shows higher average torques with respect to the other two maps. This is obvious since the model does not take into account the iron saturation. However, it is worth noticing that the behavior of the torque curves is almost identical.

Comparing the maps of the second and third column, it is possible to note that the nonlinear analytical model predicts correctly not only the

behavior of the torque maps as a function of ϑ_{b1} and ϑ_{b2}, but also its amplitude. Therefore, the nonlinear model can be used as an alternative to FE simulation to derive such a map.

For this machine configuration, the average torque is almost independent of the first barrier angle. It can be noted that the average torque reaches its maximum in a wide region. For instance, for $\vartheta^e_{b2} > 60°$ the maps are quite flat. Thus the designer is free to move within this space looking for torque ripple minima. This behaviour is reflected also by the FE map.

The *second row* shows the maps of the torque harmonic of order 6, which is the lowest order one. Independently from the model used, it appears that there is an evident minimum—highlighted by the black dot—corresponding to the angle combination $(\vartheta^e_{b1}, \vartheta^e_{b2}) = (36°, 72°)$. Such a point is coincident in the maps obtained from the linear and nonlinear analytical models, while it is a bit shifted when FE is used. This is caused by the local saturation of tooth tips and iron parts, which is not considered in the analytical models. In addition, it can be noted that the torque ripple contours obtained by the three models are in a satisfactory agreement in the whole region.

The same considerations can be made comparing the maps for the *third row*, which report the torque harmonic of order 18. Such a torque harmonic corresponds to the first magnetic scalar potential (also referred to as MMF) slot harmonic. They are the MMF harmonics produced by the winding discretized inside the slots ($18 = 36$ slots$/2$ pole pairs), which are characterized by a winding factor equal to the fundamental one. They typically cause the highest ripple. It can be noted that the number of peaks and valleys is increased with respect to the sixth torque harmonic. This trend is general: the higher the harmonic order, the higher the number of maxima and minima. Once more, peaks and valleys predicted by the linear analytical model and nonlinear analytical models are in a good agreement with those found by FE.

Finally, in the *last row* the maps compare the torque total harmonic distortion (*THD*), defined as

$$THD = \frac{\sqrt{\sum_{h \neq 0} \hat{\tau}_h^2}}{\tau_0} \tag{5.45}$$

where τ_0 is the average torque. The filled map shows *THD* contours, while the white superimposed contours refer to the average torque map. The brighter the color, the higher the *THD*. Thus, as far as the torque ripple is concerned, the better combinations of $(\vartheta^e_{b1}, \vartheta^e_{b2})$ are those corresponding to the darker areas.

Furthermore, by comparing the results of the third and fourth rows, it can be observed that bright colors correspond to the peaks of torque harmonic of 18^{th} order, which is due to the MMF slot harmonics. This highlights the heavy impact of the MMF slot harmonics on the overall torque ripple.

Finally, as an overall conclusion, the linear and nonlinear analytical models produce a behavior of average torque map very similar to that obtained through FE, with the difference that the linear map has higher

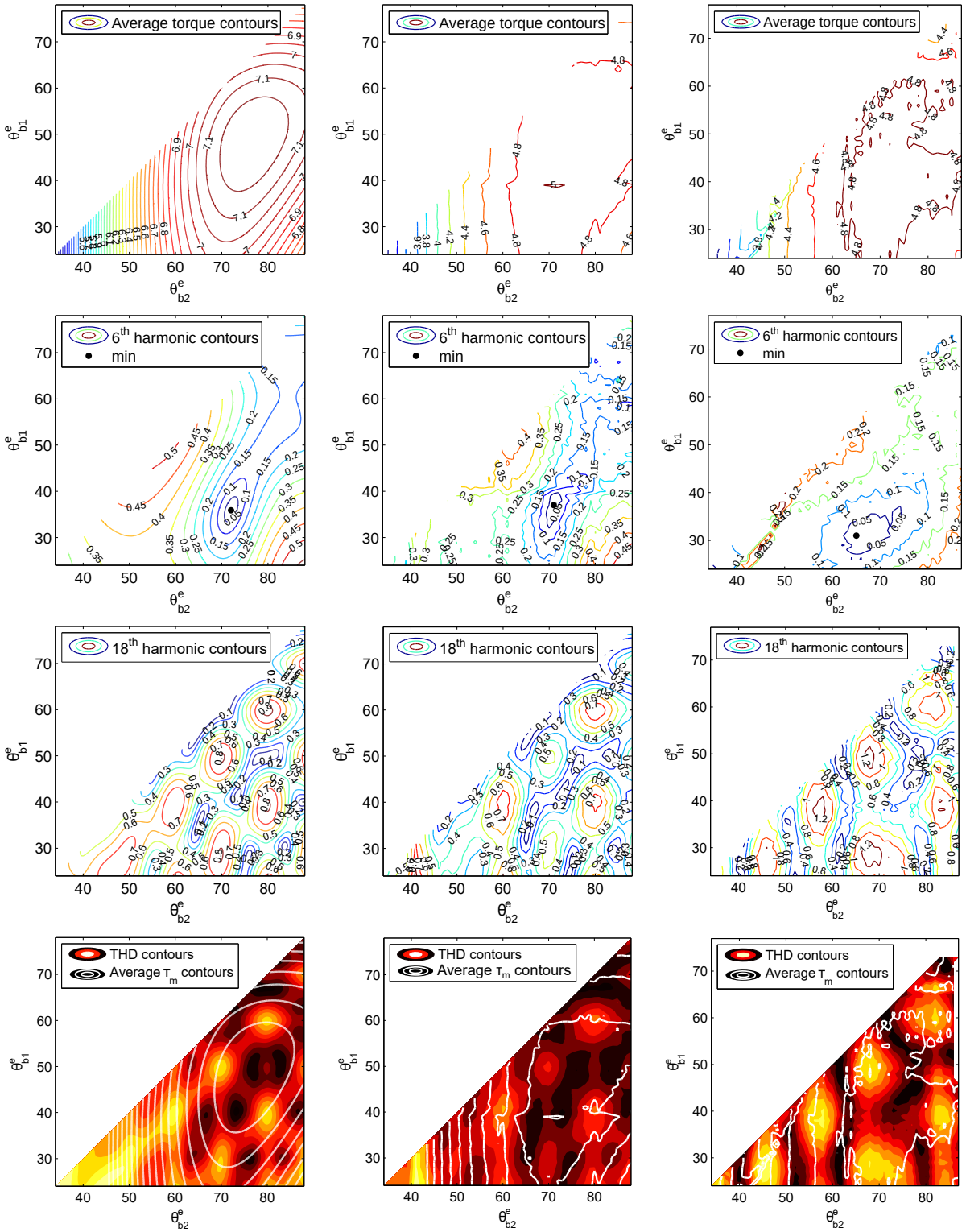

i Analytic linear *ii* Analytic saturation *iii* FE

Figure 5.8
Main torque maps of the 2-barrier rotor. The darker and cooler colors represent the valleys of the corresponding quantity.

values than the other two models. Therefore, the nonlinear analytical model has to be adopted to predict the average torque. On the other hand, both the analytical models are able to find the position of maxima and minima of the torque *THD*. Thus, it can be stated that even the linear model can be used in spite of the nonlinear one when searching for the flux-barrier angle combinations exhibiting a minimum torque ripple, with the advantage of a higher speed and similar accuracy. The slight shifts of maxima and minima found by the FE maps are mainly due to the local saturation of iron, which is not taken into account in the linear analytical model.

5.6 DISCUSSION

This chapter has shown an accurate nonlinear analytical model for the synchronous reluctance machine. A good agreement between analytical and FE simulations has been achieved, even in highly saturated machines.

Thanks to the speed of the analytical model, it is possible to quickly obtain some maps of torque harmonics as a function of the flux-barrier-end angles. These maps can be a useful design tool for the design of a SyR machine. Overall, the analytical maps are able to properly approximate the FE maps.

The average torque behavior is correctly predicted by the nonlinear analytical model, while the linear model overestimates it, obviously. However, even if there are some differences in the amplitude prediction, the flux-barrier angle combinations corresponding to the minima and maxima are estimated well, by means of both the linear and nonlinear models. This fact is quite significant because it suggests that the analytical linear model can be employed to get good design points in the flux-barrier-angle plane for a specific motor in a small amount of time (some minutes). On the other hand, the nonlinear analytical model can be used to properly predict the average torque.

6

DESIGN CRITERIA OF FLUX-BARRIERS IN SYNCHRONOUS RELUCTANCE MACHINES

In this chapter, a criteria to design the rotor of multi flux-barrier synchronous reluctance machines is proposed. In particular, the focus will be on the proper design of flux-barriers geometry (Bacco et al., 2017). An analytical model is adopted to compute the impact of the rotor flux-barriers on the torque, focusing on the torque ripple.

Contrary to the model proposed in (Bianchi et al., 2006) and further extended in Chapter 5, not all the MMF harmonics are considered, but only those which cause the highest torque ripple. As a consequence, the analytical model becomes lighter and it is possible to derive a simple equation to predict the suitable geometry of the rotor flux-barriers. The above simplification can be verified in many publications, such as (Bianchi et al., 2009b) where the 12^{th} torque harmonic is dominant, and in (Vagati et al., 1998) where the main source of torque ripple is the 18^{th} harmonic.

Rotors with one, two and three flux-barriers per rotor pole are taken into account. Some examples referring to 4-pole synchronous reluctance machines with different numbers of stator slots are investigated and illustrated. The results are compared with a full-featured analytical model and validated through finite element simulations.

6.1 THE SIMPLIFIED ANALYTICAL MODEL

The analytical model presented hereafter is derived from the model that was proposed in (Bianchi et al., 2009b) and further developed in Chapter 5, and used to determine the geometry of a SyR motor with one, two or three flux-barriers per pole. The assumptions considered in the analytical model are:

1. to neglect the stator and rotor magnetic voltage drops,
2. to neglect the stator slotting effect, and
3. to neglect the rotor iron ribs.

Table 6.1
Geometrical data of the SyR machine.

Quantity	Symbol	Value	u.m.
Stack length	L_{stk}	40	mm
Outer stator diameter	D_{s}	200	mm
Inner stator diameter	D_{e}	125	mm
Air-gap length	g	0.35	mm
Number of pole pairs	p	2	

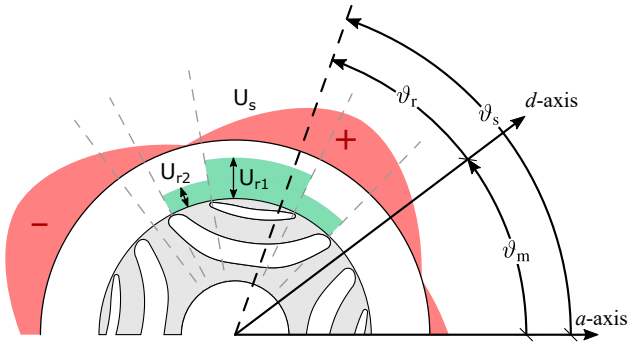

Figure 6.1
Sketch of the fundamental stator magnetic scalar potential and rotor reaction magnetic scalar potential.

For a given stator winding and rotor geometry, the aim of the model is to correctly predict the combinations of flux-barrier angles which lead to the lower (and higher too) torque ripples.

6.1.1 *Application of a nonlinear model*

An objection that might be raised to the model above is that it is basically a simple linear model, which does not consider the actual iron *B-H* characteristic while usually the saturation is quite high in SyR machines. Consequently, the model should not be able to predict the proper torque waveform (and consequently design the proper rotor geometry) when the SyR machine is strongly saturated.

This remark is only partially true. Experimental results shown in (Barcaro et al., 2009; Bianchi et al., 2008b; Bianchi et al., 2006) highlight that the optimal solutions of the rotor flux-barrier angles found through the linear model are effective to achieve a machine exhibiting smooth torque even at high load. The percentage of torque ripple, due to the interaction between electromagnetic fields, is properly predicted (Vagati et al., 1998; Barcaro et al., 2011; Bianchi et al., 2009b).

6.1.2 *Simplification of the model*

It can be demonstrated that electromagnetic torque is produced by the interaction between the electric loading, $\mathcal{K}_s(\vartheta_r, \vartheta_m)$, and the rotor magnetic potential, $\mathcal{U}_r(\vartheta_r, \vartheta_m)$.[1] The electric loading contains many space harmonics, produced by the arrangement of the winding within the stator slots. The electric loading gives rise to a stator magnetic scalar potential, whose fundamental moves synchronous with the rotor while the other harmonics move asynchronous.

The rotor magnetic potential, U_{r1}, is caused by the flux crossing the flux-barrier. It is mainly produced by the electric loading fundamental, while the harmonics cause slight oscillations of U_{r1}.

1 See Chapter 5.

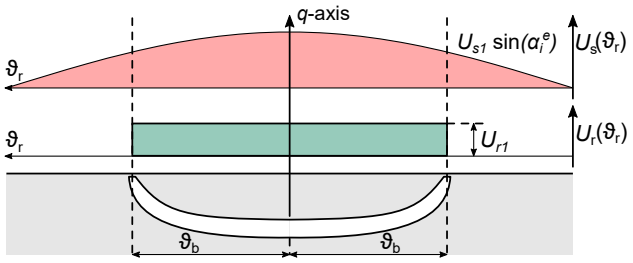

Figure 6.2
Sketch of a linearized one flux-barrier SyR rotor, with the stator and rotor scalar magnetic potentials shown.

The torque expression can be split into two terms:

$$\begin{aligned} T_\mathrm{m}(\vartheta_\mathrm{m}) &= k_T \int_0^{2\pi} \mathcal{K}_\mathrm{s}(\vartheta_\mathrm{r}, \vartheta_\mathrm{m})\, \mathcal{U}_\mathrm{r}(\vartheta_\mathrm{r}, \vartheta_\mathrm{m})\ \mathrm{d}\vartheta_\mathrm{r} \\ &= \langle T_\mathrm{m} \rangle + \Delta T_\mathrm{m}(\vartheta_\mathrm{m}) \end{aligned} \tag{6.1}$$

where k_T is a factor depending on the motor geometry. The first term, $\langle T_\mathrm{m} \rangle$, is constant and corresponds to the average torque while the second term, ΔT_m, represents the torque ripple, which is a function of the rotor position, ϑ_m. All the harmonics of electric loading cause torque oscillations, but the highest ripple is due to the slot harmonics (i.e., those characterized by a winding factor equal to the fundamental one). In the following, the focus is on the first two slot harmonics, with order $\nu = 1 \pm Q/p$, which are responsible for the highest torque ripple. As an example, a machine with a combination of 24 slots and 4 poles has the highest ripple component which oscillates 12 times the frequency of the fundamental, caused by the electric loading harmonics of order 11 and 13.

6.2 ONE FLUX-BARRIER ROTOR

At first, a rotor with one flux-barrier has been studied. The complete expression of the rotor magnetic scalar potential is

$$\begin{aligned} U_\mathrm{r1} &= a \int_{-\vartheta_\mathrm{b}}^{\vartheta_\mathrm{b}} \mathcal{U}_\mathrm{s}(\vartheta_\mathrm{r}, \vartheta_\mathrm{m})\ \mathrm{d}\vartheta_\mathrm{r} \\ &= -aD_\mathrm{s} \sum_\nu \frac{\hat{K}_\nu}{(\nu p)^2} \cos(\lambda_\nu) \sin(\nu p \vartheta_\mathrm{b}) \end{aligned} \tag{6.2}$$

where

$$a = \frac{\frac{D_\mathrm{s}}{2g}\frac{t_\mathrm{b}}{l_\mathrm{b}}}{1 + \frac{D_\mathrm{s}}{2g}\frac{t_\mathrm{b}}{l_\mathrm{b}} 2\vartheta_\mathrm{b}}, \quad \lambda_\nu = \frac{\nu\pi}{2} + (\nu - 1)p\vartheta_\mathrm{m} - \alpha_i^\mathrm{e}$$

By assumption, any variation of the rotor magnetic potential is neglected. U_r1 is assumed to be independent on the rotor position and due to the fundamental of $\mathcal{K}_\mathrm{s}$ only. Thanks to such hypothesis, its expression becomes

$$U_\mathrm{r1} = -\frac{aD_\mathrm{s}\hat{K}_1}{p^2} \cos\left(\tfrac{\pi}{2} - \alpha_i^\mathrm{e}\right) \sin(p\vartheta_\mathrm{b})$$

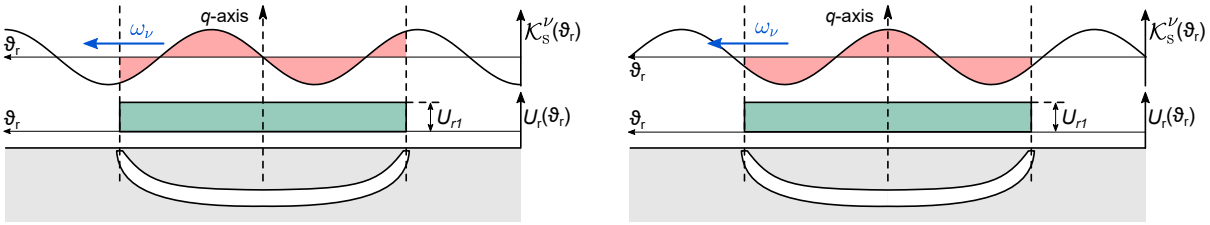

(a) Sine electric loading harmonic waveform.

(b) Cosine electric loading harmonic waveform.

Figure 6.3
Electric loading harmonic waveform (moving at ω_ν) with respect to the rotor flux-barrier (fixed) in two different rotor positions.

The torque is computed integrating the product between electric and magnetic loadings over the flux-barrier:

$$T_\mathrm{m}(\vartheta_\mathrm{m}) = k_T 2p \int_{-\vartheta_\mathrm{b}}^{\vartheta_\mathrm{b}} U_{\mathrm{r}1} \mathcal{K}_\mathrm{s}(\vartheta_\mathrm{r}, \vartheta_\mathrm{m})\ \mathrm{d}\vartheta_\mathrm{r} \tag{6.3}$$

Let us consider the electric loading harmonic of order ν which travels asynchronous with respect to the rotor. It is

$$\mathcal{K}_\mathrm{s}^{(\nu)}(\vartheta_\mathrm{r}, \vartheta_\mathrm{m}) = \hat{K}_\nu \sin[\nu p \vartheta_\mathrm{r} + (\nu - 1) p \vartheta_\mathrm{m} - \alpha_i^\mathrm{e}]$$

Such electric loading harmonic produces a torque contribution expressed as

$$T_\nu = k_T\, 2p \int_{-\vartheta_\mathrm{b}}^{\vartheta_\mathrm{b}} U_{\mathrm{r}1}\, \mathcal{K}_\mathrm{s}^{(\nu)}(\vartheta_\mathrm{r}, \vartheta_\mathrm{m})\ \mathrm{d}\vartheta_\mathrm{r} \tag{6.4}$$

Regardless of the rotor position, the torque ripple produced by this harmonic can be simply evaluated considering two opposite situations, according to the waveform of the $\mathcal{K}_\mathrm{s}^{(\nu)}$ harmonic with respect to the q-axis: *(a)* when it is odd and *(b)* when it is even. The two situations are sketched in Figure 6.3.

In the time instant when the waveform is odd (sine waveform in Figure 6.3(a)) the torque contribution resulting from (6.4) is zero. On the contrary, in the time instant when the waveform is even (cosine waveform in Figure 6.3(b)), there is either a positive or negative instantaneous torque contribution. The resulting torque ripple due to the considered harmonic is estimated by the amplitude found when the waveform is even with respect to the barrier. Therefore, the torque contribution becomes

$$\begin{aligned} T_\nu &\propto \hat{K}_\nu \int_{-\vartheta_\mathrm{b}}^{\vartheta_\mathrm{b}} \cos(\nu p \vartheta_\mathrm{r})\ \mathrm{d}\vartheta_\mathrm{r} \\ &\propto 2\hat{K}_\nu \frac{\sin(\nu p \vartheta_\mathrm{b})}{p\nu} \end{aligned} \tag{6.5}$$

However, each torque harmonic is produced by a pair of electric loading harmonics. For a better understanding, let us consider the complete torque expression given in (Barcaro, 2011) by

$$T_{\mathrm{m}}(\vartheta_{\mathrm{m}}) = -\frac{\mu_0}{g}\frac{D_{\mathrm{s}}^2 L_{\mathrm{stk}}\, U_{\mathrm{r1}}}{2}\cdot \\ \cdot \sum_{\nu}\frac{\hat{K}_\nu}{\nu}\sin(\nu p\vartheta_{\mathrm{b}})\sin\nu\tfrac{\pi}{2}\cos\left[(\nu-1)p\vartheta_{\mathrm{m}}-\alpha_i^{\mathrm{e}}\right] \tag{6.6}$$

The torque ripple of order h is due to two electric loading harmonics, namely $\nu_1 = (1-h)$ and $\nu_2 = (1+h)$, where $h = 6n$, $n \in \mathbb{N}$. The torque contributions of these two harmonics are

$$T_{\mathrm{m},\nu_1}(\vartheta_{\mathrm{m}}) = T_{\nu_1}\cos[(\nu_1-1)p\vartheta_{\mathrm{m}}-\alpha_i^{\mathrm{e}}]$$
$$T_{\mathrm{m},\nu_2}(\vartheta_{\mathrm{m}}) = T_{\nu_2}\cos[(\nu_2-1)p\vartheta_{\mathrm{m}}-\alpha_i^{\mathrm{e}}]$$

After some computations, the torque amplitude due to the considered harmonic results:

$$T_\nu = k_T^* U_{\mathrm{r1}}\frac{\hat{K}_\nu}{\nu}\sin(\nu\tfrac{\pi}{2})\sin(\nu p\vartheta_{\mathrm{b}}) \tag{6.7}$$
$$k_T^* = -\frac{\mu_0 D_{\mathrm{s}}^2 L_{\mathrm{stk}}}{g}$$

and it can be either positive or negative. It is then possible to compute amplitude and phase of the torque harmonic of order h. Referring to the current vector angle $\alpha_i^{\mathrm{e}} = 45°$, they are

$$T_h = \sqrt{T_{\nu_1}^2 + T_{\nu_2}^2} \tag{6.8}$$

$$\phi_h = \arctan\left(\frac{T_{\nu_2}-T_{\nu_1}}{T_{\nu_2}+T_{\nu_1}}\right) \tag{6.9}$$

From (6.5), the torque ripple expression for the two harmonics becomes

$$T_h^2 \propto \left[\frac{\sin\nu_1\vartheta_{\mathrm{b}}^{\mathrm{e}}}{\nu_1}\right]^2 + \left[\frac{\sin\nu_2\vartheta_{\mathrm{b}}^{\mathrm{e}}}{\nu_2}\right]^2$$

employing electrical angles, $\vartheta_{\mathrm{b}}^{\mathrm{e}} = p\vartheta_{\mathrm{b}}$. In general

$$\frac{\mathrm{d}}{\mathrm{d}\vartheta_{\mathrm{b}}^{\mathrm{e}}}\left\{\left[\frac{\sin\nu_1\vartheta_{\mathrm{b}}^{\mathrm{e}}}{\nu_1}\right]^2 + \left[\frac{\sin\nu_2\vartheta_{\mathrm{b}}^{\mathrm{e}}}{\nu_2}\right]^2\right\} = 0$$
$$\frac{2}{\nu_1}\sin\nu_1\vartheta_{\mathrm{b}}^{\mathrm{e}}\cos\nu_1\vartheta_{\mathrm{b}}^{\mathrm{e}} + \frac{2}{\nu_2}\sin\nu_2\vartheta_{\mathrm{b}}^{\mathrm{e}}\cos\nu_2\vartheta_{\mathrm{b}}^{\mathrm{e}} = 0$$
$$\nu_2\sin(2\nu_1\vartheta_{\mathrm{b}}^{\mathrm{e}}) + \nu_1\sin(2\nu_2\vartheta_{\mathrm{b}}^{\mathrm{e}}) = 0$$

Imposing to zero the derivative of the torque ripple with respect to $\vartheta_{\mathrm{b}}^{\mathrm{e}}$, it results

$$\nu_2\sin(2\nu_1\vartheta_{\mathrm{b}}^{\mathrm{e}}) + \nu_1\sin(2\nu_2\vartheta_{\mathrm{b}}^{\mathrm{e}}) = 0 \tag{6.10}$$

This transcendental equation can be solved numerically for the flux-barrier angle $\vartheta_{\mathrm{b}}^{\mathrm{e}}$. The solutions found through (6.10) are the minima and maxima of the torque ripple.

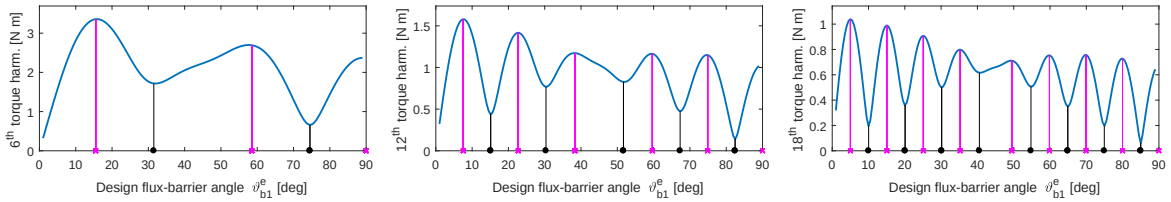

(a) $Q = 12, 2p = 4, \nu_1 = -5, \nu_2 = 7$ *(b)* $Q = 24, 2p = 4, \nu_1 = -11, \nu_2 = 13$ *(c)* $Q = 36, 2p = 4, \nu_1 = -17, \nu_2 = 19$

Figure 6.4
Analytical torque maps of the first slot harmonics for different number of slots Q and number of poles $2p$ combinations in one-barrier machines. The vertical lines represent the positions of the torque ripple minima found by means of (6.10).

Figure 6.5
Geometries of two one flux-barrier solutions with different flux-barrier angles.

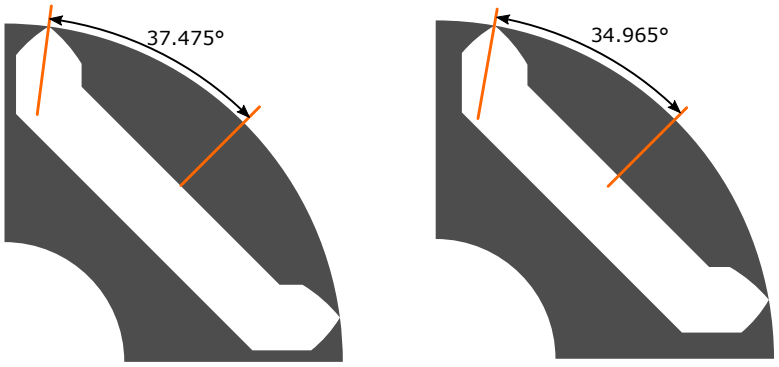

(a) Low torque ripple geometry. *(b)* High torque ripple geometry.

6.2.1 *Practical results*

To validate the model previously derived, Figure 6.4 reports the torque behaviors due to the first two slot harmonics ($\nu = 1 \pm Q/p$) versus the electrical flux-barrier angle, ϑ^e_b. For a 4-pole machine ($2p = 4$), they are the 5^{th} and 7^{th} order harmonics for the machine with $Q = 12$, the 11^{th} and 13^{th} for $Q = 24$, and the 17^{th} and 19^{th} for $Q = 36$. These waveforms are obtained through the complete model of the SyR machine expressed by (6.6) as in (Bianchi et al., 2009b; Barcaro, 2011). In addition, the vertical lines identify the flux-barrier angles found by the simple formulation derived in (6.10).

The perfect prediction of the torque minima by (6.10) can be noted: they correspond to the minima computed by means of the complete analytical magnetic model of the machine. Furthermore, this occurs for different combinations of slots per pole.

6.2.2 *FE validation*

To support the previous results, two rotors with different flux-barrier angles are selected from Figure 9.3(a) and the corresponding motor features are compared. A low torque ripple and a high torque ripple points have been chosen for some FE simulations. The considered motor has $Q = 36$ and $2p = 4$, so that it refers to Figure 9.3(a). An RMS current density of about 6.3 A/mm² is imposed. The magnetic insulation ratio,

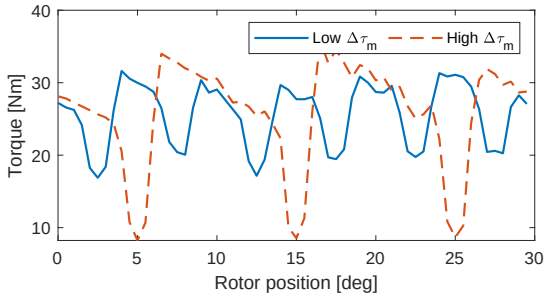

(a) Comparison of the torque waveforms with linear iron.

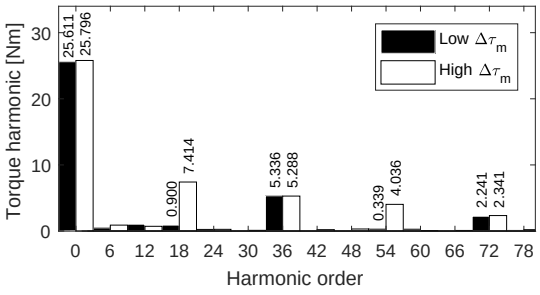

(b) Comparison of the torque spectra with linear iron.

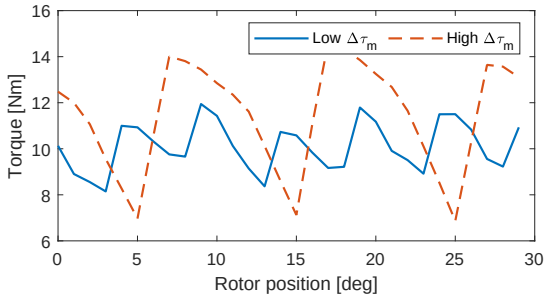

(c) Comparison of the waveforms spectra with nonlinear iron.

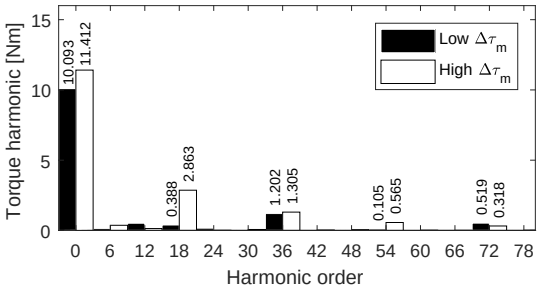

(d) Comparison of the torque spectra with nonlinear iron.

Figure 6.6
Torque waveforms and spectra of one flux-barrier solutions with different flux-barrier angles.

k_{air} (which accounts for the air length along the q-axis with respect to the total available length), is set to 0.3. The flux-barrier electrical angle, ϑ_b^e, is set as follows:

1. $\vartheta_b^e = 74.95°$ for the low torque ripple solution
2. $\vartheta_b^e = 69.93°$ for the high torque ripple solution

The corresponding mechanical angles result 37.48° and 34.97°, respectively, so that the difference is 2.5° only. However, it does not represent a problem since common manufacturing tolerances are well below these values. With one flux-barrier per pole, the chosen flux-barrier angle is quite large because it generally leads to a higher average torque. In fact, it can be demonstrated that the average torque of one flux-barrier SyR motor is proportional to $\sin^2 \vartheta_b^e / \vartheta_b^e$. Such a function exhibits a maximum at $\vartheta_b^e = 66.7°$ (that is $\vartheta_b = 33.35°$). The geometries and the results are reported in Figure 6.5 and Figure 6.6. It can be seen that the two geometries are practically identical in the middle of the rotor, and their only difference lies in the flux-barrier-end position. At first, the simulations are carried out with a linear ferromagnetic material in order to obtain a fair comparison with the analytical model.

Figure 6.6 reports the harmonic content of the torque behavior achieved from FE simulations. Black bars correspond to the low ΔT_m solution, and white bars correspond to the high ΔT_m solution. To achieve accurate torque results with FEA, it is mandatory to design a proper

mesh at the air-gap of the machine. Typically, three to four elements along the radial direction are sufficient.

Figure 6.6(b) highlights that the correct choice of the flux-barrier-end position heavily affects the 18^{th} harmonic amplitude and its odd multiple harmonics. In this particular case, the overall torque ripple results 53.5% for the low ripple geometry and 106.7% for the high ripple one. This results remarks that such a notable improvement is due to the proper choice of flux-barrier angle ϑ_{b} so as to minimize the torque ripple contribution due to the first two slot harmonics.

Figure 6.6(d) reports the torque harmonic content achieved considering a nonlinear ferromagnetic material. Obviously, the resulting average torque and torque harmonic amplitudes are quite lower with respect to the linear iron case. Also the overall torque ripple results to be lower, being 37.6% and 67.9% for the low ΔT_{m} and high ΔT_{m} solutions, respectively. However, the choice of the flux-barrier-end angle, ϑ_{b}, still affects the torque ripple caused by the slot harmonics.

Other simulations have been performed varying the magnetic insulation coefficient (i.e. the coefficient k_{air}) of the flux-barriers to the aim of showing the effect of a higher ratio on the low ripple geometry. While the average torque results lower (due to increased saturation), the torque ripple remains the same.

At last, it was also observed that, in case of nonlinear iron, the shape of the flux-barrier-end affects the torque harmonic content. In fact, they affect the distribution of the flux entering the rotor. This effect, particularly evident in one flux-barrier rotors, may change the effective position of the flux-barrier-end, leading to a different torque spectrum. This is why the analyzed motors shown in Figure 6.5(a) and Figure 6.5(b) exhibit a quite sharp flux-barrier-end.

6.3 TWO FLUX-BARRIER ROTOR

Also in this case the two magnetic scalar potentials of the rotor islands, U_{r1} and U_{r2}, are assumed to be constant (as depicted in Figure 6.1). As said above, this means that the machine is considered to be magnetized only by the fundamental harmonic of the stator magnetic scalar potential, U_{s1}. The resulting complete torque expression is given by (Bianchi et al., 2009b; Barcaro, 2011):

$$\begin{aligned} T_{\text{m}}(\vartheta_{\text{m}}) = -\frac{\mu_0 D_{\text{s}}^2 L_{\text{stk}}}{4g} \Bigg[U_{\text{r2}} \sum_{\nu} \frac{K_\nu}{\nu} \sin \nu \tfrac{\pi}{2} \sin \nu \vartheta_{\text{b2}}^{\text{e}} + \\ + (U_{\text{r1}} - U_{\text{r2}}) \sum_{\nu} \frac{K_\nu}{\nu} \sin \nu \tfrac{\pi}{2} \sin \nu \vartheta_{\text{b1}}^{\text{e}} \Bigg] \cdot \\ \cdot \cos\left[(\nu - 1) p \vartheta_{\text{m}} - \alpha_i^{\text{e}}\right] \end{aligned} \tag{6.11}$$

Therefore, the torque produced by a single harmonic is proportional to

$$T_\nu \propto (U_{\text{r1}} - U_{\text{r2}}) \frac{\sin \nu \vartheta_{\text{b1}}^{\text{e}}}{\nu} + U_{\text{r2}} \frac{\sin \nu \vartheta_{\text{b2}}^{\text{e}}}{\nu} \tag{6.12}$$

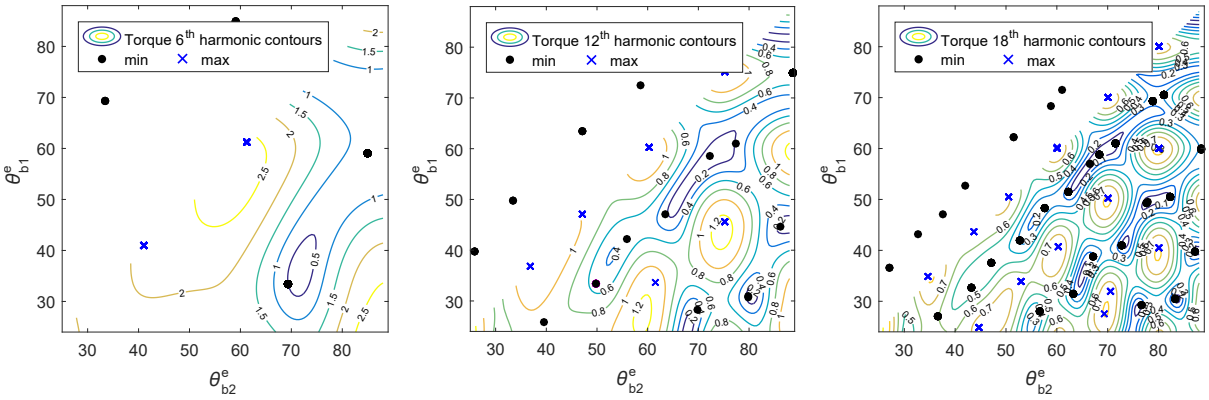

(a) $Q = 12, 2p = 4$ (b) $Q = 24, 2p = 4$ (c) $Q = 36, 2p = 4$

Figure 6.7
Analytical torque maps of the first slot harmonics for different slots and poles combinations in a two flux-barrier machine. The black dots show the minima found by means of the model proposed here. Contour lines are obtained by means of the complete model.

A further assumption can be made: the rotor magnetic voltage drops are considered to be equal (as depicted in Figure 6.1), such that

$$\Delta U_r = U_{r1} - U_{r2} = U_{r2}$$

This assumption is often verified, thanks to the choice of the magnetic insulation (i.e. the flux-barrier thicknesses) distribution in the rotor. Thus, (6.12) becomes

$$T_\nu \propto \frac{\sin \nu \vartheta^e_{b1}}{\nu} + \frac{\sin \nu \vartheta^e_{b2}}{\nu}$$

As above, the actual torque ripple harmonic amplitude is obtained by considering a couple of harmonics. As usual, the first two slot harmonics are considered, which means $h = Q/p$ and $\nu_1 = 1 - h$, $\nu_2 = 1 + h$, so that:

$$\begin{aligned} T_h^2 \propto & \left[\frac{\sin \nu_1 \vartheta^e_{b1}}{\nu_1} + \frac{\sin \nu_1 \vartheta^e_{b2}}{\nu_1} \right]^2 + \\ & + \left[\frac{\sin \nu_2 \vartheta^e_{b1}}{\nu_2} + \frac{\sin \nu_2 \vartheta^e_{b2}}{\nu_2} \right]^2 \end{aligned} \tag{6.13}$$

In order to get the minima, (6.13) is derived by the first barrier angle, ϑ^e_{b1}, and then by the second one, ϑ^e_{b2}.

$$\begin{cases} 2 \left[\frac{\sin \nu_1 \vartheta^e_{b1}}{\nu_1} + \frac{\sin \nu_1 \vartheta^e_{b2}}{\nu_1} \right] \cos \nu_1 \vartheta^e_{b1} + 2 \left[\frac{\sin \nu_2 \vartheta^e_{b1}}{\nu_2} + \frac{\sin \nu_2 \vartheta^e_{b2}}{\nu_2} \right] \cos \nu_2 \vartheta^e_{b1} = 0 \\ 2 \left[\frac{\sin \nu_1 \vartheta^e_{b1}}{\nu_1} + \frac{\sin \nu_1 \vartheta^e_{b2}}{\nu_1} \right] \cos \nu_1 \vartheta^e_{b2} + 2 \left[\frac{\sin \nu_2 \vartheta^e_{b1}}{\nu_2} + \frac{\sin \nu_2 \vartheta^e_{b2}}{\nu_2} \right] \cos \nu_2 \vartheta^e_{b2} = 0 \end{cases} \tag{6.14}$$

It results as in (6.14). This represents a transcendental system of two equations in two variables, $(\vartheta^e_{b1}, \vartheta^e_{b2})$, and it is solved numerically, both searching for minima and maxima.

Figure 6.8
Low and high ripple geometries with two flux-barriers.

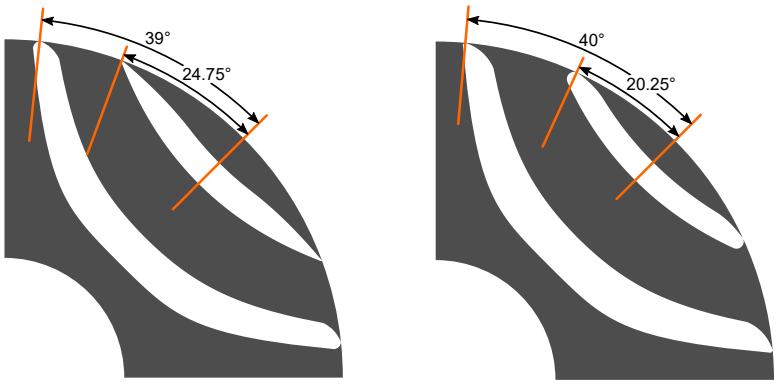

(a) Low torque ripple geometry.

(b) High torque ripple geometry.

6.3.1 *Practical results*

Again, to validate the model, Figure 6.7 reports the torque behaviors due to the first two slot harmonics in the plane of the two electrical flux-barrier angles $\vartheta^{\mathrm{e}}_{\mathrm{b1}}$ and $\vartheta^{\mathrm{e}}_{\mathrm{b2}}$. These harmonics are of the same order of the previous ones. The 2D torque harmonic maps are again obtained through a complete model of the two flux-barrier SyR machine, from (6.11).

Then the points marked by black dots and blue crosses are found by means of the model proposed in (6.14). They identify the flux-barrier angles which correspond to the torque ripple minima and maxima, respectively. Once again, this model is able to predict these points with satisfactory precision, despite the additional assumption of constant magnetic voltage drop across each flux-barrier.

6.3.2 *FE validation*

Also in this case a low torque ripple and two high torque ripple points have been chosen for FE simulations. The main data of the considered motor are the same, so $Q = 36$ and $2p = 4$, with an RMS current density equal to $6.3\,\mathrm{A/mm^2}$, and it refers to Figure 9.3(b). The flux-barrier electrical angles, $(\vartheta^{\mathrm{e}}_{\mathrm{b1}}, \vartheta^{\mathrm{e}}_{\mathrm{b2}})$, are set to

1. $(49.5°, 78°)$ for the low torque ripple solution
2. $(49.5°, 70°)$ for the first high torque ripple solution
3. $(40.5°, 80°)$ for the second high torque ripple solution

Figure 6.9(c) reports the comparison between the torque versus rotor position behaviors of the low and high torque ripple solutions with nonlinear ferromagnetic material. It can be observed how the different choice of just one flux-barrier angle (between the first two solutions) greatly affects the resulting torque waveform and the relative harmonic content. This is highlighted in Figure 6.9(d) which reports the low ΔT_{m} solution torque spectrum with black bars, and the high ΔT_{m} solutions torque spectra in gray and white. The saturation of the ferromagnetic

	$\langle T_m \rangle$ [N m]	ΔT_m [%]
Linear case		
Low ripple sol.	27.39	42.66
1st high ripple sol.	27.24	103.64
2nd high ripple sol.	27.57	99.06
Nonlinear case		
Low ripple sol.	13.50	38.41
1st high ripple sol.	13.52	76.23
2nd high ripple sol.	13.63	68.34

Table 6.2
Comparison of average torque and torque ripple for low and high ripple solutions.

material affects the shape of all the torque waveforms, which appear smoother, so all the ripples result to be lower.

A final comparison between the average torques and ripples is reported in Table 6.2 in both linear and nonlinear case. As expected, the average torque and ripple are higher with linear ferromagnetic material, but the gap among low and high ripple solutions remains.

6.4 THREE FLUX-BARRIERS ROTOR

At this point, the model can be easily extended to three flux-barriers rotors. In fact, using the same assumptions as before

$$\Delta U_r = U_{r1} - U_{r2} = U_{r2} - U_{r3} = U_{r3}$$

the torque harmonic expression due the electric loading harmonic becomes

$$T_\nu \propto \frac{\sin \nu \vartheta^e_{b1}}{\nu} + \frac{\sin \nu \vartheta^e_{b2}}{\nu} + \frac{\sin \nu \vartheta^e_{b3}}{\nu}$$

and, therefore, the actual torque ripple harmonic results in

$$\begin{aligned} T_h^2 \propto & \left[\frac{\sin \nu_1 \vartheta^e_{b1}}{\nu_1} + \frac{\sin \nu_1 \vartheta^e_{b2}}{\nu_1} + \frac{\sin \nu_1 \vartheta^e_{b3}}{\nu_1} \right]^2 + \\ & + \left[\frac{\sin \nu_2 \vartheta^e_{b1}}{\nu_2} + \frac{\sin \nu_2 \vartheta^e_{b2}}{\nu_2} + \frac{\sin \nu_2 \vartheta^e_{b3}}{\nu_2} \right]^2 \end{aligned} \tag{6.15}$$

Once again, this equation can be minimized numerically to find suitable flux-barrier angles. In this case, the number of minima far exceeds the number of maxima. In particular, the maxima are either degenerated three flux-barriers rotors, or the flux-barrier angles are displaced by a stator slot angle.

On the other hand, the minima can be found on some lines in the 3D space created by the three flux-barrier angles and so they are very numerous.

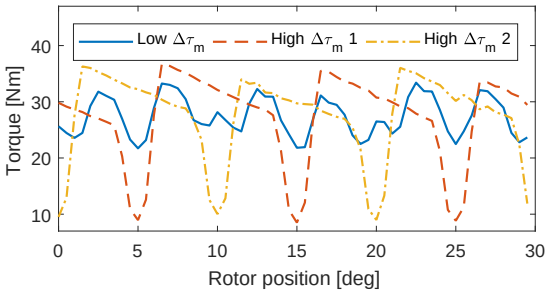

(a) Comparison of the torque spectra with linear iron.

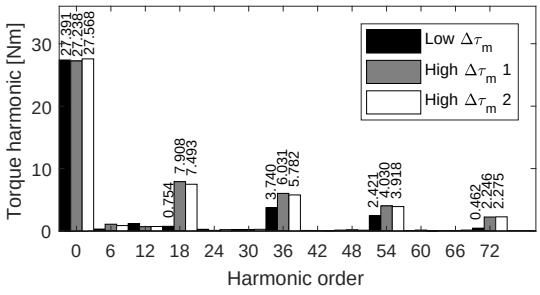

(b) Comparison of the torque spectra with linear iron.

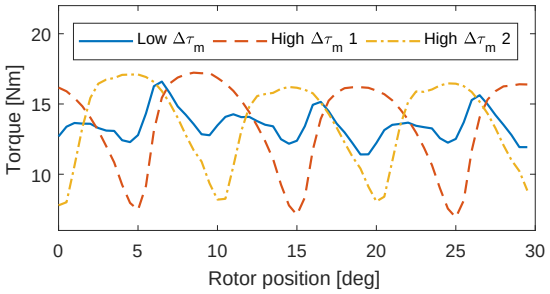

(c) Comparison of the torque spectra with nonlinear iron.

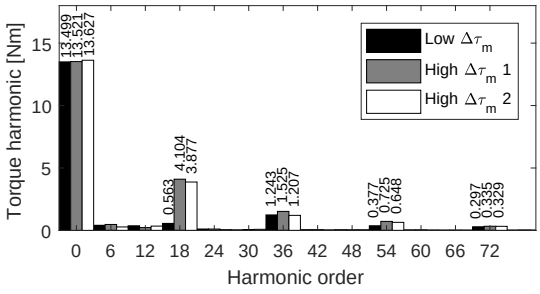

(d) Comparison of the torque spectra with nonlinear iron.

Figure 6.9
Torque waveforms and spectra of two flux-barriers solutions with different flux-barrier angles.

6.4.1 *FE validation*

One low and one high torque ripple geometries have been chosen for FE validation. The respecting flux-barrier angles $(\vartheta^{e}_{b1}, \vartheta^{e}_{b2}, \vartheta^{e}_{b3})$ are:

- $(21.67°, 51.31°, 76.34°)$ for low torque ripple solution
- $(19.89°, 59.98°, 79.99°)$ for high torque ripple solution

It can be noted that the high ripple solution is characterized by flux-barrier angles which are multiples of the slot angle, while the low ripple solution does not have evenly spaced angles.

Figure 6.10 shows the comparison between the low and the high torque ripple geometries. As expected, the high torque ripple geometry exhibits high torque harmonics, in particular the first slot harmonic (the 18^{th}). Overall, the torque ripple results to be 17.9% for the low ripple geometry while it is 72.9%.

6.5 DESIGN OF ASYMMETRIC FLUX-BARRIERS IN SYRM

In this section, the previous simple model is extended to asymmetric synchronous reluctance machines, so machines with different flux-barriers between adjacent rotor poles, so as to obtain a sort of compensation of the torque harmonics. This time a different machine is studied, and its data are reported in Table 6.3.

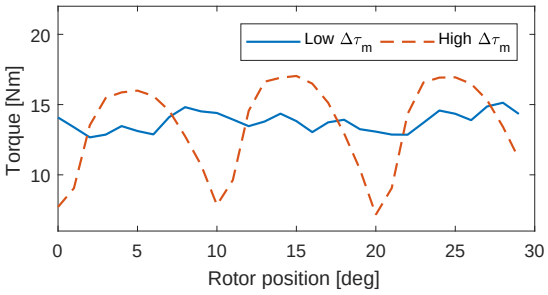

(a) Comparison of the torque spectra with nonlinear iron.

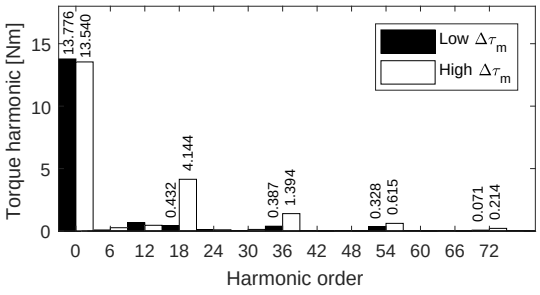

(b) Comparison of the torque spectra with nonlinear iron.

Figure 6.10
Geometries and spectra of three flux-barriers solutions with different flux-barrier angles.

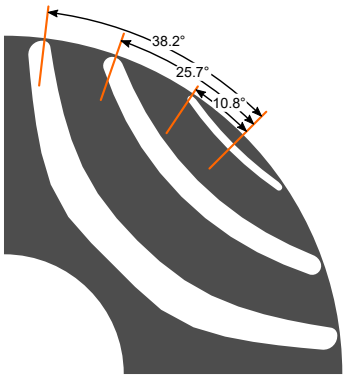

(a) Low torque ripple geometry.

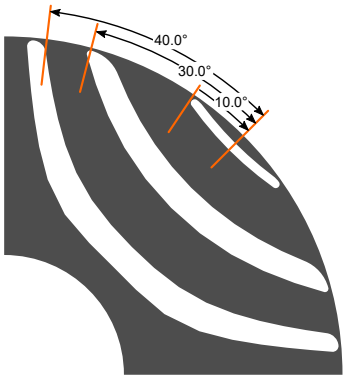

(b) High torque ripple geometry.

Figure 6.11
Low and high ripple geometries with three flux-barriers.

6.5.1 *Determination of solutions getting minimum torque harmonic*

Equation (6.8) can be minimized numerically for the barrier angle $\vartheta_b^e = p\vartheta_b$. It allows to determine the flux-barrier angles ϑ_b^e which minimize the torque oscillations due to the harmonics of electric loading of order ν_1 and ν_2.

Figure 6.12 reports the torque behaviors of the first two slot harmonics versus the electrical flux-barrier angle, ϑ_b^e. Referring to a machine with $Q = 24$ slots and $2p = 4$ poles, they are the harmonics of 11^{th} and 13^{th} order and 23^{rd} and 25^{th} order (which are the first two and the second two electric loading slot harmonics). The black dots identify the

Quantity	Symbol	Value	u.m.
Stack length	L_{stk}	40	mm
Outer stator diameter	D_e	120	mm
Inner stator diameter	D_s	70	mm
Air-gap length	g	0.4	mm
Number of stator poles	$2p$	4	
Number of stator slots	Q	24	

Table 6.3
Geometrical data of the SyR machine used as an example in the analysis.

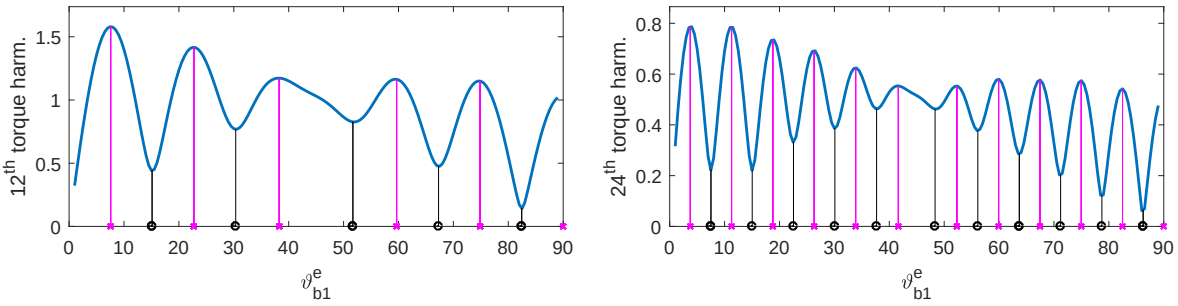

(a) $\nu_1 = 11$, $\nu_2 = 13$. *(b)* $\nu_1 = 23$, $\nu_2 = 25$.

Figure 6.12
Analytical torque maps of the first four slot harmonics for a motor with $Q = 24$, $2p = 4$ with one-barrier per pole. Black dots corresponds to angles of minimum torque harmonic.

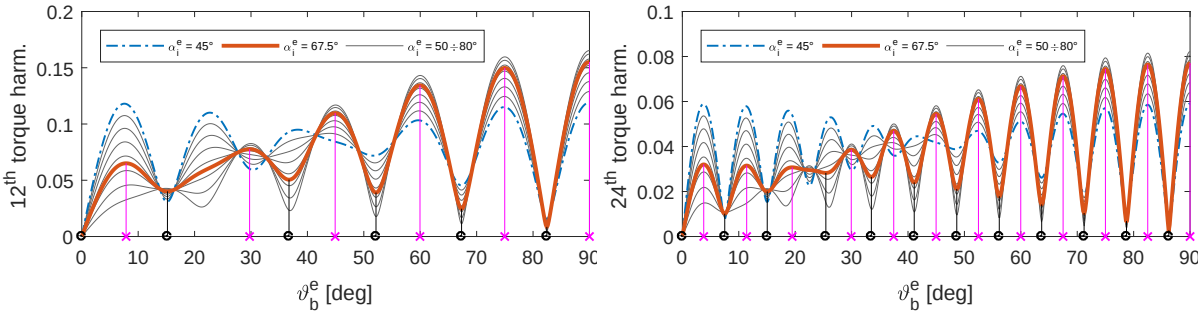

(a) $\nu_1 = 11$, $\nu_2 = 13$. *(b)* $\nu_1 = 23$, $\nu_2 = 25$.

Figure 6.13
Torque maps of the first four slot harmonics for a motor with $Q = 24$, $2p = 4$ with one-barrier per pole for different current angles. Black dots corresponds to angles of minimum torque harmonic at $\alpha_i^e = 67.5°$.

flux-barrier angles found by the minimization of (6.8). Comparing with the waveforms obtained through a complete model of the SyR machine, the vertical lines starting from the dots show that the position of the minima are properly predicted.

Both the simple and the complete analytical model (Bianchi et al., 2009b; Bacco et al., 2017) considered the current vector angle to be $\alpha_i^e = 45°$. On the other hand, rarely a SyR machine works at 45° in Maximum Torque Per Ampere (MTPA) because of saturation. It works at higher angles and even up to 80° or more when flux-weakening. More generally, instead of (6.8) and (6.9), the actual h^{th} torque harmonic amplitude and phase are

$$T_h = \sqrt{T_{\nu_1}^2 + T_{\nu_2}^2 + 2T_{\nu_1}T_{\nu_2}\cos 2\alpha_i^e} \tag{6.16}$$

$$\phi_h = \arctan\left(\frac{T_{\nu_2} - T_{\nu_1}}{T_{\nu_1} + T_{\nu_2}}\tan\alpha_i^e\right) \tag{6.17}$$

It can be noted that the final amplitude of the torque harmonic depends on the amplitudes of the two components of torque harmonic and also on the current vector angle. The choice of such angle could lead to quite

#	1	2	3	4	5	6
ϑ_b^e [°]	7.5	15.0	25.4	33.5	41.1	48.6
#	7	8	9	10	11	
ϑ_b^e [°]	56.2	63.7	71.2	78.7	86.2	

Table 6.4
Set $S_h = \{\vartheta_{bi}^e\}_{i=1}^n$ of flux-barrier angles corresponding to minima of the 24th torque harmonic (Figure 6.13(b)).

different results, especially for small flux-barrier angles, as it can be seen in Figure 6.13. However, high flux-barrier angles (typically greater than $\vartheta_b^e = 60°$) are of interest, since they generally lead to a higher average torque and, hence, better performance.

In order to consider a general case, the torque function (6.16) can be tested at 67.5°, which is halfway from 45° through 90°. In this way, (6.16) and (6.17) are simplified to

$$T_h = \sqrt{T_{\nu_1}^2 + T_{\nu_2}^2 - \sqrt{2} T_{\nu_1} T_{\nu_2}} \tag{6.18}$$
$$\phi_h = \arctan\left(\frac{T_{\nu_2} - T_{\nu_1}}{T_{\nu_1} + T_{\nu_2}}\left(1 + \sqrt{2}\right)\right)$$

Depending on the sign of the two torque functions, using equation (6.18) or (6.8) could lead to different results varying the current angle. The results are reported in Figure 6.13 with a red line. The blue dash-dotted line is the function given by (6.8), whose minima and maxima perfectly correspond to the one of Figure 6.12. It is evident that for small flux-barrier angles, the two functions minima match perfectly for flux-barrier angles greater than 45°. The list of the minima found for the 24th harmonic is reported in Table 6.4.

6.5.2 *Combination of minima solutions*

The previous analysis allowed to find those flux-barrier angles, ϑ_b^e, yielding a minimum of a fixed harmonic of the torque. A pair of such solutions can be adopted and combined together in the same rotor obtaining an asymmetric rotor (Bianchi et al., 2009b). It exhibits different flux-barrier geometries that are alternated between the poles. In this way:

1. the torque harmonic that has been minimized as described above remains of low value, and
2. a sort of compensation of the other torque harmonics is achieved.

This means that two torque harmonics can be minimized: one through the choice of flux-barrier angles and the other one through an asymmetric rotor. The two harmonics are referred to as h and k in the following.

The easiest way to make the compensation of torque harmonics is to use phasors. Let T_k' be the k^{th} torque harmonic produced by the first pole, with phase ϕ_k', and T_k'' be the k^{th} torque harmonic produced by the second pole (different from the first), with phase ϕ_k''. Both poles

have flux-barrier angles that minimize the h^{th} torque harmonic. Then their vector sum results in

$$T'_k e^{j\phi'_k} + T''_k e^{j\phi''_k}$$

and so the problem to solve is as follows:

$$\min_{i \neq j} \left| T_k^{(i)} e^{j\phi_k^{(i)}} + T_k^{(j)} e^{j\phi_k^{(j)}} \right| \tag{6.19}$$

where i and j are the indexes of the set $S_h = \{\vartheta_{\text{b}i}^{\text{e}}\}_{i=1}^{n}$ of flux-barrier angles that already minimize the h^{th} torque harmonic.

For the combination in pairs with (6.19) there are two options:

1. find flux-barrier angles that minimize the h^{th} torque harmonic, and find the minimum of the k^{th} torque harmonic using optimal combination of the angles previously found;
2. find flux-barrier angles that minimize the k^{th} torque harmonic, and find the minimum of the h^{th} torque harmonic using optimal combination of the angles previously found.

Since most of the ripple is due to the first four slot harmonics of the electric loading, which cause the first two slot harmonics of the torque, it is advisable to take k as the first torque slot harmonic, and $h = 2k$ as the second one, or vice versa. Note, however, that the two criteria differ greatly. In fact, the number of $2k$-combinations is higher than the k-ones due to the higher number of minima found minimizing $2k^{\text{th}}$ torque harmonics. So the first criteria leads to a higher probability of finding proper combinations, and it is the one which is adopted in the following.

6.5.3 *Combinations for one flux-barrier rotor and validation*

The combinations in pairs of the angles in Table 6.4 could be ranked based on the predicted 12^{th} torque harmonic by (6.19). The result of such procedure is reported in the first column of Table 6.5. Since there were 66 combinations, only the first 10 are reported.

Many of these combinations were tested by FEA to see whether the ripple is lower than in the respective symmetric rotors, and to check if the ranking is effectively sorted.

The FEA results are reported in Table 6.5. It can be noticed that the ranking is not perfectly sorted. This is due to the effect of local saturation which virtually changes the position of the flux-barrier end, hence it changes the flux-barrier angle. However, some results are excellent because the ripple is less than half the original one (the improvement can be seen from the example of Figure 6.14(a) and from (Bacco et al., 2017)).

Figure 6.14 shows the torque waveforms and spectra of one suitable combination of the flux-barrier angles found above. The chosen combination is the fourth of Table 6.5. labeled as '10 and 8', whose pair of flux-barrier angles is $\vartheta_{\text{b}}^{\text{e}} = 78.7°$ and $\vartheta_{\text{b}}^{\text{e}} = 63.7°$ (see Table 6.4). The

i and j	Torque [N m]	Ripple [%]	12^{th} harm. [N m]	24^{th} harm. [N m]
11 and 9	1.54	26.1	0.095	0.140
11 and 10	1.50	41.8	0.289	0.007
9 and 7	1.56	36.9	0.234	0.068
10 and 8	1.56	21.7	0.035	0.124
8 and 6	1.52	47.5	0.281	0.087
7 and 5	1.44	28.4	0.112	0.097
6 and 4	1.31	21.3	0.024	0.107
5 and 3	1.11	29.1	0.084	0.089
10 and 7	1.54	25.3	0.048	0.132
9 and 8	1.55	38.4	0.258	0.036

Table 6.5
FEA results of average torque and ripple achieved adopting the predicted combinations of flux-barrier angles (first column). Rotor with one flux-barrier per pole.

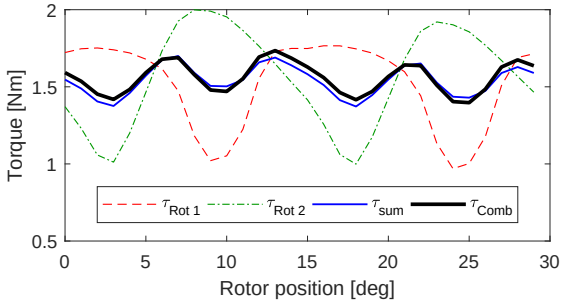

(a) Torque waveforms.

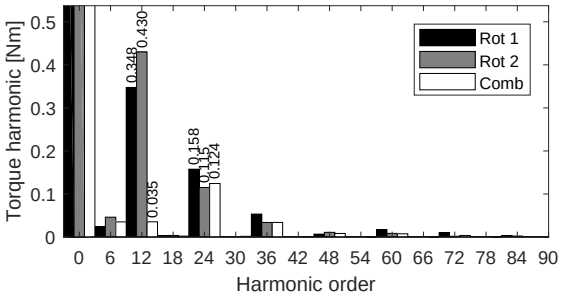

(b) Torque spectra.

Figure 6.14
FE torque waveforms and spectra of the two single one-barrier rotors and their combination.

expected average torque is about 1.56 N m while the torque ripple is 21.7%. It can be noted that the two torque waveforms combine and tend to lower the first torque slot harmonic. In fact, the second harmonic visible in Figure 6.14(a) corresponds to the first torque slot harmonic ($Q/p = 24/2 = 12$) since only a sixth of electrical period is shown. The compensation of this harmonic is evident also from the spectrum in Figure 6.14(b).

6.6 ROTOR WITH TWO FLUX-BARRIERS PER POLE

The torque harmonic equation (6.7) is slightly modified. In particular, there is an additional term which depends on the second flux-barrier angle. Hence the torque contribution of the electric loading harmonic ν results in

$$T_\nu = k_T^* \Delta U_\text{r} \frac{\hat{K}_\nu}{\nu} \sin(\nu \tfrac{\pi}{2}) \left[\sin \nu \vartheta_{\text{b1}}^\text{e} + \sin \nu \vartheta_{\text{b2}}^\text{e}\right] \tag{6.20}$$

The amplitude of the torque harmonic of order h is still obtained through (6.8) or (6.18), taking into account the corresponding electric loading harmonics.

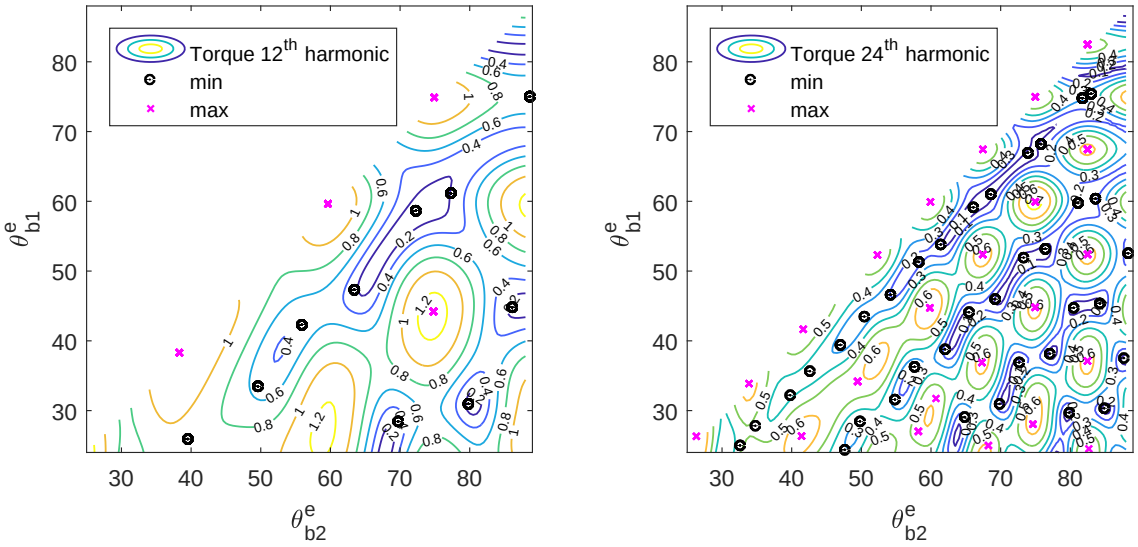

(a) $\nu_1 = 11, \nu_2 = 13$. *(b)* $\nu_1 = 23, \nu_2 = 25$.

Figure 6.15
Analytical torque maps of the first slot harmonics for a motor with $Q = 24$, $2p = 4$ in a two-barriers machine. Black dots show the minima found through the proposed model.

Figure 6.16
Tested two flux-barriers geometries.

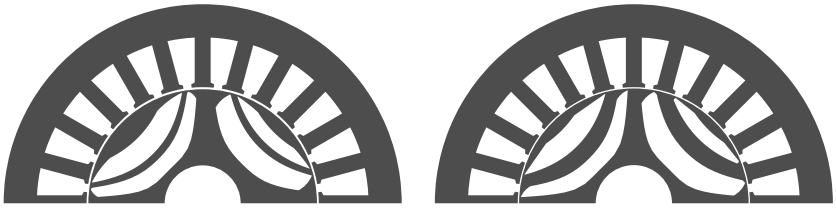

33+26 *(a)* First geometry. 28+23 *(b)* Second geometry.

Figure 6.15 reports the torque behaviors due to the first four slot harmonics versus the two electrical barrier angles, $(\vartheta^e_{b1}, \vartheta^e_{b2})$. The 2D maps are again obtained through a complete model of the two flux-barriers SyR machine. On the other hand, The black dots and the magenta crosses identify the barrier angles which corresponds to minima and maxima, respectively, found by the simple model. This model is well suited to predict these points with great precision.

In the following, the minima found through (6.18) are used to combine the rotor poles. Similarly to the single flux-barrier rotor, the minima obtained through (6.18) are the same of (6.8) for large angles, while they could be different for small angles. Such angles are reported in Table 6.6. The combination procedure for a two flux-barriers rotor is exactly the same as that previously developed, so the problem to solve is again expressed by (6.19). Since now there are 35 solutions of minima, about 600 asymmetric combinations are available to be tested. They were sorted based on the predicted 12th order harmonic and then the first solutions were further analyzed. Table 6.7 reports the first ten combinations. It

#	1	2	3	4	5	6	7	8
ϑ^{e}_{b1} [°]	24.9	24.3	27.7	28.3	29.0	30.2	30.8	29.6
ϑ^{e}_{b2} [°]	32.7	47.7	34.9	49.9	65.0	85.0	70.0	80.0
#	9	10	11	12	13	14	15	16
ϑ^{e}_{b1} [°]	32.1	31.5	36.8	35.5	36.2	38.0	37.4	39.3
ϑ^{e}_{b2} [°]	39.9	54.9	72.8	42.7	57.8	77.1	87.8	47.1
#	17	18	19	20	21	22	23	24
ϑ^{e}_{b1} [°]	38.7	43.4	44.0	45.2	46.5	44.6	45.9	51.2
ϑ^{e}_{b2} [°]	62.1	50.6	65.6	84.4	54.3	80.6	69.3	58.4
#	25	26	27	28	29	30	31	32
ϑ^{e}_{b1} [°]	51.8	53.7	53.1	60.3	59.0	59.6	60.9	66.8
ϑ^{e}_{b2} [°]	73.4	61.5	76.5	83.7	66.2	81.2	68.7	74.0
#	33	34	35					
ϑ^{e}_{b1} [°]	68.1	74.7	75.3					
ϑ^{e}_{b2} [°]	75.9	81.9	83.1					

Table 6.6
Set $S_h = \{(\vartheta^{e}_{b1}, \vartheta^{e}_{b2})_i\}_{i=1}^{n}$ of flux-barrier angles corresponding to minima of the 24th torque harmonic (Figure 6.13(b)) for a rotor with two flux-barriers per pole.

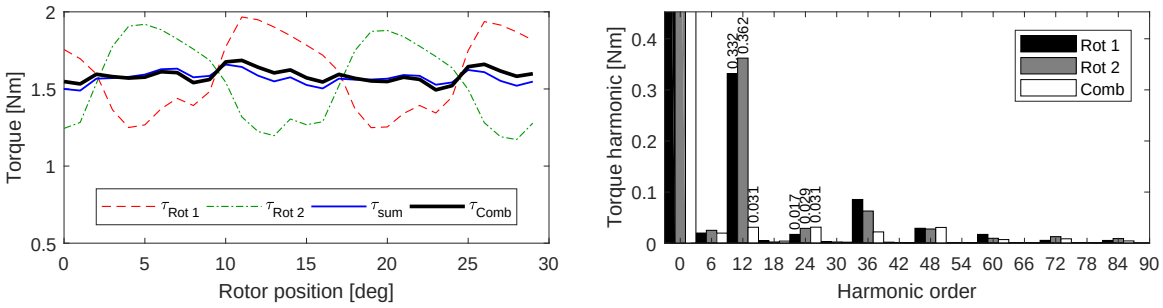

(a) Torque waveforms.

(b) Torque spectra.

Figure 6.17
FE torque waveforms and spectra of the first combination ('33 and 26') of two single rotors and their combination.

can be observed again that the ranking is not perfectly sorted when they are analyzed by means of FEA. In addition, the achievable torque ripple results almost always lower than that of one flux-barrier rotors.

6.6.1 *Validations*

As an example, two combinations minimizing (6.19) are studied. They are the '33 and 26' and the '28 and 23' combinations. The first one corresponds to the two pairs of barrier angles $\vartheta^{e}_{b1} = 68.1°, \vartheta^{e}_{b2} = 75.9°$ and $\vartheta^{e}_{b1} = 53.7°, \vartheta^{e}_{b2} = 61.5°$. The geometry is shown in Figure 6.16(a).

The second combination corresponds to the two pairs of barrier angles $\vartheta^{e}_{b1} = 60.3°, \vartheta^{e}_{b2} = 83.7°$ and $\vartheta^{e}_{b1} = 45.9°, \vartheta^{e}_{b2} = 69.3°$. The relative geometry is reported in Figure 6.16(b).

Table 6.7
FEA result of the predicted combinations of two flux-barriers rotors.

i and j	Torque [N m]	Ripple [%]	12^{th} harm. [N m]	24^{th} harm. [N m]
33 and 26	1.61	12.1	0.031	0.031
18 and 5	1.52	23.2	0.092	0.096
34 and 29	1.56	20.1	0.074	0.081
28 and 23	1.61	12.0	0.059	0.022
16 and 10	1.43	24.7	0.118	0.014
29 and 22	1.63	20.5	0.152	0.045
27 and 15	1.63	22.4	0.144	0.050
22 and 6	1.62	23.0	0.174	0.029
28 and 22	1.62	19.0	0.134	0.023
26 and 23	1.59	21.9	0.122	0.022
22 and 10	1.53	13.5	0.089	0.021

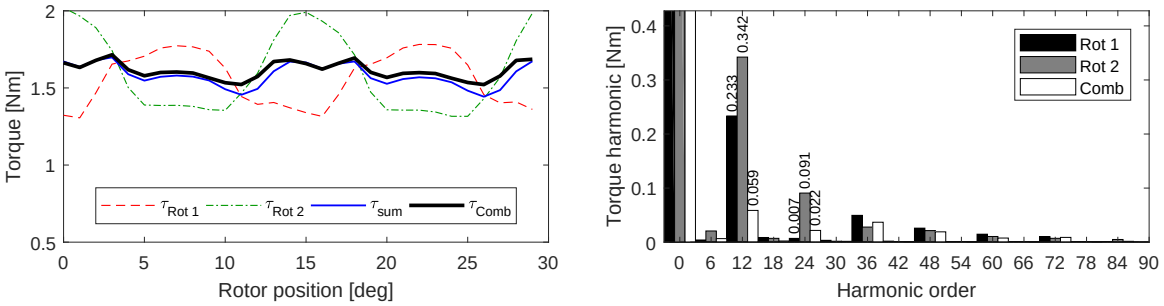

(a) Torque waveforms.

(b) Torque spectra.

Figure 6.18
FE torque waveforms and spectra of the second combination ('28 and 23') of two single rotors and their combination.

The FEA results are reported in Figure 6.17 and Figure 6.18 for both combinations. In Figure 6.17(a) and Figure 6.18(a) dashed line refers to the torque behavior of a rotor with the first pair of angles, and dash-dotted line refers to the second pair. It is evident that the torque oscillations are out of phase, even though they are not perfectly equal in amplitude. This results from the minimization of (6.19). When the two flux-barrier geometries are combined in the same rotor (Figure 6.16 shows the resulting rotors), the torque behavior is smoother as observed in Figure 6.17(a) and Figure 6.18(a), with the solid lines. Furthermore, Figure 6.17(b) and Figure 6.18(b) highlights the reduction of the torque harmonic, especially the 12^{th} one which is the highest.

6.7 EXPERIMENTAL MEASUREMENTS

The results of a symmetric and an asymmetric two flux-barriers IPM prototypes were previously available (Bianchi et al., 2009b). The asymmetric geometry was designed with a different technique, searching

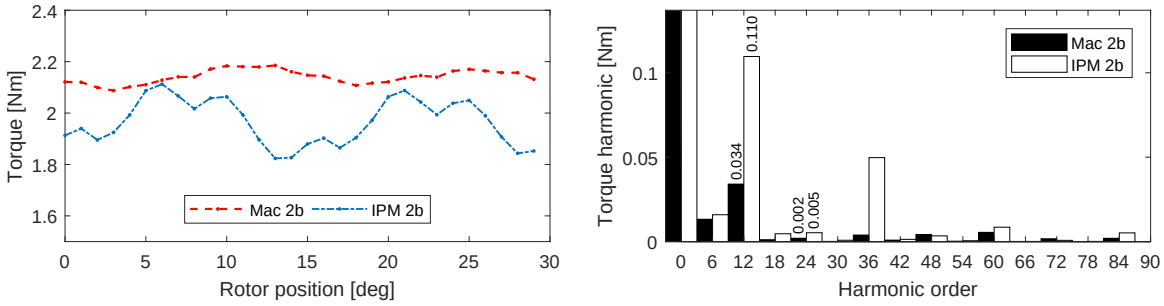

(a) Torque waveforms.

(b) Torque spectra.

Figure 6.19
Comparison of FE torque waveforms and spectra of the available IPM and Machaon prototypes.

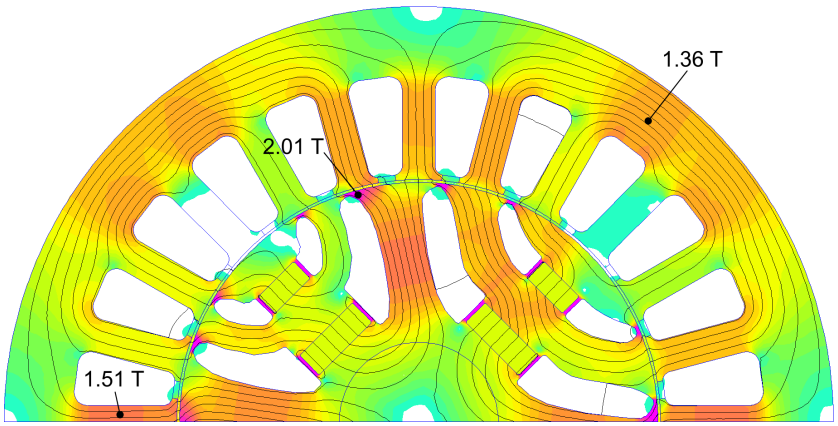

Figure 6.20
Magnetostatic solution of the Machaon two flux-barriers rotor.

for flux-barrier angles which minimize and compensate two torque harmonics, as described in (Bianchi et al., 2009b). The angles of the flux-barrier ends are $\vartheta^{e}_{b1} = 29.6°$ and $\vartheta^{e}_{b2} = 54.8°$ for the even poles, $\vartheta^{e}_{b1} = 44.4°$ and $\vartheta^{e}_{b2} = 80.4°$ for the odd poles. It should be highlighted that the first two flux-barrier angles are very close to the 10^{th} solution of the set reported in Table 6.6, while the other one is close to the 22^{nd} reported solution. Furthermore, the combinations of such solutions appear in the complete list in position 44, so within the first 10% of all the possible combinations, and it corresponds to the one labeled '22 and 10' in Table 6.7.

The FEA results are shown in Figure 6.19. They confirm that the asymmetric rotor (also referred to as "Machaon" in (Bianchi et al., 2009b)) is able to generate a smoother torque waveform. It is also evident from Figure 6.19(b) that the harmonic content of the Machaon rotor is very low. In particular its average torque results 2.14 N m, with a ripple of 4.57%, while the IPM motor has an average torque of 1.97 N m with a ripple of 14.7%. A magnetostatic FEA solution of the Machaon IPM is also reported in Figure 6.20.

Some measured results are reported in Table 6.8. The torque harmonics are referred to the average torque. From this results it is evident that the asymmetric rotor allows to minimize the torque oscillations.

Table 6.8
Measured torque harmonics in the two prototypes.

harmonic order	symmetric rotor	asymmetric rotor
12	5.36	1.61
24	1.56	0.44
total	13.1	4.76

In particular the study has been carried out focusing on the higher torque harmonic components (related to the slot harmonics), which are of 12th and 24th order. It is worth noting that both harmonics are strongly reduced. As a consequence the total torque ripple is reduced to one third with respect that of a machine with symmetric rotor.

6.8 DISCUSSION

This chapter dealt with the design procedure for a quick and practical choice of flux-barriers in SyR machines. In particular, a simple but effective model has been derived, useful to select the flux-barrier angles in order to minimize the highest torque harmonics. The adopted assumptions are:

1. only the first two electric loading slot harmonics are considered because they produce the majority of torque ripple,
2. the rotor magnetic scalar potentials are considered constant.

According to that, the model reduces to the numerical solution of a single equation (or system of equations). This fact ensures a great convenience of the presented model, so the designer can opt for the minimization of any torque harmonic of interest.

The results have been compared with the full torque harmonic functions, derived by a complete analytical model. It has been shown a perfect match between the minima, for many combinations of number of flux-barriers and slots per pole.

Furthermore, the combination of proper flux-barrier angles into an asymmetric rotor structure has been presented. This strategy is based on the following two-step design procedure.

1. At first, a set of flux-barrier angles is identified so as to minimize a torque harmonic of given order.
2. Then, pairs of geometries belonging to this set are combined together so that a specific torque harmonic is compensated.

After that, many combinations of these minima have been tried to compensate the first, and highest, slot harmonics. One of these combinations corresponds to an available prototype previously optimized by a series of FEA simulations, which effectively compensated the first slot harmonic. Therefore, this model becomes a practical tool for the design of SyR motors.

Part III

OPTIMIZATION APPLICATIONS

7

HIGH-TORQUE LOW-SPEED PERMANENT MAGNET ASSISTED SYNCHRONOUS RELUCTANCE MOTOR DESIGN

Direct-drive electric machines represent a valid solution for low-speed applications thanks to the absence of the gear-box. This ensures lower weight, noise, axial length and lower mechanical losses. Furthermore, a higher reliability of the overall system is guaranteed, and this is a very important requirement when the machine is installed in harsh environments (Grauers, 1996; Lampola, 1998; Popescu et al., 2013; Zhou et al., 2017). Such machines find applications in energy production, electrical propulsion, industrial automation, low-head pumps and so on. They typically employs strong RE magnets with high pole numbers. However, in this application ferrite magnets have to be preferred, because of the high cost of RE magnets. This means that the machine should exploit the reluctance torque component as much as possible. Therefore, a PMASYR machine is the topology of choice.

The structure of the chapter is as follows: at first the specifications and constraints are listed; after that, some parametric analyses are carried out (Wang et al., 2017). Then, a multi-objective optimization coupled to finite element analysis is performed to find the best possible design solutions. Finally, a thorough electromagnetic analysis is performed on one possible design solution.

7.1 SPECIFICATIONS, REQUIREMENTS AND HYPOTHESIS

The motor outer dimensions are the constraints of the application and they are reported in Table 10.1. In particular, they are 2500 mm for the outer diameter, and 1500 mm for the stack length. The power requirement is 1 MW at 22 rpm, which results in a torque of about 434 kN m. To achieve such performance, a machine with a high pole number is required. Furthermore, a modular machine has to be preferred, where all the machine sectors are independent. This limits the choice of the winding arrangement and the number of poles. In fact, either two or three three-phase systems has to be employed for supplying the machine. This means that the number of pole pairs (one sector) should be a multiple of two, three or both.

The slot shape is rectangular to ease the manufacturing of the machine, and the conductors are chosen to be rectangular too. Such conductors do not represent a problem for skin and proximity effects since the supply frequency is extremely low. Iron losses are negligible too, so the iron flux densities could be increased to higher values.

To start with an initial design, some hypotheses and choices have been made. They are reported in Table 10.1. In particular, a high split ratio is chosen since the machine has large external diameter and high

Table 7.1
Motor specifications, constraints and hypothesis.
* Efficiency requirement not realistic.

Quantity	Value	u.m.
Power	1	MW
Speed	22	rpm
DC bus voltage	690	V
Air-gap	2	mm
Outer diameter	2500	mm
Stack length	1500	mm
Efficiency*	96	%
Torque ripple	1	%
Hypothesis		
Split ratio	0.92	
Slot p. pole p. phase	4	
Power factor	0.875	
Estimated fill factor	0.6	
Packing factor	0.97	
Current density	6	A/mm^2
Air-gap flux density	1.1	T
Yoke flux density	1.6	T
Tooth flux density	1.8	T

poles number. In order to improve the mmf waveform and reduce torque ripple, the number of slots per pole and per phase is selected to be four.

The choice of the pole number results from a compromise between the minimum slot width (which should not be too small for manufacturing issues), and the iron weight. The reduction of the iron weight obviously implies an overall weight and material cost reductions, as the iron losses do not represent an issue (Vagati et al., 2012). On the other hand, the slot width is mainly due to the number of slots per pole per phase, which should be relatively high to reduce the torque ripple (Bacco et al., 2017; Bianchi et al., 2009b; Mohanarajah et al., 2018). Thus, for the initial design, 36 poles and 4 slots per pole per phase are adopted. Through a preliminary design it has been found that the efficiency target is too high, because it would require a high amount of copper and a low current density. So a more realistic target, equal to 93%, has been set.

7.2 PARAMETRIC ANALYSES

At first, some parametric analyses have been carried out in order to better understand the dependency of the performance factors on the design variables.

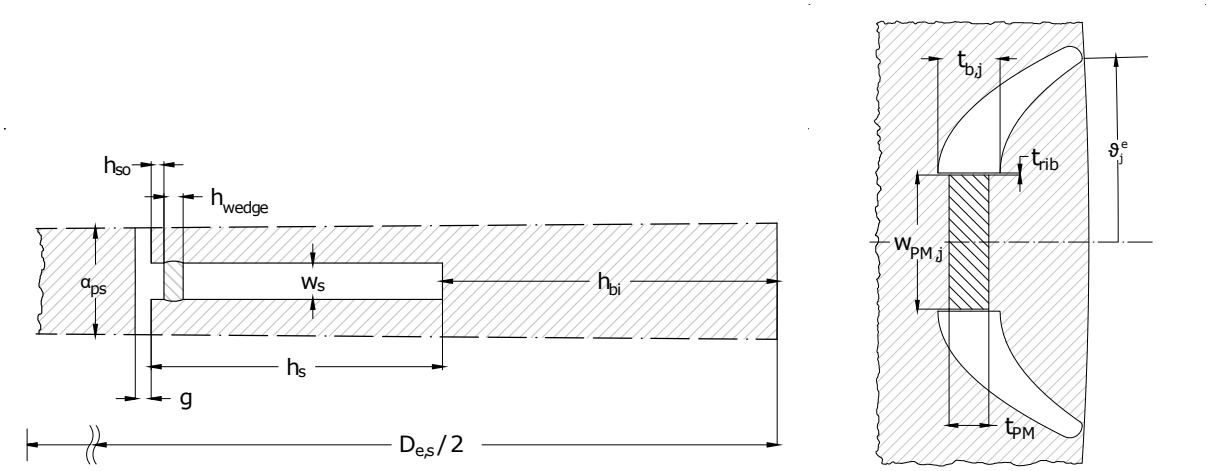

(a) Stator *(b)* Rotor

Figure 7.1
Machine geometrical parameters.

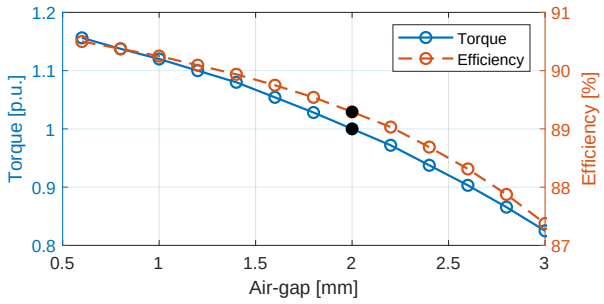

Figure 7.2
Torque and efficiency parametric analysis varying the air-gap thickness.

7.2.1 *Air-gap thickness*

The first one is the variation of the air-gap thickness. Since the torque depends on the air-gap flux density, which is almost inversely proportional to the air-gap thickness with the same PM and currents, an increase in the air-gap reduces the available torque. The results of the parametric analysis are shown in Figure 7.2, while a comparison of the actual flux density maps is reported in Figure 7.3.

As expected, the available torque increases with the decrease of the air-gap. This could potentially reduce the current needed to reach the desired torque and, thus, increase the efficiency. However, the minimum air-gap has been set to 2 mm according to mechanical constraints, given the large stator diameter. From Figure 7.3 it is evident that a smaller air-gap results in a more magnetized machine, with all the other parameters constant.

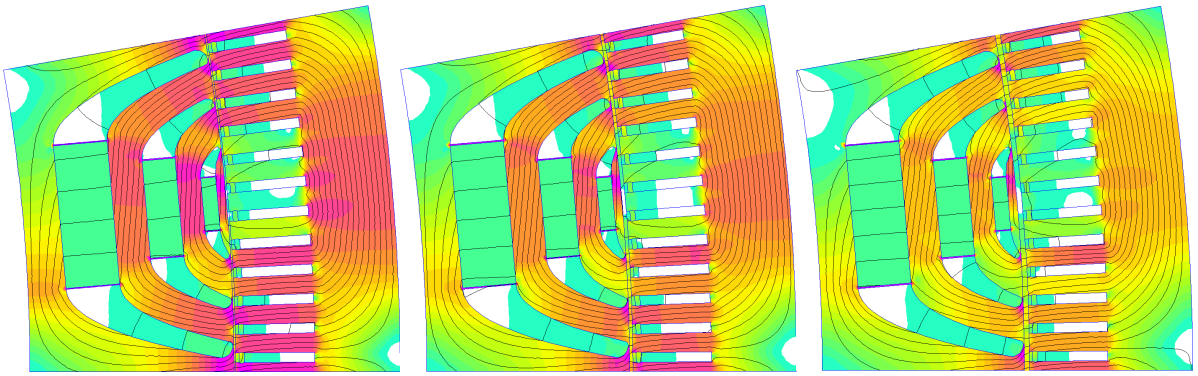

(a) $g = 1\,\text{mm}$ (b) $g = 2\,\text{mm}$ (c) $g = 3\,\text{mm}$

Figure 7.3
Parametric analysis varying air-gap.

Figure 7.4
Torque and torque ripple parametric analysis varying k_{air}.

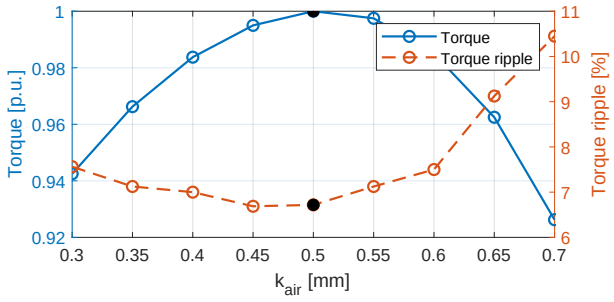

7.2.2 *Magnetic insulation ratio*

Another parametric analysis deals with the magnetic insulation ratio, k_{air}. This factor determines how much space is reserved for flux-barriers in the rotor. Generally speaking, this parameter strongly affects the reluctance torque, but less the ripple. These aspects can be observed from Figure 7.4, where the average torque and torque ripple are plotted against this factor. The initial choice of $k_{\text{air}} = 0.5$ (so as much air as iron) represents the best compromise for this kind of machine. At this stage of the design, the thickness of the magnets is the same as the one of the corresponding barrier. It can also be noted that the torque ripple remains almost constant up to a value of k_{air} equal to 0.6. After this value, the ripple increases. This is due to the fact that the large flux-barrier thicknesses compromise the actual position of the flux-barrier-end angle, leading to a different air-gap flux density distribution and to a different torque behavior.

7.2.3 *Magnets dimensions*

Another parametric analysis that has been carried out deals with the variation of the magnets dimensions. The response variable is the average torque. Since only one rotor position was evaluated, the *dq* torque was used as the best estimate of the average torque.

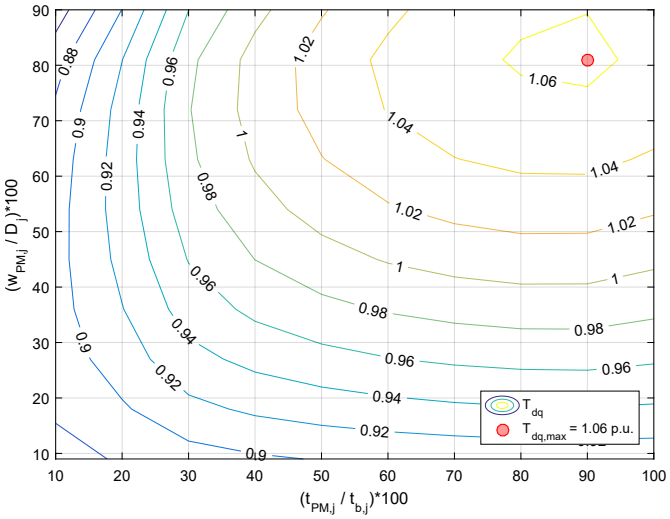

(a) Torque contours versus magnet thickness and width.

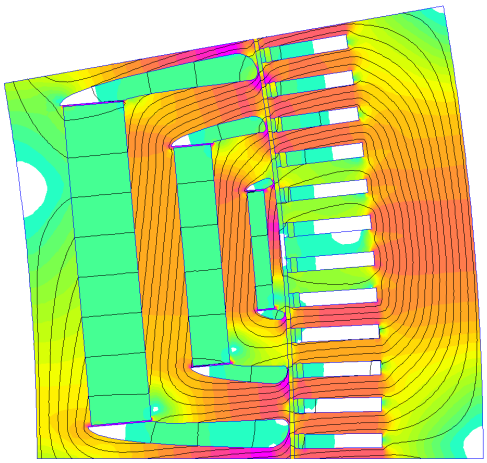

(b) Magnetostatic solution of the maximum torque geometry after the magnet dimensions parametric analysis.

Figure 7.5
Results of the parametric analysis changing the magnet dimensions.

The results are reported in Figure 7.5(a). The magnet thickness, on the x-axis, is varied between 10 and 100% with respect to the relative flux-barrier thickness, while the magnet width, on the y-axis, between 10 and 90% of the flux-barrier projection on the rotor periphery. It can be seen that there exists a maximum for the torque at a specific combination of magnets thickness and width, and it exhibits a torque about 6% higher than the initial design.

Such a geometry and a magnetostatic simulation is reported in Figure 7.5(b). It can be noted that the magnets are really wide and they cover almost all of the available space, especially comparing it to the initial design of Figure 7.2. Despite the great increase in the magnet size, the torque increase is modest. This is due to the use of ferrite and probably such a solution is not reasonable when the magnet cost is considered.

7.2.4 *Number of poles and slots*

The most defining parametric analysis is the variation of the number of poles and the number of slots per pole per phase, though. In this case, the geometry and the current change accordingly to the following constraints:

- output torque equal to 440 kN m,
- current density equal to 6 A/mm^2,
- flux-barrier electrical angles equal to $\{28°, 52°, 76°\}$,
- maximum tooth flux density equal to 1.8 T and stator yoke flux density equal to 1.6 T,

Table 7.2
Slots and pole combinations analyzed in the parametric analysis.

		$2p$									
		26	28	30	32	34	36	38	40	42	44
q	3	•	•	•	•	•	•	•	•	•	•
	4	•	•	•	•	•	•	•	•	•	•
	5	•	•	•	•						

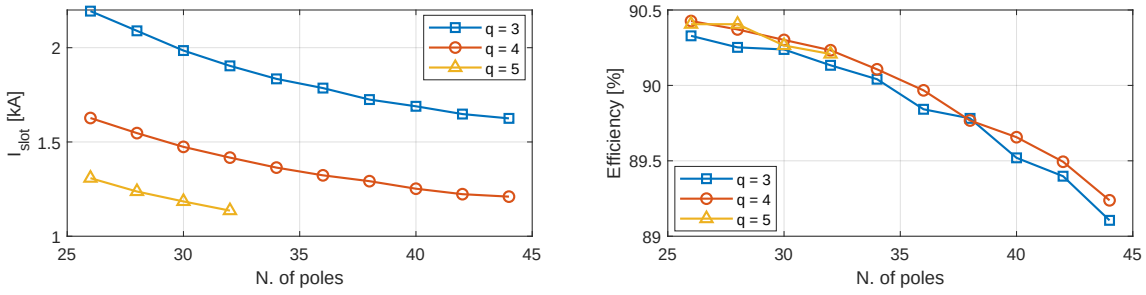

(a) Slot current *(b)* Efficiency

Figure 7.6
Results of the parametric analysis varying the number of pole pairs p and the number of slots per pole per phase q.

- magnetic insulation ratio, k_{air}, equal to 0.5,
- equal magnet volume.

As it can be seen from Figure 7.6(a), the required slot current decreases as the number of poles increases, as expected. In fact, the electric loading can be defined as

$$\hat{K}_{\text{s}} = \frac{k_{\text{w}} \hat{I}_{\text{slot}}}{p_{\text{s}}} \tag{7.1}$$

where k_{w} is the winding factor, $\hat{I}_{\text{slot}}$ the peak slot current, and p_{s} the slot pitch. It is evident that as the number of poles increases, the slot pitch decreases and so does the current to keep the same electric loading, thus the same torque. Furthermore, the current required decreases as the number of slots increases. However, the overall efficiency of the motor decreases as the number of poles increases, because of the increase of the copper quantity. Since the current density is kept constant, the overall Joule losses increase. On the other hand, the rotor diameter increases and the iron volume decreases. From these analyses, it is clear that the efficiency requirement cannot be met with such current density. This is also highlighted in Figure 7.6(b), where the maximum achievable efficiency is 90.4% for the machine with the lowest pole pairs number. Therefore, the supply condition of the machine should be modified to better approach the efficiency requirement.

Symb.	Value	u.m.	Symb.	Value	u.m.
h_y	$50 \pm 50\%$	mm	k_b	$0.1 \div 0.7$	1
h_s	$45 \pm 50\%$	mm	w_{pm1}	$45 \pm 25\%$	mm
w_s	$5.7 \pm 50\%$	mm	w_{pm2}	$85 \pm 25\%$	mm
ϑ^e_{b1}	$30 \pm 10\%$	°	w_{pm3}	$125 \pm 25\%$	mm
ϑ^e_{b2}	$50 \pm 10\%$	°	t_{pm1}	$8 \pm 25\%$	mm
ϑ^e_{b3}	$70 \pm 10\%$	°	t_{pm2}	$18 \pm 25\%$	mm
k_{air}	$0.4 \div 0.7$	1	t_{pm3}	$28 \pm 25\%$	mm

Table 7.3
Optimization parameters and ranges.

7.3 OPTIMIZATION

Geometries with 30 poles will be optimized, to not penalize the efficiency too much and to guarantee the feasibility of three three-phase systems. Only 4 slots per pole per phase are considered in the following since this combination achieved the best torque ripple results and it allows a wide enough slot. A multi-objective optimization has been carried out, with 14 parameters and 3 objectives.[1] The parameters, together with their limits, are reported in Table 7.3. They are: the yoke height h_y, the slot height h_s, the slot width w_s, the three flux-barrier angles $\vartheta^e_{b1}, \vartheta^e_{b2}, \vartheta^e_{b3}$, the magnetic insulation ratio k_{air}, the flux-barrier-end shape factor k_b, the three magnets width $w_{pm1}, w_{pm2}, w_{pm3}$, and the three magnets height $t_{pm1}, t_{pm2}, t_{pm3}$.

70 individuals over 120 generations were evaluated, so a total of 8470 function evaluations have been performed. Each evaluation lasts for about 150 s, meaning an optimization time of about 6 days with parallel computations. The current was adjusted so as to always reach the target torque.

The three objectives are the active material cost, the torque ripple and the efficiency. One of the possible results plot is shown in Figure 7.7(a). This represents a common and expected result, which highlights the relationship between efficiency and cost. It is evident that newer generations are closer to the Pareto front, shown with black diamonds, so newer generations have better efficiency for the same cost, and it means that the optimizer is actually improving the objective functions. Furthermore, efficiency equal to the target can be reached, but only at higher costs, which means with a heavier machine, generally speaking.

Figure 7.7(b) reports the torque ripple versus the cost. The dimension of the markers is proportional to the efficiency. It can be noted that the torque ripple is basically independent of the cost of the machine, proving once again that it is mostly due to the rotor geometry. In addition, the achievable torque ripple is lower than 5%, which is a remarkable result for this kind of machine. The target was 1%, but that was very ambitious for a machine relying heavily on the reluctance torque.

1 See Chapter 3.

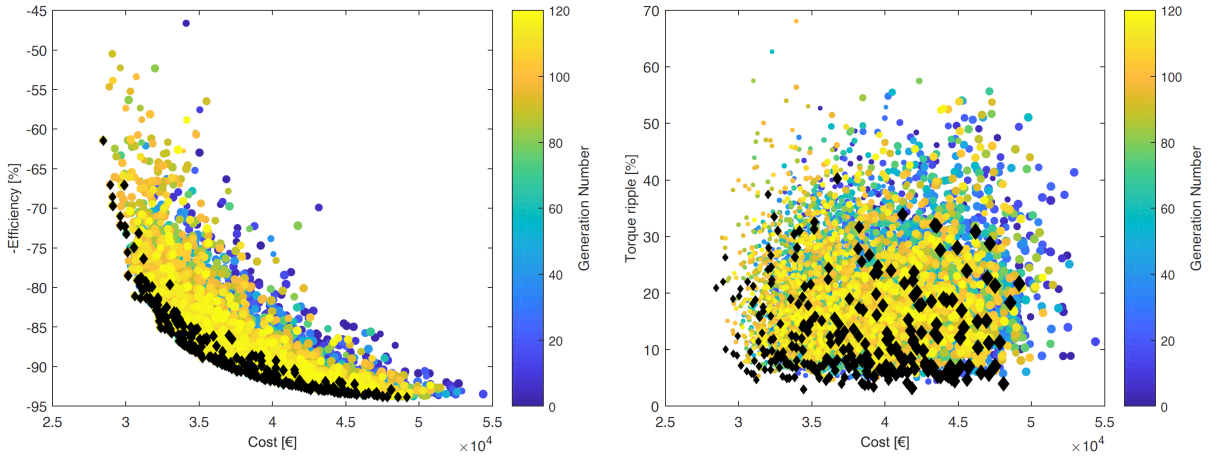

(a) Efficiency versus cost plane

(b) Torque ripple versus cost plane

Figure 7.7
Optimization objectives planes. Lighter colors represent newer generations, while black diamonds are the points belonging to the Pareto front. The size of the markers is proportional to the objective not shown.

Figure 7.8 reports a summary of the optimization results, where each objective is plotted against each parameter. This kind of plot enables the designer to understand the relationships existing between different quantities. The first thing that is evident is that the cost has a linear relationship with the slot height and width (h_s and w_s), due to the amount of copper needed. Also the Pareto points creates a sort of straight line in those planes. As a consequence, as already seen from Figure 7.7(a), the efficiency is proportional to these two parameters, but less than linearly. Furthermore, there is an upper and lower bound for the cost as function of these two parameters.

Another thing that can be noted is that solutions with small second and third magnets are preferred, thanks to the decrease in cost. In fact, newer generations and Pareto points are close the the lower bound of that quantity, meaning that it is convenient to keep these magnets small, both from a performance and from a cost point of view.

At last, low torque ripple can be achieved only with certain combinations of flux-barrier angles. This can be deduced easily from Figure 7.9(a), where the leftmost points appear only at specific combinations of the three angles (for instance, the one with $\vartheta^e_{b1} \simeq 30°$, $\vartheta^e_{b2} \simeq 56°$, $\vartheta^e_{b3} \simeq 68°$).

One of the optimal solutions belonging to the Pareto front was selected for deeper electromagnetic and thermal investigations. Figure 7.9(b) reports the geometry and the magnetostatic solution of this optimum. It can be noticed that the yoke height is quite large, and the slot is tall and narrow. This would imply a high slot leakage inductance but, thanks to the low frequency, the voltage drop due to it is still quite low. The magnets dimensions were changed as little as possible in order to obtain their widths and heights proportional and so decreasing supply and manufacturing costs.

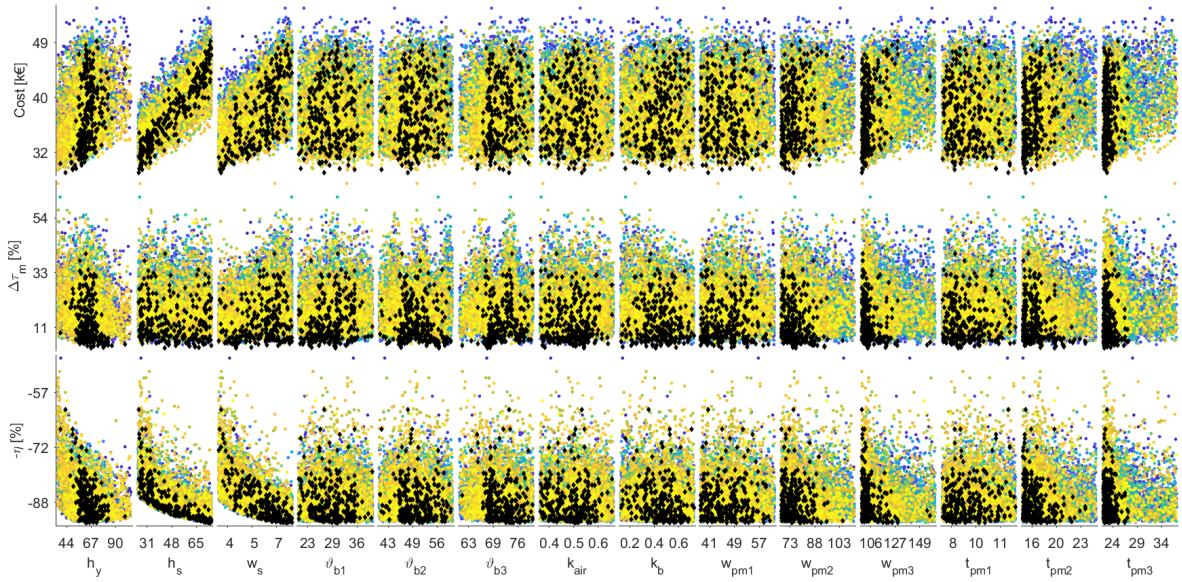

Figure 7.8
Summary of the optimization. Lighter colors represent newer generations, while black diamonds are Pareto points.

The main performance of this machine are reported in Table 7.4. The motor is able to almost reach the efficiency target, reducing the conductor current density, though. It can be noted that iron losses are negligible, thanks to the very low frequency. The power factor is also quite low, which may result in inverter oversizing. Finally, the torque ripple is very good for this kind of machine. The corresponding torque waveform is reported in Figure 7.10(a). Here, a sixth of an electrical period is shown. It is immediate to notice a first harmonic, which corresponds to the sixth harmonic of torque. After that, the highest visible harmonic is the eighth, which corresponds to the 24^{th} in a full electrical period. This is the second slot harmonic ($2Q/p$), while the

Table 7.4
Chosen optimal motor performance, weight and cost results.

Quantity	Value	u.m.
Current	2905	A
Current Density	4.4	A/mm^2
Average torque	446.5	kN m
Torque ripple	3.7	%
Joule losses	69.9	kW
Iron losses	4897	W
Efficiency	92.6	%
Power factor	0.741	1
Material weight	25.5	t
Material cost	45.9	k€
Torque density	17.5	N m/kg

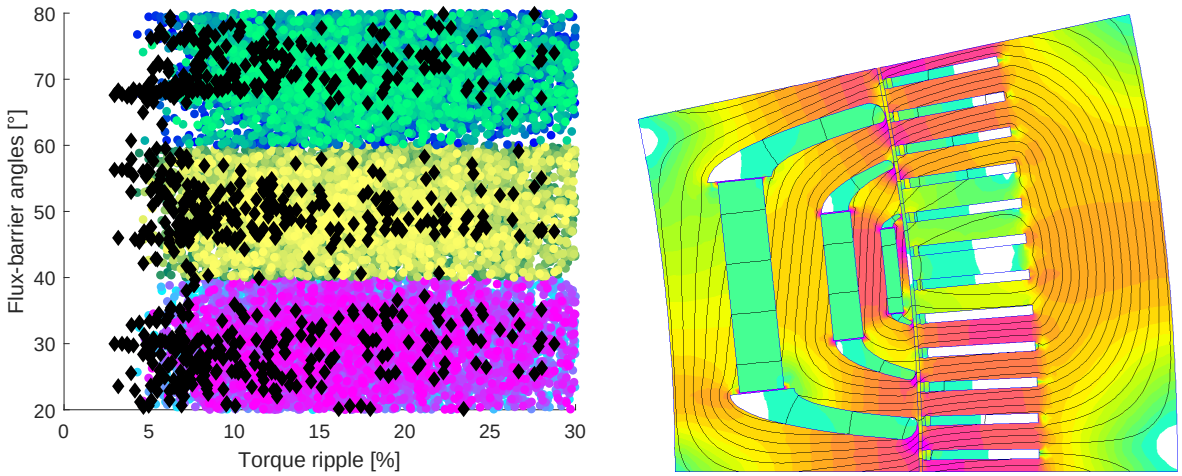

(a) Flux-barrier angles versus torque ripple.

(b) Magnetostatic solution of one optimum.

Figure 7.9
Optimization results.

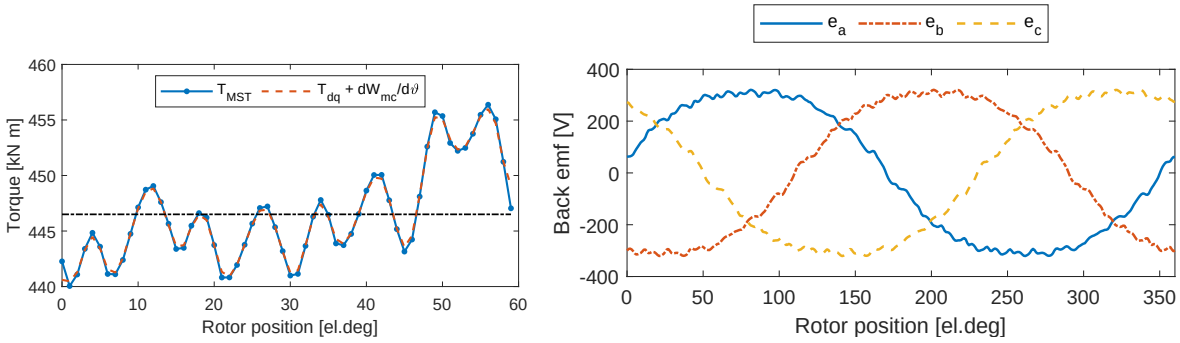

(a) Torque waveform

(b) BEMF waveforms

Figure 7.10
Simulation results for the chosen optimum.

first slot harmonic (Q/p) has been minimized during the optimization. Figure 7.10(b) also reports the resulting phase back electromotive force (BEMF). On top of the desired sinusoidal waveform there are some higher order harmonics. This aspect is quite typical for synchronous reluctance and permanent magnet assisted synchronous reluctance machines.

A thermal analysis has also been carried out to estimate whether the selected cooling system meets the requirement. In particular, the conductor temperature should not exceed 120°C, which is the supposed temperature for the electromagnetic computations. The ambient temperature is 25°C, and the machine is water-cooled on the outer surface. An equivalent air region has been added between the stator iron and the frame to model the non-ideal contact between the two parts. The rotor is virtually without losses, so it is not necessary to model it. Figure 7.11

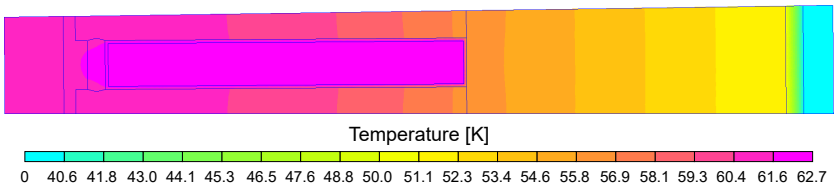

Figure 7.11
Thermal simulation of one stator slot.

shows the temperature distribution in one stator slot when the machine is on full load. The conductor relative temperature reaches 62°C, so 87°C absolute, which is far below the supposed one. This means that the Joule losses could be lower, and the efficiency higher. Alternatively, the cooling system could be made smaller. The absolute rotor temperature results about 86°C, which means that a slightly higher PM flux density may be expected.

7.4 DISCUSSION

In this chapter, a comprehensive feasibility study of a permanent magnet assisted synchronous reluctance motor for direct-drive cableway application has been done. The overall performance and limits of this kind of machine have been highlighted. In particular, the motor is able to exhibit good performance, compromising slightly some of the requirements (in particular torque ripple, which was very ambitious). Parametric analysis and multi-objective optimization coupled to finite element analysis have proven to be fundamental tools in the design of these machines, in particular when the design space is wide. In conclusion, the permanent magnet assisted synchronous reluctance machine is suitable to reach the given targets and dimensions constraints.

8

SYNCHRONOUS RELUCTANCE MOTOR OPTIMIZATION FOR PUMPING APPLICATION

A multi-objective optimization of a synchronous reluctance motor is carried out in this chapter. This work has been done in collaboration with a company, which wanted to substitute some PM servomotors with SyR motors for variable-speed pumping applications. The requirements are listed in Table 8.2(a). In particular, a torque of at least 90 N m was required at 2000 rpm. The overload torque is double the rated one, which represents quite a demanding requirement for this kind of machine. Lastly, a flux-weakening speed range of at least two to one was required.

8.1 ROTOR OPTIMIZATION

The optimization has been performed using the provided stator. The most common way to optimize the SyR machine is to maximize the average torque and minimize the torque ripple. Since the stator is fixed, the efficiency is directly proportional to the average torque, so it is not necessary to include it among the optimization objectives.

The optimization parameters were the three flux-barrier angles, and the magnetic insulation ratio k_{air}.

8.1.1 *Optimization Results*

The objectives plane is reported in Figure 8.1(a). This is the plane made by the first two objectives (average torque and torque ripple), while the dots dimension is proportional to the efficiency.

Obviously, being the stator fixed (constant Joule and stator iron losses), the higher the average torque, the higher the efficiency. It can be seen that all the Pareto individuals are able to reach and exceed the required torque, but a clear conflicting relationship between the average torque and the torque ripple can be observed. The lowest achievable ripple is about 8%, and the individual with the lowest ripple on the Pareto front is selected for further investigations.

8.2 CHOSEN MOTOR FOR PROTOTYPE

As written above, the selected individual is the one showing the lowest ripple belonging to the Pareto front. The parameters and the expected results of the selected individual are reported in Table 8.2(b). The results are referred to as expected because during the optimization run the electromagnetic analysis was made quick with a coarser mesh and fewer rotor rotation.

Table 8.1
Specifications, requirements and first results of the motor under investigation.

(a) Specifications and requirements of the motor.

Quantity	Symbol	Value	u.m.
Rated torque	T_B	90	N m
Overload torque	T_{max}	180	N m
Rated speed	n_B	2000	rpm
Maximum speed	n_{max}	4000	rpm
Supply voltage	U_n	380	V
Low torque ripple			
Stator outer diameter	D_e	180	mm
Stator inner diameter	D_s	110	mm
Rotor shaft diameter	D_{sh}	40	mm
Stack length	L_{stk}	288	mm
Air-gap thickness	g	0.4	mm
Number of slots	Q	36	
Number of poles	$2p$	4	
Iron ribs thickness	$t_{rib,}$	0.8	mm
Forced air cooling			

(b) Parameters and expected results of the selected individual in the first optimization.

Par.	Value	u.m.
ϑ_{b1}	18.813	°
ϑ_{b2}	27.953	°
ϑ_{b3}	35.568	°
k_{air}	0.516	
Obj.	**Value**	**u.m.**
$\langle T_m \rangle$	92.305	N m
ΔT_m	8.07	%
η	93.12	%

Table 8.3
Results of the detailed simulation on the selected individual.

Peak slot current	$\hat{I}_{slot}$	575	A
Current angle	α_i^e	68	°
Conductor current density	J	7.025	A/mm^2
Flux link./conductor	Λ/n_{cs}	0.0745	V s
Average torque	$\langle T_m \rangle$	92.195	N m
Torque ripple	ΔT_m	10.06	%
Joule losses	p_{Cu}	1093.6	W
Iron losses	p_{Fe}	198.19	W
Efficiency	η	93.14	%

A more detailed electromagnetic finite element simulation have then been performed, and the final results are reported in Table 8.3. Comparing it with Table 8.2(b), it can be seen that the average torque prediction is quite close to the final result, while the torque ripple is slightly higher than expected (due to the aforementioned simplifications). The efficiency is just a little bit higher than 93%.

The detailed electromagnetic torque behavior for a sixth of electrical period is shown in Figure 8.2(a), while the spectrum in Figure 8.2(b). Since the motor has 36 slots and 2 pole pairs, the highest torque harmonic is expected to be the first slot harmonic, which is the 18th in this case. It can be seen from Figure 8.2(b) that this torque harmonic has been properly minimized during the optimization. In addition, the 36th torque slot harmonic is lower than the 54th, which is unusual, meaning that also this torque harmonic has been minimized by the automatic algorithm.

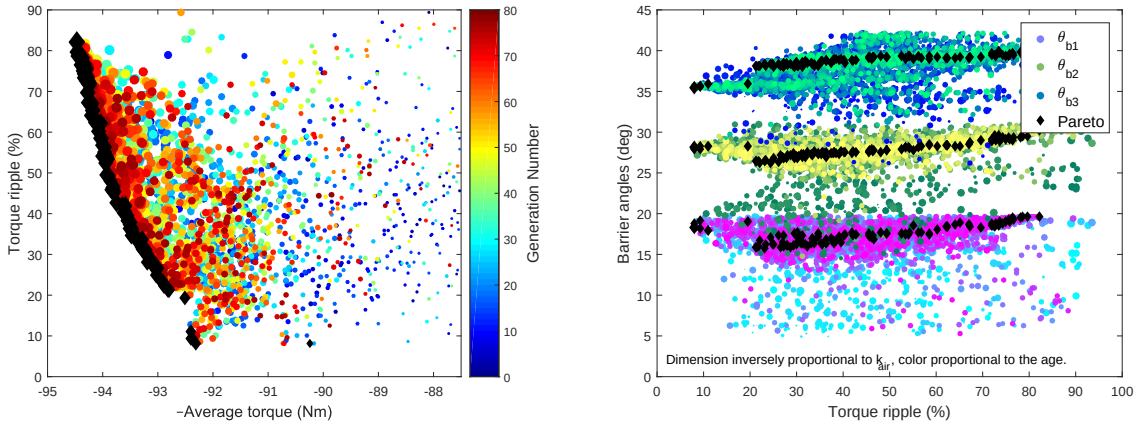

(a) Objectives plane.

(b) Flux-barrier angles versus torque ripple.

Figure 8.1
Optimization result. The colors show the evolution of the individuals, which try to reach the Pareto front, represented with black diamonds. In the first plot the size of the points is directly proportional to the efficiency, while in the second one it is inversely proportional to the magnetic insulation ratio.

Figure 8.3 reports the final geometry. The only notable things are that the first flux-barrier angle is quite large, and then the angular step between one flux-barrier and the other is quite small. The second thing is that there is more air than iron along the rotor q-axis, even though it is still larger than the stator back-iron. So a higher iron saturation is expected to be found in the stator rather than in the rotor.

8.2.1 *Winding design*

Starting from the steady-state on-load simulation it is possible to design the winding. The winding is star-connected, therefore the RMS available phase voltage results

$$U_{\mathrm{w}} = 220\,\mathrm{V}$$

Supposing a voltage drop on the winding resistance and end-winding reactance of about 10%, the BEMF should result about

$$E_{\mathrm{w}} = 200\,\mathrm{V}$$

Knowing that

$$\hat{E}_{\mathrm{w}} = \omega\hat{\Lambda} = 2\pi f\,\hat{\Lambda}$$

and using the computed value of λ/n_{cs} it results that n_{cs} should be 9.

Now it is also possible to compute the winding resistance.

$$L_{\mathrm{stk}} = 288\,\mathrm{mm}$$
$$L_{\mathrm{ew}} = 138\,\mathrm{mm}$$
$$L_{\mathrm{c}} = 426\,\mathrm{mm}$$
$$S_{\mathrm{slot}} = 145\,\mathrm{mm}^2$$

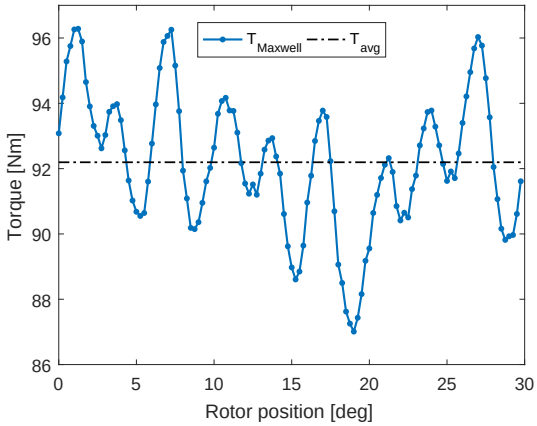

(a) Torque waveform.

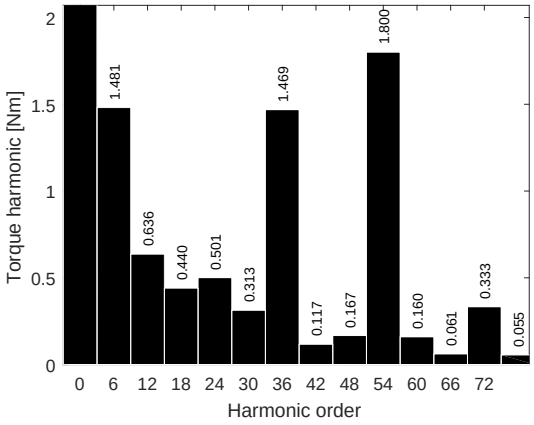

(b) Torque waveform.

Figure 8.2
Torque waveform and spectrum of the selected candidate.

Figure 8.3
Geometry of the optimized selected individual.

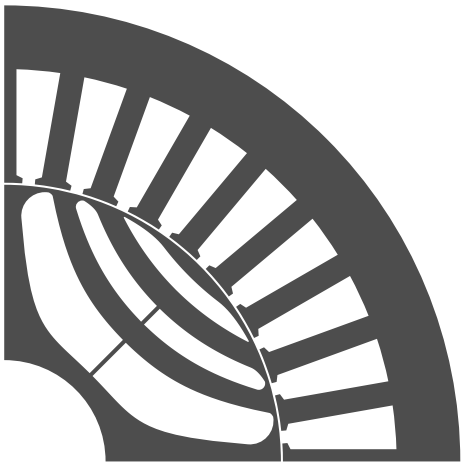

The number of parallel paths is chosen equal to $n_{\text{pp}} = 2$, so that

$$n_{\text{c}} = 18$$
$$S_{\text{c}} = 3.2\,\text{mm}^2$$

The closest commercial conductor size is the one with diameter equal to 2 mm. Therefore the conductor cross-section area should be recomputed accordingly, and so the slot fill factor:

$$d_{\text{c}} = 2\,\text{mm}$$
$$S_{\text{c}}^{\star} = 3.14\,\text{mm}^2$$
$$S_{\text{c,eq}} = 6.28\,\text{mm}^2$$
$$R = \frac{\rho_{\text{Cu}}^{@T} N_{\text{c}} L_{\text{c}}}{S_{\text{c,eq}}} = 138\,\text{m}\Omega$$
$$k_{\text{fill}}^{\star} = 0.39$$

Flux link./conductor	$\hat{\Lambda}/n_{cs}$	0.0745	V s
N. series cond./slot	n_{cs}	9	1
N. cond./phase	N_c	108	1
N. parallel paths	n_{pp}	to be decided	1
Flux linkage	$\hat{\Lambda}$	0.6705	V s
Peak BEMF	$\hat{E}$	281	V
RMS BEMF	E	199	V
Winding Current	I_w	45.2	A

Table 8.4
Winding quantities for the selected motor after the winding design.

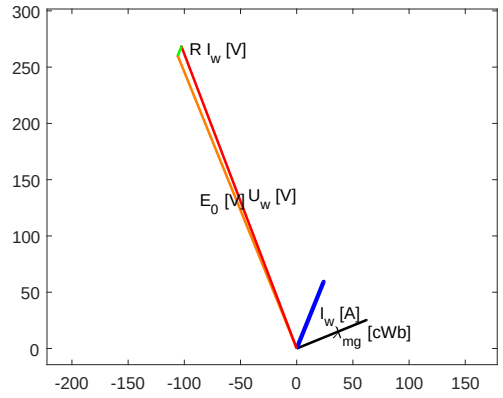

Figure 8.4
Vector diagram in the base point.

Once the winding resistance is known, the vector diagram of the motor can be drawn (Figure 8.4). Thus, it is possible to derive the value of the external power factor, equal to

$$\cos\varphi = 0.732$$

8.2.2 *Motor mapping*

The selected motor has been further simulated mapping the (I_d, I_q)-plane. The map is reported in Figure 8.5(a). The black circle represents the rated torque limit. The highlighted green torque contour is the rated torque (90 N m). The red curve represents the MTPA trajectory, which continues along the green Maximum Torque Per Volt-Ampere (MTPVA) region, and it ends finally with the Maximum Torque Per Voltage (MTPV) trajectory, which is basically a straight line.

The base point is the point lying on the MTPA at the rated current. It can be noted that the corresponding current angle is quite high, meaning that the motor is working under heavy saturation. This is also evident from the shape of the MTPA trajectory: it starts from the origin along a line at 45° and then it curves at low current values and it continues in a straight line.

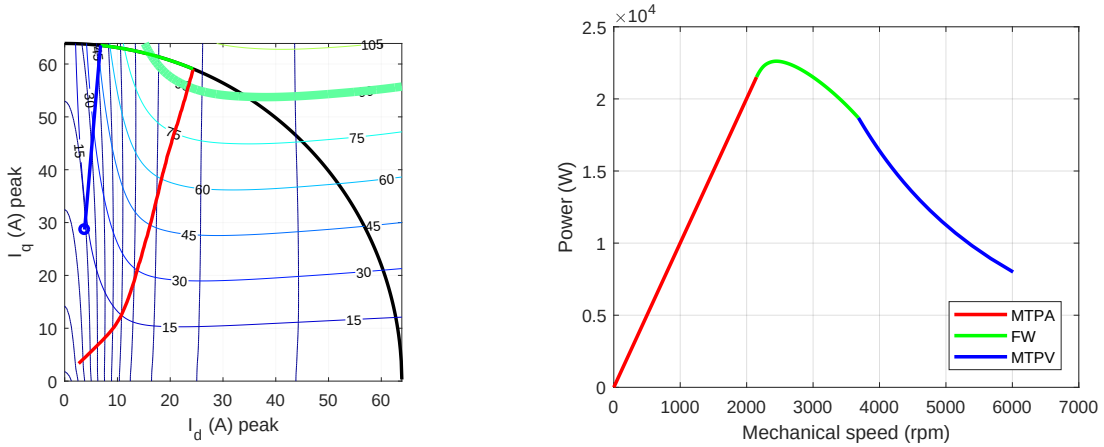

(a) Map of the (I_d, I_q)-plane.

(b) Power-vs-speed limit curve.

Figure 8.5
Map of the (I_d, I_q)-plane and rated power-vs-speed limit curve for the chosen motor geometry.

8.2.3 *Structural Analysis*

The selected geometry has also been analyzed mechanically under centrifugal load. The speed was set to 8000 rpm, well above the operating speed. Despite this fact, the maximum Von Mises stress is found in the last radial iron rib, and it results about 85 MPa. This is quite a low stress value for iron alloys, whose ultimate tensile strength usually starts at around 400 MPa. Of course, the corners of the flux-barriers should be properly rounded to avoid stress concentrations. In addition, the maximum deformation of the rotor at the air-gap results about 18 µm, which is very small compared to the air-gap thickness ($g = 0.4$ mm).

8.3 EXPERIMENTAL MEASUREMENTS

The prototyped motor is a scaled down version of the actual machine. In particular, the rated torque of the prototype is 20 N m, so 4.5 times lower than the original torque. This results in a 4.5 times lower stack length of the prototype. In addition, to overcome the limitation of the test bench DC bus voltage, current supply and maximum speed, the winding has been rearranged to reach 500 rpm as the rated speed, and 1000 rpm as the desired flux-weakening high-speed operation. Magnetically, if the supplied current is scaled accordingly, nothing changes. A summary of the specifications for the prototype is given in Table 8.5.

Typically, two kind of test can be conducted on synchronous machines:

- low-speed rotation to acquire the torque waveform and measure the torque map in the (I_d, I_q)-plane
- high-speed rotation to acquire the flux linkages and measure the respective maps in the (I_d, I_q)-plane

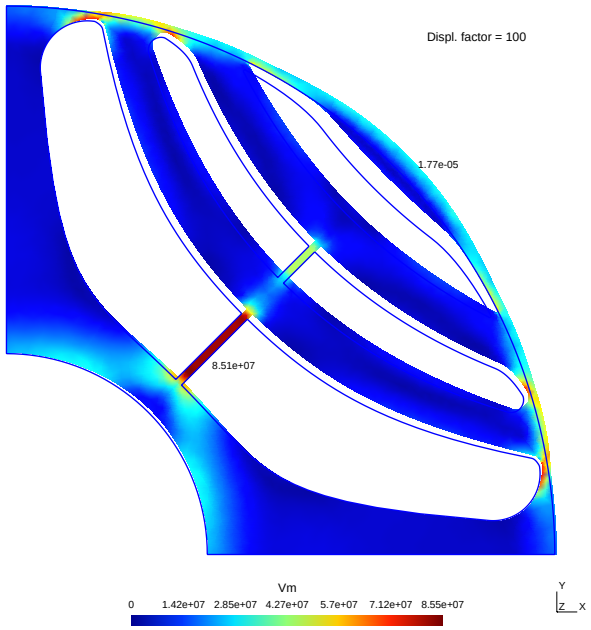

Figure 8.6
Von Mises stress plot at 8000 rpm of the optimized rotor. The maximum displacement at the air-gap is 17.7 µm, while the maximum Von Mises stress in the innermost rib is 85.1 MPa.

Quantity	Symbol	Value	u.m.
Rated torque	T_B	20	N m
Overload torque	T_{max}	40	N m
Rated speed	n_B	500	rpm
Maximum speed	n_{max}	1000	rpm
Stack length	L_{stk}	64.5	mm

Table 8.5
Specifications of the scaled down prototype.

These kinds of measurements are performed in two different test benches.

In addition, MTPA and MTPVA operations for a specific current amplitude at the respective speed may be done, to measure external performance indexes as efficiency and power factor.

8.3.1 *Torque waveform*

The first test is the rotation of the rotor at low-speed with the many current amplitudes and the correct MTPA current angle for each amplitude.

Figure 8.7 report the torque waveforms obtained during this test. It can be noted that the motor is able to reach the target torque, both at rated and at overload condition. However, the torque waveforms show a higher harmonic content than predicted by FEA. In particular, the torque ripple results about 14%, and the waveform shows a distinctive 18^{th} harmonic, which was not found in FEA. The torque ripple value is consistent for different current values, as it can be verified from the overload current.

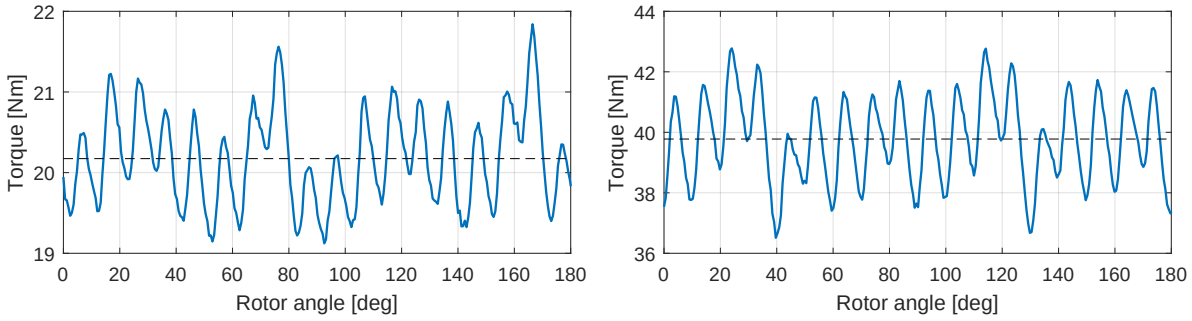

(a) Rated current

(b) Double the rated current

Figure 8.7
Torque waveforms versus the rotor position for two different current levels.

Figure 8.8
Flux linkages behavior as functions of the two axes currents.

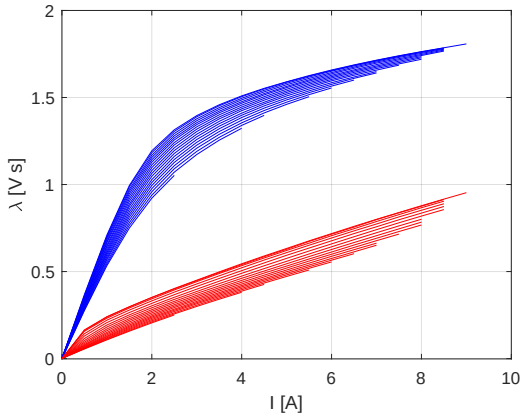

8.3.2 *Flux maps*

The second test, the one done at relatively high-speeds, is used to determine the flux linkage maps versus the d- and q-axis currents. Their behavior is reported in Figure 8.8. As expected for this kind of machine, the d-axis flux linkage is always higher than the q-axis one. There two families of curves due to the cross-saturation effect: the higher flux linkage is obtained with the respective axis current when the other axis current is kept to zero; as soon as there is also the other axis current, the flux linkage decreases. While a q-axis flux decrease is beneficial, typically the decrease of the d-axis flux linkage is higher than the decrease of the q-axis, leading to worse performance. Another interesting fact that can be appreciated from Figure 8.8 is that the slope of q-axis flux linkage near the origin is quite similar to the q-axis one. This is due to the presence of the iron ribs, which must be saturated for the machine to shown appreciable saliency.

The behavior of the flux linkages can be plotted also in the (I_d, I_q)-plane as contours. They are shown in Figure 8.9. The effect of cross-saturation is evident from the curvature of the isolines.

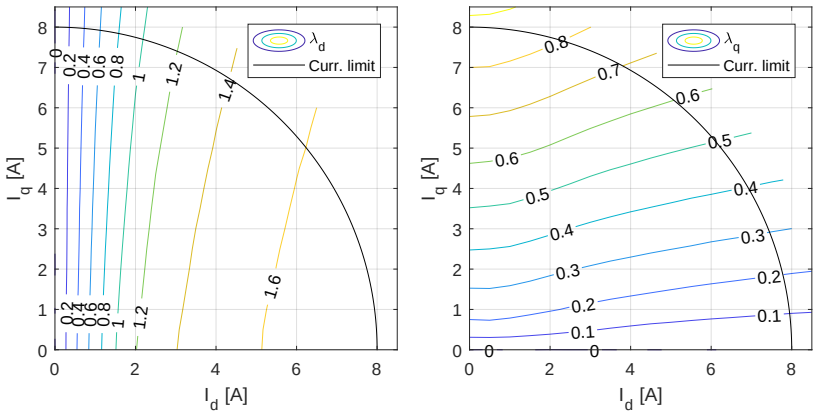

(a) d-axis flux linkage

(b) q-axis flux linkage

Figure 8.9
Flux linkages maps in the (I_d, I_q)-plane.

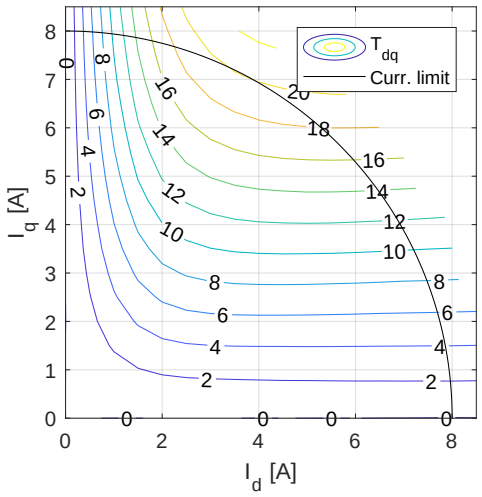

Figure 8.10
Torque map in the (I_d, I_q)-plane.

Even though the torque has been measured during the low-speed test of the motor, it is possible to estimate its value in the (I_d, I_q)-plane using the well-known relationship

$$T_\mathrm{m} = \frac{3}{2} p \left(\lambda_d i_q - \lambda_q i_d \right)$$

as done in FEA. The results are shown in Figure 8.10. This map can be directly compared with the one obtained through FEA (considering the scaling factor, of course). As long as the rotational speed is low (therefore iron losses are negligible), there should be good accuracy between the measurements and finite elements.

8.3.3 *Flux-Weakening and MTPV*

Using the high-speed test bench and imposing the appropriate I_d and I_q, it is possible to reconstruct the whole Flux-Weakening (FW) operation, so moving along the MTPVA and MTPV trajectory. The torque and

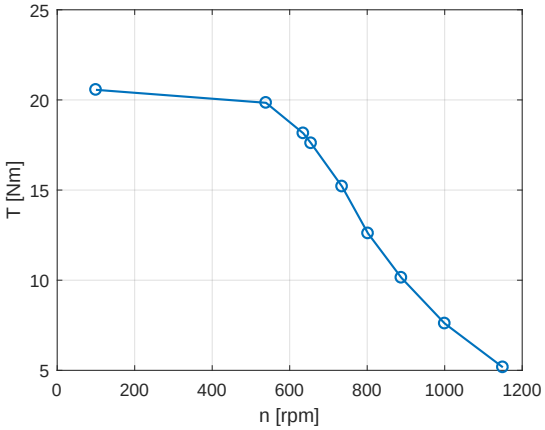

(a) Torque versus speed

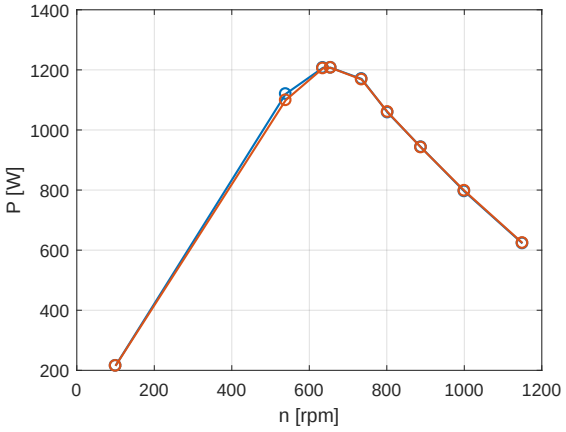

(b) Power versus speed

Figure 8.11
Torque and power versus speed characteristics of the prototype at rated current.

Figure 8.12
Efficiency plot along the power versus speed curve.

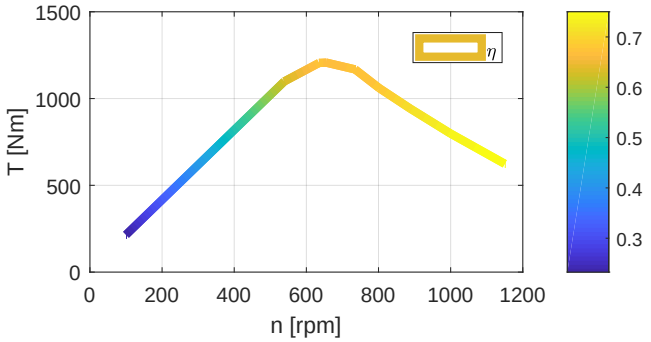

power versus speed characteristics of the prototype at the rated current are reported in Figure 8.11. It is noticeable that the torque is decreasing with the speed, despite the fact that the motor is working in MTPA operation. This may be due to the friction and ventilation losses. The corner speed is just above 500 rpm. At this point the machine has to be flux-weakened. The peak power is reached at about 650 rpm, and after that point the power rapidly decreases.

The rated output power of the prototype is about 1.1 kW, and considering the scaling factor for the stack length (4.5) and the base speed ratio (4), the actual motor power should result 18 times higher.

Using a wattmeter during this test, it is possible also to compute the efficiency of the motor. The plot is reported as a colored contour in Figure 8.12. Since smaller motors are intrinsically less efficient than large ones, the efficiency values of the prototype are not a good performance index for the actual machine. However, the variation of this quantity in that plane is still a good metric to check the progress of the measurement and a proper motor operation.

8.4 DISCUSSION

In this chapter a multi-objective optimization has been done to design a synchronous reluctance motor within a defined size. Due to time constraints, the automatic optimization represents the best tool to reach a sound design in the shortest time. The chosen design was able to reach all the requirements, in terms of torque, power and efficiency. The torque ripple was the most critical aspect, though. In fact, the prototyped scaled down motor displayed higher harmonic content than the expected simulation result.

Anyway, the motor performance in MTPA and FW operations were properly satisfied, so the design was a suitable candidate for the application under investigation. In particular, no new stator lamination was required, minimizing the fixed manufacturing cost.

9

HIGH-SPEED SYNCHRONOUS RELUCTANCE MACHINES

This chapter describes a guideline to properly design synchronous reluctance machines suitable for high-speed applications. The main target is to give some guidelines for an accurate design of the rotor geometry to obtain a robust mechanical structure, a quite high torque density and a low torque ripple. A particular care is paid to the rotor rib thicknesses, designed to guarantee the structural integrity of the rotor (Barcaro et al., 2014b) and to minimize the q-axis magnetic flux. In fact, the thickness of these iron ribs has to be wide enough to mechanically sustain the rotor and it increases as the design speed increases (Babetto et al., 2017). This is a significant drawback, since a quite large part of the magnetic flux flows through them, reducing the available saliency and, consequently, the machine torque.

9.1 DESIGN METHODOLOGY FOR HIGH-SPEED SYNCHRONOUS RELUCTANCE MACHINES

In this section, an analytical model is first adopted to derive a preliminary geometry (Bianchi et al., 2009b). The stator geometry is fixed and the focus is on the rotor structure. The effect of iron ribs and their influence on the increase of q-axis flux is taken into account. The flux-barrier-end angles are selected so as to minimize the torque oscillation (Bacco et al., 2017; Bianchi et al., 2009b; Jahns et al., 1996; Vagati et al., 1998). Then, the purpose is to maximize the average electromagnetic torque, according to a fixed speed. This is done through adjusting the quantity of air present in the rotor.

A FE analysis is carried out to validate the results obtained by means of the analytical approach. Then, an optimization is employed to op-

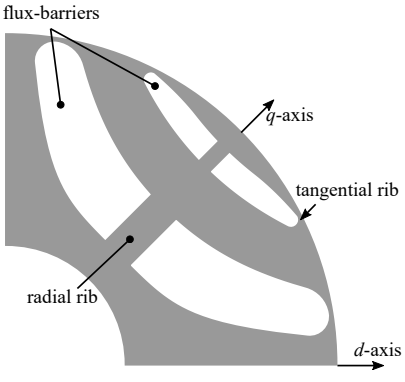

(a) Example of one rotor pole with two flux-barriers per pole.

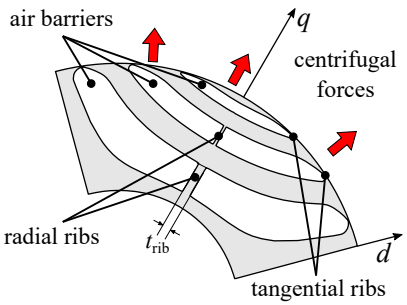

(b) Sketch of one pole with three flux-barriers. Distinction between the tangential and the radial ribs is made.

Figure 9.1
Sketches of synchronous reluctance machines for high-speed applications

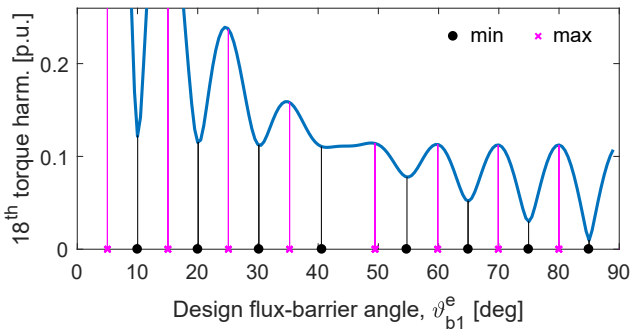

(a) One flux-barrier machine. The vertical lines represent the positions of the torque ripple minima and maxima found by means of the model presented in Chapter 6.

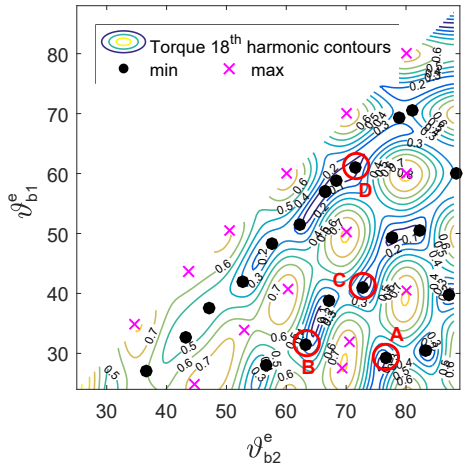

(b) Analytical torque maps of the first slot harmonic in a two flux-barriers machine. The black dots show the minima found through model presented in Chapter 6.

Figure 9.3
Analytical torque maps of the first slot harmonic as a function of the design flux-barrier angles for a 36-slot 4-pole machine. The continuous lines are computed through the complex analytical model presented in Chapter 5, while the lines and the markers are obtained with the model described in Chapter 6.

timize the position of the flux-barrier in the rotor, with the purpose of reducing the q-axis flux through the iron bridges (which causes the decrease of rotor anisotropy and average torque), and the torque ripple. The Pareto front is reported highlighting the potentials and the drawback of the optimal solutions. Finally, a thorough analysis of one optimal solution has been performed. It includes a full electromagnetic analysis to determine also accurate iron losses and a mechanical analysis under centrifugal stress to determine local stresses on the rotor and to verify the integrity of the structure.

9.1.1 *Analytical approach*

9.1.1.1 *Choice of flux-barrier angles*

Thanks to the model presented in Chapter 6, it is possible to easily predict the combinations of flux-barrier angles which lead to the lower torque ripples.

ONE FLUX-BARRIER ROTOR Figure 9.3(a) reports the torque behavior due to the first two slot harmonics as a function of the electrical flux-barrier angle, ϑ^e_b. According to a 4-pole machine ($2p = 4$), they are the 17^{th} and 19^{th} for the machine with $Q = 36$. These waveforms are obtained through the complete model of the SyR machine, shown in Chapter 5. This figure shows how much the choice of the flux-barrier angle affects the torque ripple resulting from the harmonic under study. In addition, the vertical lines identify the flux-barrier angles found by the simple formulation derived in Chapter 6. It can be noted that the prediction of the torque minima and maxima perfectly corresponds to

the minima computed by means of the complete analytical magnetic model of the machine. As an example, a proper choice of the flux-barrier angle would be about 75° and not 70°.

TWO FLUX-BARRIERS ROTOR Figure 9.3(b) reports the torque behaviors due to the first two slot harmonics in the plane of the two electrical flux-barrier angles ϑ^{e}_{b1} and ϑ^{e}_{b2}. These harmonics are of the same order of the previous ones. The two-dimensional maps are again obtained through a complete model of the two flux-barrier SyR machine, shown in Chapter 5 Then the points marked by black dots and magenta crosses are found by means of the model proposed in (6). They identify the flux-barrier angles which correspond to the torque ripple minima and maxima, respectively. Once again this model is able to predict these points with satisfactory precision, despite additional assumptions.

9.1.1.2 *Flux-barriers and flux-carriers design*

While the choice of the flux-barrier-ends mainly affects the torque ripple, the selection of the magnetic insulation quantity along the q-axis mainly affect the average torque capability of the machine. The thickness of the flux-barriers is an important design parameter in order to achieve a good rotor saliency and, therefore, high performance. However, their thicknesses are limited by the level of saturation desired in the rotor iron. This is also the common guideline to choose a proper insulation ratio, k_{air}. In fact it is often desirable to let the rotor saturate more than the stator teeth, in order to reduce teeth iron losses. The coefficient k_{air} can be computed through the following equation:

$$k_{air} = 1 - \frac{B_g}{B_r} \cdot \frac{D_r}{p(D_r - D_{sh})} \tag{9.1}$$

where B_g is the peak air-gap flux density, B_r is the desired rotor flux density, D_r the rotor diameter, D_{sh} the shaft diameter and p the number of pole pairs. It represents the sum of the flux-barrier thicknesses along the q-axis, that means

$$k_{air} = \frac{l_{air}}{l_{tot}} \tag{9.2}$$

where $l_{air} = t_{b1} + t_{b2}$ is the amount of magnetic insulation along the q-axis, t_{b1}, t_{b2} the thickness of the first and second flux-barriers, respectively, and l_{tot} is the available space given by $(D_r - D_{sh})/2$. Its value typically ranges between 0.4 and 0.6.

FLUX-BARRIER THICKNESSES Once the total amount of air is chosen through the coefficient k_{air}, the individual thickness of the flux-barriers is chosen according to the stator MMF in front of each flux-barrier: the higher the MMF step between two flux-barriers, the thicker the flux-barrier.

Figure 9.4(a) shows a sketch of a two flux-barrier rotor with a sinusoidal q-axis magnetization. $\mathcal{U}_s(\vartheta_r)$ and $U_r(\vartheta_r)$ represent the stator and

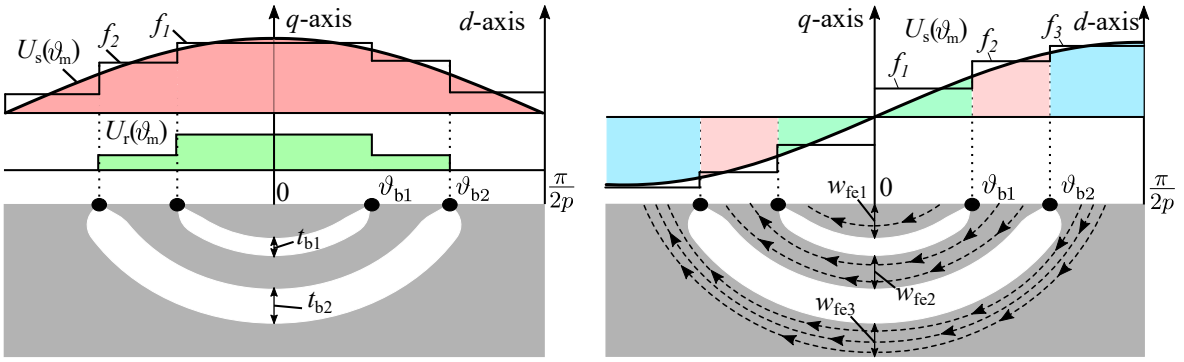

(a) q-axis magnetization. The flux-barrier thicknesses are also indicated.

(b) d-axis magnetization. The the flux-carrier widths are also indicated.

Figure 9.4
Sketches of a two flux-barriers per pole rotor with different stator magnetization.

the rotor scalar magnetic potentials, respectively. The mean value of $\mathcal{U}_s(\vartheta_r)$ computed between the flux-barrier end angle $\vartheta^e_{b(j-1)}$ and ϑ^e_{bj} is f_j. For a rotor with two flux-barriers they are:

$$\begin{aligned} f_1 &= \frac{\sin \vartheta^e_{b1}}{\vartheta^e_{b1}} & \Delta f_1 &= f_1 - f_2 \\ f_2 &= \frac{\sin \vartheta^e_{b2} - \sin \vartheta^e_{b1}}{\vartheta^e_{b2} - \vartheta^e_{b1}} & \Delta f_2 &= f_2 \end{aligned} \tag{9.3}$$

A common design rule adopted for the flux-barrier thickness ratio is (Vagati et al., 1998)

$$\frac{t_{b2}}{t_{b1}} = \frac{\Delta f_2}{\Delta f_1}\sqrt{\frac{\vartheta^e_{b2}}{\vartheta^e_{b1}}} \tag{9.4}$$

and then (Wang et al., 2017)

$$t_{b1} = \frac{k_{air} l_{tot}}{1 + \frac{\Delta f_2}{\Delta f_1}\sqrt{\frac{\vartheta^e_{b2}}{\vartheta^e_{b1}}}} \tag{9.5}$$

so that t_{b2} can be easily obtained through (9.4). The thickness of each flux-barrier is computed with respect to the q-axis as shown in Figure 9.4(a).

FLUX-CARRIER WIDTHS The flux-carrier widths are designed assigning a width proportional to the MMF at the air-gap. Figure 9.4(b) shows a sketch of a two flux-barrier rotor with a sinusoidal d-axis magnetization. The meaning of f_j is the same of the previous subsection and the flux-carrier widths are computed with respect the q-axis.

The flux-carrier width ratio is defined as

$$\frac{w_{cj}}{w_{ck}} = \frac{f_j}{f_k}, \quad j,k = 1,2,3 \tag{9.6}$$

where

$$f_1 = \frac{1 - \cos \vartheta^{\mathrm{e}}_{\mathrm{b}1}}{\vartheta^{\mathrm{e}}_{\mathrm{b}1}}$$
$$f_2 = \frac{\cos \vartheta^{\mathrm{e}}_{\mathrm{b}1} - \cos \vartheta^{\mathrm{e}}_{\mathrm{b}2}}{\vartheta^{\mathrm{e}}_{\mathrm{b}2} - \vartheta^{\mathrm{e}}_{\mathrm{b}1}} \tag{9.7}$$
$$f_3 = \frac{\cos \vartheta^{\mathrm{e}}_{\mathrm{b}2}}{\frac{\pi}{2} - \vartheta^{\mathrm{e}}_{\mathrm{b}2}}$$

Then

$$w_{\mathrm{c}1} = \frac{(1 - k_{\mathrm{air}}) l_{\mathrm{tot}}}{1 + \frac{f_1}{f_2} + \frac{f_1}{f_3}} \tag{9.8}$$

and the remaining flux-carrier widths can be determined from (9.6).

9.1.1.3 *Iron ribs computation*

The thickness of the tangential iron bridges near the air-gap are set equal to the minimum manufacturing length or to the lamination width. Their effect on the structural integrity is negligible.

The radial iron ribs, in the middle of the flux-barriers, are properly designed at the rated speed of the motor with the aim of containing the centrifugal stress due to the rotation. A simple analytical method to design the radial rib of each flux-barrier has been described in (Babetto et al., 2017). Once the flux-barrier-end angles are known it is possible to compute the thickness of the j^{th} flux-barrier as follows:

$$t_{\mathrm{rib},j} = \frac{\nu_\sigma (1 - k_{\mathrm{air}}) \gamma_{\mathrm{Lam}} \omega_{\mathrm{m}}^2 D_{\mathrm{r}}^3 \left(2\vartheta_{\mathrm{b}j} - \sin 2\vartheta_{\mathrm{b}j}\right) \cos \vartheta_{\mathrm{b}j}}{8\sigma_{\mathrm{r}}} \tag{9.9}$$

where ν_σ is a safety factor, γ_{Lam} is the lamination mass density, D_{r} is the rotor diameter, ω_{m} is the mechanical rotor speed and σ_{r} is the tensile strength of the lamination. ω_{m} is often selected slightly higher than the nominal one and ν_σ is set in the range between 2 and 3 (Barcaro et al., 2014b).

9.1.2 *Optimization approach*

For synchronous reluctance machines, an optimization of the rotor is almost always necessary to obtain a good design. This statement is reinforced when dealing with high-speed synchronous reluctance machines. In fact the presence of iron ribs along the q-axis greatly affects the performance of the machine.

One of the most used optimization algorithms in electromagnetic designs is DE.[1] Typically it guarantees good performance and convergence in a reasonable amount of time.

Typical objectives for high-speed machines include the maximization of average torque (or power), of the saliency, of the power factor, the

1 see Chapter 3

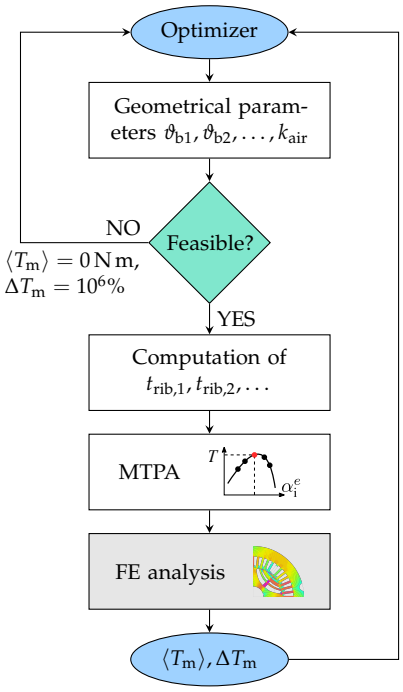

Figure 9.5
Flowchart of the objectives evaluation done by the optimizer.

minimization of the torque ripple, of the losses or of the cost. The solutions found should also exhibit a proper robustness against slight variations of the design parameters. It is evident that the optimization of such machines is multi-objective from the start. Therefore there will not be a single optimum, but many optimal solutions which are called Pareto solutions. In fact they have at least one of their objectives which is the best among all the solutions.

Figure 9.5 shows the flowchart of the evaluation procedure performed for each individual. The geometrical feasibility is evaluated considering the optimizer input parameters. The unfeasible individuals are discarded setting zero average torque and a high torque ripple. For the feasible individuals the algorithm computes the radial rib thicknesses, finds the MTPA current angle and evaluates the average torque, its oscillation and the motor losses in a sixth of electrical period.

9.1.3 *Sensitivity analysis*

To estimate the robustness of good candidates (high average torque and low torque ripple), a sensitivity analysis on the results has been carried out. The dimensions of the parameter space is equal to the number of parameters, four in the considered optimization. Furthermore all the parameters are normalized within the interval 0 and 1.

It is useful to consider a 3-dimensional space first. In the case study, the parameters can be the flux-barrier end angles as shown qualitatively in Figure 9.6. Each dot in the space corresponds to an individual with an associated average torque and a torque ripple. For example, the point j in Figure 9.6 is characterized by the objectives (T_{mj}, ΔT_{mj}).

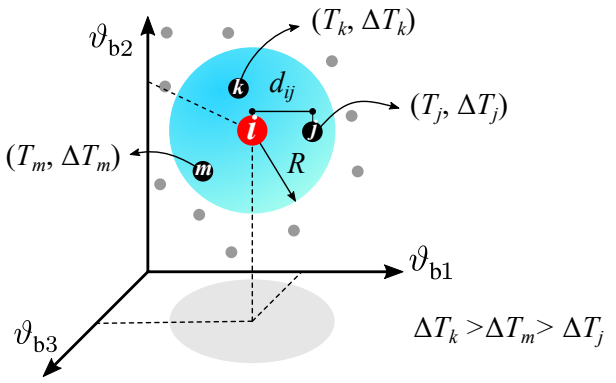

Figure 9.6
Space of parameters. Meaning of the hypersphere and distance d_{ij} between the points i and j. T_{mk} and ΔT_{mk} are the average torque and the torque ripple of the k^{th} individual.

The sensitivity analysis is carried out for each point in the parameter space. The distance between two points is computed with the euclidean norm. It is verified that $d_{ij} = d_{ji}$ since the distance is a symmetric property. The matrix of the distances, $\boldsymbol{D}$, is symmetric and its order is the number of the individuals N. The element in the i^{th} row and in the j^{th} column is the distance d_{ij} defined above. Obviously the matrix has all the diagonal elements equal to zero.

$$\boldsymbol{D} = \begin{bmatrix} 0 & d_{12} & \cdots & d_{1N} \\ & \ddots & & \\ d_{i1} & \cdots & 0 & d_{iN} \\ d_{N1} & \cdots & \cdots & 0 \end{bmatrix} \tag{9.10}$$

To the purpose of analyzing a restricted volume around each single point, it is useful to define a radius R of an hypersphere. The sensitivity can be computed locally in each point. In the normalized research space, the maximum normalized radius of the hypersphere, that includes all the individuals from each one of them, is equal to $\sqrt{N_{par}}$ where N_{par} is the number of parameters.

Referring to Figure 9.6, the hypersphere around the individual i includes only the points j, k and m. The other ones are not considered. This means that a restricted number of elements of the i^{th} row of the matrix $\boldsymbol{D}$ are useful. Among these remaining individuals the maximum and the minimum torque ripple are researched. The figure reports that the maximum and the minimum torque ripple correspond to the individual k and j respectively.

The sensitivity of the i^{th} individual is finally given by:

$$s_i = \frac{\max(\Delta T_m)\big|_i - \min(\Delta T_m)\big|_i}{\Delta T_{mi}} \tag{9.11}$$

where the subscripts at the numerator indicates the maximum and the minimum torque ripple among the individuals inside the hypersphere centered on the individual i. The result of (9.11) is obviously a function of the hypersphere radius.

Table 9.1
Main motor data for the first high-speed (HS) application.

MOTOR OUTPUT			
Rated voltage (RMS)	V_N	400	V
Number of poles	$2p$	4	1
Mechanical speed	n	30 000	rpm
GEOMETRICAL DATA			
Outer diameter	D_e	152	mm
Inner diameter	D_s	90	mm
Stack length	L_{stk}	100	mm
Number of poles	$2p$	4	1
Number of slots	Q	36	1
Slot height	h_s	16.3	mm
Tooth width	w_t	4.14	mm
Mechanical Air-gap	g	0.7	mm
WINDING			
Conductors in slot	n_c	6	1
Number of parallel paths	n_{pp}	2	1
Coil pitch	y_q	8	1
MATERIALS			
Iron Lamination			NO20

9.2 FIRST APPLICATION EXAMPLE

An example of a high-speed synchronous reluctance motor design is presented hereafter. Two different design methods are used: a Semi-Analytical Design Approach (SADA) and Finite-Element-based Approach (FEO). In the former, the analytical method is used to select the proper flux-barrier angles combination and to compute the radial rib thicknesses while the FE analysis is used to determine the best insulation ratio and the motor outputs (i.e. average torque, inductances) (Meeker, 2015). The latter needs an optimization algorithm and FE simulations only. The SADA procedure is faster since it does not require an optimization. However, the iron saturation is not considered in the flux-barrier angle choice. On the contrary, the total FE procedure requires a higher computational time, but it is more accurate since it takes into account the iron saturation.

The design only deals with the rotor geometry. The stator, the winding and the materials are given and reported in Table 9.1. Through (9.9) it is possible to estimate if a design for such speed is feasible. In particular, an estimation of the required maximum rib thickness can be made based on the desired design speed. It is sufficient to select ϑ_b equal to the maximum allowable one, which is $\frac{\pi}{2p}$. Then, the rib

Rotor	ϑ^{e}_{b1} [°]	ϑ^{e}_{b2} [°]	ϑ_{b1} [°]	ϑ_{b2} [°]
A	29.25	76.63	14.63	38.32
B	31.49	63.25	15.75	31.63
C	40.96	72.73	20.48	36.37
D	61.02	71.61	30.51	35.81

Table 9.2
Flux-barrier-end angles combinations that exhibit the lowest torque ripple found through Figure 9.3(b).

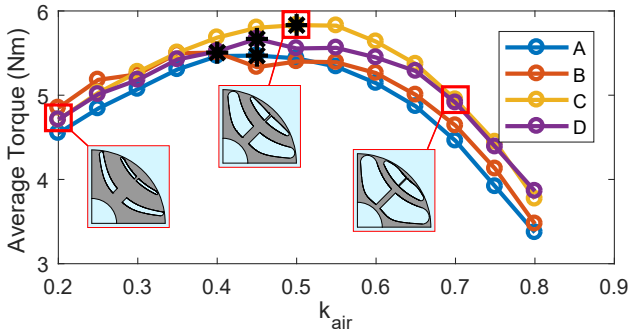

Figure 9.7
Average torque versus magnetic insulation ratio for different flux-barrier angles.

thickness will be a fraction of the maximum space available, which means $t_{\text{rib},} = c\, D_r \sin\vartheta_b$, where c measures the fraction. So

$$c = \frac{\nu_\sigma\,(1-k_{air})\gamma_{Lam}\omega_m^2 D_r^2\left(\frac{\pi}{p}-\sin\frac{\pi}{p}\right)}{8\sigma_r\,\tan\frac{\pi}{2p}} \tag{9.12}$$

In the present case, considering $k_{air} = 0.5$, $\sigma_r = 500\,\text{MPa}$, $\nu_\sigma = 2.5$, $\gamma_{Lam} = 7650\,\text{kg/m}^3$, it results $c = 0.1$.

9.2.1 *Analytical design*

In Table 9.2 some flux-barrier angle combinations, which exhibit the lowest torque ripple, are reported. They are selected from the map in Figure 9.3(b).

The magnetic insulation ratio, k_{air}, can be selected trough (9.1), which gives a value around 0.55 for this machine. However, in this case the optimal k_{air} has been selected by means of a parametric FE analysis for each considered solution. The results are shown in Figure 9.7. The figure also shows the rotor geometry variations with the insulation ratio. It is evident that k_{air} strongly affects the flux-barrier shape and the radial rib thicknesses. In fact, as the coefficient increases, the amount of rotor iron is lower and so, the radial ribs become thinner.

It can be noted that the maximum average torque is achieved with a k_{air} between 0.4 and 0.55. The motor C exhibits the highest average torque among the selected ones. The main motor outputs are reported in Table 9.3(a).

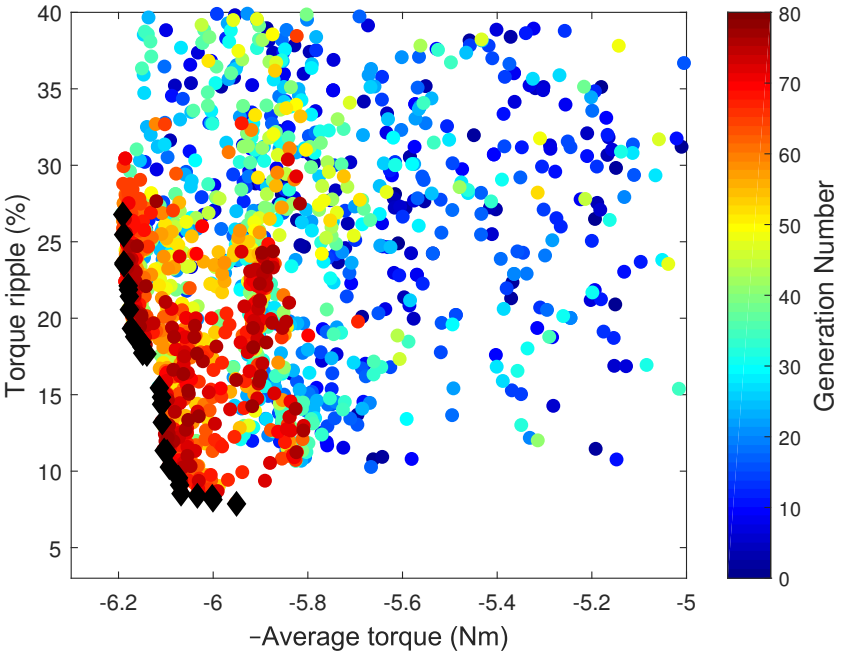

Figure 9.8
Simulated individuals in the objectives plane and Pareto front (black diamonds) at 30 000 rpm.

9.2.2 *Finite Element optimization*

The FE optimization is carried out with an RMS current density equal to 5.6 A/mm². The selection of the current density is based on an a-priori thermal analysis of the machine.

In this case, the chosen objectives are the average torque, $\langle T_\mathrm{m} \rangle$, and the torque ripple, ΔT_m. The geometrical parameters are the two flux-barrier angles, $\vartheta_{\mathrm{b}1}$, $\vartheta_{\mathrm{b}2}$, and the magnetic insulation ratio, k_air, while the other geometrical quantities are derived from these parameters (Wang et al., 2017).

The optimization has been carried out with a population size of 25 individuals and 80 generations and it took about two days. The final objectives plane is shown in Figure 9.8. The black diamonds represent the Pareto front. For high-speed applications it is mandatory to limit the torque oscillation that causes dangerous mechanical vibrations and acoustic noise. For this reason, the individual with the lowest torque ripple has been selected. The average torque is about 6 N m while the torque ripple is about 9% with respect to the average torque. The relative flux-barrier angles are $\vartheta_{\mathrm{b}1} = 20.70°$ and $\vartheta_{\mathrm{b}2} = 31.81°$ while the insulation ratio is $k_\mathrm{air} = 0.429$. With respect to the flux-barrier-end angles analytically predicted, the first one is practically the same while the second one is 9.12° (electrical) smaller. The different rotor configurations justifies the mismatch of the torque ripple obtained with the two methods.

Table 9.3
Main electromagnetic results of the motors analyzed.

(a) Results obtained through FEA of the machines designed with SADA and FEO.

Design Method	α_i^e [°]	$\langle T_m \rangle$ [N m]	ΔT_m [%]	L_d [mH]	L_q [mH]	ξ 1	$\cos\varphi$ 1
SADA	52.5	5.83	17.6	0.896	0.344	2.61	0.43
FEO	47.5	5.91	9.16	0.910	0.367	2.48	0.40

(b) Motor losses in different parts.

Part	Losses [W]		
	Fund. Harm.	Space Harm.	Total
Copper	194	0	194
Stator iron	479	100	579
Rotor iron	0	159	159
Total	673	259	932

9.2.3 *Electromagnetic Analysis*

After the selection of the most promising solution, an in-depth electromagnetic analysis is required to precisely evaluate the machine performance. In particular the average torque and the torque ripple found through the optimization are confirmed and better estimated, as reported in Figure 9.10(a). The numerical results are also reported in Table 9.3(a).

The flux density plot of the FE optimal motor is shown in Figure 9.9(a). It can be noted that the iron saturation within the tangential ribs covers a larger area and the iron saturation of channels is not negligible. These aspects highly affect the analytical model hypothesis and explains the different torque ripple predicted by the approaches.

The high-speed of rotation involves high frequency for the current supply. Even though thin lamination sheets have been considered, iron losses may play an important role in the overall machine performance. So, to accurately estimate the losses, the flux density for every mesh element has been recorded in both x and y directions for a complete electrical rotation. This allows to split the flux density fluctuations in Fourier series and, thus, to find the losses for all the harmonics involved. The harmonic losses are caused by the staircase MMF waveform and by the effect of stator slots. Current distortion may introduce additional losses, but it is not considered in this study.

The loss density map is reported Figure 9.9(b). It can be noted that the maximum loss density appears near the rotor periphery and near sharp corners. However the volumes involved are rather small. On the other hand, stator teeth and back-iron see lower loss densities but they are diffused, filling almost the entire volume. In fact, the stator iron is subjected also to the fundamental harmonic of the flux density, which is obviously the highest harmonic.

The comparison among the losses is reported in Table 9.3(b). The majority of losses is due to the iron losses in the stator caused by the fundamental of the flux density. Joule losses in the stator winding are the second main cause. Then it can also be seen that the additional

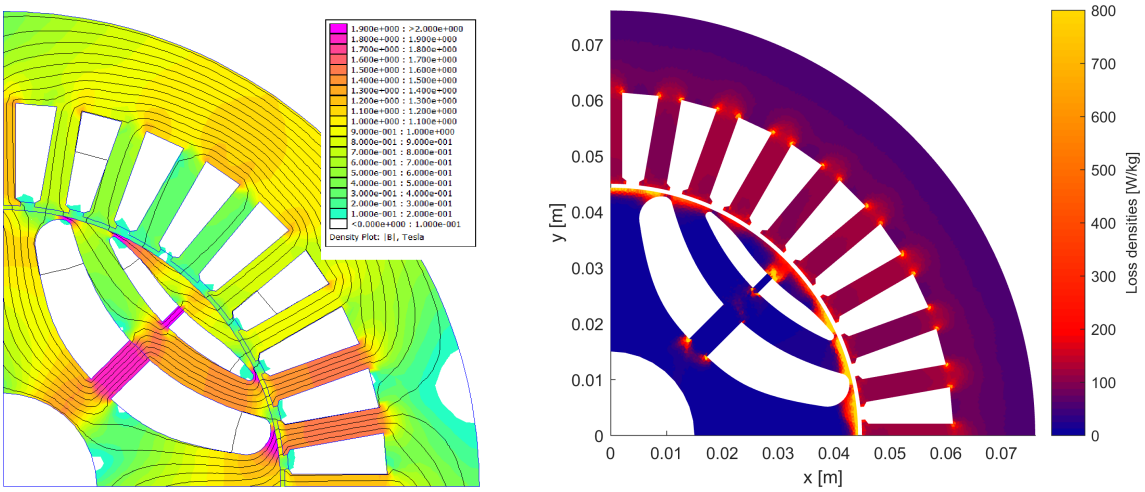

(a) Flux density plot.

(b) Loss density map at the MTPA operating point.

Figure 9.9
Plots of the rotor designed with the FEO approach.

losses introduced by the harmonics are not negligible at this speed, as they represent almost 30% of the total electromagnetic losses.

9.2.4 *Structural Analysis*

Lastly, a structural FE analysis has to be performed to verify whether the radial iron ribs are able to sustain the centrifugal load of the rotor iron paths (Dular et al., n.d.; Geuzaine et al., 1998). In the present study, only the rotor design with the FE optimizations is considered since it achieves better performance. Furthermore, the two rotor geometry are similar from the mechanical point of view.

The rotor sharp corners have been smoothed out in order to avoid dangerous stress concentrations. The von Mises stress and the displacement plots are shown in Figure 9.10(b). The ultimate tensile strength of the selected material is 500 MPa, while the chosen safety factor is 2.5 (Barcaro et al., 2014b). The scale of the von Mises stress has been set to the desired stress value, which is 200 MPa for this study. It can be observed that the target stress value is never reached within the radial iron ribs. Stress concentration is present near corners, but it will lead only to some yielding.

9.2.5 *Discussion*

The aim of this section was to propose a design procedure for high-speed synchronous reluctance motors. Only the rotor geometry has been properly designed while the stator and the winding have been kept fixed. The goals of the rotor design were to achieve the maximum torque density with the lowest torque ripple and to ensure the structural integrity against the high centrifugal force. To do that, the

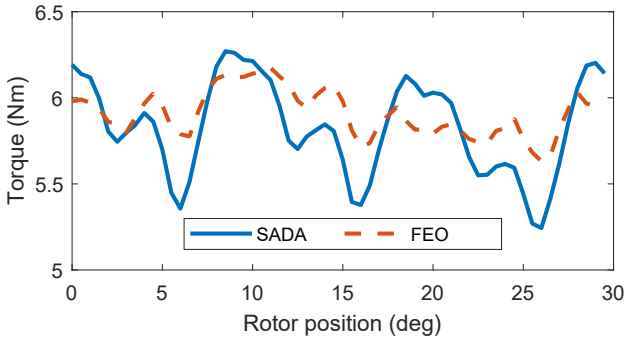

(a) Finite element torque versus rotor position with different flux-barrier angles.

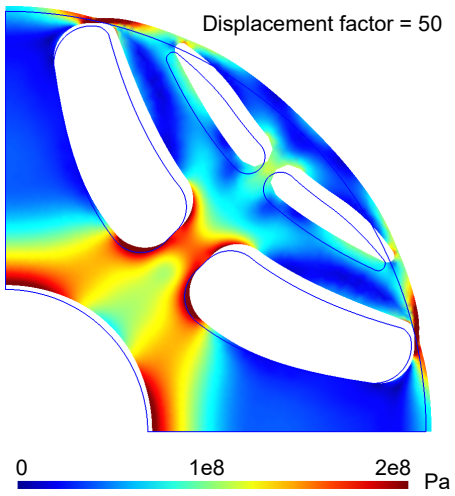

(b) Plot of von Mises stress of the optimized rotor for 30 krpm.

Figure 9.10
Plots resulting from the electromagnetic and mechanical FE analyses.

flux-barrier geometries (i.e. angles, thicknesses) and the radial ribs have been designed. Two design approaches have been proposed: one is semi-analytical while the other is based on FE optimization. The former is faster and finds suitable flux-barrier angles by means of a simple analytical model. The motor performance is then precisely evaluated through FE analysis. The latter is more accurate since it considers the iron saturation but requires more time because of the optimization algorithm. The comparison between the two methods revealed that the non-localized saturation of the tangential ribs and the radial rib thicknesses strongly affect the torque ripple estimation of the analytical model. For this reason, the torque oscillation obtained by means of the FE optimization is about 52% of that resulting from the semi-analytical approach.

The losses computation has shown that rotor losses have to be taken into account for an accurate efficiency prediction, especially at such high speeds. In fact, the rotor losses represent about 30% of the total. The structural analysis confirmed the validity of the radial ribs design method giving a suitable stress distribution within the rotor.

In conclusion, the semi-analytical method is a quick procedure that allows to obtain a good initial design of a synchronous reluctance rotor. However, to get more sound designs, a multi-objective optimization algorithm should be employed.

9.3 SECOND APPLICATION EXAMPLE

The aim of this section is to investigate the potential of high-speed synchronous reluctance machines. An optimization is carried out so as to maximize the machine performance (high power, proper power factor, low vibration) at a given speed. The machine size is fixed and

Table 9.4
Main data of the machine under optimization for the second HS application

Motor part	Symbol	Value
Outer diameter	D_e	240 mm
Inner diameter	D_s	140 mm
Stack length	L_{stk}	140 mm
Pole number	$2p$	4
Slot number	Q	48
Slot height	h_s	25 mm
Tooth width	w_t	5 mm
Air-gap	g	1 mm
Iron lamination		NO20

the focus is on the rotor geometry, with the purpose of maximizing the electromagnetic torque, according to the necessary thickness of the ribs. It is shown that, even if the ribs are thick, it is possible to reach a proper torque density. However, the optimal solutions are quite sensitive to the geometrical variations, so that a particular care is required in the manufacturing of the machine. Finally, the power limit of the synchronous reluctance motor with barrier rotor is found.

A sketch of a 4-pole synchronous reluctance rotor with three flux-barriers per pole is shown in Figure 9.2(b). It also distinguishes the radial iron ribs (in the middle of the barrier) from the tangential iron bridge (near the air-gap). The radial bold arrows represent qualitatively the centrifugal force that acts on the rotor lamination.

To the purpose of investigating the potentials of high-speed synchronous reluctance machines, some optimizations are carried out. The objective is to maximize the machine performance, expressed as electric power, power factor, and low vibration at a given high-speed, which is set to be equal to 20 000 rpm.

The dimensions of the stator are fixed and reported in Table 9.4. The optimizations are focused on the rotor geometry. The position of the flux-barriers is quite important to reduce the centrifugal forces, while the position of the ends of the flux-barriers is important to reduce the torque oscillation (Jahns et al., 1996; Sanada et al., 2004; Bianchi et al., 2009b). The purpose is to maximize the electromagnetic torque, according to the necessary thickness of the ribs.

9.3.1 *Choice of the optimization parameters and iron ribs computation*

9.3.1.1 *Optimization parameters and objectives*

The selected rotor parameters are the flux-barrier angles shown in Figure 9.11 and the magnetic insulation ratio k_{air} defined as:

$$k_{air} = \frac{l_{air}}{l_{air} + l_{fe}} \tag{9.13}$$

where $l_{air} = \sum_j t_{bj}$ and $l_{fe} = \sum_i w_{ci}$ are the total central thickness of the flux-barriers and of the iron, respectively. Usually three flux-barriers

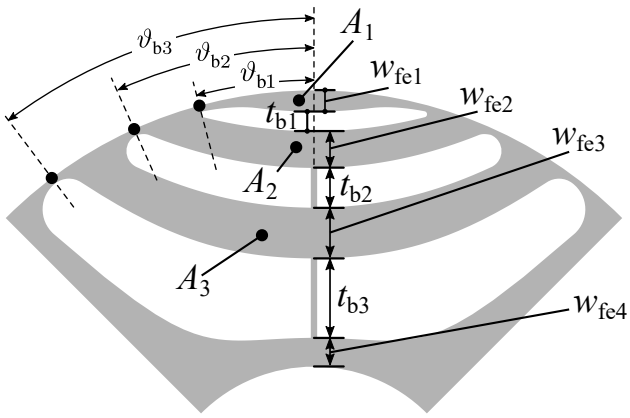

Figure 9.11
Sketch of a one pole REL rotor with three flux-barriers per pole. The flux-carrier widths and the flux-barrier thickness are also marked.

per pole are employed because they lead to a higher and smoother torque. The shape of such flux-barriers derives from the magnetic flux lines which would flow if the rotor were solid (see Chapter 4). As reported in Figure 9.11 the flux-barrier angles are sorted in ascending order from the outer flux-barrier to the inner one. The objectives of the optimizations are the average torque and the torque ripple, computed as

$$\langle T_\mathrm{m} \rangle = \frac{1}{2\pi} \int_0^{2\pi} T_\mathrm{m}(\vartheta_\mathrm{m}) \, \mathrm{d}\vartheta_\mathrm{m} \tag{9.14}$$

and

$$\Delta T_\mathrm{m} = \frac{\max\left[T_\mathrm{m}(\vartheta_\mathrm{m})\right] - \min\left[T_\mathrm{m}(\vartheta_\mathrm{m})\right]}{\langle T_\mathrm{m} \rangle} \tag{9.15}$$

respectively, where $T_\mathrm{m}(\vartheta_\mathrm{m})$ is the torque computed with the Maxwell stress tensor (see Appendix B). The agreement between this torque computation and experimental tests have been proven in numerous works, such as (Bianchi et al., 2009b; Bianchi et al., 2016).

9.3.1.2 *Computations of the radial iron bridges*

At high-speed operation the rotor structure has to sustain high centrifugal stresses that may cause rotor deformations and mechanical issues. In order to improve the rotor integrity, the following two solutions are evaluated:

i. use of radial iron ribs;

ii. addition of a containing sleeve with high tensile strength.

The design of the radial ribs is carried out with the following safety precautions. The ultimate tensile strength of the rotor lamination is set to $\sigma_\mathrm{R} = 500\,\mathrm{MPa}$ while the safety factor is $\nu_\sigma = 2.5$ (Barcaro et al., 2014a). This is a proper choice to guarantee an infinite lifetime. Furthermore the structural contribution of the tangential iron ribs is neglected.

The mass and the center of gravity of each island are directly computed from the actual geometry, and they are referred to as m_i and $R_{\mathrm{G},i}$,

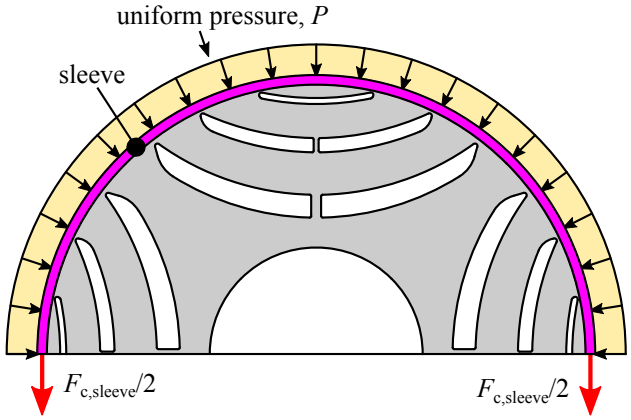

Figure 9.12
Scheme of the computation of the sleeve thickness.

respectively, for the i^{th} island. The j^{th} rib has to sustain the centrifugal load due to the mass M_j given by:

$$M_j = \sum_{i=1}^{j} m_i \qquad R_{G,j} = \frac{\sum_{i=1}^{j} m_i R_{G,i}}{\sum_{i=1}^{j} m_i} \tag{9.16}$$

It follows that, the centrifugal force of the j^{th} mass is:

$$F_j = M_j \, \omega_m^2 R_{G,j} \tag{9.17}$$

where $R_{G,j}$ is the radius of the center of gravity of the j^{th} mass while ω_m is the mechanical angular speed. From (9.17) the rib thickness can be derived as (Babetto et al., 2017):

$$t_{rib,j} = \nu_\sigma \frac{F_j}{\sigma_R L_{stk}} \tag{9.18}$$

9.3.1.3 *Computation of the sleeve thickness*

The sleeve counteracts the centrifugal force through a uniform radial pressure sketched in Figure 9.12. The chosen sleeve material is a carbon fiber composite with an ultimate tensile strength equal to $\sigma_{CF} = 2000\,\text{MPa}$ and safety factor $\nu_{CF} = 2$.

The formulation comes from the membrane theory since the sleeve thickness, t_{sleeve}, is much smaller than the rotor radius. Hence the relationship between the centrifugal force and the radial pressure is the following:

$$F_{c,sleeve} = \int_{-\pi/2}^{\pi/2} P \cos\vartheta \, \frac{D_r L_{stk}}{2} \, d\vartheta = P D_r L_{stk} \tag{9.19}$$

where P is the pressure at the air-gap and ϑ is the angular coordinate. The pressure is assumed to be uniformly distributed along the rotor periphery so as to link the centrifugal force and the sleeve thickness through:

$$t_{sleeve} = \nu_{CF} \frac{F_{c,sleeve}}{2\sigma_{CF} L_{stk}} \tag{9.20}$$

The sleeve allows to reduce the stress on the radial ribs, hence their thickness. However, the air-gap length is kept constant whilst the rotor diameter is decreased to include the sleeve. So the equivalent gap becomes $g_{\mathrm{eq}} = g + t_{\mathrm{sleeve}}$.

Both solutions affects negatively the average torque because the iron ribs increase the q-axis flux while the sleeve increases the effective air-gap. Thus a comprise between the two solutions could exploit better performances and it will be evaluated later on.

9.3.2 *Optimization*

The optimization procedure used in the present section implements a multi-objective DE algorithm.[2]

The analysis optimization is carried out with an electrical loading of about 47 000 A/m, which corresponds to an RMS current density equal to 7.15 A/mm^2.

The chosen objectives have been defined above and they are the average torque, $\langle T_{\mathrm{m}} \rangle$, and the torque ripple, ΔT_{m}. The geometrical parameters are the flux-barrier angles, $\vartheta_{\mathrm{b1}}, \vartheta_{\mathrm{b2}}, \vartheta_{\mathrm{b3}}$, and the magnetic insulation ratio, k_{air}. The remaining geometrical quantities are derived from these four parameters. The choice of such parameters greatly affects the final performance of the machine. The FE-aided design has been validated in previous works (Bianchi et al., 2009b; Bianchi et al., 2016) for lower speeds. The experimental results have confirmed the ones found by means of simulations, in particular for the objectives of interest.

The optimization flowchart, without computation of the sleeve, is shown in Figure 9.5. At first, the input parameters defined above are selected and the feasibility of the rotor geometry is evaluated. If it is not realizable, the individual is discarded setting zero average torque (i.e. $\langle T_{\mathrm{m}} \rangle = 0$) and a high torque ripple (i.e. 10^6%). Otherwise, the algorithm computes the radial rib thicknesses according to (9.17) and the FE motor model is built.

For each individual, the MTPA point at rated current is found varying the current angle α_i^{e}. This requires about four additional simulations. The objectives are thus evaluated using the actual MTPA angle. Finally the optimizer processes the outputs and proceeds with the next individual.

9.3.3 *First optimization*

9.3.3.1 *Results*

The first optimization is performed with 1-mm air-gap and no sleeve, at the speed of 20 000 rpm. The optimization is carried out with 80 generations constituted by 40 individuals. The results of the whole optimization is reported in the objectives plane in Figure 9.13, together

2 see Chapter 3

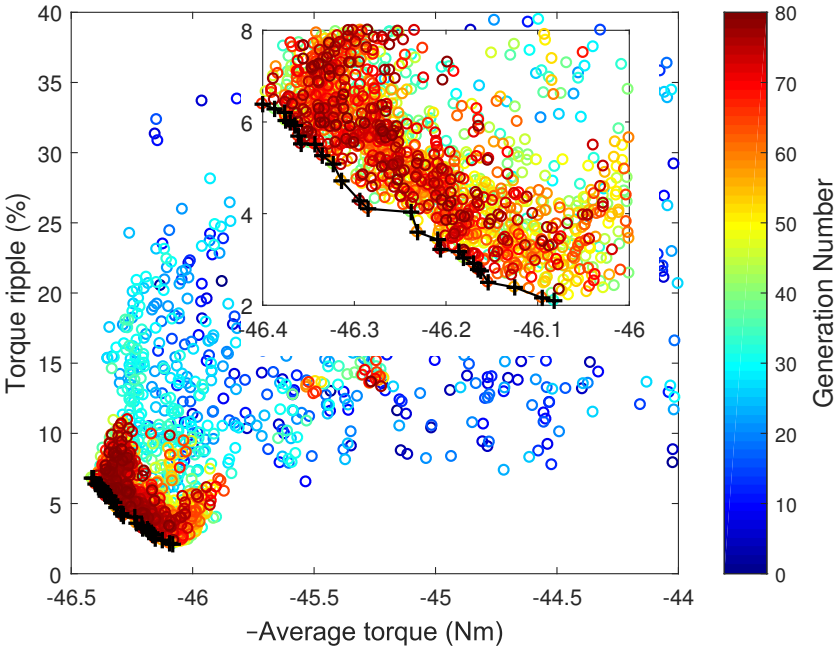

Figure 9.13
Simulated motors in the objectives plane and Pareto front at 20 krpm.

with the Pareto front. On the x-axis there is the opposite of the average torque, $\langle T_\mathrm{m} \rangle$, while on the y-axis the torque ripple, ΔT_m, is reported.

It can be observed that the solutions converges to the optimal ones, located near the bottom left corner of the plot. The resulting Pareto front is steep, since the torque ripple has high variations around similar average torque values. Nonetheless the results show that the rotor with three flux-barriers is able to reach a proper average torque with many combinations of the input parameters.

In order to highlight the dependence of the torque ripple on the flux-barrier angles, Figure 9.14(a) shows the barrier angles sorted by the relative torque ripple. The points lying on the Pareto front are highlighted by black dots. Many of them are near the angles $(\vartheta_{\mathrm{b}1}, \vartheta_{\mathrm{b}2}, \vartheta_{\mathrm{b}3}) = (17°, 29°, 34°)$. The value of the fourth parameter, k_air, is close to 0.42. The Pareto points are all close to the aforementioned angles, slight deviations from these values cause an increase in the torque ripple and/or the leaving of the front.

Moreover, Figure 9.14(a) shows that the flux-barrier angles are not evenly spaced since the third flux-barrier angle is close to the second one. In fact, the third angle is directly related to the average torque so, generally, the greater the third flux-barrier angle the higher the torque. However, the decrease of such an angle permits to reduce the respective island mass and, as a consequence, the rib thickness. It is clear that a compromise solution has been found by the optimizer.

9.3.3.2 *Sensitivity analysis of the results*

Figure 9.14(b) shows the sensitivity of the optimization results for two different radii, $R_1 = 0.1$ and $R_2 = 0.3$. The radius has to be sufficiently small to correctly evaluate the sensitivity of each point, but also suffi-

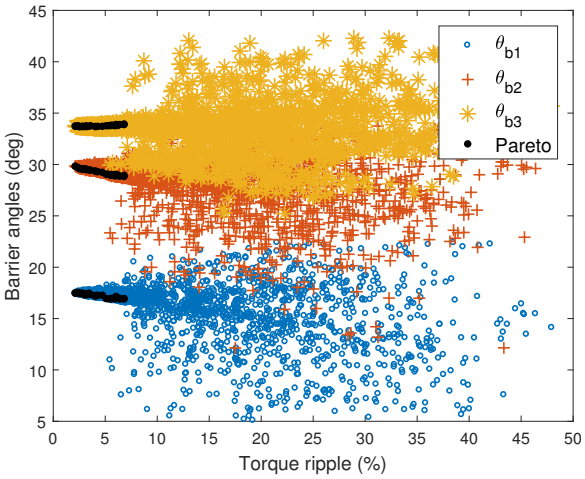

(a) Angles of flux-barrier-ends versus torque ripple at 20 000 rpm.

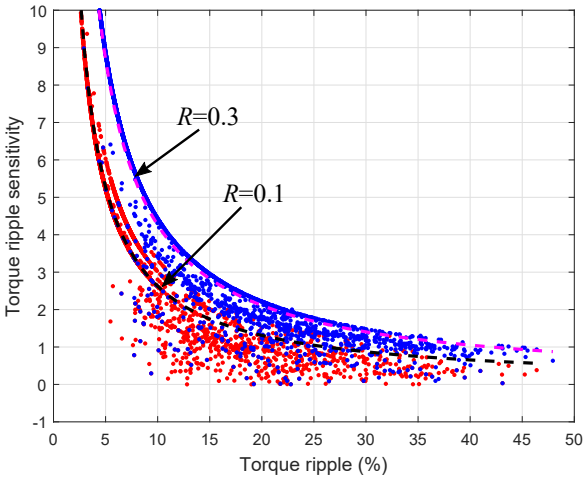

(b) Torque ripple sensitivity versus the torque ripple percentage for different radius at speed 20 000 rpm.

Figure 9.14
Plots resulting from the multi-objective optimization procedure.

ciently large to find other points around each one. Figure 9.14(b) also reports the tendency lines of the sensitivity, which would otherwise be very scattered. These lines clearly point out how the lower torque ripple values are more sensible to geometric variations of the chosen parameters. Additionally the larger the variation—so the larger R—the higher the torque ripple change. This fact highlights the importance of good manufacture of the rotor, which therefore needs small tolerances.

9.3.3.3 *Structural analysis of the optimized rotor*

The structural integrity of one optimal individual has been verified with finite element using GetDP (Dular et al., n.d.; Geuzaine, 2008). The von Mises stress map is shown in Figure 9.15. The full-scale value is set to 200 MPa that represents the acceptable rib stress limit. It can be noted that the average iron rib stress is always lower than the maximum limit according to the preliminary design. Higher stress values are concentrated in the proximity of the edges.

The tangential iron ribs of the first flux-barrier (the outer one) are not stressed while the other ones presents values higher than 200 MPa. This is due to the local deformation of these ribs, which do not participate in counteracting the centrifugal force, though.

The maximum displacement is about 83 µm, and it has been observed in the third island, while close to the air-gap the value is about 70 µm. This results in a 7% variation of the air-gap thickness, which is quite negligible.

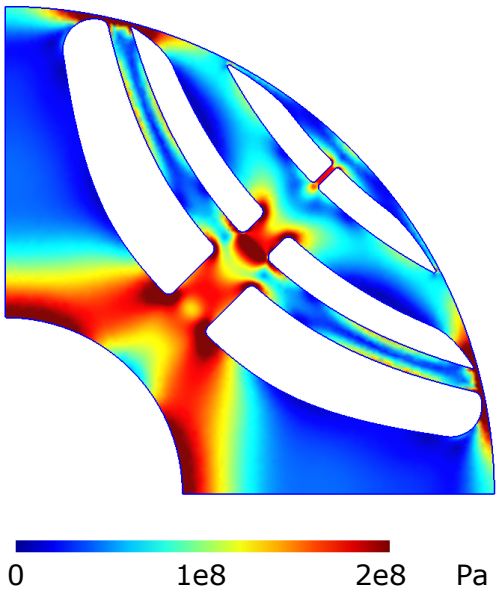

Figure 9.15
Map of the von Mises stress of the optimized rotor for 20 000 rpm.

Table 9.5
Average torque for different thicknesses of the sleeve at 20 krpm.

t_{sleeve}	[mm]	0	0.25	0.5
$\langle T_{\text{m}} \rangle$	[N m]	46.3	43.9	42.1

9.3.3.4 *Optimizations with sleeve*

The same optimization has been carried out with the following sleeve thicknesses: 0.25 mm and 0.5 mm. Hence the effective gaps are 1.25 mm and 1.5 mm, respectively.

The corresponding sleeve force is obtained through (9.20). The force that the j^{th} radial rib has to sustain is decreased by $F_{\text{c,sleeve}}$. If such a difference is negative, the thickness of the j^{th} rib is set equal to the lamination width. Finally, the radial iron ribs are computed from (9.18), neglecting the tangential rib contribution as well.

The results, reported in Table 9.5, show that the adoption of the sleeve greatly reduces the available torque. This aspect has been verified with the optimistic assumption of no sleeve precompression. In fact, the rotor iron ribs should be designed according to the precompression stress at zero speed, otherwise lateral deflection of radial ribs might occur. This requires thicker radial ribs, decreasing the machine anisotropy hence the average torque. Therefore, a rotor with a precompressed sleeve would have an worst reduced performance.

9.3.3.5 *Salient pole comparison*

The performance of a synchronous salient-pole rotor with the same stator has also been investigated. This structure allows to avoid the mechanical constraints of the flux-barrier geometry. The pole shoe spans 50% of the pole pitch. The average torque results about 42 N m with a torque ripple higher than 78% so that a rotor skewing is mandatory.

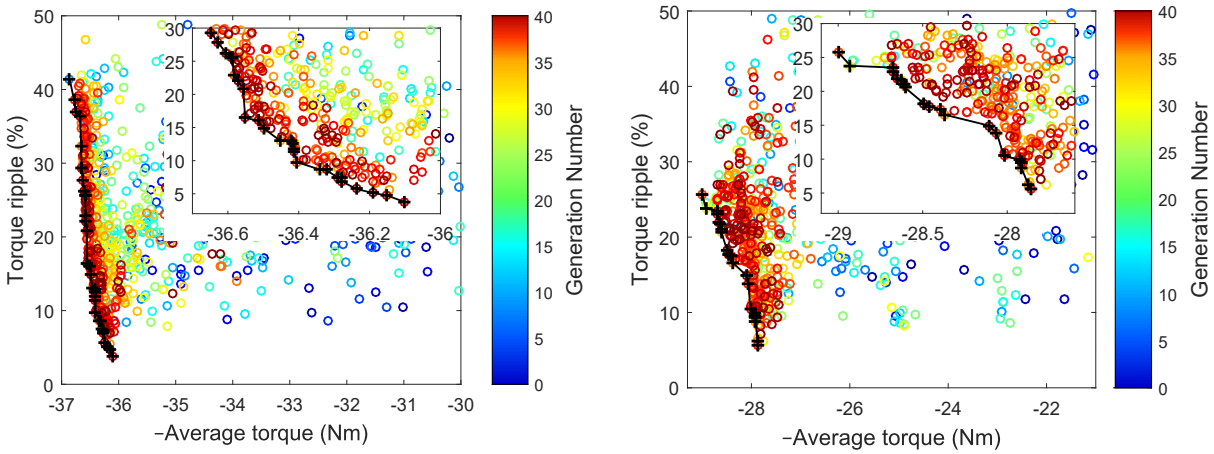

(a) 30 000 rpm.

(b) 40 000 rpm.

Figure 9.16
Simulated individuals in the objectives plane (average torque and torque ripple) and Pareto front. Two different speeds have been considered.

With a skewed rotor, the torque oscillation has been reduced to 4.1% with an average torque of about 40 N m.

Even if the salient pole is mechanically robust, for the rated speed it does not represent a valid alternative to the flux-barrier rotor since the average torque is lower.

9.3.4 *Optimization at higher speeds*

Further optimizations at different speeds are presented hereafter. The aim of these investigations is to determine the influence of the speed on the overall performance and on the rotor flux-barriers shape. The stator geometry is kept fixed with and the same slot current is imposed. As in the previous case, the optimization is focused on the rotor geometry.

The objectives plane of the optimization at 30 000 rpm is reported in Figure 9.16(a). It can be noted that the average torque is lower than before and it is around 36 N m. In addition the minimum torque ripple achievable is slightly higher than the one at 20 000 rpm. The Pareto front is very steep and different from the front obtained above (Figure 9.13).

The optimization has been repeated for a speed of 40 000 rpm. The objective plane is reported in Figure 9.16(b). As expected, the average torque, which results about 26 N m and is lower than the previous optimizations since the leakage flux of the radial iron ribs is higher.

9.3.5 *Comparison of the optimization results*

Figure 9.17 shows the flux density plots of the selected individuals at the speeds 20 krpm, 30 krpm and 40 krpm. It is worth noticing that the radial iron ribs increase as the speed increases because of the higher centrifugal load. Furthermore, the magnetic insulation ratio, k_{air}, increases too. This effect is because the optimizer finds the compromise

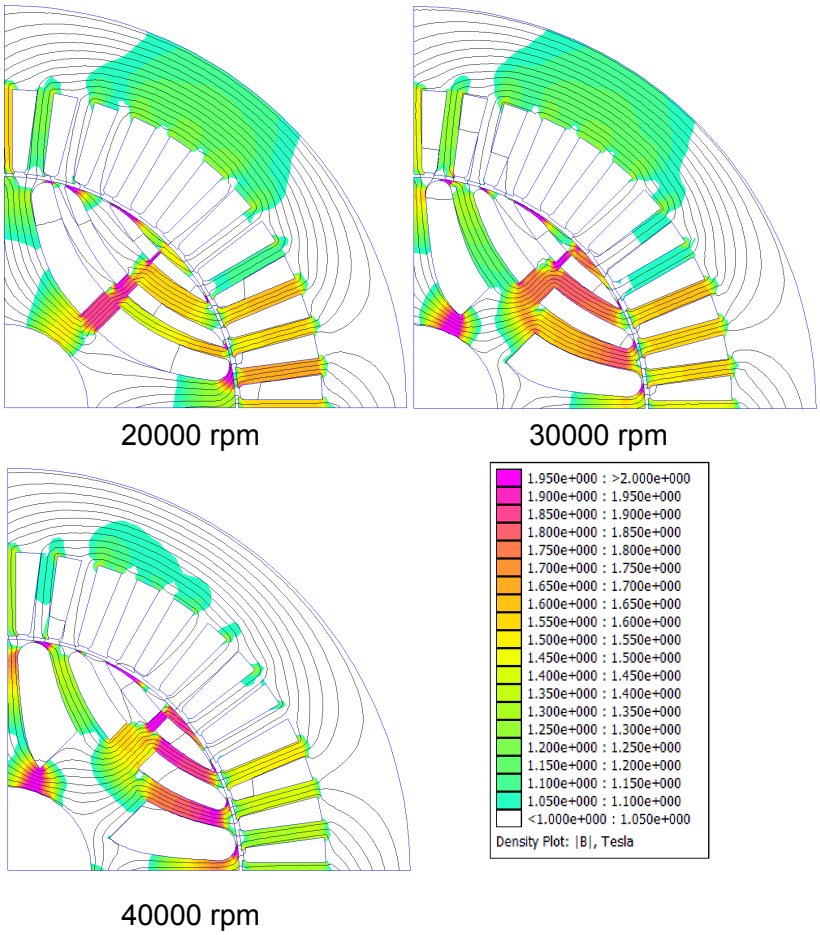

Figure 9.17
Comparison of the flux density plots of the optimized motors for different speeds.

between wider ribs and lighter islands. It can also be noted that the saturation of the radial iron ribs decreases as the speed increases. On the contrary, the iron paths between the flux-barriers becomes more and more saturated. The behaviors of the torque versus the rotor position of the optimal individuals are reported in Figure 9.18 for the different speeds. For each plot, the average torque and the ripple are also reported. It can be noted that the average torque at 20 000 rpm is higher than the other ones. In particular, at 30 000 rpm the average torque is about 21% lower while at 40 000 rpm the decrease is about 43%. Furthermore it can be observed that the torque ripple tends to increase with the speed. In fact, at the lower speed it is 4.77% while at 40 000 rpm it is 12.88%. In Table 9.6 the d- and q-axis inductances, the saliency ratio (ξ), the difference between the inductances and the power factor are reported for motors designed for different speeds. All values are expressed in per unit, referring to the direct axis inductance obtained with the lowest radial rib thicknesses, i.e. for motor running at 1500 rpm. It is possible to observe that at the highest speed the d-axis inductance is 30% lower than the reference one. The q-axis inductance increases of about 120%, this is essentially due to the larger radial ribs thicknesses. The reduction of rotor anisotropy related to the speed is

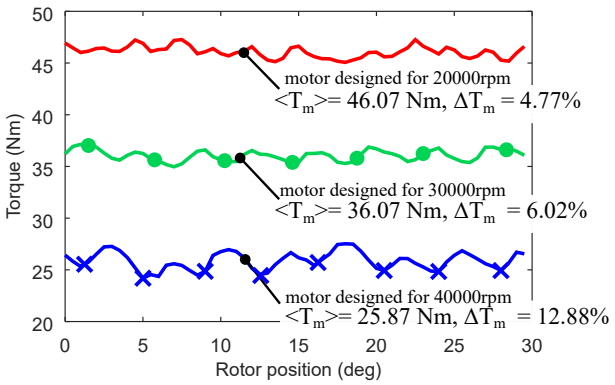

Figure 9.18
Torque versus rotor position waveforms for the motors optimized at different speeds.

n [rpm]	L_d [p.u.]	L_q [p.u.]	ξ [1]	$L_d - L_q$ [p.u.]	PF [1]
1500	1	0.157	6.38	0.843	0.652
20 000	0.937	0.267	3.50	0.670	0.542
30 000	0.810	0.313	2.59	0.497	0.427
40 000	0.708	0.348	2.03	0.359	0.339

Table 9.6
Per-unit d- and q-axes inductances and saliency ratios for different rated speeds. The reference value is the d-axis inductance at 1500 rpm.

evident considering both the saliency ratio and, mainly, the difference between d- and q-axis inductances. With respect to the reference one, the former parameter decreases of about 68% while the latter of 57%. The power factor worsens with the speed decreasing from 0.652 to 0.339.

This aspect can be explained considering the flux density plots at different speeds reported in Figure 9.17. It is evident that, at low speed, the radial ribs are saturated and so the iron islands can be considered magnetically isolated from each other. Conversely, as the speed increases, the radial ribs are no more saturated and so the islands are far from being magnetically isolated.

The results of all the optimizations at different speeds are summarized in Figure 9.19. It can be noted that the maximum output power is a function of the speed.

It increases up to the speed 37 500 rpm, then it decreases for higher speeds. This aspect represents a limit of the transverse-laminated reluctance machines for the geometry under investigation.

Another interesting aspect that can be deduced from Figure 9.19 is that the magnetic insulation, measured by k_{air}, increases as the speed increases. Clearly, such increase leads to a decrease of the overall iron mass and, consequently, a decrease of the rib thicknesses.

9.3.6 *Discussion*

This section dealt with the investigation of the potential and the optimization of the geometry of high-speed synchronous reluctance motors. The optimization was focused on the rotor geometrical parameters,

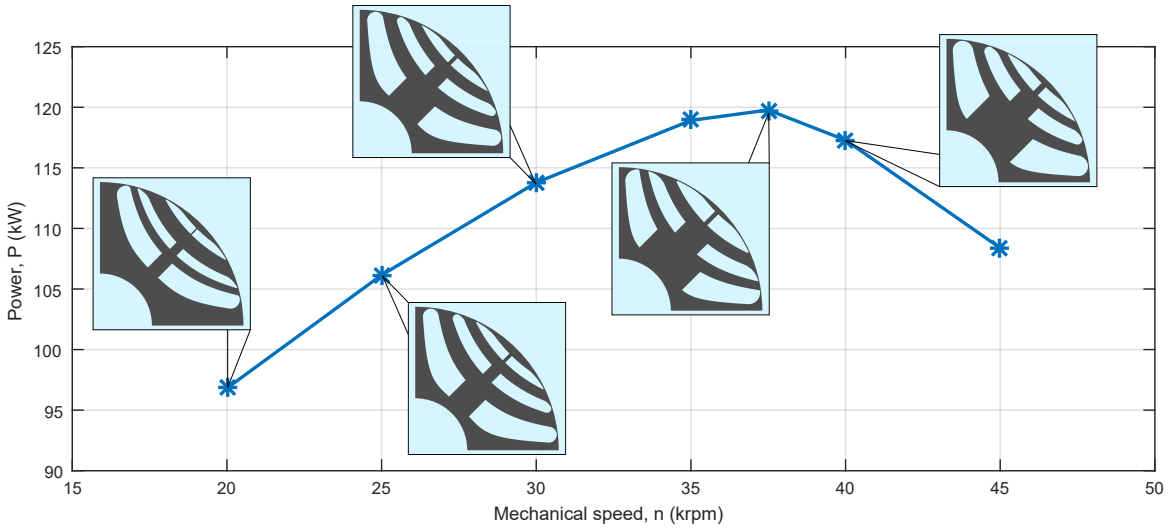

Figure 9.19
Maximum output power versus mechanical speed. For each speed the rotor geometry is different, as obtained by a specific optimization.

such as flux-barrier angles and insulation ratio. The goals were high power and low torque ripple.

It has been verified that, at rated speed of 20 000 rpm, the flux-barrier geometry is the most suitable solution. Alternative solutions, such as the use of a retaining sleeve and a salient pole rotor, do not meet the requirements. A sensitivity analysis on the optimization results has also been carried out. It has been observed that low-ripple solutions have a high sensitivity and thus require a high manufacturing precision.

To the aim of investigating the potential of the flux-barrier synchronous reluctance motor, the analysis has been carried out for high-speeds. Because of the increase of the rib thicknesses with the speed, the motor with flux-barrier rotor presents a power limit, corresponding to a speed close to 37 500 rpm. Furthermore the higher rib thickness worsens the rotor anisotropy and consequently the power factor.

10

SELF-SENSING-ORIENTED OPTIMIZATION OF SYNCHRONOUS RELUCTANCE MACHINE DESIGN

This chapter deals with self-sensing-oriented optimization of synchronous reluctance machines. This kind of machine is among the most challenging to control without the position sensor at low speed. In fact, typical position estimations adopt high-frequency voltage injection which heavily relies on the intrinsic machine saliency. However, both at low and high currents, such a saliency is not guaranteed due to the presence of the iron ribs and to the saturation of the iron material, respectively. Furthermore, the estimation algorithm could also become unstable due to the absence of convergence points. The aim of the chapter is to tackle this issue, embedding proper sensorless-control capability into the design through multi-objective optimizations.

Several works in the past tried to enhance the self-sensing capability of IPM motors (Bianchi et al., 2009a; Bianchi et al., 2013; Kano, 2014), focusing on avoiding that the MTPA trajectory crosses the point where the current error signal is zero. Despite that, few or no research is available for SyRM, where the convergence issue is different in nature. In this chapter, the non-convergence issue is tackled from early electromagnetic design phase, trying to embed the solution into a complete optimization of the motor. The sensorless technique considered hereafter is the injection of high-frequency pulsating voltage along the estimated d-axis, referred to as $\tilde{d}$, and the response is the $\tilde{q}$-axis current (Figure 10.1(a)). A scheme of the electric drive with the HF injection is shown in Figure 10.1(b). So the applied HF voltage vector is:

$$u_{\tilde{d}h}(t) = U_{\tilde{d}h} \cos \omega_h t \,, \qquad u_{\tilde{q}h}(t) = 0 \tag{10.1}$$

where ω_h is the HF signal angular frequency and $U_{\tilde{d}h}$ is the injected voltage amplitude. The resulting current error signal is

$$\begin{aligned} i_{\tilde{q}h}(t) &= I_{\tilde{q}h} \sin \omega_h t \\ I_{\tilde{q}h} &= \frac{-U_{\tilde{d}h}}{\omega_h [\ell_d \ell_q - \ell_{dq}^2]} \left[\ell_\Delta \sin 2\Delta\vartheta + \ell_{dq} \cos 2\Delta\vartheta \right] \end{aligned} \tag{10.2}$$

where $\Delta\vartheta$ is the electrical position estimation error, and ℓ_x are the differential inductances.[1] If there was no ℓ_{dq}, such a response would be zero when the position estimation error is zero. Figure 10.2 reports the ideal error signal, $\Gamma_{\tilde{q}\tilde{d}}$. It is a pure sinusoid, which crosses zero twice in a semi-period. One of the zeros is stable, the green one, while the other one is unstable, the red one. The stable convergence point is slightly leading the correct rotor position (zero estimating error $\Delta\vartheta$) due to the presence of the cross-saturation differential inductance, ℓ_{dq}.

1 See Appendix E for the derivation.

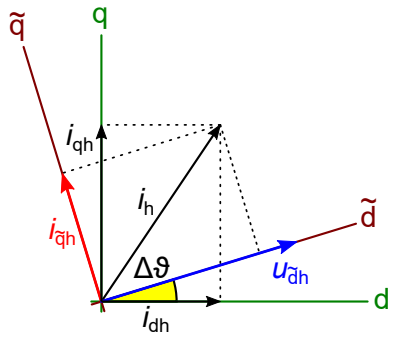

(a) Position estimation error and current error signal.

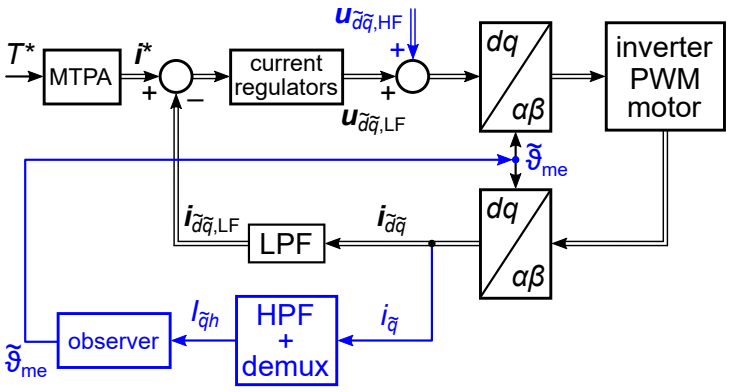

(b) Control scheme of the electric drive with high-frequency signal injection.

Figure 10.1
Operating principle and control scheme implementation of the high-frequency signal injection for sensorless rotor position estimation.

Figure 10.2
Ideal error signal, $\Gamma_{\tilde{q}\tilde{d}}$, with constant differential inductances.

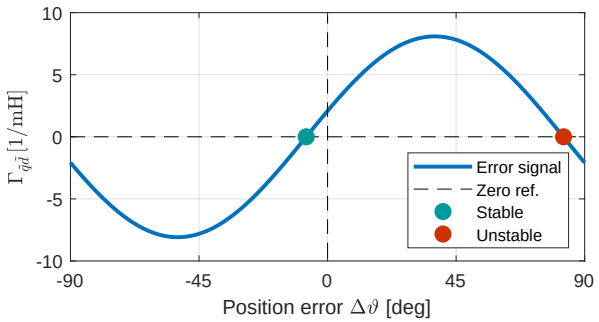

The chapter is organized as follows: at first, a classical optimization is performed on the rotor of the machine to maximize the output torque and minimize the torque ripple. One optimal geometry is then investigated to determine its HF sensorless control capability through error signal maps. Next, the stator and rotor are optimized jointly with the additional objective of minimizing the cross-saturation differential inductance. Finally, one more objective is added to the multi-objective optimization to further improve the self-sensing capability of the motor.

10.1 EXAMPLE OF A TYPICAL OPTIMIZATION

The specifications and the constraints of the machine under analysis are reported in Table 10.1. In particular, the requirement is to obtain about 90 N m with the highest possible efficiency within the given dimensions. At first, also the stator geometry is a constraint, and its data is also reported in Table 10.1.

A state-of-the-art optimization coupled to FEA has been performed in order to assess the feasibility of the design and to get the overall machine performance. The main objectives for synchronous reluctance machines are average torque and torque ripple. Since most of the losses

Table 10.1
Specifications of the motor.

Quantity	Value	u.m.
Torque	90	N m
Speed	2000	rpm
Efficiency	92	%
Stator outer diameter	180	mm
Stack length	288	mm
Number of slots	36	
Number of poles	4	
Stator inner diameter	110	mm
Tooth width	4.83	mm
Slot height	22.4	mm
Slot opening width	2.5	mm
Slot opening height	1	mm
Slot wedge height	0.5	mm

are located in the stator and in this optimization the stator is kept the same, the efficiency depends only upon the average torque.

The objectives plane is reported in Figure 10.3. Every dot represents a simulated individual. Each evaluation took about 150 seconds. The color of the dot represents the age of the individual, while the black diamonds are the Pareto points, which are those individuals that are not dominated by others: this means that no other individual has both objectives better. Thanks to the fact that almost all Pareto points exhibit proper average torque, the individual with the lowest ripple at 92.3 N m has been selected for further investigations. The corresponding efficiency is 93.1%.

A complete mapping of the (i_d, i_q) plane has been carried out on this individual with FEA. In particular, the flux linkages $\lambda_d(i_d, i_q)$ and $\lambda_q(i_d, i_q)$ are computed and they are reported in Figure 10.4. These two maps are the fundamental elements for the following analysis. In fact, the electromagnetic torque can be readily computed, neglecting the dependence on the rotor position, through

$$T_{\mathrm{m}}(i_d, i_q) = \frac{3}{2} p \left[\lambda_d(i_d, i_q) i_q - \lambda_q(i_d, i_q) i_d \right] \tag{10.3}$$

Then, the differential inductances are defined as:

$$\ell_d = \frac{\partial \lambda_d}{\partial i_d}, \quad \ell_{dq} = \frac{\partial \lambda_d}{\partial i_q} = \frac{\partial \lambda_q}{\partial i_d} = \ell_{qd}, \quad \ell_q = \frac{\partial \lambda_q}{\partial i_q} \tag{10.4}$$

These inductances are defined locally and strongly depends on the machine saturation. The half difference between ℓ_q and ℓ_d is defined as $\ell_\Delta = (\ell_q - \ell_d)/2$ and this quantity displays the available saliency for HF signals. Also ℓ_Δ results to be a map of the (i_d, i_q) plane. In Figure 10.5 such a map is reported. The contour $\ell_\Delta = 0$ is highlighted in red, the MTPA trajectory with black dots, while the rated current circle is the black line.

Figure 10.3
Objectives plane for the first rotor optimization.

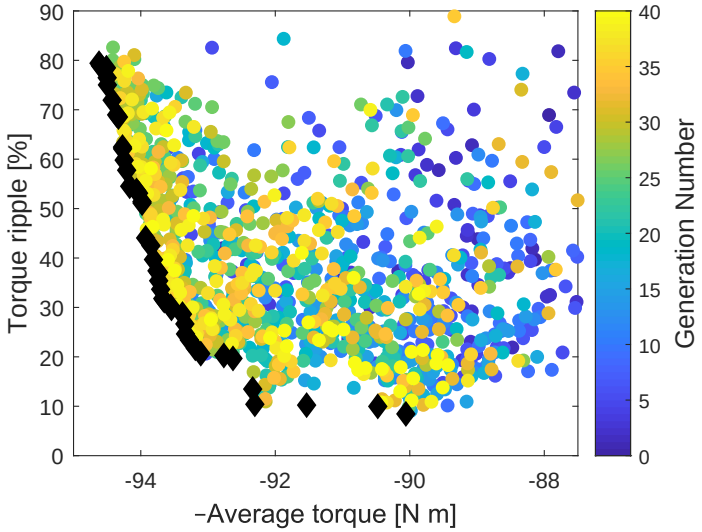

Figure 10.4
Flux linkages as functions of the two axes currents.

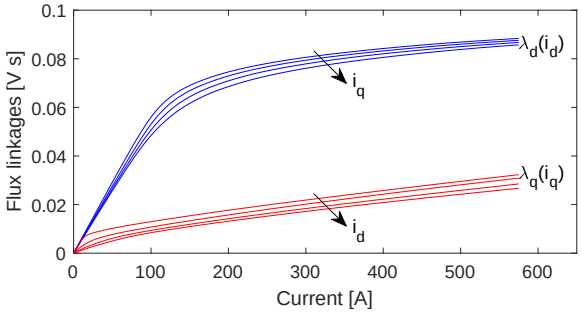

Often in literature the region where $\ell_\Delta = 0$ has been reported as an unfeasible region for HF-injection sensorless control due to the loss of error signal proportional to ℓ_Δ. However, thanks to the presence of ℓ_{dq}, the sensorless estimation would still converge to a value of $\Delta\vartheta = \frac{\pi}{2}$. In the specific machine under analysis, the MTPA trajectory is quite far from the problematic $\ell_\Delta = 0$ contour. Even though this fact seems to guarantee proper convergence of the estimating algorithm, when the position is not known the control may apply a current vector which is very different from the desired one. For instance, let us consider the base point, which is the MTPA point at the rated current. That point will be the reference from which the estimation error $\Delta\vartheta$ will be measured. And since the control may apply any current vector with that amplitude, the estimation error signal is a complicated function of $\Delta\vartheta$ (the dependency of the quantities on the current references (i_d^*, i_q^*) is omitted for convenience):

$$I_{\tilde{q}h}(\Delta\vartheta) = \frac{U_{\tilde{d}h}}{\omega_h} \underbrace{\left[-\frac{\ell_\Delta(\Delta\vartheta)\sin 2\Delta\vartheta + \ell_{dq}(\Delta\vartheta)\cos 2\Delta\vartheta}{\ell_d(\Delta\vartheta)\ell_q(\Delta\vartheta) - \ell_{dq}^2(\Delta\vartheta)} \right]}_{\Gamma_{\tilde{q}\tilde{d}}} \tag{10.5}$$

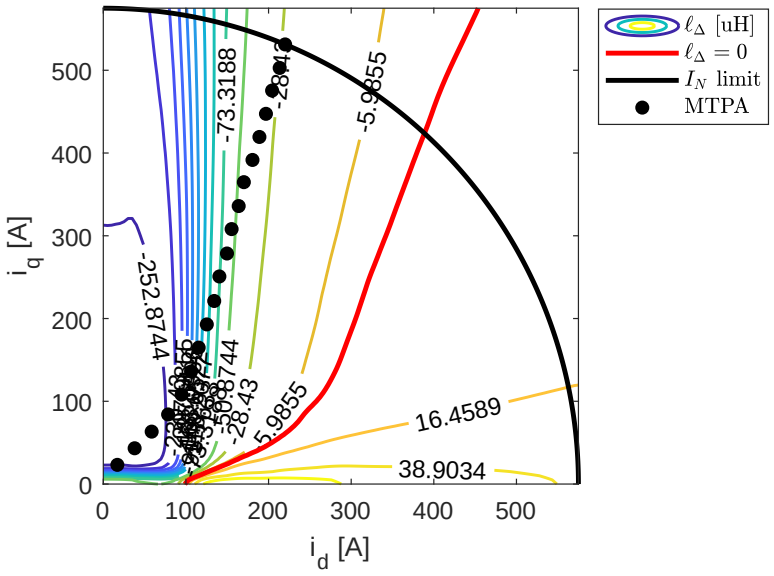

Figure 10.5
Map of the differential inductance ℓ_Δ in the (i_d, i_q) plane.

The term between brackets in (10.5) is referred to as $\Gamma_{\tilde{q}\tilde{d}}$ in the following, because it acts like the inverse of an inductance.

In Figure 10.6(a) the behavior of $\Gamma_{\tilde{q}\tilde{d}}$ as a function of $\Delta\vartheta$ is reported. The most notable thing is that this waveform does not cross the x-axis, which means that the observer would not be able to converge to any working point, not even a wrong one. Recent works tried to tackle this issue with a current, angle, or current and angle compensations (Kwon et al., 2017; Manzolini et al., 2018). The scheme of the drive with the HF sensorless rotor position estimation with current and angle compensations is shown in Figure 10.7.

Repeating the same computation of $\Gamma_{\tilde{q}\tilde{d}}$ for all the possible working points along the MTPA, a map of $\Gamma_{\tilde{q}\tilde{d}}$ as a function of the output torque and estimation error can be obtained. The map for the motor under analysis is shown in Figure 10.6(b). The contour $\Gamma_{\tilde{q}\tilde{d}} = 0$ identifies the operational limit of the HF-injection sensorless control. In fact, each horizontal slice of the map in Figure 10.6(b) is the estimation error signal (Figure 10.6(a)) used by the observer for the selected torque level. It can be noted that for this machine the last achievable torque level without any compensation is at about 45 N m (49% of the rated one).

Since $\Gamma_{\tilde{q}\tilde{d}}(\Delta\vartheta)$ stays always positive when convergence problems appear (see Figure 10.6(a)), the convergence region can also be found in the whole (i_d, i_q) plane for every working point looking at the minimum value of the $\Gamma_{\tilde{q}\tilde{d}}$ waveform: if this value is lower than zero, then there is a zero-crossing and therefore the estimating algorithm converges. Thus, the contour $\min \Gamma_{\tilde{q}\tilde{d}} = 0$ delimits the unfeasible region. In Figure 10.8 it can be observed that such a region is quite wide. The cause of this issue is the presence of harmonics in both ℓ_Δ and ℓ_{dq} along the current circles.

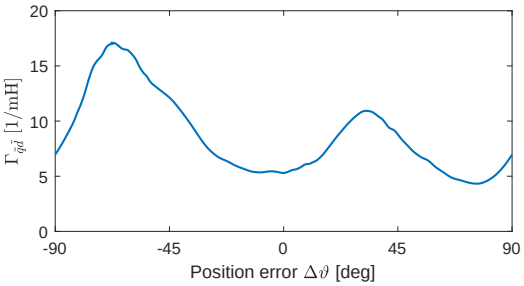

(a) $\Gamma_{\tilde{q}\tilde{d}}$ as a function of $\Delta\vartheta$ for the base point at the rated current.

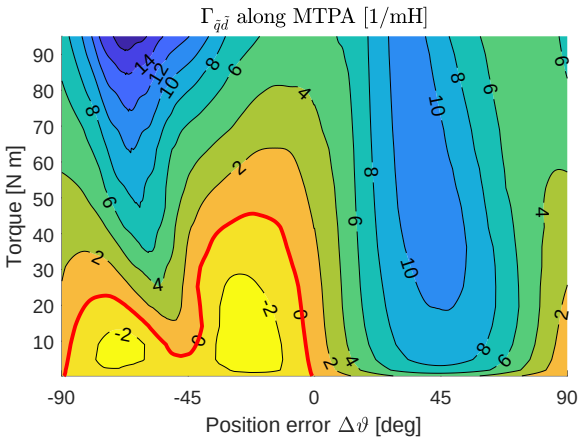

(b) $\Gamma_{\tilde{q}\tilde{d}}$ as a function of the output torque and position estimation error.

Figure 10.6
$\Gamma_{\tilde{q}\tilde{d}}$ plots for the base point and for every point along the MTPA trajectory.

The ℓ_Δ and ℓ_{dq} behaviors are reported in Figure 10.9 as functions of the position estimation error $\Delta\vartheta$ for $\alpha_i^e = \alpha_{i\,\mathrm{MTPA}}^e$.

The presence of a second order harmonic is evident (in the figure only a semi-period is shown). The error signal can be computed substituting ℓ_Δ and ℓ_{dq} harmonics into the numerator of (10.5). Defining ϑ_i the angle starting from the d-axis, the error angle $\Delta\vartheta$ is defined through $\vartheta_i = \alpha_i^e + \Delta\vartheta$, where α_i^e is the reference current angle. So

$$\begin{aligned}
\ell_\Delta(\vartheta_i) &\approx \ell_\Delta^{(0)} + \ell_\Delta^{(2)} \cos 2\vartheta_i \\
&\approx \ell_\Delta^{(0)} + \ell_\Delta^{(2)} \cos 2\alpha_i^e \cos 2\Delta\vartheta - \ell_\Delta^{(2)} \sin 2\alpha_i^e \sin 2\Delta\vartheta \\
\ell_{dq}(\vartheta_i) &\approx \ell_{dq}^{(2)} \sin 2\vartheta_i \\
&\approx \ell_{dq}^{(2)} \sin 2\alpha_i^e \cos 2\Delta\vartheta + \ell_{dq}^{(2)} \cos 2\alpha_i^e \sin 2\Delta\vartheta
\end{aligned} \tag{10.6}$$

and then

$$\begin{aligned}
\Gamma_{\tilde{q}\tilde{d}} \sim \underbrace{\left(\frac{\ell_{dq}^{(2)} - \ell_\Delta^{(2)}}{2}\right) \sin 2\alpha_i^e}_{\text{bias}} + \underbrace{\ell_\Delta^{(0)} \sin 2\Delta\vartheta}_{\text{useful signal}} + \\
+ \left(\frac{\ell_\Delta^{(2)} + \ell_{dq}^{(2)}}{2}\right) \left[\cos 2\alpha_i^e \sin 4\Delta\vartheta + \sin 2\alpha_i^e \cos 4\Delta\vartheta\right]
\end{aligned} \tag{10.7}$$

It can be seen that the second order harmonics in ℓ_Δ and ℓ_{dq} are responsible for a bias that shifts vertically the $\Gamma_{\tilde{q}\tilde{d}}$ waveform. It should be noted that ℓ_{dq} is also the source of steady-state position estimation error, which is defined as

$$\epsilon = \frac{1}{2} \arctan_2(\ell_{dq}, -\ell_\Delta) \tag{10.8}$$

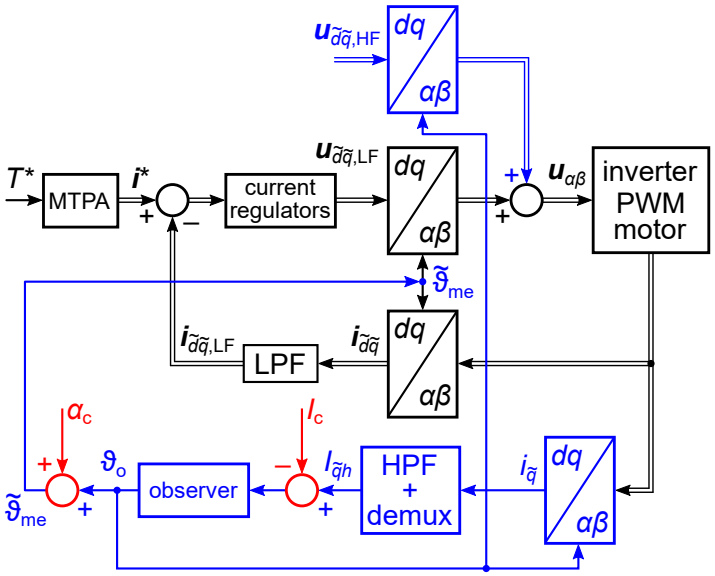

Figure 10.7
Control scheme of the electric drive with high-frequency signal injection and current and angle compensation.

In fact, if there was no ℓ_{dq}, the estimation error signal $\Gamma_{\tilde{q}\tilde{d}}$ would always go to zero when $\Delta\vartheta = 0$, regardless of the ℓ_Δ behavior. On the other hand, a large ℓ_Δ value is desirable to get a high HF current.

10.2 SELF-SENSING-ORIENTED OPTIMIZATION

Two different optimizations have been carried out, with the aim of extending the HF-injection self-sensing torque range. The first optimization tried to minimize the cross-saturation differential inductance ℓ_{dq} for an intermediate current angle $\alpha_i^{\mathrm{e}} = 45°$ at the rated current. The second optimization aims at minimizing also the ratio R_Δ, defined as

$$R_\Delta = \frac{\ell_\Delta^{(0)}}{|\ell_\Delta^{(2)}|} \approx \frac{2\langle \ell_\Delta \rangle}{|\ell_\Delta^{90°} - \ell_\Delta^{0°}|} \tag{10.9}$$

which is equal to maximize the absolute value of the average of ℓ_Δ (numerator) along the rated current circle and, at the same time, to minimize its second order harmonic (denominator). To compute all these quantities, some linearized incremental permeability simulations are performed, which do not add too much computational load to the optimization procedure.

10.2.1 *First self-sensing-oriented optimization*

In this optimization there were three objectives: torque ripple, efficiency and cross-saturation differential inductance. The parameters (degrees of freedom) were the three flux-barrier angles, the magnetic insulation ratio, the stator split ratio, the stator tooth width and slot height.

The results of the first optimization are reported in Figure 10.10. It can be observed that the cross-saturation differential inductance ℓ_Δ is proportional to the efficiency. So the higher the efficiency, the

Figure 10.8
$\min \Gamma_{\tilde{q}\tilde{d}}(\Delta\vartheta)$ map in the (i_d, i_q) plane for every working point.

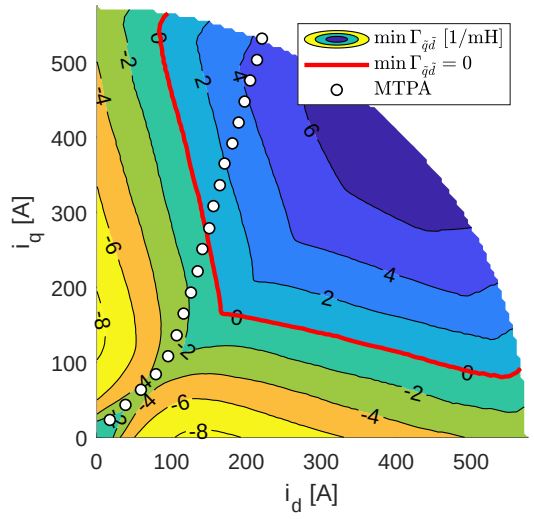

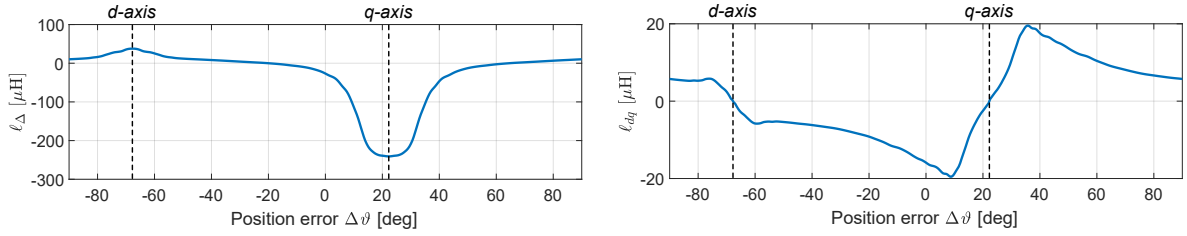

(a) ℓ_Δ (b) ℓ_{dq}

Figure 10.9
The differential inductances ℓ_Δ and ℓ_{dq} as functions of position estimation error at rated current.

higher ℓ_{dq}. Such a quantity strongly depends on the saturation of the machine, which is affected by the geometrical parameters (and so is the torque, thus the efficiency). Larger iron areas improve ℓ_{dq} but negatively affects the motor torque and so the efficiency. In fact the rotor diameter decreases to leave more space for the stator yoke, and the slots shrink to obtain larger teeth. As a consequence the slot area has to decrease, and so the copper losses increase.

In this optimization the Pareto front is a 3D surface. In Figure 10.10 the efficiency and ℓ_{dq} are reported in the two axes, while the torque ripple is displayed through the size of the markers: the bigger the marker, the lower the ripple. The average torque is not an objective now, but it is implicitly taken into account in the torque ripple and in the efficiency. Some individuals on the Pareto front were selected for the complete mapping of the (i_d, i_q) plane to test their HF sensorless control capabilities.

The map of $\Gamma_{\tilde{q}\tilde{d}}$ for one individual is shown in Figure 10.11. It can be seen that the highest torque which guarantees the convergence of the observer is now about 58 N m. So the minimization of ℓ_{dq} improved the torque range of the sensorless control, even though the error signal still has a large negative bias: the negative values of the map are larger than

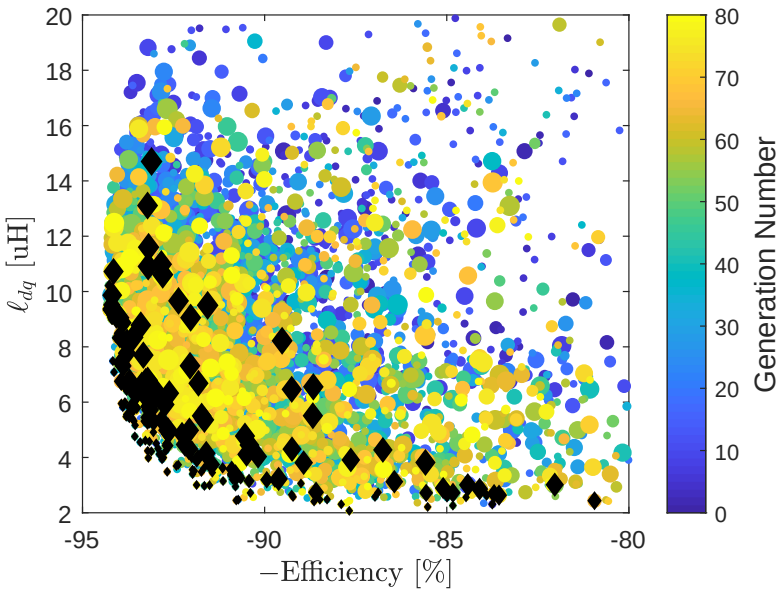

Figure 10.10
Objectives plane for the first self-sensing-oriented optimization. The dimension of the marker is inversely proportional to the torque ripple. The black diamonds are the Pareto points.

the positive ones in absolute value. Also the $\Gamma_{\tilde{q}\tilde{d}}$ behavior at high torque for position error values between −90° and 0° is improved (Figure 10.11), because now the highest values are closer to zero (the x-axis), requiring a lower current amplitude compensation (Manzolini et al., 2018).

10.2.2 *Second self-sensing-oriented optimization*

This time two cascaded optimizations were performed: the first one considered three objectives (efficiency, cross-saturation differential inductance and the ratio R_Δ introduced in (10.9)), while the second one focused on the torque ripple and average torque only. This is due to the fact that the torque ripple is mainly due to the rotor geometry, while the

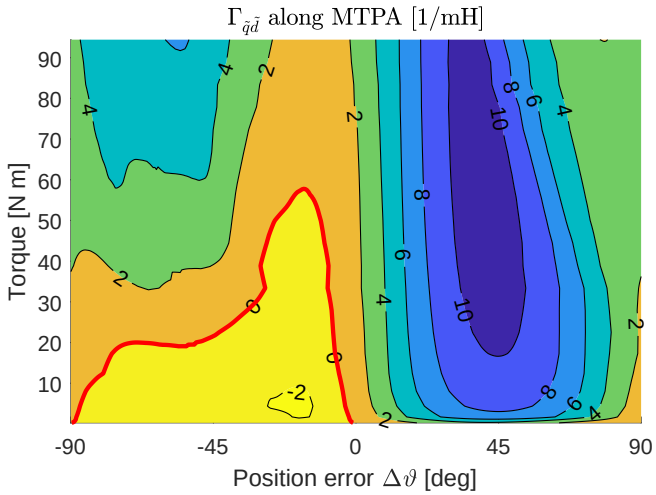

Figure 10.11
$\Gamma_{\tilde{q}\tilde{d}}$ as a function of the output torque and estimation error.

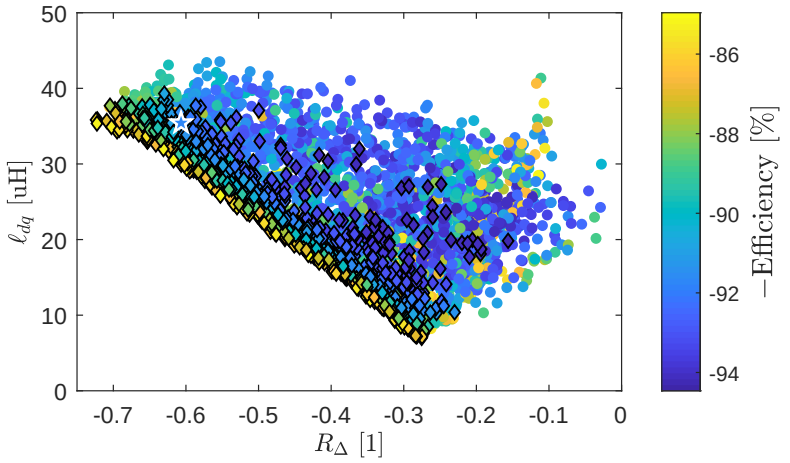

Figure 10.12
Objectives plane for the second self-sensing-oriented optimization. The color is proportional to the efficiency. The diamonds are the Pareto points, the star the solution which has been further investigated.

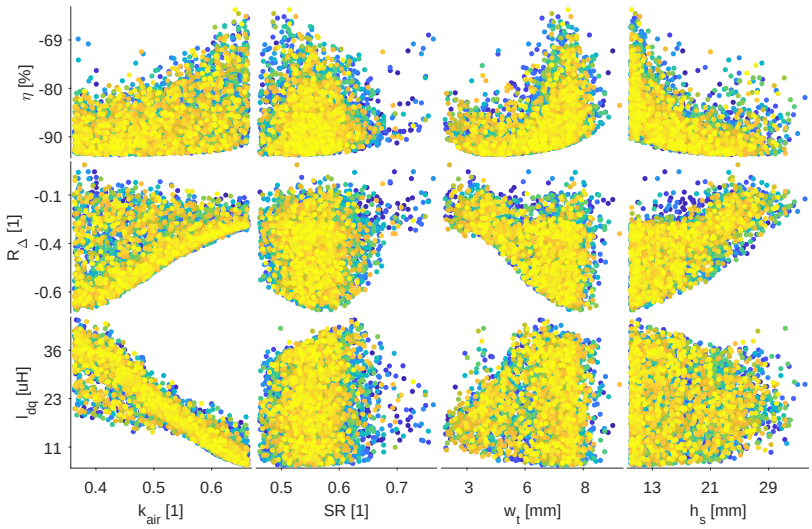

Figure 10.13
Objectives versus parameters plots for the third self-sensing-oriented optimization.

self-sensing capability mainly depends on the stator parameters. The R_Δ numerator, $\langle \ell_\Delta \rangle$, is computed using four samples along the current limit circle: at 0°, 45°, 90° and at 67.5°, where also ℓ_{dq} was sampled. So the R_Δ numerator results

$$\langle \ell_\Delta \rangle = \frac{2\ell_\Delta^{0°} + 3\ell_\Delta^{45°} + 2\ell_\Delta^{67.5°} + \ell_\Delta^{90°}}{8} \tag{10.10}$$

from a stepped average of the quantity.

The results of the second self-sensing-oriented optimization are summarized in Figure 10.12. The figure displays ℓ_{dq} and R_Δ of the simulated motors along the two axes, while the color is proportional to the value of the efficiency, so a darker color means a higher efficiency. The diamond are the individual on the Pareto front. A very clear relationship between ℓ_{dq} and R_Δ can be noticed, since there seems to be a linear limit on the values that these quantities may assume. In addition, the efficiency increases on a direction almost perpendicular to this fictitious

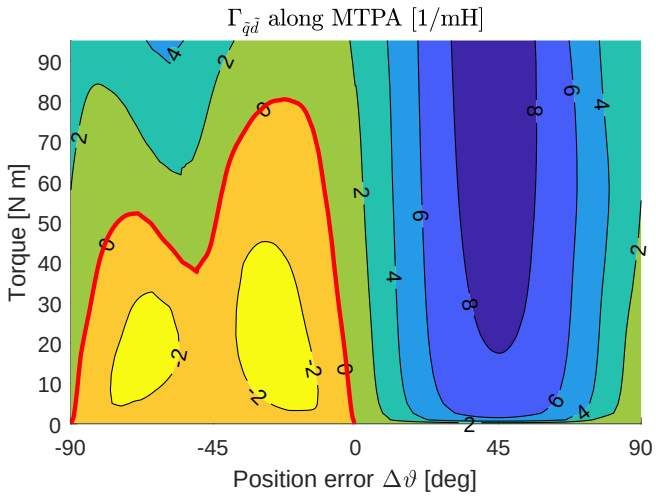

Figure 10.14
$\Gamma_{\tilde{q}\tilde{d}}$ as a function of the output torque and estimation error.

Figure 10.15
Investigated geometries resulting from the two optimizations.

(a) Typical optimization with given stator.

(b) Second self-sensing-oriented optimization.

line, and this proves that efficiency is conflicting with the other two objectives.

The reason why ℓ_{dq} and R_Δ are conflicting objectives can be understood from Figure 10.13, looking at the second and third plots in the first column. In fact, there is a lower limit on the value of R_Δ as a function of k_{air}, and this limit increases with the increase of k_{air}. On the other hand, ℓ_{dq} decreases with the increase of k_{air}, which is beneficial. This means that increasing the amount of air in the rotor increases the saturation of the rotor iron, obviously, and improves the cross-saturation, which is mostly due to the saturation of the stator yoke. But it also leads to a lower differential saliency, so a lower difference between the d- and q-axes inductances, and therefore to a lower absolute value of R_Δ.

Also in this case some individuals on the Pareto front have been selected for the complete mapping of the currents plane. In particular, the one marked by the star in Figure 10.12 is the most promising one, because it exhibits high R_Δ ratio and proper efficiency. In Figure 10.14 the corresponding $\Gamma_{\tilde{q}\tilde{d}}$ map is shown. It can be observed that the maximum torque which guarantees the convergence is about 80 N m, which

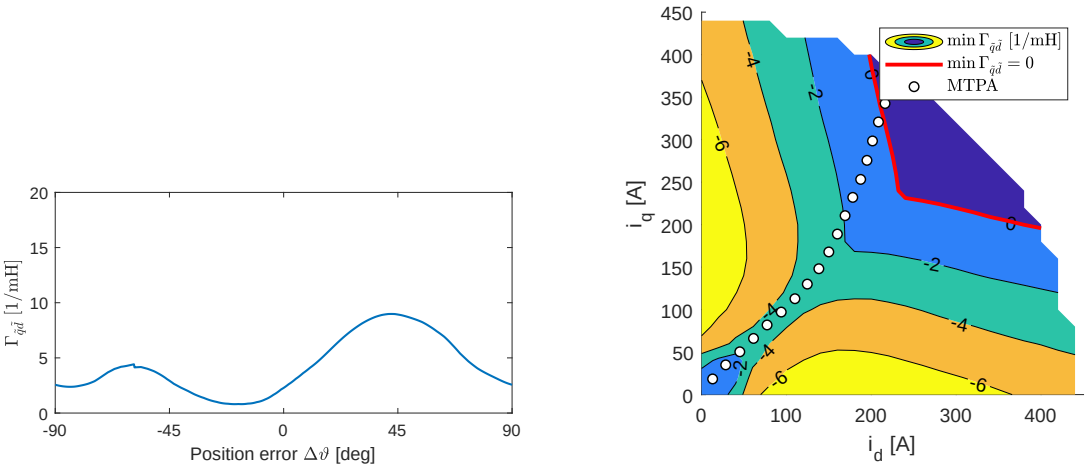

(a) $\Gamma_{\tilde{q}\tilde{d}}$ as a function of $\Delta\vartheta$ for the base point.

(b) $\max \Gamma_{\tilde{q}\tilde{d}}(\Delta\vartheta)$ map in the (i_d, i_q) plane for every working point.

Figure 10.16
$\Gamma_{\tilde{q}\tilde{d}}$ plots for the selected individual of the second self-sensing oriented optimization.

corresponds to 87% of the rated torque. This has been possible only thanks to the combined optimization of the stator and rotor geometries. Of course, this improvement comes at a cost: the efficiency drops to about 91.4%. The torque ripple has been minimized through a second optimization to a value of about 5%. It has been found that a low torque ripple is fundamental to maintain the same self-sensing performance during the rotor rotation. The extension of the self-sensing range is evident also looking at Figure 10.16(b) and comparing it to Figure 10.8. The unfeasible region now is greatly reduced and it presents lower absolute values.

In Figure 10.15 the geometry analyzed is shown and compared to the one first studied. The differences are evident. In particular, the rotor diameter is smaller, but that does not affect the torque capability of the machine. Overall, there is now more iron in the stator, both in the yoke and in the teeth. As a result, the slot area becomes smaller, which explains the decrease in the efficiency.

Finally, Figure 10.16(a) reports the waveform of $\Gamma_{\tilde{q}\tilde{d}}$ as a function of the estimation error for the base point. Comparing it with Figure 10.6(a), it can be noted that the behavior is improved even though it still does not cross the x-axis. In fact, it has less negative offset, and also the peak before $\Delta\vartheta = 0°$ is more pronounced and closer to zero. This means that smaller current and angle compensations are needed.

10.3 DISCUSSION

In this chapter a HF-injection self-sensing-oriented optimization scheme has been presented. A heavily saturated synchronous reluctance motor has been selected as a case study. At first, a typical optimization has been performed on the rotor of the machine. The torque range for

sensorless control was rather limited. After that, the source of the issue has been highlighted, together with the possible mitigating solutions. These solutions were embedded into the optimization algorithm, in two different ways. Even though the solution found was not able to exhibit self-sensing capability at the maximum torque, the torque range has been greatly extended to about 87% of the rated torque.

It has been demonstrated that the factor that affects the converge of the observer the most is R_Δ, which is mainly due to the stator saturation. However, the rotor should be designed accordingly to guarantee a high average torque, high efficiency and low torque ripple. Finally, it has been deduced that a better self-sensing capability comes at the cost of lower efficiency. This fact highlights the importance of considering HF-injection sensorless control at early design phases.

CONCLUSIONS

The research carried out in this thesis covered many aspect of passive-rotor anisotropic synchronous machines. A lot of emphasis has been given on the design of machines using advanced optimization algorithms coupled to finite element analysis, which nowadays is the most effective tool for electric machines design.

At first, a nonlinear analytical model of synchronous reluctance machines have been developed, and it has been applied to estimate the motor performance in terms of average torque and torque ripple. In particular, some torque design maps have been presented, which allow the designer to properly pick good flux-barrier combinations at early design phases. This aspect has been further developed trying to simplify the previous model to only look at the main causes of torque ripple: slot harmonics. In fact, a simple transcendental system of equations has been derived, and it can be easily solved numerically. In addition, the simple model has also been applied to the design of asymmetric rotors of synchronous reluctance machines.

The third part of this thesis focused on multi-objective optimization applied to the design of electric machines. It represents the state-of-the-art tool for designing machines. The first example is the feasibility study of a high-torque low-speed permanent magnet assisted synchronous reluctance motor, and it resulted that this kind of machine was able to reach the target specifications. The second one is a pure synchronous reluctance motor for pumping applications. The scaled-down prototype of this motor has been manufactured and tested. The third example dealt with high-speed synchronous reluctance motors. At first, some design guidelines have been formulated based on electromagnetic and mechanical analytical models. After that, the optimization algorithm has been applied to design some machines and to investigate the potential of this kind of machines for high-speed applications.

Lastly, multi-objective optimization has also been applied for self-sensing-oriented design of SyRM, that is designed the motor considering sensorless-control issues early on in the design phase.

Part IV

APPENDIX

A

MMF DISTRIBUTION ALONG THE STATOR PERIPHERY

Suppose to modulate a spatial sinusoid

$$f(\vartheta) = \sin\vartheta \tag{A.1}$$

with a cosinusoidal time signal of angular frequency ω

$$\tilde{f}(\vartheta, t) = \sin\vartheta\cos\omega t = \tfrac{1}{2}\big(\sin(\vartheta+\omega t) + \sin(\vartheta-\omega t)\big) \tag{A.2}$$

The obtained signal is a spatial sinusoid which oscillates in time with frequency ω, just like a standing wave in a stretched rope. Moreover this very same signal can be reproduced by superposition of two traveling waves, as shown in the right-hand side (RHS) term of equation (A.2).

In order to better understand the characteristics of these traveling waves, let us consider just the second addendum of the RHS.

$$\sin(\vartheta-\omega t) = \sin\left(\frac{2\pi}{\lambda}\,x - \omega t\right) = \sin\left(k\,(x-ct)\right)$$

Here λ is the wavelength of the wave, equal to twice the pole pitch in an electrical machine

$$2\tau = \frac{\pi D}{p}$$

k is the wavenumber, spatial analogous to the angular frequency

$$k = \frac{2\pi}{\lambda}$$

and $c = \lambda f$ is the speed of propagation. The speed c can be derived also considering to "ride the wave", so to move synchronously with the wave on top of the same point. So

$$\frac{2\pi}{\lambda}\,x - \omega t = \text{const.}$$

and taking the derivative and expliciting the speed

$$c = \frac{\mathrm{d}x}{\mathrm{d}t} = \frac{\omega}{\frac{2\pi}{\lambda}} = \frac{2\pi f}{2\pi}\,\lambda = f\lambda$$

A.1 SPATIAL HARMONIC

Let us suppose now that the spatial sinusoid has higher wavenumber, so smaller wavelength.

$$\tilde{f}^{\nu} = \sin\nu\vartheta\cos\omega t\,, \qquad k^{\nu} = \nu k \qquad \lambda^{\nu} = \frac{\lambda}{\nu}\,, \qquad \nu \in \mathbb{Z}_0 \tag{A.3}$$

Repeating the same step as before, we can easily find out that the speed of the associated waves must be lower than before and it is

$$c^\nu = \frac{c}{\nu} \tag{A.4}$$

This is especially true if one thinks that in the same period (ω is the same) the wave travels for one oscillation, the wavelength, which is much smaller, so the speed must be smaller too.

In electrical machines we are interested in angular velocity, obtainable through

$$\Omega^\nu = \frac{c^\nu}{\frac{D}{2}} = \frac{f\lambda^\nu}{\frac{D}{2}} = \frac{2f\,2\tau}{D} = \frac{2f\,\pi D}{\nu p\,D} = \frac{2\pi f}{\nu p} = \frac{\omega_\mathrm{m}}{\nu}$$

so the angular velocity of the ν-th harmonic is $1/\nu$ times the speed of the fundamental. However the quantities shown before were all mechanical quantities, and we are interested in the electrical ones. So what happens is that every harmonic speed has to be multiplied by the correct number of pole, which is $p^\nu = \nu p$. For instance a fifth harmonic has an equivalent number of poles which is $5p$ due to the five wavelengths contained in one fundamental wavelength.

A.2 ROTATING MMF

Let us now suppose to have three balanced and symmetrical MMF waves, displaced in space *and* time

$$\begin{aligned}
\tilde{f}_1(\vartheta, t) &= F \sin\vartheta \cos\omega t \\
\tilde{f}_2(\vartheta, t) &= F \sin\left(\vartheta - \frac{2}{3}\pi\right) \cos\left(\omega t - \frac{2}{3}\pi\right) \\
\tilde{f}_3(\vartheta, t) &= F \sin\left(\vartheta - \frac{4}{3}\pi\right) \cos\left(\omega t - \frac{4}{3}\pi\right)
\end{aligned}$$

Decomposing each of them in the same way as before, we can see that they are sum of a progressive wave and a regressive one, just like before. Summing them together though, the regressive terms cancel each other and what we obtain is a progressive term equal to

$$f(\vartheta, t) = \frac{3}{2} F\, \sin\left(\vartheta - \omega t\right) \tag{A.5}$$

This is the rotating fundamental MMF due to a three-phase system of symmetrical currents flowing in three sets of coils displaced in space by 120°. This MMF causes a rotating flux density distribution along the airgap.

A.2.1 *Rotating harmonics*

Repeating the same steps we can find that for every harmonic one type of traveling wave cancels and the other "survives". For example, the fifth harmonic travels in the opposite way of the fundamental, with

the speed computed before. So it is convenient to assign the harmonic order a sign to express the direction of motion of the associated MMF. All the harmonics present in the described three-phase system are

$$\nu = 6k+1\,, \quad k \in \mathbb{Z} \qquad (\text{e.g. } \nu = +1, -5, +7, -11, +13, \dots) \tag{A.6}$$

In order to get the correct result one must remember that a spatial displacement of a signal result in different displacement of the harmonics proportional to the harmonic order.

$$y(\vartheta) \overset{\mathcal{FS}}{\longleftrightarrow} c_\nu \tag{A.7}$$

$$y(\vartheta+\beta) \overset{\mathcal{FS}}{\longleftrightarrow} \mathrm{e}^{\mathrm{j}\nu\beta}\, c_\nu \tag{A.8}$$

Resuming the fifth harmonic, the set of single phase MMF equations is

$$\begin{aligned}
f_1^{(-5)}(\vartheta,t) &= F^{(-5)} \sin[-5\vartheta]\cos(\omega t) \\
f_2^{(-5)}(\vartheta,t) &= F^{(-5)} \sin\left[-5\left(\vartheta - \frac{2}{3}\pi\right)\right]\cos\left(\omega t - \frac{2}{3}\pi\right) \\
f_3^{(-5)}(\vartheta,t) &= F^{(-5)} \sin\left[-5\left(\vartheta - \frac{4}{3}\pi\right)\right]\cos\left(\omega t - \frac{4}{3}\pi\right)
\end{aligned}$$

Then the generic rotating MMF harmonic can be expressed as

$$f^\nu(\vartheta,t) = \frac{3}{2} F^\nu \sin(\nu\vartheta - \omega t) \tag{A.9}$$

Notice that if ν is negative, we can collect the minus sign and bring it out of the sine, so what remains inside the operator is a regressive wave with negative amplitude where the fundamental is positive.

B

MAXWELL STRESS TENSOR DERIVATION

First recall the set of differential Maxwell's equations

$$\nabla \cdot \boldsymbol{D} = \rho \tag{B.1}$$

$$\nabla \times \boldsymbol{E} = \frac{\partial \boldsymbol{B}}{\partial t} \tag{B.2}$$

$$\nabla \cdot \boldsymbol{B} = 0 \tag{B.3}$$

$$\nabla \times \boldsymbol{H} = \boldsymbol{J} + \frac{\partial \boldsymbol{D}}{\partial t} \tag{B.4}$$

and the equivalent integral formulation

$$\oint_{\partial\Omega} \boldsymbol{D} \cdot \hat{\boldsymbol{n}} \, \mathrm{d}S = \int_{\Omega} \rho \, \mathrm{d}V \tag{B.5}$$

$$\oint_{\partial\Sigma} \boldsymbol{E} \cdot \hat{\boldsymbol{t}} \, \mathrm{d}l = \frac{\mathrm{d}}{\mathrm{d}t} \int_{\Sigma} \boldsymbol{B} \cdot \hat{\boldsymbol{n}} \, \mathrm{d}S \tag{B.6}$$

$$\oint_{\partial\Omega} \boldsymbol{B} \cdot \hat{\boldsymbol{n}} \, \mathrm{d}S = 0 \tag{B.7}$$

$$\oint_{\partial\Sigma} \boldsymbol{H} \cdot \hat{\boldsymbol{t}} \, \mathrm{d}l = \int_{\Sigma} \boldsymbol{J} \cdot \hat{\boldsymbol{n}} \, \mathrm{d}S + \frac{\mathrm{d}}{\mathrm{d}t} \int_{\Sigma} \boldsymbol{D} \cdot \hat{\boldsymbol{n}} \, \mathrm{d}S \tag{B.8}$$

The most used ones in electrical machines are (B.6),(B.8), respectively Faraday's and Ampère's laws. Usually the former is in the form

$$e = \frac{\mathrm{d}\lambda}{\mathrm{d}t}$$

where e is the BEMF while λ is the flux linkage of the considered winding. In the latter, the time-derivative is usually neglected because it has almost no effect at low frequencies.

In order to derive the force acting on bodies subjected to electromagnetic fields, we have to start from the Lorentz force on a charged particle:

$$\boldsymbol{F} = q\,(\boldsymbol{E} + \boldsymbol{v} \times \boldsymbol{B}) \qquad [\mathrm{N}] \tag{B.9}$$

where q is the charge of the particle and $\boldsymbol{v}$ is its speed. This formula can be generalized to the force density on a continuum media, so

$$\begin{aligned} \boldsymbol{f} &= \rho \boldsymbol{E} + \boldsymbol{J} \times \boldsymbol{B} \qquad [\mathrm{N/m^3}] \\ &= (\nabla \cdot \boldsymbol{D})\,\boldsymbol{E} + (\nabla \times \boldsymbol{H}) \times \boldsymbol{B} - \frac{\partial \boldsymbol{D}}{\partial t} \times \boldsymbol{B} \end{aligned}$$

The time derivative can be rewritten

$$\frac{\partial}{\partial t}(\boldsymbol{D} \times \boldsymbol{B}) = \frac{\partial \boldsymbol{D}}{\partial t} \times \boldsymbol{B} + \boldsymbol{D} \times \frac{\partial \boldsymbol{B}}{\partial t}$$

Therefore

$$\frac{\partial \boldsymbol{D}}{\partial t} \times \boldsymbol{B} = \frac{\partial}{\partial t}(\boldsymbol{D} \times \boldsymbol{B}) + \boldsymbol{D} \times (\nabla \times \boldsymbol{E})$$

$$\begin{aligned} \boldsymbol{f} &= \left[(\nabla \cdot \boldsymbol{D})\,\boldsymbol{E} - \boldsymbol{D} \times (\nabla \times \boldsymbol{E})\right] + \left[-\boldsymbol{B} \times (\nabla \times \boldsymbol{H})\right] + \frac{\partial}{\partial t}(\boldsymbol{D} \times \boldsymbol{B}) \\ &= \left[(\nabla \cdot \boldsymbol{D})\,\boldsymbol{E} - \boldsymbol{D} \times (\nabla \times \boldsymbol{E})\right] + \left[(\nabla \cdot \boldsymbol{B})\,\boldsymbol{H} - \boldsymbol{B} \times (\nabla \times \boldsymbol{H})\right] - \frac{\partial}{\partial t}(\boldsymbol{D} \times \boldsymbol{B}) \end{aligned}$$

Through the vector calculus identity

$$\boldsymbol{A} \times (\nabla \times \boldsymbol{A}) = \tfrac{1}{2}\nabla(\boldsymbol{A} \cdot \boldsymbol{A}) - (\boldsymbol{A} \cdot \nabla)\boldsymbol{A}$$

$$\begin{aligned} \boldsymbol{f} &= \left[(\nabla \cdot \boldsymbol{D})\,\boldsymbol{E} + (\boldsymbol{D} \cdot \nabla)\,\boldsymbol{E}\right] + \left[(\nabla \cdot \boldsymbol{B})\,\boldsymbol{H} + (\boldsymbol{B} \cdot \nabla)\,\boldsymbol{H}\right] \\ &\quad - \tfrac{1}{2}\,\nabla(\boldsymbol{D} \cdot \boldsymbol{E} + \boldsymbol{B} \cdot \boldsymbol{H}) - \frac{\partial}{\partial t}(\boldsymbol{D} \times \boldsymbol{B}) \\ &= \nabla \cdot (\boldsymbol{D} \otimes \boldsymbol{E} + \boldsymbol{B} \otimes \boldsymbol{H}) - \tfrac{1}{2}\nabla(\boldsymbol{D} \cdot \boldsymbol{E} + \boldsymbol{B} \cdot \boldsymbol{H}) - \frac{\partial}{\partial t}(\boldsymbol{D} \times \boldsymbol{B}) \end{aligned}$$

where $\otimes$ is the dyadic product, or tensor product.[1] It can be shown that

$$\nabla(\boldsymbol{D} \cdot \boldsymbol{E}) = \nabla \cdot \big((\boldsymbol{D} \cdot \boldsymbol{E})\,\boldsymbol{I}\big)$$

where $\boldsymbol{I}$ is the identity matrix. Therefore

$$\boldsymbol{f} = \nabla \cdot \Big(\underbrace{\boldsymbol{D} \otimes \boldsymbol{E} + \boldsymbol{B} \otimes \boldsymbol{H} - \tfrac{1}{2}(\boldsymbol{D} \cdot \boldsymbol{E} + \boldsymbol{B} \cdot \boldsymbol{H})\,\boldsymbol{I}}_{\overleftrightarrow{M}}\Big) - \frac{\partial}{\partial t}\Big(\varepsilon\mu\,\underbrace{\boldsymbol{E} \times \boldsymbol{H}}_{\boldsymbol{S}}\Big)$$

$$\boldsymbol{f} = \nabla \cdot \overleftrightarrow{\boldsymbol{M}} - \varepsilon\mu\frac{\partial \boldsymbol{S}}{\partial t}$$

This equation fully shows the force due to the presence of the electromagnetic fields. $\overleftrightarrow{\boldsymbol{M}}$ is the Maxwell Stress Tensor (MST), while $\boldsymbol{S}$ is the Poynting vector, representing either a sort of electromagnetic momentum density or alternatively the directional energy flux density. Noticing that the last term on the RHS derives from the rate of change in time of the displacement field, in the quasi-magnetostatic case (usual for electrical machines) it can be neglected. Thus

$$\boldsymbol{f} = \nabla \cdot \overleftrightarrow{\boldsymbol{M}} \tag{B.10}$$

In order to get the total force acting on a body contained in the volume Ω, we integrate

$$\boldsymbol{F} = \int_{\Omega} \nabla \cdot \overleftrightarrow{\boldsymbol{M}}\ \mathrm{d}V = \oint_{\Sigma} \overleftrightarrow{\boldsymbol{M}} \cdot \hat{\boldsymbol{n}}\ \mathrm{d}S \tag{B.11}$$

1 Let $\boldsymbol{a}$ and $\boldsymbol{b}$ be two column vectors: the dot (scalar) product can be defined as

$$\boldsymbol{a} \cdot \boldsymbol{b} = \boldsymbol{a}^{\mathrm{T}}\boldsymbol{b} = \sum_i a_i\, b_i$$

while the dyadic product is defined as

$$\boldsymbol{a} \otimes \boldsymbol{b} = \boldsymbol{a}\,\boldsymbol{b}^{\mathrm{T}} = \begin{bmatrix} a_1 b_1 & \cdots & a_1 b_n \\ \vdots & \ddots & \vdots \\ a_n b_1 & \cdots & a_n b_n \end{bmatrix}$$

Therefore in order to compute the total electromagnetic force acting on a body enclosed by the surface Σ (where $\Sigma = \partial\Omega$ is the boundary of Ω), it is sufficient to compute the flux of the MST through it.

The MST can be written also as

$$\sigma_{ij} = D_i E_j - \tfrac{1}{2}\delta_{ij} \sum_k D_k E_k + B_i H_j - \tfrac{1}{2}\delta_{ij} \sum_k B_k H_k$$

where δ_{ij} is the Kronecker's delta.[2]

Even though electrical machines have the adjective electrical, the electromechanical energy conversion is realized through the interaction of magnetic fields. So the electrical terms in the MST are not needed in the following:

$$\overleftrightarrow{M} = \boldsymbol{B} \otimes \boldsymbol{H} - \tfrac{1}{2}(\boldsymbol{B} \cdot \boldsymbol{H})\boldsymbol{I} \tag{B.12}$$

The second term on the RHS resembles the magnetic pressure (which is also the energy density), and it contributes to the MST only in the diagonal terms. Hence in the cartesian coordinate system

$$\overleftrightarrow{M} = \begin{bmatrix} \frac{1}{2}B_x H_x - \frac{1}{2}B_y H_y - \frac{1}{2}B_z H_z & B_x H_y & B_x H_z \\ B_y H_x & \frac{1}{2}B_y H_y - \frac{1}{2}B_x H_x - \frac{1}{2}B_z H_z & B_y H_z \\ B_z H_x & B_z H_y & \frac{1}{2}B_y H_y - \frac{1}{2}B_x H_x - \frac{1}{2}B_y H_y \end{bmatrix} \tag{B.13}$$

However, typical electrical machines have a cylindrical rotor, so it is rather convenient to express the MST in cylindrical coordinates and in terms of stresses:

$$\overleftrightarrow{M} = \begin{bmatrix} \sigma_{rr} & \sigma_{r\theta} & \sigma_{rz} \\ \sigma_{\theta r} & \sigma_{\theta\theta} & \sigma_{\theta z} \\ \sigma_{zr} & \sigma_{z\theta} & \sigma_{zz} \end{bmatrix} \tag{B.14}$$

At this point, the electromagnetic torque generated by the machine will be the electromagnetic torque times the lever arm. If R is the rotor radius, the lever arm vector (in cylindrical coordinates) is

$$\boldsymbol{b} = \{R, 0, 0\}^{\mathrm{T}}$$

and the torque

$$\boldsymbol{T}_{\mathrm{em}} = \boldsymbol{F} \times \boldsymbol{b}$$

where $\times$ is the vector (cross) product of vectors. After some simple steps, we would get

$$\boldsymbol{T}_{\mathrm{em}} = \{0, RF_z, -RF_\theta\}^{\mathrm{T}}$$

2 It is simply

$$\delta_{ij} = \begin{cases} 1 & \text{if } i = j \\ 0 & \text{if } i \neq j \end{cases}$$

What we are interested in is the last term, so $T_{\mathrm{m},z} = RF_\theta$, regardless of the sign.

Since we are adopting cylindrical coordinates, the normal versor in (B.11) is simply $\hat{\boldsymbol{r}} = \{1, 0, 0\}^{\mathrm{T}}$, and so

$$\overleftrightarrow{\boldsymbol{M}} \cdot \hat{\boldsymbol{n}} = \overleftrightarrow{\boldsymbol{M}} \cdot \hat{\boldsymbol{r}} = \begin{bmatrix} \sigma_{rr} & \sigma_{r\theta} & \sigma_{rz} \\ \sigma_{\theta r} & \sigma_{\theta\theta} & \sigma_{\theta z} \\ \sigma_{zr} & \sigma_{z\theta} & \sigma_{zz} \end{bmatrix} \cdot \begin{Bmatrix} 1 \\ 0 \\ 0 \end{Bmatrix} = \begin{Bmatrix} \sigma_{rr} \\ \sigma_{\theta r} \\ \sigma_{zr} \end{Bmatrix}$$

Therefore, choosing a cylinder as the integration surface right at the rotor periphery, we can look at the tangential component of the force only, expressed as

$$\begin{aligned} F_\theta &= \oint_\Sigma \sigma_{\theta r} \, \mathrm{d}S \\ &= L \oint_0^{2\pi} \sigma_{\theta r} R \, \mathrm{d}\theta \\ &= 2\pi R L \langle \sigma_{\theta r} \rangle \end{aligned} \tag{B.15}$$

where L is the active length of the machine, and $\langle \sigma_{\theta r} \rangle$ is the average air-gap stress. So the torque results simply

$$T_{\mathrm{em}} = 2\pi R^2 L \langle \sigma_{\theta r} \rangle = 2V_{\mathrm{r}} \langle \sigma_{\theta r} \rangle \tag{B.16}$$

where V_{r} is the rotor volume, and

$$\langle \sigma_{\theta r} \rangle = \langle B_\theta H_r \rangle = \langle B_r H_\theta \rangle = \langle \sigma_{r\theta} \rangle$$

because of the symmetry of the MST. If the stator current is distributed on an infinitely thin sheet $H_\theta = K_{\mathrm{s}}$, where K_{s} is the electric loading. If this quantity and the air-gap magnetic flux density are sinusoidally distributed quantities

$$\langle \sigma_{r\theta} \rangle = \frac{\hat{B}_r \hat{H}_\theta}{2} = \frac{\hat{B}_{\mathrm{g}} \hat{K}_{\mathrm{s}}}{2}$$

Doing the last step

$$T_{\mathrm{em}} = V_{\mathrm{r}} \, \hat{B}_{\mathrm{g}} \hat{K}_{\mathrm{s}} \tag{B.17}$$

we would get Esson's rule.

C

RADIAL BASIS FUNCTION INTERPOLATION

C.1 THEORY

A Radial Basis Function (RBF) is a real-valued function, ϕ, whose value depends only on the distance from the origin. Any function that satisfies the property $\phi(\boldsymbol{x}) = \phi(\|\boldsymbol{x}\|)$ is a radial function.

RBFs are commonly used to build up function approximations of the form

$$y(\boldsymbol{x}) = \sum_{j=1}^{N} w_j \, \phi(\|\boldsymbol{x} - \boldsymbol{x}_j\|) \tag{C.1}$$

where $\boldsymbol{x}_j$ are the sampled data points. To find the best approximations, we should tune the parameters (weights) w_j.

RBFs are used to interpolate functions too, so the weights can be found from the solution of the linear system

$$y(\boldsymbol{x}_i) = \sum_{j=1}^{N} w_j \, \phi(\|\boldsymbol{x}_i - \boldsymbol{x}_j\|) \qquad \forall i \tag{C.2}$$

Even though the RBFs may be nonlinear, this system is nonetheless linear in the weights w_j, which are our unknowns. In fact $\phi(\|\boldsymbol{x}_i - \boldsymbol{x}_j\|) = \phi_{ij}$ which is just a number. Then

$$\boldsymbol{\Phi} \boldsymbol{w} = \boldsymbol{y} \quad \Rightarrow \quad \boldsymbol{w} = \boldsymbol{\Phi}^{-1} \boldsymbol{y} \tag{C.3}$$

C.1.1 *Types of Radial Basis Functions*

Let $r = \|\boldsymbol{x} - \boldsymbol{c}\|$, where $\boldsymbol{c}$ is the center of the RBF, and let ε be the inverse of a critical radius, h. Some of the possible RBFs are:

GAUSSIAN

$$\phi(r) = \mathrm{e}^{-(\varepsilon r)^2}$$

MULTIQUADRIC

$$\phi(r) = \sqrt{1 + (\varepsilon r)^2}$$

INVERSE QUADRATIC

$$\phi(r) = \frac{1}{1 + (\varepsilon r)^2}$$

INVERSE MULTIQUADRIC

$$\phi(r) = \frac{1}{\sqrt{1 + (\varepsilon r)^2}}$$

LINEAR

$$\phi(r) = r$$

POLYHARMONIC SPLINE

$$\phi(r) = r^k, \qquad k = 1, 3, 5, \ldots$$

$$\phi(r) = r^k \ln r, \qquad k = 2, 4, 6, \ldots$$

CUBIC SPLINE

$$\phi(r) = r^3$$

MULTILOG SPLINE

$$\phi(r) = \ln[1 + (\varepsilon r)^2]$$

EXPONENTIAL

$$\phi(r) = \mathrm{e}^{-r}$$

RATIONAL QUADRATIC

$$r^2(1 + r^2)$$

THIN PLATE SPLINE

$$r^2 \ln r$$

C.2 TESTS

C.2.1 *1D sinusoid*

Let the real function be

$$y = f(x) = -\sin 3x \tag{C.4}$$

in the compact domain $[-1, 1]$. We are going to approximate the function through an RBF network. And we will try with a different number of samples.

C.2.1.1 *Gaussian RBF linear vs random distribution*

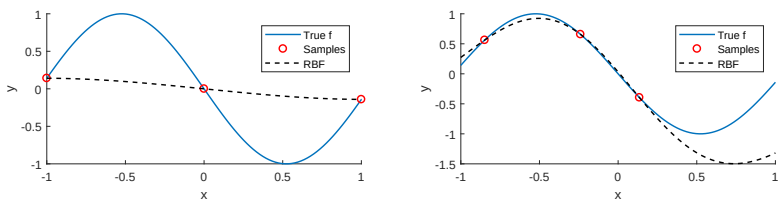

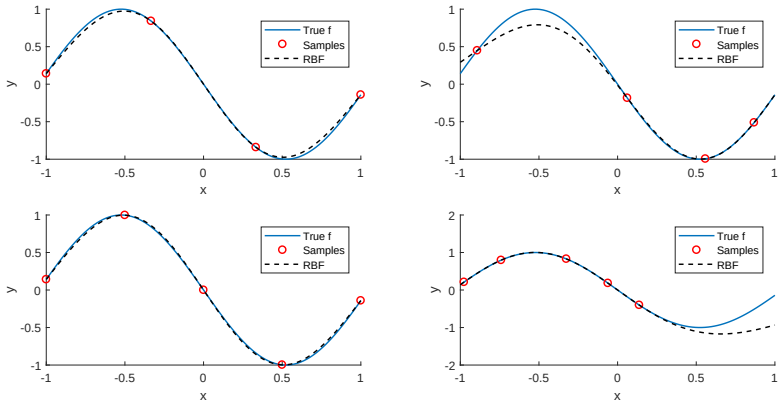

C.2.2 *1D faster sinusoids*

In the same domain, our function is now

$$f(x) = 1 + \sin 2x \cos 5x \tag{C.5}$$

Intuitively, a good approximation of the function requires more sample points.

C.2.2.1 *Gaussian RBF linear vs random distribution*

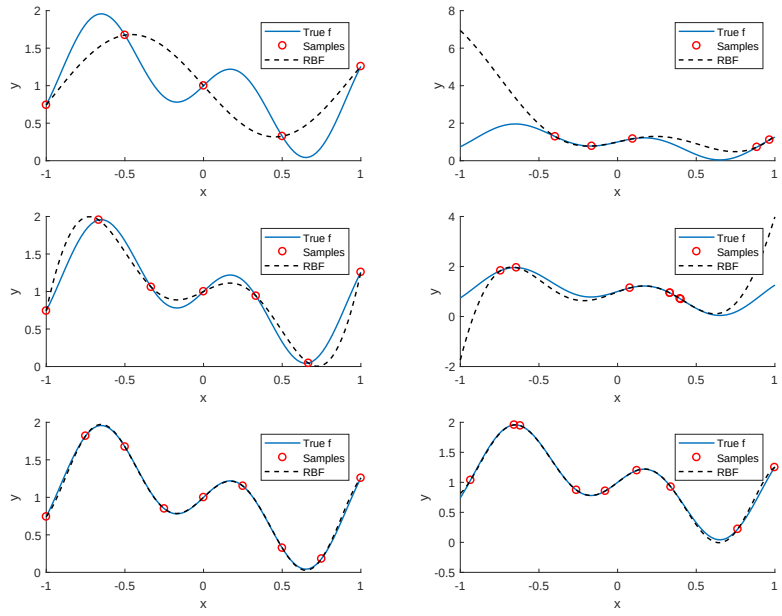

C.2.3 *2D sinusoids*

$$f(x, y) = \cos x \sin 2y + 0.1y \tag{C.6}$$

C.2.3.1 *Gaussian RBF linear vs random distribution*

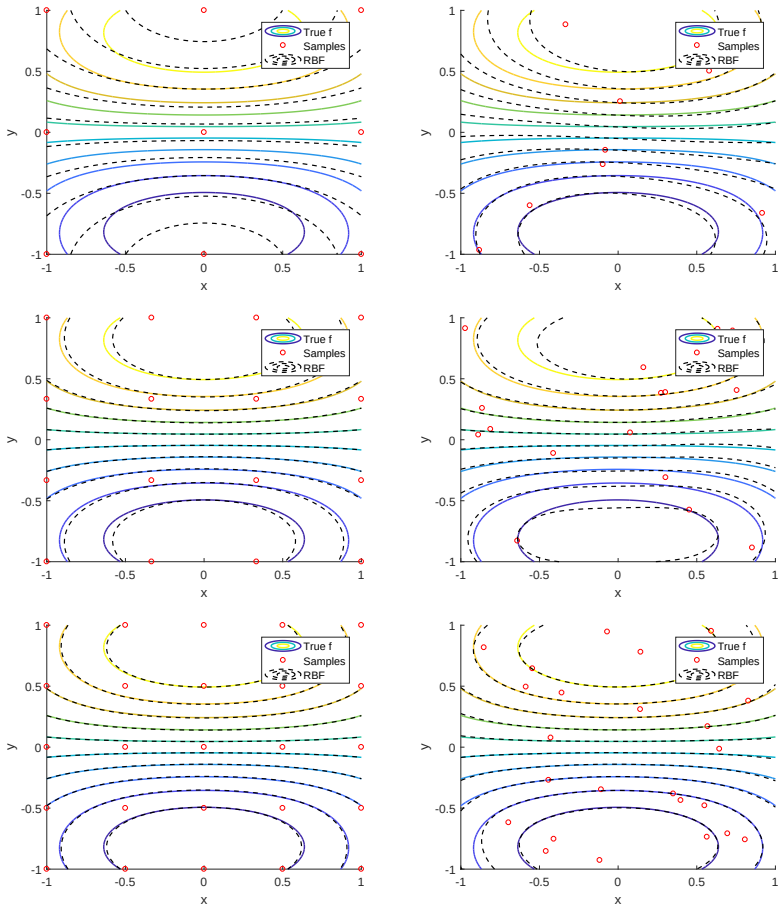

C.3 2D CAMEL FUNCTION

The 2D camel function is

$$z = f(x, y) = 4x^2 - 2.1x^4 + \frac{1}{3}x^6 + xy - 4y^2 + 4y^4 \tag{C.7}$$

This function is often used as an example for single objective optimization due to the presence of two equal minima and to its flatness around this area.

C.3.1 *Gaussian RBF linear vs random distribution*

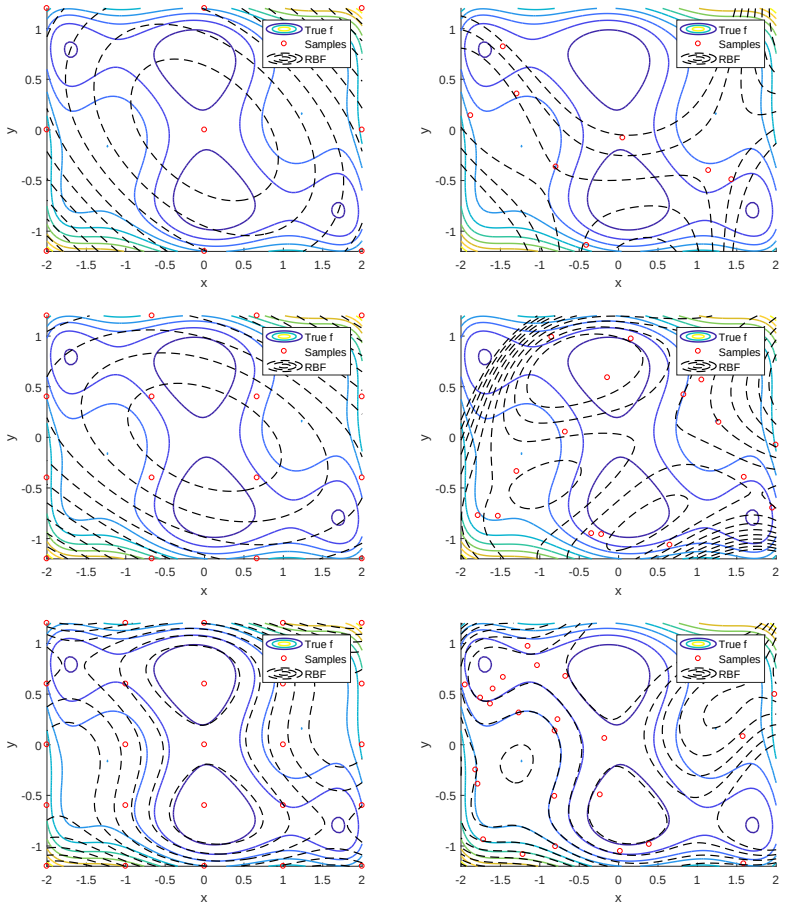

C.4 ERROR ESTIMATION

Since in general we do not know the function we are interpolating and/or approximating, we need an estimation of the error based on our observations only. The most commonly used method is the leave-out-one (LOO) technique. It basically means to build the model N times (where N is the number of samples), leaving out one sample at a time. Let k be the sample that we drop from the training set, $\boldsymbol{w}^{(-k)}$ the weights computed without sample k, $\tilde{y}^{(-k)}$ the function estimation without such sample.

$$\boldsymbol{w}^{(-k)} = \boldsymbol{\Phi}_{(-k)}^{-1} \boldsymbol{y}^{(-k)} \tag{C.8}$$

$$\tilde{y}_k^{(-k)} = \tilde{y}^{(-k)}(\boldsymbol{x}_k) = \sum_{j \neq k} w_j^{(-k)} \phi(\|\boldsymbol{x}_k - \boldsymbol{x}_j\|) \tag{C.9}$$

Then our estimation error is the average of the errors we are making each time we drop one sample:

$$EE = \frac{1}{N}\sum_{k=1}^{N}\left(y_k - \tilde{y}_k^{(-k)}\right)^2 \tag{C.10}$$

We are going to define also the individual LOO errors, as

$$ee_k = \left(y_k - \tilde{y}_k^{(-k)}\right)^2 \tag{C.11}$$

$$EE = \frac{1}{N}\sum_{k=1}^{N} ee_k \tag{C.12}$$

Since we would like to have these errors as relative quantities, we are going to normalize them

$$\xi_k = \left(\frac{y_k - \tilde{y}_k^{(-k)}}{\max_j y_j - \min_j y_j}\right)^2 \tag{C.13}$$

$$\Xi = \frac{1}{N}\sum_{k=1}^{N}\xi_k \tag{C.14}$$

C.5 SELECTION OF THE CRITICAL RADIUS h

If the sample points are uniformly distributed, it is reasonable to assign to each point a region of space proportional to the total amount of space divided by the number of sample points. Let D be the domain maximum dimension

$$D = \prod_{l=1}^{N}\left[\max_i x_l^{(i)} - \min_i x_l^{(i)}\right] \tag{C.15}$$

then

$$h \propto \sqrt[d]{\frac{D}{N}} \tag{C.16}$$

where d is the number of features of the inputs.[1] A good guess could be

$$h = 3\sqrt[d]{\frac{D}{N}} \tag{C.17}$$

C.5.1 *Normalization*

In order to properly apply RBF interpolation, it is usually necessary to normalize the parameters space to make the radial nature of the function to be effective in every direction.

1 I am not really sure of $\sqrt[d]{\cdot}$ instead of simply $\sqrt{\cdot}$.

Alternatively, one could adopt a critical radius which is a vector, which normalizes the parameters by itself. Therefore, defining

$$\boldsymbol{d} = \{d_l\}_l = \left\{ \max_i x_l^{(i)} - \min_i x_l^{(i)} \right\}_l \tag{C.18}$$

and

$$c = \sqrt[d]{\frac{1}{N}}$$

the vector critical radius results proportional to $\boldsymbol{h} \propto c\boldsymbol{d}$. Empirically, a good value could be

$$\boldsymbol{h} = c\boldsymbol{e}\boldsymbol{d} \tag{C.19}$$

C.6 REGULARIZATION

Sometimes, the values of the weights can become very large, and this generally leads to wrong approximation of the function in the unsampled domain. The function approximating the true function is now of the form:

$$y(\boldsymbol{x}) = \sum_{j=1}^{N} w_j \, \phi(\|\boldsymbol{x} - \boldsymbol{x}_j\|) + \boldsymbol{x}^{\mathrm{T}}\boldsymbol{p} + a \tag{C.20}$$

where $\boldsymbol{p}$ is a vector of "biases", while a is a scalar bias. So we introduced $(d+1)$ biases. Therefore, we need $(d+1)$ additional equations. Let us rewrite the previous equation in a matrix form

$$y(\boldsymbol{x}) = \phi(\|\boldsymbol{x} - \boldsymbol{C}\|)\boldsymbol{w} + \{1 \quad \boldsymbol{x}^{\mathrm{T}}\}\boldsymbol{b} \tag{C.21}$$

where $\boldsymbol{C}$ is a matrix containing all the samples along its columns and $\boldsymbol{b}$ has been defined as

$$\boldsymbol{b} = \begin{Bmatrix} a \\ \boldsymbol{p} \end{Bmatrix}$$

Now, to find the weights and the biases we have to solve the following system:

$$\begin{cases} \boldsymbol{\Phi}\boldsymbol{w} + \{\mathbf{1} \quad \boldsymbol{X}^{\mathrm{T}}\}\boldsymbol{b} = \boldsymbol{y} \\ \{\mathbf{1} \quad \boldsymbol{X}^{\mathrm{T}}\}^{\mathrm{T}}\boldsymbol{w} = \mathbf{0} \end{cases} \tag{C.22}$$

Defining $\boldsymbol{S} = \{\mathbf{1} \quad \boldsymbol{X}^{\mathrm{T}}\}$, we can have the same system in matrix form:

$$\underbrace{\begin{bmatrix} \boldsymbol{\Phi} & \boldsymbol{S} \\ \boldsymbol{S}^{\mathrm{T}} & \mathbf{0} \end{bmatrix}}_{\boldsymbol{M}} \cdot \underbrace{\begin{Bmatrix} \boldsymbol{w} \\ \boldsymbol{b} \end{Bmatrix}}_{\boldsymbol{z}} = \underbrace{\begin{Bmatrix} \boldsymbol{y} \\ \mathbf{0} \end{Bmatrix}}_{\boldsymbol{g}} \tag{C.23}$$

and finally

$$\boldsymbol{z} = \boldsymbol{M}^{-1}\boldsymbol{g} \tag{C.24}$$

D

IRON LOSSES INSIGHTS

In this chapter, some insights on iron losses are investigated.

D.1 EDDY CURRENTS IRON LOSSES COEFFICIENT

Consider an infinitely long conductive sheet of thickness d along the y-axis, depicted in Figure D.1. Let $\boldsymbol{B}(t)$ be the forcing time-varying magnetic flux density, parallel to the z-axis

$$\boldsymbol{B}(t) = \{0, 0, B_z(t)\}^{\mathrm{T}}$$

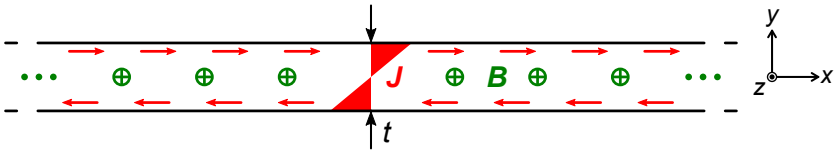

Figure D.1
Conductive lamination sheet of thickness d and chosen reference frame.

Recalling Faraday–Neumann–Henry–Lenz's law

$$\nabla \times \boldsymbol{E} = -\frac{\partial \boldsymbol{B}}{\partial t}$$

Since $\boldsymbol{B}$ has z-component only, $\nabla \times \boldsymbol{E}$ must be parallel to it.

$$(\nabla \times \boldsymbol{E}) \cdot \hat{\boldsymbol{z}} = \partial_x E_y - \partial_y E_x$$

Looking at Figure D.1, we can see that eddy currents are directed along the x-axis only. And because of the constitutive equation (Ohm's law)[1]

$$\boldsymbol{J} = \sigma \boldsymbol{E}$$

the $\boldsymbol{E}$ field must have x-component only. Therefore

$$\begin{aligned} -\partial_y E_x &= -\partial_t B_z \\ \frac{\partial E_x}{\partial y} &= \frac{\partial B_z}{\partial t} \end{aligned} \tag{D.1}$$

This is a first order one-dimensional partial differential equation. Employing Steinmetz (or Fourier) transform, we can transform it into a complex first order ordinary differential equation.[2]

$$\frac{\mathrm{d}\underline{E}_x}{\mathrm{d}y} = \mathrm{j}\omega \underline{B}_z \tag{D.2}$$

1 Assuming a uniform, homogeneous and isotropic material.
2 With '_' we denote a phasor quantity. In this case, the phasor expresses the peak value of the underlying quantity.

Since $\underline{B}_z$ is supposed to be imposed and uniform, this differential equation is trivial to solve, and thanks to the proper choice of the reference frame, the integration constant is zero.

$$\underline{E}_x = \mathrm{j}\omega \underline{B}_z y$$

As shown in Figure D.1, both the electric field and the current density field have a linear distribution along the y-coordinate. In fact:

$$\underline{J}_x = \mathrm{j}\omega\sigma \underline{B}_z y \tag{D.3}$$

Now we can compute the associated power losses due to eddy currents. Also the losses will result a function of the y-coordinate[3]

$$p_J = \frac{1}{2}\rho|\underline{J}_x|^2 = \frac{1}{2}\omega^2\sigma\underline{B}_z^2 y^2$$

At this point we can compute the space average of these power losses, doing

$$\begin{aligned}\langle p_J \rangle &= \frac{1}{d}\int_{-\frac{d}{2}}^{\frac{d}{2}} \frac{1}{2}\omega^2\sigma\underline{B}_z^2 y^2 \,\mathrm{d}y \\ &= \frac{\omega^2\sigma\underline{B}_z^2}{2d}\left.\frac{y^3}{3}\right|_{-\frac{d}{2}}^{\frac{d}{2}} \\ &= \frac{\omega^2\sigma\underline{B}_z^2 d^2}{24} = \frac{4\pi^2 f^2\sigma\underline{B}_z^2 d^2}{24} = \frac{\pi^2\sigma d^2}{6}\underline{B}_z^2 f^2\end{aligned}$$

At this point, we can define the eddy currents coefficient, g_{ec}, as

$$g_{\mathrm{ec}} = \frac{\pi^2\sigma d^2}{6\gamma} \qquad [\mathrm{W}/(\mathrm{kg}\,\mathrm{T}^2\,\mathrm{Hz}^2)] \tag{D.4}$$

where γ is the volumetric mass density of the material.

D.2 ELEMENT-BY-ELEMENT IRON LOSSES

The partial differential equation which governs low frequency electromagnetic problems is the following:

$$\nabla \times \nu\nabla \times \boldsymbol{A} = \boldsymbol{J} \tag{D.5}$$

The current density vector may be due to many causes, in particular to the supply or to eddy currents.

$$\begin{aligned}&\nabla \times \nu\nabla \times \boldsymbol{A} = \boldsymbol{J}_{\mathrm{s}} - \sigma\nabla V - \sigma\frac{\partial \boldsymbol{A}}{\partial t} && \text{with e.c. and voltage supply} \\ &-\nabla\cdot\nu\nabla A_z = J_{\mathrm{s}} - \sigma\frac{\partial A_z}{\partial t} && \text{in 2D} \\ &-\nabla\cdot\nu\nabla \underline{A}_z = \underline{J}_{\mathrm{s}} - \mathrm{j}\omega\sigma\underline{A}_z && \text{in 2D and in frequency} \\ &\nabla\cdot\nu\nabla\underline{A}_z - \mathrm{j}\omega\sigma\underline{A}_z + \underline{J}_{\mathrm{s}} = 0 && \text{standard form}\end{aligned}$$

3 We need the factor 1/2 because we are using phasors with peak values.

D.2.1 *Permanent Magnets eddy currents*

In magnets we have to guarantee that only zero-sum currents flow.

$$\int_{\Omega_{\mathrm{PM}}} J_{\mathrm{eddy}}\,\mathrm{d}S = 0 \tag{D.6}$$
$$J_{\mathrm{eddy}}(x,y,t) = -\frac{\partial A_z(x,y,t)}{\partial t}$$

But if we were to compute the eddy currents with the derivative, errors due to noise may occur. We want to show that imposing (D.6) in time is the same as imposing it in frequency. In fact, we can write

$$J_{\mathrm{eddy}}(x,y,t) = \sum_{h=1}^{+\infty} j_h(x,y)\,\mathrm{e}^{\mathrm{j}h\omega t}$$

and substitute in (D.6):

$$\int_{\Omega_{\mathrm{PM}}} \sum_{h=1}^{+\infty} j_h(x,y)\,\mathrm{e}^{\mathrm{j}h\omega t}\,\mathrm{d}S = 0$$
$$\sum_{h=1}^{+\infty} \mathrm{e}^{\mathrm{j}h\omega t} \int_{\Omega_{\mathrm{PM}}} j_h(x,y)\,\mathrm{d}S = 0$$

Since the basis functions $\mathrm{e}^{\mathrm{j}h\omega t}$ are never zero, we need

$$\int_{\Omega_{\mathrm{PM}}} j_h(x,y)\,\mathrm{d}S = 0$$

which is valid for every time instant, as requested.

D.2.2 *Harmonic iron losses*

Iron losses in ferromagnetic material can be estimated knowing the time variation of the flux density in each part of the machine. In FEA, the flux density components $(B_x(t), B_y(t))$ are known in every mesh element. Referring to them as $(B_x^e(t), B_y^e(t))$, we can express them in Fourier series as

$$B_x^e(t) = \sum_{h=0}^{\infty} B_{xh}^e \cos(h\omega t - \phi_h)$$
$$B_y^e(t) = \sum_{h=0}^{\infty} B_{yh}^e \cos(h\omega t - \psi_h)$$

Since iron losses depend on the square of the element flux densities, we can write

$$B_{h,e}^2 = (B_{xh}^e)^2 + (B_{yh}^e)^2$$

Determining appropriately the hysteresis and iron losses coefficients, one could express the iron losses due to all the harmonics as

$$p_{\mathrm{Fe}}^e = \sum_{h=1}^{+\infty} \left(c_{\mathrm{hy}} B_{h,e}^2 h f + c_{\mathrm{ec}} B_{h,e}^2 h^2 f^2 \right) \qquad [\mathrm{W/kg}]$$

To get the total iron losses, we multiply the element iron losses with the respective element weight:

$$P_{\mathrm{Fe}} = \sum_{e=1}^{N_{\mathrm{e}}} \sum_{h=1}^{+\infty} \left(c_{\mathrm{hy}} B_{h,e}^2 h f + c_{\mathrm{ec}} B_{h,e}^2 h^2 f^2 \right) \gamma V_e \qquad [\mathrm{W}] \tag{D.7}$$

where N_{e} is the number of mesh elements of the iron, γ is the material volumetric mass density and V_e is the volume of the element e.

E

HIGH-FREQUENCY SIGNAL INJECTION MATHEMATICAL MODEL

Start from the general voltage equation of any passive-rotor[1] synchronous electric machine:

$$\begin{cases} u_d = Ri_d + \dfrac{\mathrm{d}\lambda_d}{\mathrm{d}t} - \omega_{\mathrm{me}}\lambda_q \\ u_q = Ri_q + \dfrac{\mathrm{d}\lambda_q}{\mathrm{d}t} + \omega_{\mathrm{me}}\lambda_d \end{cases} \tag{E.1}$$

At low speed

$$\begin{cases} u_d = Ri_d + \dfrac{\mathrm{d}\lambda_d}{\mathrm{d}t} \\ u_q = Ri_q + \dfrac{\mathrm{d}\lambda_q}{\mathrm{d}t} \end{cases} \tag{E.2}$$

Neglecting the resistive terms, considering the small-signal model of the motor and using phasors for these signals

$$\underline{\boldsymbol{U}} = \mathrm{j}\omega \boldsymbol{L} \underline{\boldsymbol{I}} \tag{E.3}$$

Let $\boldsymbol{T}$ be the transformation matrix from the estimated reference frame to the correct one, and $\Delta\vartheta$ the estimation error angle:

$$\boldsymbol{T} = \begin{bmatrix} \cos\Delta\vartheta & -\sin\Delta\vartheta \\ \sin\Delta\vartheta & \cos\Delta\vartheta \end{bmatrix}$$

Defining $\boldsymbol{\Gamma} = \boldsymbol{L}^{-1}$, we could write:

$$\begin{aligned} \underline{\boldsymbol{I}} &= \frac{1}{\mathrm{j}\omega}\boldsymbol{\Gamma}\underline{\boldsymbol{U}} \\ \boldsymbol{T}\underline{\tilde{\boldsymbol{I}}} &= \frac{1}{\mathrm{j}\omega}\boldsymbol{\Gamma}\boldsymbol{T}\underline{\tilde{\boldsymbol{U}}} \\ \boldsymbol{T}^{-1}\boldsymbol{T}\underline{\tilde{\boldsymbol{I}}} &= \frac{1}{\mathrm{j}\omega}\boldsymbol{T}^{-1}\boldsymbol{\Gamma}\boldsymbol{T}\underline{\tilde{\boldsymbol{U}}} \\ \underline{\tilde{\boldsymbol{I}}} &= \frac{1}{\mathrm{j}\omega}\tilde{\boldsymbol{\Gamma}}\underline{\tilde{\boldsymbol{U}}} \end{aligned}$$

where

$$\boldsymbol{\Gamma} = \frac{1}{\ell_d\ell_q - \ell_{dq}^2}\begin{bmatrix} \ell_q & -\ell_{qd} \\ -\ell_{dq} & \ell_q \end{bmatrix} \tag{E.4}$$

$$\tilde{\boldsymbol{\Gamma}} = \frac{1}{\ell_d\ell_q - \ell_{dq}^2}\begin{bmatrix} \ell_\Sigma + \ell_\Delta\cos 2\Delta\vartheta - \ell_{dq}\sin 2\Delta\vartheta & -\ell_\Delta\sin 2\Delta\vartheta - \ell_{dq}\cos 2\Delta\vartheta \\ -\ell_\Delta\sin 2\Delta\vartheta - \ell_{dq}\cos 2\Delta\vartheta & \ell_\Sigma - \ell_\Delta\cos 2\Delta\vartheta + \ell_{dq}\sin 2\Delta\vartheta \end{bmatrix} \tag{E.5}$$

1 no winding on the rotor

E.1 INDUCTION MOTOR

The induction motor requires double the voltage equations needed for its mathematical model

$$\begin{cases} u_{sd} = R_s i_{sd} + \dfrac{\mathrm{d}\lambda_{sd}}{\mathrm{d}t} - \omega_s \lambda_{sq} \\ u_{sq} = R_s i_{sq} + \dfrac{\mathrm{d}\lambda_{sq}}{\mathrm{d}t} + \omega_s \lambda_{sd} \\ 0 = R_r i_{rd} + \dfrac{\mathrm{d}\lambda_{rd}}{\mathrm{d}t} - \omega_{\mathrm{sl}} \lambda_{rq} \\ 0 = R_r i_{rq} + \dfrac{\mathrm{d}\lambda_{rq}}{\mathrm{d}t} + \omega_{\mathrm{sl}} \lambda_{rd} \end{cases} \tag{E.6}$$

At low speeds and slips

$$\begin{cases} u_{sd} = R_s i_{sd} + \dfrac{\mathrm{d}\lambda_{sd}}{\mathrm{d}t} \\ u_{sq} = R_s i_{sq} + \dfrac{\mathrm{d}\lambda_{sq}}{\mathrm{d}t} \\ 0 = R_r i_{rd} + \dfrac{\mathrm{d}\lambda_{rd}}{\mathrm{d}t} \\ 0 = R_r i_{rq} + \dfrac{\mathrm{d}\lambda_{rq}}{\mathrm{d}t} \end{cases} \tag{E.7}$$

The fluxes-currents relationships for the induction machine are more complex, since we have more windings and mutual couplings. Let us consider the small-signal model, so the linearized machine model around a specific working point. We are going to refer to (differential) inductances of the same set as ℓ, while to inductances of different set as m. Then, the cause-effect relationship is going to be expressed as $\ell_{\text{effect}}^{\text{cause}}$.

In general,

$$\boldsymbol{\lambda} = \begin{Bmatrix} \lambda_{sd} \\ \lambda_{sq} \\ \lambda_{rd} \\ \lambda_{rq} \end{Bmatrix} = \begin{bmatrix} \ell_{sd}^{sd} & \ell_{sd}^{sq} & m_{sd}^{rd} & m_{sd}^{rq} \\ \ell_{sq}^{sd} & \ell_{sq}^{sq} & m_{sq}^{rd} & m_{sq}^{rq} \\ m_{rd}^{sd} & m_{rd}^{sq} & \ell_{rd}^{rd} & \ell_{rd}^{rq} \\ m_{rq}^{sd} & m_{rq}^{sq} & \ell_{rq}^{rd} & \ell_{rq}^{rq} \end{bmatrix} \begin{Bmatrix} i_{sd} \\ i_{sq} \\ i_{rd} \\ i_{rq} \end{Bmatrix} = \boldsymbol{L}\boldsymbol{i} \tag{E.8}$$

$$\begin{Bmatrix} \lambda_s \\ \lambda_r \end{Bmatrix} = \begin{bmatrix} \boldsymbol{\ell}_s^s & \boldsymbol{m}_s^r \\ \boldsymbol{m}_r^s & \boldsymbol{\ell}_r^r \end{bmatrix} \begin{Bmatrix} \boldsymbol{i}_s \\ \boldsymbol{i}_r \end{Bmatrix}$$

Adopting the same hypotheses as before, we would end up with the same expression of (E.3).

F

IDENTIFICATION OF THE ROTOR DIRECT AXIS

Let us consider the general torque expression in the synchronous reference frame

$$T_\mathrm{m} = \frac{3}{2} p (\lambda_d i_q - \lambda_q i_d) \tag{F.1}$$

Now, using the fluxes-currents relationships of a linear machine

$$\begin{cases} \lambda_d &= \lambda_\mathrm{mg} + L_d i_d \\ \lambda_q &= L_q i_q \end{cases}$$

the torque expression can be further developed

$$\begin{aligned} T_\mathrm{m} &= \frac{3}{2} p \left(\lambda_\mathrm{mg} i_q + L_d i_d i_q - L_q i_q i_d\right) \\ &= \frac{3}{2} p \left(\lambda_\mathrm{mg} i_q - (L_q - L_d) i_d i_q\right) \\ &= \frac{3}{2} p \left(\lambda_\mathrm{mg} i_q - 2 L_\Delta i_d i_q\right) \end{aligned}$$

Let ϑ_i be the current angle and $\vartheta_\mathrm{m}^\mathrm{e}$ the electrical angular position of the rotor, in a generic reference frame. The current can be split in the two components, $i_d = i \cos(\vartheta_i - \vartheta_\mathrm{m}^\mathrm{e})$ and $i_q = i \sin(\vartheta_i - \vartheta_\mathrm{m}^\mathrm{e})$

$$\begin{aligned} T_\mathrm{m} &= \frac{3}{2} p \left[\lambda_\mathrm{mg} i \sin(\vartheta_i - \vartheta_\mathrm{m}^\mathrm{e}) - 2 L_\Delta i^2 \sin(\vartheta_i - \vartheta_\mathrm{m}^\mathrm{e}) \cos(\vartheta_i - \vartheta_\mathrm{m}^\mathrm{e})\right] \\ &= \frac{3}{2} p \left[\lambda_\mathrm{mg} i \sin(\vartheta_i - \vartheta_\mathrm{m}^\mathrm{e}) - L_\Delta i^2 \sin\big(2(\vartheta_i - \vartheta_\mathrm{m}^\mathrm{e})\big)\right] \end{aligned}$$

It is evident the distinction between the permanent magnet torque and the reluctance torque components. The periodicity of the reluctance torque is twice the one of the PM torque. Defining the angle $\alpha_i^\mathrm{e} = \vartheta_i - \vartheta_\mathrm{m}^\mathrm{e}$, the curves can be easily analyzed.

Consider an SPM machine first:

$$T_\mathrm{m} = \frac{3}{2} p \left[\lambda_\mathrm{mg} i \sin \alpha_i^\mathrm{e}\right] \tag{F.2}$$

SPM

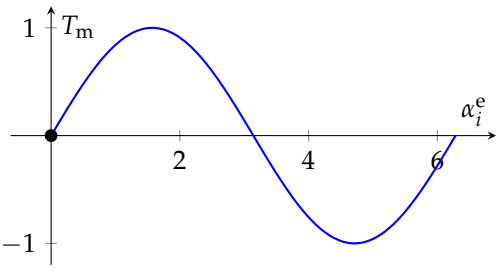

The angle α_i^e can be interpreted as the one that the rotor tends to follow with its zero-torque stable points. Impose a certain angle α_i^e

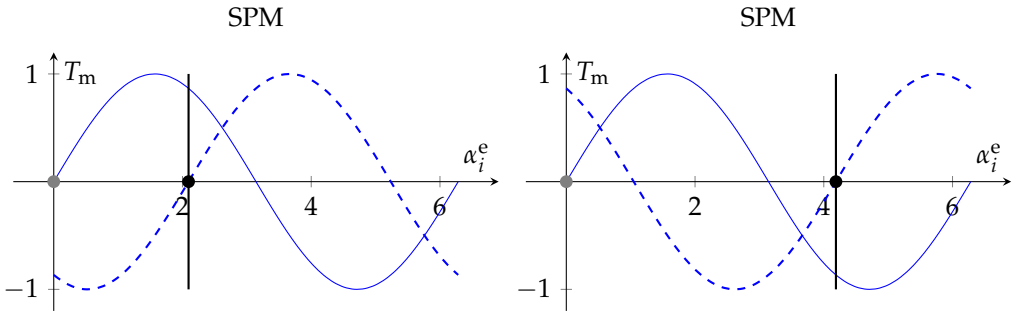

So the current angle α_i^e identifies the torque which pushes the characteristic: if the torque is positive, it pushes it forward, otherwise the torque pushes it backward. This happens until the zero-torque equilibrium point coincides with the imposed angle. Therefore, for an SPM machine, the d-axis is found imposing a DC current and saving the angle where the rotor positions itself.

Now consider a SyR machine

$$T_m = -\frac{3}{2} p \left[L_\Delta i^2 \sin 2\alpha_i^e \right] \tag{F.3}$$

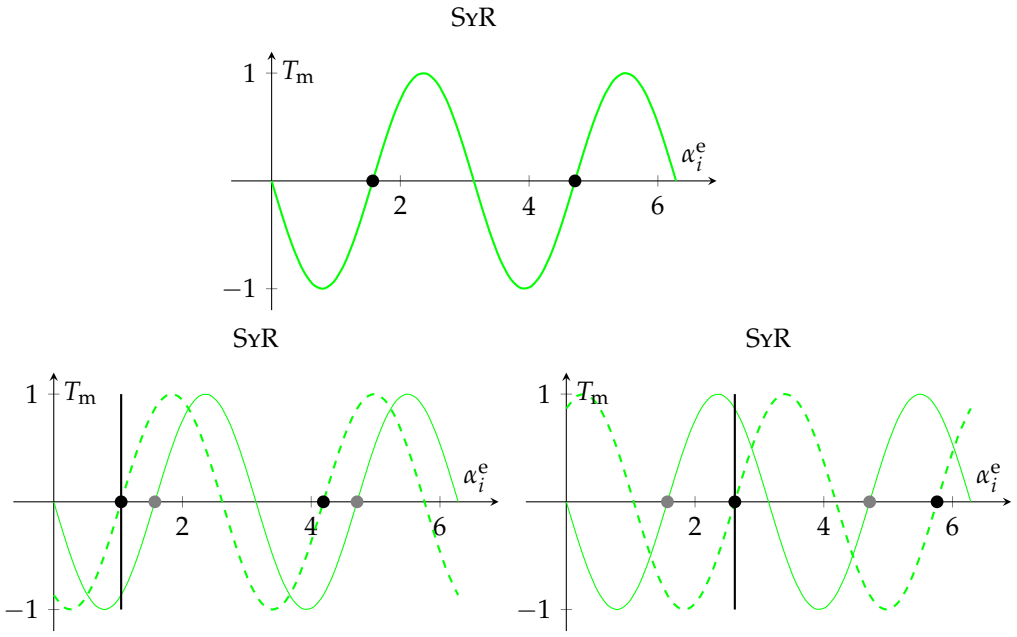

The SyR motor presents the zero-torque stable point at 90° with respect to the d-axis (IPM convention). So when a DC current is applied, it tends to align the q-axis with the current vector. The d-axis position is just 90 degrees in advance.

Some IPM configurations are reported hereafter. If the reluctance torque is low (which means when the anisotropy of the rotor is weak, or when the imposed current is small), the characteristic does not differ much from the SPM one. The equilibrium point is again at 0°.

When the reluctance torque becomes significant, the stable position is in between the stable positions of the SPM and SyR machines.

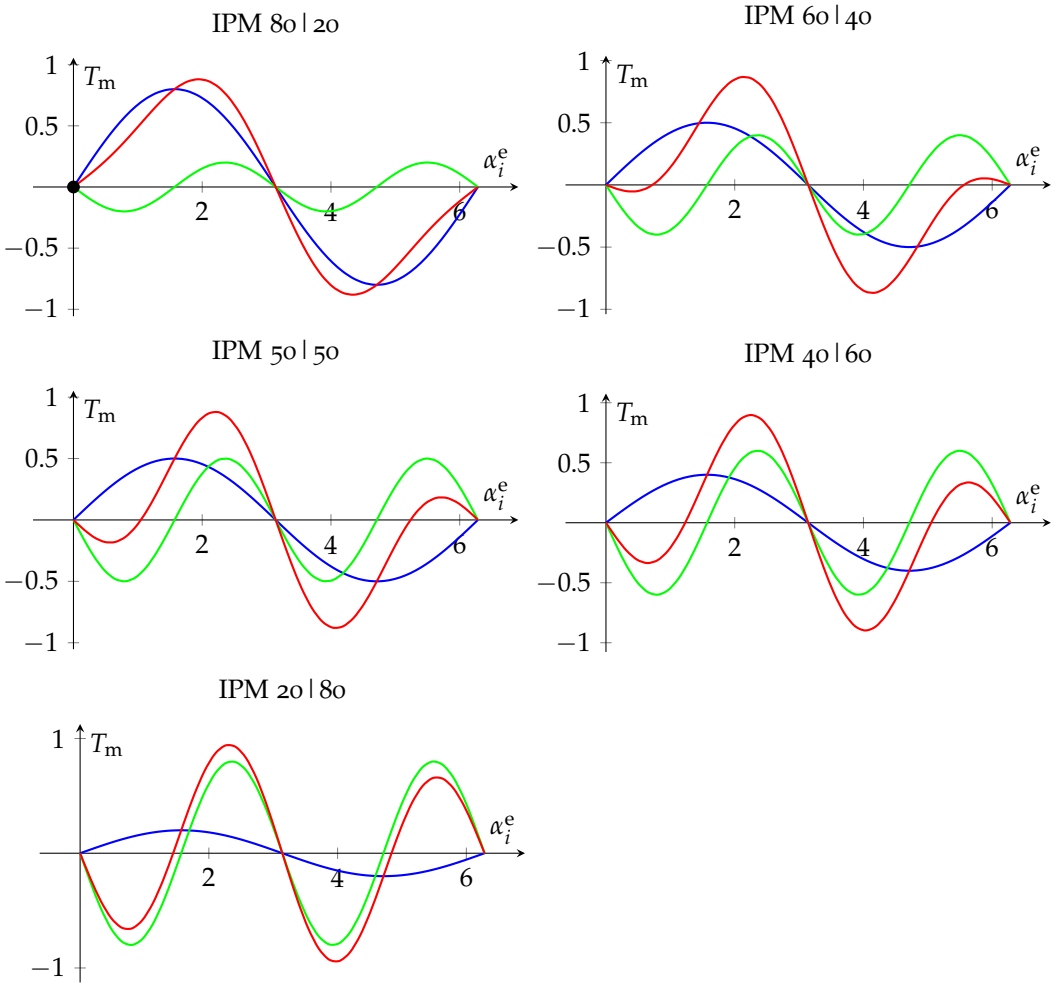

Now, let us focus on the 50 | 50 IPM machine. Applying a DC current we find the first stable point, located between 45 and 90°. The stable points are the ones with positive derivative.

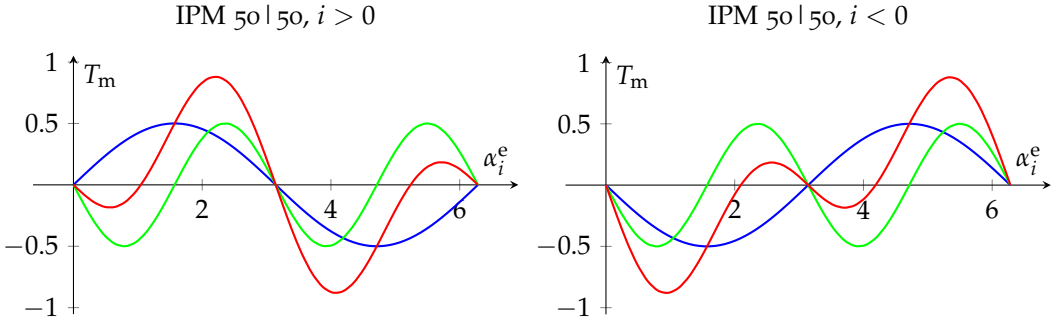

Suppose that the rotor is aligned with the first stable point. Now we reverse the sign of the current (RHS characteristic). In that instant the rotor is in the same position as before, but with a negative torque apply to it. So the characteristic is pushed backward till the new stable point is met. Taking the average between the previous position and the new one, the q-axis can be found.

F.1 DETECTION OF THE QUADRATURE-AXIS POSITION THROUGH THE SUPPLY OF AN ALTERNATING CURRENT

Reconsider the equation of the torque:

$$T_\mathrm{m} = \frac{3}{2} p \Big[\lambda_\mathrm{mg} i \sin \alpha_i^\mathrm{e} - L_\Delta i^2 \sin 2\alpha_i^\mathrm{e} \Big]$$

and let the current be a sinusoidal waveform, with the form

$$i = I \cos \omega t$$

The torque becomes

$$\begin{aligned} T_\mathrm{m} &= \frac{3}{2} p \Big[\lambda_\mathrm{mg} I \cos \omega t \sin \alpha_i^\mathrm{e} - L_\Delta I^2 \cos^2 \omega t \sin 2\alpha_i^\mathrm{e} \Big] \\ &= \frac{3}{2} p \Big[\lambda_\mathrm{mg} I \cos \omega t \sin \alpha_i^\mathrm{e} - \frac{L_\Delta I^2}{2} \sin 2\alpha_i^\mathrm{e} - \frac{L_\Delta I^2}{2} \cos 2\omega t \sin 2\alpha_i^\mathrm{e} \Big] \end{aligned}$$

It is evident that the two side terms have a zero average torque, and the resulting average torque is just the one due to the reluctance of the machine.

$$\langle T_\mathrm{m} \rangle = -\frac{3}{2} p \Big[\frac{L_\Delta I^2}{2} \sin 2\alpha_i^\mathrm{e} \Big] \tag{F.4}$$

The characteristic simply becomes the one of a pure SyRM (with the inconvenience that the torque is half of the full reluctance torque), and the rotor tends to align the q-axis to the current vector.

G

INCREMENTAL PERMEABILITY SIMULATIONS FOR DIFFERENTIAL INDUCTANCES COMPUTATION

In this chapter incremental permeability simulations are used to estimate the differential inductances of the machine around a specific working point.

The considered motor is a synchronous reluctance motor, and its geometry is depicted in Figure G.1.

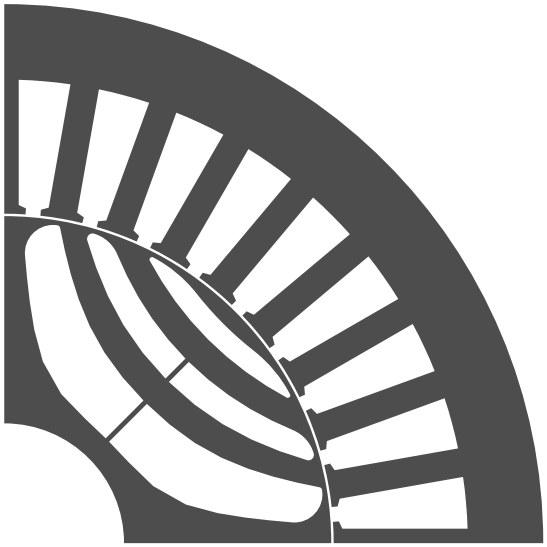

Figure G.1
Geometry of the SyR motor analyzed.

It resulted from a multi-objective optimization, aiming at a high average torque and a low torque ripple. Only the rotor was modified during the optimization.

G.1 DIFFERENTIAL INDUCTANCE COMPUTATION

The fluxes-currents relationships are the following:

$$\begin{aligned} \delta\lambda_d &= \ell_d\,\delta i_d + \ell_{dq}\,\delta i_q \\ \delta\lambda_q &= \ell_{qd}\,\delta i_d + \ell_q\,\delta i_q \end{aligned} \tag{G.1}$$

and to get the differential inductance, we can just do

$$\begin{aligned} \ell_d &= \left.\frac{\delta\lambda_d}{\delta i_d}\right|_{\delta i_q=0} & \ell_{qd} &= \left.\frac{\delta\lambda_q}{\delta i_d}\right|_{\delta i_q=0} \\ \ell_{dq} &= \left.\frac{\delta\lambda_d}{\delta i_q}\right|_{\delta i_d=0} & \ell_q &= \left.\frac{\delta\lambda_q}{\delta i_q}\right|_{\delta i_d=0} \end{aligned} \tag{G.2}$$

and for the reciprocity of the linear mutual inductor $\ell_{dq} = \ell_{qd}$.

To estimate these differential inductances we can do in two ways:

- magneto-static nonlinear simulations around the working point
- magneto-static linear simulations around the working point using the previous element permeability (incremental permeability)

In any case, the number of magneto-static simulations required are three. However, for the former case, they are "full" nonlinear magneto-static simulations, while for the latter only one "full" nonlinear simulation is required, and the following increments are just linear simulations, which are very quick.

In the following, we will compare the two methods.

G.2 PLAIN MAGNETO-STATIC ONLY SIMULATIONS

The most basic idea to compute differential inductances is to look in the neighborhood of the working point, slightly moving the d- and q-axes currents individually.

Let I_N and α_i^e be the rated current vector amplitude and angle. Then

$$I_d = I_\mathrm{N} \cos \alpha_i^\mathrm{e}$$
$$I_q = I_\mathrm{N} \sin \alpha_i^\mathrm{e}$$

The first simulations is done with these currents.

The second one:

$$I_d = I_\mathrm{N} \cos \alpha_i^\mathrm{e} + \delta I$$
$$I_q = I_\mathrm{N} \sin \alpha_i^\mathrm{e}$$

and the third one

$$I_d = I_\mathrm{N} \cos \alpha_i^\mathrm{e}$$
$$I_q = I_\mathrm{N} \sin \alpha_i^\mathrm{e} + \delta I$$

From the post-processed results, it is easy then to derive the increments of the quantities (flux linkages, energies, et cetera) and the differential inductances.

G.3 INCREMENTAL PERMEABILITY SIMULATIONS

For this method, the first simulation required is the same as in the previous case, because we have to extract the incremental and cross-coupling permeability for every mesh element.

The following simulations are just incremental, in the sense that the imposed currents are only the increments. So, for the second simulation

$$I_d = \delta I$$
$$I_q = 0$$

while for the third

$$I_d = 0$$
$$I_q = \delta I$$

The obtained flux linkages are then directly the incremental ones.

G.4 RESULTS COMPARISON

For the previous motor, considering $n_{cs} = 1$, $I_N = 575\,\mathrm{A}$, $\alpha_i^e = 64°$ and $\delta I = I_N/1000$, the results are the following:

	Nonlinear	Incremental
T [s]	10.5	6.5
ℓ_d	$6.9223 \cdot 10^{-5}$	$6.9359 \cdot 10^{-5}$
ℓ_{qd}	$-1.4570 \cdot 10^{-5}$	$-1.4582 \cdot 10^{-5}$
ℓ_{dq}	$-1.4578 \cdot 10^{-5}$	$-1.4582 \cdot 10^{-5}$
ℓ_q	$3.6114 \cdot 10^{-5}$	$3.6121 \cdot 10^{-5}$

It can be noted that the "full" nonlinear simulation takes about 60% longer time to complete. While this seems quite a lot, in an optimization function evaluation, which lasts about 100 s for this motor example, it reduces to a 3% saving time.

These results were obtained before the `21Apr2019` release of FEMM, which introduced the possibility to start the linearized system from the previous nonlinear solution. So the use of the incremental permeability technique is less justified when computing the differential inductances from a computational time point of view.

G.5 MEANING OF INCREMENTAL PERMEABILITY

At first, consider a unidimensional problem, where it is true that

$$B = \mu H$$

Taking the derivative with respect to H, we obtain the incremental permeability definition

$$\mu_{\mathrm{inc}}(H) = \frac{\mathrm{d}B}{\mathrm{d}H} = \frac{\mathrm{d}\mu}{\mathrm{d}H} H + \mu \tag{G.3}$$

In a 2-dimensional cartesian coordinate system we may write

$$\boldsymbol{B} = \mu(\boldsymbol{H})\boldsymbol{H} = \mu(|\boldsymbol{H}|)\boldsymbol{H}$$

where

$$|\boldsymbol{H}| = \sqrt{H_x^2 + H_y^2}$$

Explicitly, this means

$$\begin{Bmatrix} B_x \\ B_y \end{Bmatrix} = \mu(|\boldsymbol{H}|) \begin{Bmatrix} H_x \\ H_y \end{Bmatrix}$$

provided that the material is isotropic in the considered plane. We could write the linearized problem using Taylor first order approximation

around a working point, identified by the magnetic field $\boldsymbol{H}_0$ and the magnetic flux density $\boldsymbol{B}_0$:

$$\boldsymbol{B} \approx \boldsymbol{B}_0 + \left.\frac{\partial \boldsymbol{B}}{\partial \boldsymbol{H}}\right|_{\boldsymbol{H}_0} \cdot (\boldsymbol{H} - \boldsymbol{H}_0) \tag{G.4}$$

where $\cdot$ is the scalar product between the matrix and the vector. The term $\partial \boldsymbol{B}/\partial \boldsymbol{H}$ is the 2-by-2 Jacobian matrix, and it is actually the definition of the incremental permeability $\overleftrightarrow{\boldsymbol{\mu}}$ tensor. In 2D cartesian coordinates, it results

$$\mu_{xx} = \frac{\partial B_x}{\partial H_x} = \frac{\partial \mu}{\partial H}\frac{H_x^2}{\sqrt{H_x^2 + H_y^2}} + \mu$$

$$\mu_{xy} = \frac{\partial B_x}{\partial H_y} = \frac{\partial \mu}{\partial H}\frac{H_x H_y}{\sqrt{H_x^2 + H_y^2}}$$

$$\mu_{yy} = \frac{\partial B_y}{\partial H_y} = \frac{\partial \mu}{\partial H}\frac{H_y^2}{\sqrt{H_x^2 + H_y^2}} + \mu$$

$$\mu_{yx} = \frac{\partial B_y}{\partial H_x} = \mu_{xy}$$

When we are interested in the increment of $\boldsymbol{B}$, we may write (G.4) simply with

$$\boldsymbol{\delta B} = \overleftrightarrow{\boldsymbol{\mu}} \cdot \boldsymbol{\delta H}$$

Now, let us consider the case of a horizontal magnetic field, $\boldsymbol{H}_0$, so

$$\boldsymbol{H}_0 = \begin{Bmatrix} H_0 \\ 0 \end{Bmatrix}, \qquad \boldsymbol{B}_0 = \begin{Bmatrix} B_0 \\ 0 \end{Bmatrix} = \begin{Bmatrix} \mu(H_0) H_0 \\ 0 \end{Bmatrix}$$

Then the incremental magnetic permeability tensor becomes

$$\mu_{xx} = \left.\frac{\partial B_x}{\partial H_x}\right|_{\boldsymbol{H}_0} = \left.\frac{\partial \mu}{\partial H}\right|_{\boldsymbol{H}_0} H_0 + \mu(H_0)$$

$$\mu_{xy} = \left.\frac{\partial B_x}{\partial H_y}\right|_{\boldsymbol{H}_0} = \left.\frac{\partial B_y}{\partial H_x}\right|_{\boldsymbol{H}_0} = \mu_{yx} = 0$$

$$\mu_{yy} = \left.\frac{\partial B_y}{\partial H_y}\right|_{\boldsymbol{H}_0} = \mu(H_0)$$

Looking at the first of these equations, we see that the μ_{xx} expression coincides with the definition of incremental permeability given in (G.3).

Expressing the increments of the quantities, we may write

$$\delta B_x = \mu_{xx}\, \delta H_x = \mu_{\text{inc}}(H_0)\, \delta H_x$$

$$\delta B_y = \mu_{yy}\, \delta H_y = \mu(H_0)\, \delta H_y$$

It can be noted that the magnetic permeability acting along the main flux lines is the incremental one, while the apparent permeability is acting on the perpendicular direction.[1]

1 The incremental permeability represents the slope of the tangent to the *B*-*H* characteristic. The apparent permeability is the slope of the line connecting the working point along the *B*-*H* curve to the origin.

BIBLIOGRAPHY

Alberti, Luigi, Emanuele Fornasiero, Nicola Bianchi, and Silverio Bolognani (Aug. 2008). "Impact of Rotor Losses in a 12-Slot 10-Pole Axial Flux PM Machine". In: *2008 IEEE Industry Applications Society Annual Meeting*, pp. 1–8. DOI: 10.1109/08IAS.2008.52 (cit. on p. 7).

Alotto, Piergiorgio, Massimo Barcaro, Nicola Bianchi, and Massimo Guarnieri (2011). "Optimization of interior PM motors with Machaon rotor flux barriers". In: *IEEE Transactions on Magnetics* 47.5, pp. 958–961. ISSN: 00189464. DOI: 10.1109/TMAG.2010.2073450 (cit. on p. 4).

Babetto, Cristian, Giacomo Bacco, and Nicola Bianchi (2017). "Analytical Approach to Determine the Power Limit of High-Speed Synchronous Reluctance Machines". In: *2017 IEEE International Electric Machines and Drives Conference, IEMDC 2017*. Miami, FL, pp. 2306–2312. ISBN: 9781509042814. DOI: 10.1109/IEMDC.2017.8002316 (cit. on pp. 107, 111, 122).

Bacco, Giacomo (2018). *fluid: Free Fluid Flux-Barriers Rotor for Synchronous Reluctance Motor Drawing*. DOI: 10.5281/zenodo.1214465. URL: https://github.com/gbacco5/fluid (visited on 05/11/2019) (cit. on p. 29).

Bacco, Giacomo and Nicola Bianchi (2017). "Choice of flux-barriers position in synchronous reluctance machines". In: *2017 IEEE Energy Conversion Congress and Exposition (ECCE)*. Cincinnati, OH, pp. 1872–1879. DOI: 10.1109/ECCE.2017.8096023 (cit. on pp. 4, 59, 72, 74, 84, 107).

Barcaro, M. and N. Bianchi (May 2011). "Torque components in integral- and fractional-slot IPM machines". In: *in 2011 IEEE International Electric Machines Drives Conference (IEMDC)*, pp. 1340–1345. DOI: 10.1109/IEMDC.2011.5994800 (cit. on p. 60).

Barcaro, M., N. Bianchi, and F. Magnussen (May 2009). "Rotor flux-barrier geometry design to reduce iron losses in synchronous IPM motors under FW operations". In: *IEEE International Electric Machines and Drives Conference, 2009. IEMDC '09*, pp. 928–935. DOI: 10.1109/IEMDC.2009.5075315 (cit. on pp. 5, 60).

Barcaro, M., N. Bianchi, and F. Magnussen (2010). "Rotor Flux-Barrier Geometry Design to Reduce Stator Iron Losses in Synchronous IPM Motors Under FW Operations". In: *IEEE Transactions on Industry Applications* 46.5, pp. 1950–1958. ISSN: 0093-9994. DOI: 10.1109/TIA.2010.2060175 (cit. on p. 5).

Barcaro, Massimo (2011). "Design and Analysis of Interior Permanent Magnet Synchronous Machines for Electric Vehicles". PhD Thesis.

University of Padova, p. 203. URL: http://paduaresearch.cab.unipd.it/3497/ (cit. on pp. 3, 42, 63, 64, 66).

Barcaro, Massimo and Nicola Bianchi (2014a). "Interior PM machines using ferrite to replace rare-earth surface PM machines". In: *IEEE Transactions on Industry Applications* 50.2, pp. 979–985. ISSN: 00939994. DOI: 10.1109/TIA.2013.2272549 (cit. on pp. 3, 121).

Barcaro, Massimo, Giovanni Meneghetti, and Nicola Bianchi (2014b). "Structural analysis of the interior PM rotor considering both static and fatigue loading". In: *IEEE Transactions on Industry Applications* 50.1, pp. 253–260. ISSN: 00939994. DOI: 10.1109/TIA.2013.2268048 (cit. on pp. 107, 111, 118).

Barcaro, Massimo, Mattia Morandin, Thomas Pradella, Nicola Bianchi, and Ivan Furlan (2016). "Iron saturation impact on high frequency sensorless control of synchronous permanent magnets motor". In: *Proceedings - 2016 22nd International Conference on Electrical Machines, ICEM 2016* 53.6, pp. 1085–1091. ISSN: 0093-9994. DOI: 10.1109/ICELMACH.2016.7732660 (cit. on p. 7).

Bianchi, N., S. Bolognani, D. Bon, and M. Dai Prè (Oct. 2006). "Rotor flux-barrier design for torque ripple reduction in synchronous reluctance motors". In: *Conference Record of the 2006 IEEE 41st Industry Application Annual Meeting*. Vol. 3. Tampa, FL, pp. 1193–1200. DOI: 10.1109/IAS.2006.256683 (cit. on pp. 5, 59, 60).

Bianchi, Nicola (2005). *Electrical Machine Analysis Using Finite Elements*. Power Electronics and Applications. Boca Raton: CRC Press. ISBN: 9781420057874 (cit. on p. 54).

Bianchi, Nicola (2006). "Analysis of the IPM motor - Part I". In: *Design, Analysis, and Control of Interior PM Synchronous Machines, Tutorial Course Notes IAS*. Ed. by Nicola Bianchi and Thomas M. Jahns. First. Seattle: CLEUP Padova. Chap. 3. ISBN: 8871788982 (cit. on p. 46).

Bianchi, Nicola and Massimo Barcaro (2008a). "Iron losses reduction in synchronous motors with anisotropic rotor". In: *Proceedings - 34th Annual Conference of the IEEE Industrial Electronics Society, IECON 2008*. 1. Orlando, FL, pp. 1258–1263. ISBN: 9781424417667. DOI: 10.1109/IECON.2008.4758135 (cit. on p. 48).

Bianchi, Nicola and Silverio Bolognani (2009a). "Sensorless-oriented design of PM motors". In: *IEEE Transactions on Industry Applications* 45.4, pp. 1249–1257. DOI: 10.1109/TIA.2009.2023387 (cit. on p. 131).

Bianchi, Nicola, Silverio Bolognani, Diego Bon, and Michele Dai Prè (2007). *Torque ripple of a synchronous reluctance motor: effect of the position of the flux–barriers and rotor design for its reduction*. Tech. rep. (cit. on p. 42).

Bianchi, Nicola, Silverio Bolognani, Diego Bon, and Michele Dai Prè (2009b). "Rotor flux-barrier design for torque ripple reduction in synchronous reluctance and PM-assisted synchronous reluctance motors". In: *IEEE Transactions on Industry Applications* 45.3, pp. 921–

928. ISSN: 00939994. DOI: 10.1109/TIA.2009.2018960 (cit. on pp. 4, 42, 46, 47, 54, 59, 60, 64, 66, 72, 73, 78, 79, 84, 107, 120, 121, 123).

Bianchi, Nicola, Silverio Bolognani, and Fabio Luise (2004). "Potentials and limits of high-speed PM motors". In: *IEEE Transactions on Industry Applications* 40.6, pp. 1570–1578. DOI: 10.1109/TIA.2004.836173 (cit. on p. 7).

Bianchi, Nicola, Siverio Bolognani, Diego Bon, and Michele Dai Prè (2008b). "Torque harmonic compensation in a synchronous reluctance motor". In: *IEEE Transactions on Energy Conversion* 23.2. ISSN: 08858969. DOI: 10.1109/TEC.2007.914357 (cit. on pp. 4, 5, 60).

Bianchi, Nicola and Emanuele Fornasiero (June 2009c). "Impact of MMF Space Harmonic on Rotor Losses in Fractional-Slot Permanent-Magnet Machines". In: *IEEE Transactions on Energy Conversion* 24.2, pp. 323–328. ISSN: 0885-8969. DOI: 10.1109/TEC.2008.2006557 (cit. on p. 7).

Bianchi, Nicola, Emanuele Fornasiero, and Silverio Bolognani (2013). "Effect of stator and rotor saturation on sensorless rotor position detection". In: *IEEE Transactions on Industry Applications* 49.3, pp. 1333–1342. ISSN: 00939994. DOI: 10.1109/TIA.2013.2253437 (cit. on pp. 7, 131).

Bianchi, Nicola, Emanuele Fornasiero, Enrico Carraro, Silverio Bolognani, and Mosè Castiello (2014). "Electric Vehicle Traction based on a PM Assisted Synchronous Reluctance Motor". In: *2014 IEEE International Electric Vehicle Conference, IEVC 2014*. Florence, pp. 6–11. ISBN: 9781479960750. DOI: 10.1109/IEVC.2014.7056146 (cit. on p. 54).

Bianchi, Nicola, Emanuele Fornasiero, Marco Ferrari, and Mosè Castiello (2016). "Experimental comparison of PM assisted synchronous reluctance motors". In: *IEEE Transactions on Industry Applications* 52.1, pp. 163–171. ISSN: 0093-9994. DOI: 10.1109/ECCE.2014.6954017 (cit. on pp. 54, 121, 123).

Binder, A., T. Schneider, and M. Klohr (July 2006). "Fixation of buried and surface-mounted magnets in high-speed permanent-magnet synchronous machines". In: *IEEE Transactions on Industry Applications* 42.4, pp. 1031–1037. ISSN: 0093-9994. DOI: 10.1109/TIA.2006.876072 (cit. on p. 6).

Boglietti, A., A. Cavagnino, M. Pastorelli, and A. Vagati (Oct. 2005). "Experimental comparison of induction and synchronous reluctance motors performance". In: *Industry Applications Conference, 2005. Fourtieth IAS Annual Meeting. Conference Record of the 2005*. Vol. 1, 474–479 Vol. 1. DOI: 10.1109/IAS.2005.1518350 (cit. on p. 3).

Boules, Nady (1981). "Impact of slot harmonics on losses of high-speed permanent magnet machines with a magnet retaining ring". In: *Electric Machines and Power Systems* 6.6, pp. 527–539. ISSN: 15210502. DOI: 10.1080/03616968108960089 (cit. on p. 7).

Bramerdorfer, Gerd, Juan A. Tapia, Juha J. Pyrhonen, and Andrea Cavagnino (2018). "Modern Electrical Machine Design Optimization: Techniques, Trends, and Best Practices". In: *IEEE Transactions on Industrial Electronics* 65.10, pp. 7672–7684. ISSN: 02780046. DOI: 10.1109/TIE.2018.2801805 (cit. on p. 28).

Castagnini, A., M. Garavaglia, F. Moriconi, and G. Secondo (2002). "Development of a very high speed and power synchronous PM motor". In: *Proc. of Int. Conf. Elect. Machine (ICEM)*. Brugges, Belgium, pp. 25–28 (cit. on pp. 6, 7).

Cavazzuti, Marco (2013). *Optimization Methods: From Theory to Design*. Modena, Italy: Springer, p. 962. ISBN: 9783642311864 (cit. on pp. 25, 26, 28).

Chalmers, B.J. and L. Musaba (Sept. 1998). "Design and field-weakening performance of a synchronous reluctance motor with axially laminated rotor". In: *IEEE Transactions on Industry Applications* 34.5, pp. 1035–1041. ISSN: 0093-9994. DOI: 10.1109/28.720443 (cit. on p. 3).

Chua, Leon O., Charles A. Desoer, and Ernest S. Kuh (1987). *Linear and Nonlinear Circuits*. Ed. by Sanjeev Rao and Alar E. Elken. McGraw-Hill. ISBN: 0-07-010898-6 (cit. on p. 45).

Corley, M.J. and R.D. Lorenz (1998). "Rotor position and velocity estimation for a permanent magnet synchronous machine at standstill and high speeds". In: *IEEE Transactions on Industry Applications* 34.4, pp. 784–789. DOI: 10.1109/ias.1996.556994 (cit. on p. 7).

Dular, P and C Geuzaine (n.d.). *GetDP reference manual: the documentation for GetDP, a general environment for the treatment of discrete problems* (cit. on pp. 118, 125).

Ferrari, Marco, Nicola Bianchi, and Emanuele Fornasiero (2015). "Analysis of rotor saturation in synchronous reluctance and PM-assisted reluctance motors". In: *IEEE Transactions on Industry Applications* 51.1, pp. 169–177. ISSN: 00939994. DOI: 10.1109/TIA.2014.2326056 (cit. on p. 54).

Fratta, Antonino, G.P. Troglia, Alfredo Vagati, and Franco Villata (1993). "Evaluation of torque ripple in high performance synchronous reluctance machines". In: *Rec. IEEE Ind. Appl. Soc. Annu. Meet.* Toronto, ON, Canada, pp. 163–170 (cit. on pp. 4, 5).

Fratta, Antonino, Franco Villata, and Alfredo Vagati (1992). "Permanent magnet assisted synchronous reluctance drive for constant-power application: Drive power limit". In: *Intelligent Motion European Conference, PCIM*. Nurnberg, Germany, pp. 196–203 (cit. on p. 3).

Gamba, Matteo (2017). "Design of non conventional Synchronous Reluctance machine". In: DOI: 10.6092/polito/porto/2669965 (cit. on p. 54).

Gerada, David, A. Mebarki, N. L. Brown, Chris Gerada, Andrea Cavagnino, and Aldo Boglietti (June 2014). "High-Speed Electrical Machines: Technologies, Trends, and Developments". In: *IEEE Transactions on Industrial Electronics* 61.6, pp. 2946–2959. ISSN: 0278-0046. DOI: 10.1109/TIE.2013.2286777 (cit. on p. 6).

Geuzaine, C (2008). "GetDP: a general finite-element solver for the de Rham complex". In: *PAMM Volume 7 Issue 1. Special Issue: Sixth International Congress on Industrial Applied Mathematics (ICIAM07) and GAMM Annual Meeting, Zürich 2007*. Vol. 7. Wiley, pp. 1010603–1010604 (cit. on p. 125).

Geuzaine, C, P Dular, and W Legros (1998). "A General Environment for the Treatment of Discrete Problems and its Application to Coupled Finite Element and Boundary Integral Methods". In: *Proceedings of the 8th International IGTE Symposium on Numerical Field Calculation in Electrical Engineering*. Graz (Austria) (cit. on p. 118).

Grauers, Anders (1996). "Directly driven wind turbine generators". In: *International Conference on Electrical Machines (ICEM)*. Vigo (Spain), pp. 417–422 (cit. on pp. 6, 83).

Guglielmi, Paolo, Michele Pastorelli, and Alfredo Vagati (2006). "Cross-saturation effects in IPM motors and related impact on sensorless control". In: *IEEE Transactions on Industry Applications* 42.6, pp. 1516–1522. ISSN: 00939994. DOI: 10.1109/TIA.2006.882646 (cit. on p. 7).

Han, Seok-Hee, W.L. Soong, and T.M. Jahns (2007). "An Analytical Design Approach for Reducing Stator Iron Losses in Interior PM Synchronous Machines During Flux-Weakening Operation". In: *2007 IEEE Industry Applications Annual Meeting*. New Orleans, pp. 103–110. ISBN: 978-1-4244-1259-4. DOI: 10.1109/07IAS.2007.36 (cit. on p. 48).

Howey, D. A., P. R. N. Childs, and A. S. Holmes (Mar. 2012). "Air-Gap Convection in Rotating Electrical Machines". In: *IEEE Transactions on Industrial Electronics* 59.3, pp. 1367–1375. ISSN: 0278-0046. DOI: 10.1109/TIE.2010.2100337 (cit. on p. 6).

Ikäheimo, J. and Kolehmainen, J. and Känsäkangas, T. and Kivelä V. and Moghaddam, Reza Rajabi (June 2014). "Synchronous High-Speed Reluctance Machine With Novel Rotor Construction". In: *IEEE Transactions on Industrial Electronics* 61.6, pp. 2969–2975. ISSN: 0278-0046. DOI: 10.1109/TIE.2013.2253077 (cit. on p. 7).

Jahns, Thomas M. and Wen L. Soong (1996). "Pulsating torque minimization techniques for permanent magnet AC motor drives - A

review". In: *IEEE Transactions on Industrial Electronics* 43.2, pp. 321–330. DOI: 10.1109/41.491356 (cit. on pp. 3, 4, 107, 120).

Jeong, Y., R. D. Lorenz, T. M. Jahns, and S. Sul (2005). "Initial Rotor Position Estimation of an Interior Permanent Magnet Synchronous Machine using Carrier-Frequency Injection Methods". In: *IEEE Transactions on Industry Applications* 41.1, pp. 1218–1223. DOI: 10.1109/IEMDC.2003.1210395 (cit. on p. 7).

Kamper, M. J. (2013). "Reluctance Synchronous Machine Drives – a Viable Alternative ?" In: *IEEE Joint IAS/PELS/IES Chapter Meeting. Graz (Austria)*. July (cit. on p. 3).

Kamper, M.J., F.S. van der Merwe, and S. Williamson (Sept. 1996). "Direct finite element design optimisation of the cageless reluctance synchronous machine". In: *IEEE Transactions on Energy Conversion* 11.3, pp. 547–555. ISSN: 0885-8969. DOI: 10.1109/60.537006 (cit. on p. 4).

Kano, Y., T. Kosaka, and N. Matsui (Mar. 2004). "Simple nonlinear magnetic analysis for interior permanent magnet synchronous motors". In: *Second International Conference on Power Electronics, Machines and Drives, (PEMD 2004). Conf. Publ. No.498*. Vol. 2, 781–786 Vol.2. DOI: 10.1049/cp:20040388 (cit. on p. 5).

Kano, Yoshiaki (2014). "Sensorless-oriented design of IPMSM". In: *2014 International Power Electronics Conference, IPEC-Hiroshima - ECCE Asia 2014*, pp. 2457–2464. DOI: 10.1109/IPEC.2014.6869934 (cit. on p. 131).

Krings, Andreas (2014). "Iron Losses in Electrical Machines — Influence of Material Properties, Manufacturing Processes, and Inverter Operation". PhD Thesis. KTH Royal Institute of Technology. ISBN: 9789175950990 (cit. on pp. 21, 22).

Kuehl, Sascha, Peter Landsmann, and Ralph M. Kennel (2012). "Compensating Angle Estimation Errors Caused by Magnetic Saturation in Anisotropy-Based Sensorless Control Schemes". In: *3rd IEEE International Symposium on Sensorless Control for Electrical Drives, SLED 2012*. 6. Milwaukee, WI, USA: IEEE, pp. 1–6. ISBN: 9781467329668. DOI: 10.1109/SLED.2012.6422803 (cit. on p. 7).

Kwon, Yong-Cheol, Joohyun Lee, and Seung-Ki Sul (2017). "Full Torque-Range Low-Speed Sensorless Drive for Heavily Saturated IPMSMs by Manipulation of Convergence Point". In: *2017 IEEE Energy Conversion Congress and Exposition (ECCE)*. Cincinnati, pp. 865–872. ISBN: 9781509029983 (cit. on pp. 7, 135).

Lampola, Petri (1998). "Electromagnetic Design of an Unconventional Directly Driven Permanent-Magnet Wind Generator". In: *International Conference on Electrical Machines (ICEM)1*. Istanbul (Turkey), pp. 1705–1710 (cit. on pp. 6, 83).

Lipo, T. A. (1991). "Synchronous Reluctance Machines-A Viable Alternative for AC Drives?" In: *Electric Machines & Power Systems* 19.6, pp. 659–671. ISSN: 0731-356X. DOI: 10.1080/07313569108909556 (cit. on p. 3).

Lipo, Thomas Anthony, Alfredo Vagati, T.J. Miller, Luigi Malesani, I. Boldea, and T. Fukao (1994). *Synchronous Reluctance Motors and Drives - A New Alternative*. Ed. by Alfredo Vagati and Thomas Anthony Lipo. Tutorial N. Denver: IEEE Industry Applications Society (cit. on pp. 3, 4).

Lopez-Torres, Carlos, Antonio Garcia Espinosa, Jordi Roger Riba, Gerhard Lux, and Luis Romeral (2018). "Computationally efficient design and optimization approach of PMa-SynRM in frequent operating torque-speed range". In: *IEEE Transactions on Energy Conversion* 8969.c, pp. 1–11. ISSN: 08858969. DOI: 10.1109/TEC.2018.2831249 (cit. on p. 5).

Lu, T. and A. Binder (2002). "Analytical and experimental analysis of losses in inverter-fed permanent magnet high-speed machines with surface-mounted magnets". In: *Proc. of Int. Conf. Elect. Machine (ICEM)*. Brugges, Belgium, pp. 25–28 (cit. on p. 7).

Manzolini, Virginia and Silverio Bolognani (2018). "On the Rotor Position Self-sensing Capability of IPM and Reluctance Synchronous Motors". In: *2018 IEEE 9th International Symposium on Sensorless Control for Electrical Drives (SLED)*. Vol. 0. 2. Helsinki, Finland: IEEE, pp. 108–113. ISBN: 9781538644553 (cit. on pp. 7, 135, 139).

Matsuo, T and T A Lipo (1994). "Rotor design optimization of synchronous reluctance machine". In: *IEEE Transactions on Energy Conversion* 9.2, pp. 359–365 (cit. on p. 4).

Mecrow, B. C., A. G. Jack, and J. M. Masterman (Sept. 1993). "Determination of rotor eddy current losses in permanent magnet machines". In: *1993 Sixth International Conference on Electrical Machines and Drives (Conf. Publ. No. 376)*, pp. 299–304 (cit. on p. 7).

Meeker, David (2015). *Finite Element Method Magnetics*. (Visited on 03/06/2019) (cit. on p. 114).

Miller, T. J. E. (1989). *Brushless Permanent-magnet and Reluctance Motor Drives*. Monographs in electrical and electronic engineering. Glasgow: Clarendon. URL: https://books.google.it/books?id=2AmxHwAACAAJ (cit. on pp. 15, 16).

Miller, T. J. E., A. Hutton, C. Cossar, and D. A. Staton (July 1991). "Design of a synchronous reluctance motor drive". In: *IEEE Transactions on Industry Applications* 27.4, pp. 741–749. DOI: 10.1109/28.85491 (cit. on p. 3).

Miller, T.J.E., M.I. McGilp, and M. Olaru (2000). "Finite elements applied to synchronous and switched reluctance motors". In: *IEE Seminar on*

Current Trends in the Use of Finite Elements (FE) in Electromechanical Design and Analysis (Ref. No. 2000/013), pp. 3/1–3/4. DOI: 10.1049/ic:20000050 (cit. on p. 4).

Moghaddam, R.-R., F. Magnussen, and C. Sadarangani (Sept. 2012a). "Novel rotor design optimization of Synchronous Reluctance Machine for low torque ripple". In: *2012 XXth International Conference on Electrical Machines (ICEM)*, pp. 720–724. DOI: 10.1109/ICElMach.2012.6349952 (cit. on p. 5).

Moghaddam, R.R., F. Magnussen, and C. Sadarangani (2010). "Theoretical and Experimental Reevaluation of Synchronous Reluctance Machine". In: *IEEE Transactions on Industrial Electronics* 57.1, pp. 6–13. DOI: 10.1109/TIE.2009.2025286 (cit. on p. 4).

Moghaddam, R.R., F. Magnussen, and C. Sadarangani (2012b). "Novel rotor design optimization of synchronous reluctance machine for high torque density". In: *6th IET International Conference on Power Electronics, Machines and Drives (PEMD 2012)*, B32–B32. ISBN: 978-1-84919-616-1. DOI: 10.1049/cp.2012.0256. URL: http://digital-library.theiet.org/content/conferences/10.1049/cp.2012.0256 (cit. on pp. 3, 4).

Moghaddam, Reza Rajabi (2011). "Synchronous Reluctance Machine (SynRM) in Variable Speed Drives (VSD) Applications". PhD Thesis. The Royal Institute of Technology, Stockholm. ISBN: 9789174159721. URL: http://www.diva-portal.org/smash/record.jsf?pid=diva2:417890 (cit. on p. 54).

Moghaddam, Reza Rajabi and Freddy Gyllensten (Sept. 2014). "Novel High-Performance SynRM Design Method: An Easy Approach for A Complicated Rotor Topology". In: *IEEE Transactions on Industrial Electronics* 61.9, pp. 5058–5065. DOI: 10.1109/TIE.2013.2271601 (cit. on p. 4).

Mohammadi, Mohammad Hossain (2015). "Rotor Design Optimization of Permanent Magnet–Assisted Synchronous Reluctance Machines for Traction Applications". Master Thesis. McGill University, Montreal, Quebec, Canada, p. 81 (cit. on p. 28).

Mohanarajah, T., J. Rizk, A. Hellany, M. Nagrial, and Alexey Klyavlin (2018). "Torque Ripple Improvement in Synchronous Reluctance Machines". In: *2018 2nd International Conference On Electrical Engineering (EECon)*. November, pp. 44–50. ISBN: 978-1-5386-7162-7. DOI: 10.1109/EECon.2018.8541021. URL: https://ieeexplore.ieee.org/document/8541021/ (cit. on p. 84).

Narzisi, Giuseppe (2008). *Multi-Objective Optimization*. New York City. DOI: 10.1007/978-3-540-88908-3 (cit. on p. 28).

Pellegrino, Gianmario, Francesco Cupertino, and Chris Gerada (May 2013). "Barriers shapes and minimum set of rotor parameters in the automated design of Synchronous Reluctance machines". In: *2013 International Electric Machines Drives Conference*, pp. 1204–1210. DOI: 10.1109/IEMDC.2013.6556286 (cit. on p. 4).

Pellegrino, Gianmario, Paolo Guglielmi, Alfredo Vagati, and Franco Villata (2010). "Core losses and torque ripple in IPM machines: Dedicated modeling and design tradeoff". In: *IEEE Transactions on Industry Applications* 46.6, pp. 2381–2391. ISSN: 00939994. DOI: 10.1109/TIA.2010.2072971 (cit. on p. 48).

Popescu, Mihail, Andreea Mitulet, Rares Chihaia, Sergiu Nicolaie, Adrian Nedelcu, and Gabriela Oprina (2013). "Finite element analysis of a low speed permanent magnets synchronous generator with direct drive". In: *2013 - 8th International Symposium on Advanced Topics in Electrical Engineering, ATEE 2013*. ISBN: 9781467359801. DOI: 10.1109/ATEE.2013.6563398 (cit. on pp. 6, 83).

Rawlings, Rees D (2009). *Materials Science and Engineering – Volume II*. Encyclopedia of Life Support Systems; Physical Sciences, Eng. Singapore: EOLSS Publishers Company Limited. ISBN: 9781848260337 (cit. on pp. 11, 12).

Salon, S (2012). *Finite Element Analysis of Electrical Machines*. Power Electronics and Power Systems. Springer US. ISBN: 9781461523499 (cit. on p. 54).

Sanada, M., K. Hiramoto, S. Morimoto, and Y. Takeda (2004). "Torque ripple improvement for synchronous reluctance motor using an asymmetric flux barrier arrangement". In: *IEEE Transactions on Industry Applications* 40.4 (cit. on p. 120).

Silvester, P P and R L Ferrari (1996). *Finite Elements for Electrical Engineers*. Cambridge University Press. ISBN: 9780521449533 (cit. on p. 54).

Staton, D.A., T.J.E. Miller, and S.E. Wood (1993). "Maximising the saliency ratio of the synchronous reluctance motor". In: *Electric Power Applications* 140.4, pp. 249–259. DOI: 10.1049/ip-b.1993.0031 (cit. on p. 4).

Storn, Rainer and Kenneth Price (1997). "Differential Evolution – A Simple and Efficient Heuristic for global Optimization over Continuous Spaces". In: *Journal of Global Optimization* 11.4, pp. 341–359. DOI: 10.1023/A:1008202821328. URL: http://dx.doi.org/10.1023/A:1008202821328 (cit. on p. 28).

Taghavi, Seyedmorteza and Pragasen Pillay (2017). "Design Aspects of a 50hp 6-pole Synchronous Reluctance Motor for Electrified Powertrain". In: *IECON 2017*. ISBN: 9781538611265 (cit. on p. 3).

Vagati, A., B. Boazzo, P. Guglielmi, and G. Pellegrino (2012). "Ferrite assisted synchronous reluctance machines: A general approach". In: *Proceedings - 2012 20th International Conference on Electrical Machines, ICEM 2012*. ISBN: 9781467301428. DOI: 10.1109/ICElMach.2012.6350047 (cit. on p. 84).

Vagati, A., A. Canova, M. Chiampi, M. Pastorelli, and M. Repetto (July 2000). "Design refinement of synchronous reluctance motors through finite-element analysis". In: *IEEE Transactions on Industry Applications* 36.4, pp. 1094–1102. ISSN: 0093-9994. DOI: 10.1109/28.855965 (cit. on p. 4).

Vagati, A., G. Franceschini, I. Marongiu, and G.P. Troglia (1992). "Design criteria of high performance synchronous reluctance motors". In: *Conference Record of the 1992 IEEE Industry Applications Society Annual Meeting*, pp. 66–73. DOI: 10.1109/IAS.1992.244463 (cit. on p. 4).

Vagati, Alfredo, Michele Pastorelli, Giovanni Franceschini, and S. C. Petrache (1998). "Design of low-torque-ripple synchronous reluctance motors". In: *IEEE Transactions on Industry Applications* 34.4, pp. 758–765. ISSN: 00939994. DOI: 10.1109/28.703969 (cit. on pp. 3, 5, 54, 59, 60, 107, 110).

Van der Veen, J. L. F., L. J. J. Offringa, and A. J. A. Vandenput (Sept. 1997). "Minimising rotor losses in high-speed high-power permanent magnet synchronous generators with rectifier load". In: *IEE Proceedings - Electric Power Applications* 144.5, pp. 331–337. ISSN: 1350-2352. DOI: 10.1049/ip-epa:19971354 (cit. on p. 7).

Wang, L. and R.D. Lorenz (Oct. 2000). "Rotor Position Estimation for Permanent Magnet Synchronous Motor using Saliency–Tracking Self–Sensing Method". In: *Proc. IEEE Ind. App. Soc. Annual Meeting* 1, 445–450 (cit. on p. 3).

Wang, Yawei, Giacomo Bacco, and Nicola Bianchi (2017). "Geometry Analysis and Optimization of PM-Assisted Reluctance Motors". In: *IEEE Transactions on Industry Applications* 53.5, pp. 1–1. ISSN: 0093-9994. DOI: 10.1109/TIA.2017.2702111. URL: http://ieeexplore.ieee.org/document/7921587/ (cit. on pp. 83, 110, 116).

Yang, Shih Chin and Yu Liang Hsu (2017). "Full Speed Region Sensorless Drive of Permanent-Magnet Machine Combining Saliency-Based and Back-EMF-Based Drive". In: *IEEE Transactions on Industrial Electronics* 64.2, pp. 1092–1101. DOI: 10.1109/TIE.2016.2612175 (cit. on p. 7).

Zhang, F., G. Du, T. Wang, G. Liu, and W. Cao (Sept. 2015). "Rotor Retaining Sleeve Design for a 1.12-MW High-Speed PM Machine". In: *IEEE Transactions on Industry Applications* 51.5, pp. 3675–3685. ISSN: 0093-9994. DOI: 10.1109/TIA.2015.2423659 (cit. on p. 6).

Zhao, Wenliang, Dezhi Chen, Thomas A. Lipo, and Byung Il Kwon (2015). "Performance Improvement of Ferrite-Assisted Synchronous Reluctance Machines Using Asymmetrical Rotor Configurations". In: *IEEE Transactions on Magnetics* 51.11, pp. 1–4. DOI: 10.1109/TMAG.2015.2436414 (cit. on p. 4).

Zhou, Guihou, Xiaohui Xu, Yong Xiong, and Lichun Zhang (2017). "Design and analysis of low-speed high torque direct-driven permanent magnet synchronous machines(PMSM) with fractional-slot concentrated winding used in coal mine belt conveyor system". In: *2017 20th International Conference on Electrical Machines and Systems, ICEMS 2017*. ISBN: 9781538632468. DOI: 10.1109/ICEMS.2017.8056054 (cit. on pp. 6, 83).

Zhu, Z. Q., Y. Li, D. Howe, and C. M. Bingham (2007). "Compensation for rotor position estimation error due to cross-coupling magnetic saturation in signal injection based sensorless control of PM brushless AC motors". In: *Proceedings of IEEE International Electric Machines and Drives Conference, IEMDC 2007*. Vol. 1. Antalya, Turkey, pp. 208–213. ISBN: 1424407435. DOI: 10.1109/IEMDC.2007.383578 (cit. on p. 7).

Zhu, Z. Q., K. Ng, and David A Howey (1997). "Design and analysis of high-speed brushless permanent magnet motors". In: *Proc. of Electrical Machines and Drives (EMD) Conf.* Pp. 381–385 (cit. on pp. 6, 7).

BEMF	back electromotive force.
CAD	Computer-Aided Design.
CPSR	Constant Power Speed Range.
DE	Differential Evolution.
EA	Evolutionary Algorithm.
EMF	electromotive force.
FE	Finite Element.
FEA	Finite Element Analysis.
FEM	Finite Element Method.
FEO	Finite-Element-based Approach.
FW	Flux-Weakening.
GA	Genetic Algorithm.
GT	Game Theory–based Optimization.
HF	high-frequency.
HS	high-speed.
IM	Induction Motor.
IPM	Interior Permanent Magnet.
MMF	magnetomotive force.
MST	Maxwell Stress Tensor.
MTPA	Maximum Torque Per Ampere.
MTPV	Maximum Torque Per Voltage.
MTPVA	Maximum Torque Per Volt-Ampere.
PM	Permanent Magnet.
PMASYR	Permanent Magnet assisted Synchronous Reluctance.
PMASYRM	Permanent Magnet assisted Synchronous Reluctance Motor.

PSO	Particle Swarm Optimization.
RBF	Radial Basis Function.
RE	rare-earth.
RHS	right-hand side.
RMS	Root Mean Square.
SA	Simulated Annealing.
SADA	Semi-Analytical Design Approach.
SPM	Surface-mounted Permanent Magnet.
SyR	Synchronous Reluctance.
SyRM	Synchronous Reluctance Machine.

$\boldsymbol{A}$	The incidence matrix	
α_i^{e}	The current electric angle	[rad]
α_{s}	The slot angle	[rad]
$\alpha_{\mathrm{s}}^{\mathrm{e}}$	The slot electric angle	[rad]
B_{g}	The air-gap peak flux density	[T]
$\mathcal{B}_{\mathrm{g}}$	The air-gap flux density spatial distribution	[T]
B_{rem}	The remanence of a permanent magnet	[T]
B_{t}	The tooth flux density	[T]
B_{y}	The yoke flux density	[T]
D_{e}	The stator outer diameter	[m]
$\Delta\vartheta$	The position estimation error	[rad]
D_{r}	The rotor diameter	[m]
D_{s}	The stator inner diameter	[m]
D_{sh}	The shaft diameter	[m]
e	The Euler's number	
ℓ_x	The generic differential inductance	[H]
ℓ_d	The d-axis differential inductance	[H]
ℓ_Δ	The half-difference of the self differential inductances along the q and d axis	[H]
ℓ_{dq}	The cross-saturation differential inductance	[H]
ℓ_q	The q-axis differential inductance	[H]
ℓ_{qd}	The second cross-saturation differential inductance	[H]
ℓ_Σ	The half-sum of the self differential inductances along the q- and d-axis	[H]
$\Gamma_{\tilde{q}\tilde{d}}$	The inverse of the inductance which relates the estimated q-axis current with the estimated d-axis voltage	[1/H]
H_{c}	The magnetic coercive force	[A m]
$H_{\mathrm{c}B}$	The coercive force of the magnetic flux density field	[A m]

H_{cJ}	The coercive force of the magnetization field	[A m]
h_s	The slot height	[m]
h_y	The stator yoke height	[m]
$\boldsymbol{I}$	The identity matrix	
I_w	The phase winding current	[A]
j	The imaginary unit	
k_{air}	The rotor magnetic insulation ratio	
k_{fill}	The slot fill factor	
k_{pack}	The lamination packing factor	
$\mathcal{K}_s$	The stator electric loading spatial distribution	[A/m]
λ_{mg}	The PM flux linkage	[Wb]
l_b	The flux-barrier length	[m]
L_{stk}	The length of the lamination stack	[m]
$\mathcal{M}$	A generic conformal mapping	
μ_0	The magnetic permeability of free space	[H/m]
μ_{rec}	The magnet recoil permeability	
N_b	The number of flux-barriers	
N_c	The number of series conductor per phase	
n_c	The number of actual conductors in the slot	
n_{pp}	The number of the winding parallel paths	
N_s	The number of series conductor per phase	
ω	The angular frequency	[rad/s]
p	The number of pole pairs	
p_s	The slot pitch	[m]
Q	The number of stator slots	
$\mathfrak{R}$	The generic reluctance	[H^{-1}]
Res	The number of points used to discretize the domain	
S_c	The actual cross-section area of the conductors	[m^2]

$S_{c,eq}$	The equivalent cross-section area of the conductors	[m²]
S_{slot}	The surface of the slot cross section	[m²]
t_b	The flux-barrier thickness	[m]
ϑ_b	The flux-barrier angle	[rad]
ϑ_b^e	The flux-barrier electrical angle	[rad]
ϑ^e	The generic electrical angular coordinate	[rad]
ϑ_m	The rotor angular position	[rad]
ϑ_m^e	The rotor electrical angular position	[rad]
ϑ_r	The generic angular coordinate in the rotor reference frame	[rad]
ϑ_s	The generic angular coordinate in the stator reference frame	[rad]
THD	The Total Harmonic Distortion	
t	The time	[s]
t_m	The permanent magnet thickness	[m]
$\langle T_m \rangle$	The average torque	[N m]
T_m	The electromechanical torque	[N m]
ΔT_m	The torque ripple	[N m]
U_r	The rotor magnetic scalar potential	[A]
$\mathcal{U}_r$	The rotor magnetic scalar potential spatial distribution	[A]
$\mathcal{U}_s$	The stator magnetic scalar potential spatial distribution	[A]
w_c	The flux-carrier width	[m]
w_m	The permanent magnet width	[m]
w_{rib}	The width of iron ribs	[m]
w_s	The slot width	[m]
w_t	The tooth width	[m]
ξ	The saliency ratio of synchronous reluctance machines	

PUBLICATIONS

JOURNAL PAPERS

Babetto, Cristian, Giacomo Bacco, and Nicola Bianchi (2018a). "Analytical Power Limits Curves of High-Speed Synchronous Reluctance Machines". In: *IEEE Transactions on Industry Applications* 55.2, pp. 1–8. ISSN: 00939994. DOI: 10.1109/TIA.2018.2875663.

Babetto, Cristian, Giacomo Bacco, and Nicola Bianchi (2018b). "Design Methodology for High Speed Synchronous Reluctance Machines". In: *IET Electric Power Applications* 12.8. DOI: 10.1049/iet-epa.2017.0872.

Babetto, Cristian, Giacomo Bacco, and Nicola Bianchi (2018c). "Synchronous Reluctance Machine Optimization for High Speed Applications". In: *IEEE Transactions on Energy Conversion* 33.3, p. 1. ISSN: 0885-8969. DOI: 10.1109/TEC.2018.2800536.

Bacco, Giacomo and Nicola Bianchi (2019). "Design Criteria of Flux-Barriers in Synchronous Reluctance Machines". In: *IEEE Transactions on Industry Applications* 55.3, pp. 2490–2498. ISSN: 00939994. DOI: 10.1109/TIA.2018.2886778.

Bacco, Giacomo, Nicola Bianchi, and Hanafy Mahmoud (2018). "A Nonlinear Analytical Model for the Rapid Prediction of the Torque of Synchronous Reluctance Machines". In: *IEEE Transactions on Energy Conversion* 33.3. ISSN: 0885-8969. DOI: 10.1109/TEC.2018.2808168. URL: http://ieeexplore.ieee.org/document/8295251/.

Castagnaro, Emanuel, Giacomo Bacco, and Nicola Bianchi (2019). "Impact of the Geometry on the Rotor Iron Losses in Synchronous Reluctance Motors". In: *IEEE Transactions on Industry Applications*, pp. 1–1. ISSN: 0093-9994. DOI: 10.1109/tia.2019.2939508.

Mahmoud, Hanafy, Giacomo Bacco, Michele Degano, Nicola Bianchi, and Chris Gerada (2018). "Synchronous Reluctance Motor Iron losses: Considering Machine Non-Linearity at MTPA, FW, and MTPV Operating Conditions". In: *IEEE Transactions on Energy Conversion* 33.3, pp. 1402–1410. ISSN: 08858969. DOI: 10.1109/TEC.2018.2811543.

Mahmoud, Hanafy, Nicola Bianchi, Giacomo Bacco, and Nicola Chiodetto (2017). "Nonlinear Analytical Computation of the Magnetic Field in Reluctance Synchronous Machines". In: *IEEE Transactions on Industry Applications* 53.6, pp. 5373–5382. ISSN: 00939994. DOI: 10.1109/TIA.2017.2746560.

Millinger, Jonas, Giacomo Bacco, Virginia Manzolini, Oskar Wallmark, and Nicola Bianchi (2019). "Design and Evaluation of a

Short-Circuit Rotor-Ring for Enhanced Self-Sensing Capability in a Slotless PM Motor". In: *IEEE Transactions on Industrial Electronics*, pp. 1–1. ISSN: 0278-0046. DOI: 10.1109/TIE.2019.2921266. URL: https://ieeexplore.ieee.org/document/8734887/.

Wang, Yawei, Giacomo Bacco, and Nicola Bianchi (2017). "Geometry Analysis and Optimization of PM-Assisted Reluctance Motors". In: *IEEE Transactions on Industry Applications* 53.5, pp. 1–1. ISSN: 0093-9994. DOI: 10.1109/TIA.2017.2702111. URL: http://ieeexplore.ieee.org/document/7921587/.

Wang, Yawei, Mattia Filippini, Giacomo Bacco, and Nicola Bianchi (2019). "Parametric Design and Optimization of Magnetic Gears with Differential Evolution Method". In: *IEEE Transactions on Industry Applications* 55.4. DOI: 10.1109/TIA.2019.2901774.

CONFERENCE PAPERS

Babetto, Cristian, Giacomo Bacco, Grazia Berardi, and Nicola Bianchi (2017a). "High Speed Motors: a Comparison between Synchronous PM and Reluctance Machines". In: *2017 IEEE International Electric Machines and Drives Conference, IEMDC 2017*. Miami, FL, pp. 3927–3934. ISBN: 9781509029983. DOI: 10.1109/ECCE.2017.8096689.

Babetto, Cristian, Giacomo Bacco, and Nicola Bianchi (2017b). "Analytical Approach to Determine the Power Limit of High-Speed Synchronous Reluctance Machines". In: *2017 IEEE International Electric Machines and Drives Conference, IEMDC 2017*. Miami, FL, pp. 2306–2312. ISBN: 9781509042814. DOI: 10.1109/IEMDC.2017.8002316.

Bacco, Giacomo and Nicola Bianchi (2017). "Choice of flux-barriers position in synchronous reluctance machines". In: *2017 IEEE Energy Conversion Congress and Exposition (ECCE)*. Cincinnati, OH, pp. 1872–1879. DOI: 10.1109/ECCE.2017.8096023.

Bacco, Giacomo and Nicola Bianchi (2018). "Asymmetric Synchronous Reluctance Rotor Geometry Design: A Practical Approach". In: *2018 IEEE Energy Conversion Congress and Exposition, ECCE 2018*. Portland, OR. ISBN: 9781479973118. DOI: 10.1109/ECCE.2018.8558213.

Bacco, Giacomo, Nicola Bianchi, and Fabio Luise (2019). "High-Torque Low-Speed Permanent Magnet Assisted Synchronous Reluctance Motor Design". In: *2019 IEEE International Electric Machines and Drives Conference, IEMDC 2019*. San Diego, CA.

Castagnaro, Emanuel, Giacomo Bacco, and Nicola Bianchi (2018). "Rotor Iron Losses in High-Speed Synchronous Reluctance Motors". In: *Proceedings - 2018 23rd International Conference on Electrical Machines, ICEM 2018*. Alexandruopolis, pp. 1310–1316. ISBN: 9781538624777. DOI: 10.1109/ICELMACH.2018.8506888.

Lopez-Torres, Carlos, Giacomo Bacco, Nicola Bianchi, Antonio Garcia Espinosa, and Luis Romeral (2018). "A Parallel Analytical Computation of Synchronous Reluctance Machine". In: *Proceedings - 2018 23rd International Conference on Electrical Machines, ICEM 2018*. 1. Alexandruopolis, pp. 25–31. ISBN: 9781538624760. DOI: 10.1109/ICELMACH.2018.8507210.

Mahmoud, Hanafy, Michele Degano, Giacomo Bacco, Nicola Bianchi, and Chris Gerada (2018). "Synchronous Reluctance Motor Iron Losses: Analytical Model and Optimization". In: *2018 IEEE Energy Conversion Congress and Exposition, ECCE 2018*. Portland, OR. ISBN: 9781479973118. DOI: 10.1109/ECCE.2018.8558292.

Wang, Yawei, Giacomo Bacco, and Nicola Bianchi (2016). "Geometry Analysis and Optimization of PM-Assisted Reluctance Motors". In: *International Conference on Electrical Machines (ICEM)*. Lausanne, pp. 1758–1764. ISBN: 9781509025381. DOI: 10.1109/ICELMACH.2016.7732761. URL: http://ieeexplore.ieee.org/document/7921587/.

Wang, Yawei, Mattia Filippini, Giacomo Bacco, and Nicola Bianchi (2018). "Parametric Design and Optimization of Magnetic Gears with Differential Evolution Method". In: *2018 XIII International Conference on Electrical Machines (ICEM)*. Alexandruopolis: IEEE, pp. 919–925. ISBN: 9781538624760. DOI: 10.1109/ICELMACH.2018.8507160.

ACKNOWLEDGMENTS

I would like to start these acknowledgments thanking my supervisor, professor Nicola Bianchi, for giving me the opportunity to continue my studies with the PhD. He has always been extremely positive and supportive of my work and ideas, both as a supervisor and, more importantly, as a person.

I thank professors Silverio Bolognani and Luigi Alberti, who have always been helpful with their suggestions and advice in technical issues.

I am also much obliged with professor Marta Molinas for hosting me at NTNU and giving me the opportunity to live and work in the fantastic Norway.

One last person I thank among the “seniors" is Mosè Castiello. He may not be in EDLab anymore, but his speeches and technical skills are and will be unforgettable for the whole lab.

Now let’s start with the crew! There are a lot of people who crossed my path in EDLab, so I thank them all in chronological order, hoping to remember every single one of them: Damiano, Mattia, Yawei, Hanafy, Davide, Virginia, Nicola, Mahmoud, Enrico, Cristian, Grazia, Francesco, Matteo C., Milo, Emanuel, Diego, Paolo, Matteo B., Andrea, Junkyu, Chaelim, and Yongxi.

A special thank goes to Matteo Carbonieri for the invaluable technical discussions that we had on the induction motors and on electric motors in general.

I extend my acknowledgments to all the people of the other EDLabs of the network, Vicenza, Udine and Bolzano, as we had the chance to share together some nice moments, and some technicals aspects too!

I would also like to mention the visiting PhD students that we hosted in EDLab, since each one of them brought new experiences and perspectives to us: Werner, Anis, Hajer, Carlos, Jonas, and Ladislav.

Then, I would like to dedicate this work to my parents Sergio and Annalisa, and my brother Davide, whom I warmly thank for their amazing support and encouragement.

There is one last person, who has been next to me for most of this journey, that I would like to thank. But I will let this person unnamed, as it is unnecessary to say more.

COLOPHON

This document was typeset using the typographical look-and-feel `classicthesis` developed by André Miede and Ivo Pletikosić. The style was inspired by Robert Bringhurst's seminal book on typography "*The Elements of Typographic Style*". `classicthesis` is available for both LaTeX and LyX:

https://bitbucket.org/amiede/classicthesis/

The titlepage was inspired by the `suftesi` template included in the package called `frontespizio` developed by Enrico Gregorio.

Final Version as of November 26, 2019 (classicthesis v4.6).